Light-Matter Interaction in Plasmonic Systems and Atomic Vapor

by

Saumya Choudhary

Submitted in Partial Fulfillment of the

Requirements for the Degree

Doctor of Philosophy

Supervised by Professor Robert W. Boyd

Institute of Optics
Arts, Sciences and Engineering
Edmund A. Hajim School of Engineering and Applied Sciences

University of Rochester

Rochester, New York

2023

To my family and all of my teachers ...

Contents

Biographical Sketch

Saumya Choudhary was born in Bhagalpur, Bihar, India in 1991. She graduated from the Indian Institute of Technology, Dhanbad (known previously as the Indian School of Mines, Dhanbad) in 2013 with a Bachelor of Technology in Electronics and Communication Engineering. She then moved to the University of Ottawa, Canada to pursue a Master's in Applied Science in Electrical Engineering, which she obtained in 2016. While in Ottawa, she worked on metamaterials and the theory of parametric downconversion in the research group of Prof. Robert Boyd. She then joined the Institute of Optics, University of Rochester in Fall, 2015 to pursue her doctoral study, and continued her research with Prof. Boyd in Fall, 2016. She has since worked on several projects in nonlinear optics and nanophotonics under the guidance of Prof. Boyd.

The following publications were a result of the research conducted during her doctoral study:

Journal Articles

1. **S. Choudhary**, R. W. Boyd, and J. E. Sipe, "*Linear optical properties of meta-crystals of dipolar nanoantennas*". In preparation.
2. Y. Xu, **S. Choudhary**, and R. W. Boyd, "*Measurement of the bi-photon OAM spectrum with stimulated emission tomography*". In preparation.
3. **S. Choudhary**, A.N. Black, A. Antikainen, and R.W. Boyd, "*Controlling nonlinear rogue wave formation using the coherence length of phase noise*". Under review at Physical Review Research.
4. **S. Choudhary**, R.W. Boyd, and J.E. Sipe, "*Dark and bright modes, and their coherent control in dipolar metasurface bilayers*". Physical Review A, 107, 023521, 2023, Editor's suggestion.
5. **S. Choudhary**, S. Iqbal, M. Karimi, O. Reshef, M. Z. Alam, and R.W. Boyd, "*Ultra-strongly coupled plasmon polaritons in gold and epsilon-near-zero bi-films*". ACS Photonics, 10(1), pp.162-169, 2023. Featured on the cover of the issue.
6. A.N. Black, **S. Choudhary**, E. S. Arroyo-Rivera, H. Woodworth and R.W. Boyd, "*Suppression of nonlinear optical rogue wave formation using polarization-structured beams*". Physical Review Letters, 129, 133902, 2022.
7. A. Tcypkin, M. Zhukova, M. Melnik, I. Vorontsova, M. Kulya, S. Putilin, S. Kozlov, **S. Choudhary**, and R. W. Boyd, "*Giant Third-Order Nonlinear Response of Liquids at Terahertz Frequencies*". Physical Review Applied, 15(5), p.054009, 2021.
8. C. Liu, M. Z. Alam, K. Pang, K. Manukyan, O. Reshef, Y. Zhou, **S. Choudhary**, J. Patrow, A. Pennathurs, H. Song, Z. Zhao, R. Zhang, F. Alishahi, A.

Fallahpour, Y. Cao, A. Alamaiman, J. M. Dawalty, M. Tur, R. W. Boyd, and A. E. Willner, "*Photon Acceleration Using a Time-Varying Epsilon-near-Zero Metasurface*". ACS Photonics, 8(3), pp.716-720, 2021.

9. **S. Choudhary**, I. De Leon, S. Swiecicki, K.M. Awan, S.A. Schulz, J. Upham, M.Z. Alam, J.E. Sipe, and R.W. Boyd, "*Weak superradiance in arrays of plasmonic nanoantennas*". Physical Review A, 100(4), 043814, 2019.
10. S.A. Kozlov, A.A. Drozdov, **S. Choudhary**, M.A. Kniazev, and R.W. Boyd, "*Suppression of self-focusing for few-cycle pulses*". Journal of the Optical Society of America B, 36(10), pp.G68-G77, 2019.
11. **S. Choudhary**, R. Sampson, Y. Miyamoto, O.S. Magaña-Loaiza, S.M.H. Rafsanjani, M. Mirhosseini, and R. W. Boyd, "*Measurement of the radial mode spectrum of photons through a phase-retrieval method*". Optics letters, 43(24), pp.6101-6104, 2018.
12. S.G. Lukishova, A.C. Liapis, H. Zhu, E. Hebert, K. Kuyk, **S. Choudhary**, R. W. Boyd, Z. Wang, and L.J. Bissell, "*Plasmonic nanoantennas with liquid crystals for nanocrystal fluorescence enhancement and polarization selectivity of classical and quantum light sources*. Molecular Crystals and Liquid Crystals, 657(1), pp.173-183, 2017.

Conference Proceedings

1. A. Antikainen, D. Bhatt, **S. Choudhary**, and R. W. Boyd, "*Nonlinear Propagation of Polarization Knots*", presented at Frontiers in Optics and Laser Science, 2023.

2. Y. Xu, **S. Choudhary**, and R. W. Boyd, "*Efficient Measurement of Bi-photon OAM Spectrum with Stimulated Emission Tomography*", presented at Frontiers in Optics and Laser Science, 2023.
3. S. Vijayakumar, K. Vyas, O. Reshef, **S. Choudhary**, M. Song, D. H. G. Espinosa, R. W. Boyd, J. Cardenas, and K. Dolgaleva, "*Third-harmonic generation with higher-order phase-matching in silicon nitride waveguides*", in Optica Advanced Photonics Congress, Technical Digest Series (Optica Publishing Group, 2022), 2022.
4. A.N. Black, **S. Choudhary**, and R.W. Boyd, "*Suppression of caustic formation in polarization structured beams*", in Nonlinear Optics Topical meeting, 2021.
5. **S. Choudhary**, S. Iqbal, O. Reshef, M. Karimi, M. Z. Alam, and R.W. Boyd, "*Tightly-confined, long-range hybrid polaritonic modes for high-efficiency nonlinear guided wave interactions in gold and ITO bi-films*", in Nonlinear Optics Topical meeting, 2021.
6. **S. Choudhary**, S. Iqbal, O. Reshef, M. Karimi, M. Z. Alam, and R.W. Boyd, "*Ultra-strongly-coupled long-range, low-loss polaritonic modes in gold and indium tin oxide bi-films at NIR frequencies*", in Conference on Lasers and Electro-Optics, 2021.
7. **S. Choudhary**, S.D. Swiecicki, I. De Leon, S. A. Schulz, J. Upham, J. E. Sipe, and R. W. Boyd, "*Superradiance in arrays of plasmonic nanoantennas*", Frontiers in Optics , 2016.
8. **S. Choudhary**, S.D. Swiecicki, I. De Leon, S. A. Schulz, J. Upham, J.

E. Sipe, and R. W. Boyd, "*Superradiance in two-dimensional arrays of nanoantennas*", in Conference on Lasers and Electro-Optics, 2016.

Acknowledgments

My transition from a fresh college graduate to a researcher has been quite long, and very challenging at times. So first and foremost, I express my deep gratitude to my advisor Prof. Robert Boyd who has been a constant source of inspiration, support and guidance through this journey. His scientific intuition is unparalleled, and his ability to explain a complicated point very clearly and succinctly in simple language has always inspired me. Bob's immense enthusiasm for physics, his strong intuition, his attention to detail and his strong sense of ethics have been instrumental in providing me a template of what makes a great scientist. I will always value the freedom he gave to everyone of his students to pursue their ideas and broaden their research interests by engaging in a wide variety of projects.

Next, I thank Prof. John Sipe, who through his meticulousness, insight and attention to detail, has been invaluable in helping me develop my strength as a part-time theorist. I would also like to thank my committee members Prof. Jaime Cardenas and Prof. Pengfei Huo, and my committee chair Prof. Todd Krauss for

their valuable suggestions and time.

I consider myself extremely fortunate to have been surrounded by and have worked with my labmates and colleagues whom I regard as a highly talented group of scientists. I sincerely thank them for the collaboration, the enlightening discussions and the help that I have received from them. I would like to single out Nick Black, whom I worked very closely with during the latter half of my PhD. Nick is a fantastic experimentalist with a great intuition and a strong work ethic. He is also extremely organized and detail-oriented. Needless to say, I learned an awful lot by working and having many discussions with him, both scientific and otherwise. I thank the current and former members of the Boyd group in Rochester whom I have overlapped with for being excellent office and lab mates, as well as collaborators: Yiyu Zhou, Jiapeng Zhou, Boshen Gao, Mohammad Mirhosseini, Omar Magana-Loaiza, Seyed Mohammad Hashemi Rafsanjani, Saleem Iqbal, Long Nguyen, Dhanush Bhatt, Yang Xu, Yi Wang, Aku Antikainen, Surendar Vijaykumar and E. Samuel Arroyo-Rivera. I also thank Jerry Kuper for helping troubleshoot all of the various problems that popped up in the lab over these years, and for handling all of the financial aspects of research. I also thank both current and former members of the Boyd group in Ottawa for the invaluable collaboration and camaraderie over the years: Israel de Leon, Akbar Safari, Jeremy Upham, Sebastian Schulz, M. Zahirul Alam, Mohammad Karimi, Kashif Masud Awan, Orad Reshef, Boris Braverman and Giulia Marcucci.

I thank all the friends that I made in Rochester who made my long stay here way more interesting and fun: Amira Ahsan, Wooyoun Kim, Romita Chaudhuri, Sultan

Abdul Wadood, Usman Ali Javid, Zachary Manning, Gregory Jenkins, Marissa Granados-Baez, and Jesus Sanchez Juarez. They are all remarkable people who I am sure will go on to do great things in life. I also thank the people from Institute of Optics whom I have had the chance to interact with in various capacities.

Finally, I am immensely grateful for my family: my dear mother Ranjana Kumari, my father Shiv Kumar Choudhary, and my brother Rishav Choudhary. I am what I am today because of their love, support, and sacrifices that they made along the way to make sure that I got the best possible education. My parents had difficult childhoods, and had to overcome insurmountable odds in their lives. Their honesty, fortitude and work ethic will always be a source of inspiration to me. And lastly, my brother's constant unwavering support has helped me get through some of the most emotionally challenging times during grad school. He is a smart and talented scientist in his own right, and his accomplishments and work ethic continue to inspire me everyday.

Abstract

The interaction of light with a polarizable material at resonance can form hybrid states of light and matter called polaritons through strong coupling. Near-resonant interaction with light, or a vanishing material permittivity (epsilon-near-zero (ENZ)) can enhance nonlinear optical effects, such as self-focusing. We report on our studies of light-matter interaction in three different systems. Our first system is a bi-layered structure of a thin gold film on a thin ITO film that supports hybrid polariton modes. We experimentally characterize the dispersion of these modes, and show that they have propagation lengths of 4-8 μm while retaining mode confinement greater than that of the LR-SPP mode in gold films by nearly an order of magnitude. The unusual optical properties of ITO at ENZ frequencies make these bifilms useful for the active tuning of strong coupling, ultrafast switching, and enhanced nonlinear interactions at NIR frequencies.

In our second study, we show through experiment and an analytical model that in the limit where radiative broadening dominates, the extinction linewidth of a

planar array of dipolar nanoantennas scales linearly with the number of density of nanoantennas. We then extend our analytical model to a bilayer formed by stacking two such arrays with a sub-wavelength separation between them. We explain the formation of non-radiative “dark" and radiative “bright" modes through radiative coupling, and show the selective excitation of these modes through two counter-propagating normally incident fields. We further generalize our analytical model to a meta-crystal formed by multiple layers of such arrays, and derive closed form expressions for the linear optical properties of a semi-infinite meta-crystal and a thin meta-film. We observe a maximum effective refractive index of 4, and an octave-wide photonic stop band at near-infrared frequencies for realistic design parameters, and a very good agreement between their optical properties calculated through FDTD simulations and our model.

In our third study, we examine the interaction of a saturable self-focusing nonlinearity with phase instabilities on a field through the formation of rogue waves in a laser beam with added weak phase noise propagating through a hot rubidium vapor cell. We experimentally show that while the likelihood of rogue wave formation increases with laser power when the coherence length is only slightly smaller that the beam diameter, the likelihood is minimally affected by change in laser power when the coherence length is significantly smaller than the beam diameter. This result has implications for mitigating turbulence-induced breakup of intense laser beams, and developing optical radiance limiters.

Contributors and Funding Sources

This work was supervised by a dissertation committee consisting of Prof. Robert Boyd (advisor) from the Institute of Optics, Prof. Jaime Cardenas from the Institute of Optics, Prof. Pengfei Huo from the Department of Chemistry, and Prof. Todd D. Krauss (committee chair) from the Department of Chemistry and the Institute of Optics.

My contributions to each of the five projects presented in this thesis are summarized below:

1. Chapter 2: I built the experimental setup, performed the experiment and the data analysis, the numerical modeling, and wrote the first draft of the manuscript. The text in this chapter is largely a reproduction of the following published journal article that resulted from this work:

   S. Choudhary, S. Iqbal, M. Karimi, O. Reshef, M. Z. Alam, and R.W. Boyd, "*Strongly coupled plasmon polaritons in gold and epsilon-near-zero bifilms*". ACS Photonics, 10(1), pp.162-169, 2023.

Saleem Iqbal wrote the first version of the TMM code. Mohammad Karimi and Orad Reshef from University of Ottawa fabricated the bifilm samples. M. Zahirul Alam, also from the University of Ottawa, along with Orad Reshef, developed the idea for the project and had helpful inputs in the planning of the experiment. All co-authors subsequently helped in preparing the final version of the manuscript and getting it published.

2. Chapter 3: Robert Boyd conceived the original idea for this project. I built the experimental setup and performed the experiment. I also did the data analysis, the FDTD simulations, the analytical modeling, and wrote the first draft of the manuscript. The text in this chapter is largely a reproduction of the following published journal article that resulted from this work:

   S. Choudhary, I. De Leon, S. Swiecicki, K.M. Awan, S.A. Schulz, J. Upham, M.Z. Alam, J.E. Sipe, and R.W. Boyd, "*Weak superradiance in arrays of plasmonic nanoantennas*". Physical Review A, 100(4), 043814, 2019.

   Israel de Leon from the University of Ottawa helped to set up the experiment and develop the manuscript. Jeremy Upham and Sebastian Schulz did the first round of fabrication for samples that did not work as expected. Kashif Masud Awan fabricated the sample that was used for the measurements shown in the above manuscript. Prof. John Sipe from University of Toronto collaborated on developing the analytical model. Sylvia Swiecicki from University of Toronto did the first round of calculations using an earlier version of the analytical model. M. Zahirul Alam advised on some aspects of the sample design. All co-authors subsequently helped in preparing the

final version of the manuscript and getting it published.

3. Chapter 4: Prof. John Sipe conceived this project, and developed the analytical model for the bilayers. I performed all the analytical calculations, the FDTD simulations, and wrote the first draft of the manuscript. I also conceived the idea, and performed the analysis for the coherent perfect absorption part of this work. The text in this chapter is largely a reproduction of the following published journal article that resulted from this work:

   S. Choudhary, R.W. Boyd, and J.E. Sipe, "*Dark and bright modes, and their coherent control in dipolar metasurface bilayers*". Physical Review A, 107, 023521, 2023.

   All co-authors collaborated on revising the manuscript and getting it to its final form.

4. Chapter 5: Prof. John Sipe conceived this project, and developed the analytical model for the semi-infinite meta-crystal, and the meta-film with no near-field coupling between the planes. I extended the analytical model for the meta-film to the case where there is nearest-neighbor near-field coupling between the planes, performed the FDTD simulations, and described the model and the results in this chapter, which is currently in the process of being turned into a manuscript.

5. Chapter 6: Andy Nicholas Black built the experimental setup with my help, and he also helped with developing the idea and the data analysis. I conceived the idea, took the measurements, performed the data analysis, the numerical simulations and wrote the first draft of the manuscript. Aku Antikainen

helped with the numerical simulations. The text in this chapter is taken from the following manuscript that is currently under review at Physical Review Research:

S. Choudhary, A.N. Black, A. Antikainen, and R.W. Boyd, "*Controlling nonlinear rogue wave formation using the coherence length of phase noise*". All co-authors collaborated on revising the manuscript and getting it to its final form.

The content in chapter 2 was funded by the US Defense Advanced Research Projects Agency award W911NF-18-1-0369, the US Army Research Office award W911NF-18-1-0337, the Canada First Research Excellence Fund Award 072623, the Canada Research Chairs program award 950-231657, the Banting Postdoctoral Fellowships program, and the Natural Sciences and Engineering Research Council of Canada under Discovery Grant RGPIN/2017-06880. The content in chapters 4, 5 and 6 were funded by the US Office of Naval Research under Awards No. N00014-19-1-2247 and No. MURI N00014-20-1-2558, and by the Natural Sciences and Engineering Research Council of Canada and the Canada Research Chairs program. The content in chapter 3 was funded by the Natural Sciences and Engineering Research Council of Canada and the Canada Research Chairs program.

List of Figures

List of Acronyms

ENZ epsilon-near-zero

ITO tin-doped indium oxide

LR-SPP long-range surface plasmon polariton

SPP surface plasmon polariton

SR-SPP short-range surface plasmon polariton

NIR near-infrared

TM transverse magnetic

LSP(s) localized surface plasmon(s)

FDTD finite-difference time-domain

DDA discrete dipole approximation

FEM finite element method

TCO(s) transparent conducting oxide(s)

AZO aluminum-doped zinc oxide

GZO gallium-doped zinc oxide

ATR attenuated total reflection

TMM transfer matrix method

OSA optical spectrum analyzer

TE transverse electric

FWHM full width at half maximum

RWA rotating-wave approximation

NA numerical aperture

MLWA modified long wavelength approximation

CPA coherent perfect absorption

SLM spatial light modulator

LCOS liquid-crystal-on-silicon

MLE maximum likelihood estimation

NLSE nonlinear Schrödinger equation

SVD singular value decomposition

IPA isopropyl alcohol

PMMA polymethyl methacrylate

PSD power spectral density

1. Background

1.1 Introduction

The interaction of light with matter is a fundamental process behind a wide variety of phenomena studied across various disciplines such as optics, condensed matter physics, atomic physics and astrophysics. Light – an electromagnetic wave – interacts with a dielectric medium by inducing dipoles. The density of these induced dipoles is referred to as “polarization", which for sufficiently weak fields (or *linear* interactions) is proportional to the field [1]. A purely classical picture of this interaction is the Lorentz model in which each of these dipoles is modeled as a harmonic oscillator driven by the time-harmonic electric field. This picture of light-matter interaction is valid when both the field strength and the interaction are weak enough. Closer to material resonances, light-matter interaction can be strong enough to form hybrid states of light and matter called “polaritons". The dispersion curves of these polaritons shows the characteristic avoided-crossing associated with strong coupling of the photon and the material resonance. Some material excitations that form polaritons through strong coupling with light include phonons

in polar dielectrics, excitons in semiconductors [2], and plasmons in metals and doped semiconductors [3].

At large field intensities, the polarization depends *nonlinearly* on the electric field, and this scenario can be modeled by including anharmonicity in the Lorentz model [4]. For most materials, the nonlinear optical response is much weaker than the linear optical response. The nonlinear polarization is then obtained through the perturbation expansion of the anharmonic Lorentz model as a power series of the electric field. Examples of nonlinear optical effects include frequency conversion, harmonic generation, temporal soliton formation, self-focusing, beam breakup [4], and supercontinuum generation [5]. Under certain conditions, the nonlinear optical response can become large enough that it cannot be considered a perturbation to the linear optical response. One example is if the frequency of the driving field is very close to a material resonance, such as an optical transition in an atomic vapor. In the two-level approximation of this transition, the nonlinearity in this situation involves the excitation of an electron in the atom to a higher energy state by the field, and can saturate when most of the atoms have been excited. Another example of a system with a non-perturbative nonlinearity is when the material permittivity vanishes, also known as epsilon-near-zero (ENZ) [6–8]. In this regime, the change in refractive index due to nonlinearity can become as large as the linear refractive index [6].

1.2 Overview

This thesis discusses light-matter interaction in three different systems, and broadly touches on some of the aspects of this interaction mentioned above. In chapters 2-5, we study the linear optical properties of plasmonic materials. In chapter 2, we describe a bifilm structure that supports hybrid polariton modes formed by strong coupling between a surface plasmon polariton (SPP) and an ENZ mode. We discuss our experimental and theoretical characterization of the linear optical properties of these modes, and show that they inherit the desirable features of their constituent modes that make them good candidates for exploring nanophotonic applications based on large ultrafast optical nonlinearities. In chapters 3-5, we study a metamaterial made of plasmonic dipolar nanoantennas arranged in a crystal lattice – or a meta-crystal – of sub-wavelength lattice constants. We introduce in chapter 3 an analytical model based on the point dipole approximation to describe the experimentally observed number density dependent scaling of the radiative linewidth from a single array of nanoantennas. In chapter 4, we extend this analytical model to a bilayer of two of these arrays separated by a sub-wavelength distance and describe the formation of a bright (dark) mode that has a much larger (smaller) radiative damping than a single array. In chapter 5, we further extend this analytical model to a meta-crystal consisting of an infinite stack of such arrays, and a meta-film consisting of a finite number of these arrays, and derive closed-form expressions of their optical properties. We find that for realistic design parameters, it is possible to achieve an effective refractive index as large as 4 and an octave-

wide photonic stop band at near-infrared (NIR) frequencies. Additionally, our analytical model can be used to probe a wide range of geometric and material design parameters for the rational design of metamaterials for a plethora of nanophotonic applications. Finally, in chapter 6, we study the formation of nonlinear caustics and rogue waves in a laser beam with added phase noise propagating through hot rubidium vapor, which has a saturable self-focusing nonlinearity at frequencies close to the D2 transition of rubidium. The results of this study are relevant for the understanding the propagation dynamics of intense laser beams through turbulent media, and to prevent optical damage from the effects of turbulence-induced beam breakup.

Although the three systems discussed in this thesis appear disparate with regards to their platforms and application, they are connected through the overarching motivation of finding and understanding better ways to control light for applications related to communication, signal processing and computation. The next section of this chapter introduces some key concepts related to each of the three systems.

1.3 Key Concepts

1.3.1 Surface Plasmon Polaritons (SPP)

Metals and doped semiconductors possess free electrons that determine their interaction with light in contrast to dielectrics,wherein the interaction is dictated by bound charges. The material permittivity of these materials is given by the Drude model, and can have a large negative real part and a small imaginary part

at frequencies smaller than the plasma frequency. In this regime, it is possible for the free electron gas (or plasma) to support surface and volume charge density oscillations. For noble metals such as gold and silver, and doped semiconductors, this regime occurs at optical and NIR frequencies. A plasmon is a quantum of these charge density oscillations [3]. Plasmons confined at the interface of a metal (or a doped semiconductor) and a dielectric (with a positive real part of the permittivity) can couple strongly with light to form surface plasmon polaritons or SPP that can propagate along the interface. The SPP modes have a large near-field enhancement within the metal, and can localize the field below the diffraction limit at the interface. The field profile of these modes is evanescent in both media with the evanescent tail within the metal being significantly shorter than in the dielectric. The shorter evanescent tail within the lossier metal causes these modes to have long propagation lengths. For instance, the propagation length of SPP excited at the gold-air interface at a wavelength of 633 nm is $\approx 10\ \mu$m, and the length of the evanescent tails is 28 nm in gold and 328 nm in air [3]. Further, the dispersion curve of a SPP lies to the right of the dielectric's light line as its momentum is always larger than a photon propagating in the dielectric. Consequently, SPP modes cannot be excited by plane waves incident from the dielectric. The momentum matching condition that should be satisfied to excite these modes can be done through the use of evanescent waves [9] or grating couplers [10].

A metallic film with dielectrics at both interfaces supports SPP modes at each interface, which couple when the film thickness is very sub-wavelength. In a symmetric structure with the same dielectric on both sides of the film, there are two

coupled modes with even and odd field distributions about the center of the film. The even mode propagates at higher frequencies than the odd mode for the same propagation constant, and has lower losses and longer propagation than the odd mode. As such, the even mode is referred to as the “long range SPP" or LR-SPP, and the odd mode the “short range SPP" or SR-SPP [11]. In asymmetric structures with different dielectrics on both sides of the film, the LR-SPP (SR-SPP) mode becomes more confined along the interface with the dielectric of smaller (larger) refractive index. These modes can be excited through the evanescent tail of TM or p-polarized light that undergoes total internal reflection at the interface of a high-index prism and the metal-dielectric structure. In the Kretschmann-Raethar configuration of excitation, the metal film is directly in contact with the coupling prism, and SPP is launched at the interface opposite to the prism at the appropriate angle of incidence [9]. A successful excitation of the SPP manifests as a dip in the power of the reflected light as the incidence angle on the prism-metal interface is varied [3].

1.3.2 Localized Surface Plasmons (LSPs)

Localized surface plasmon(s) (LSP(s)) occur in metallic nanoparticles of sizes comparable to optical and NIR wavelengths. Here, the free electron cloud confined to their volume undergoes oscillations when excited by light at resonant frequencies. These localized plasmons can strongly absorb and scatter light at the resonance, and significantly enhance the local field [12, 13]. The optical properties of these resonances are strongly influenced by the material parameters

of the nanoparticle and its surrounding medium, as well as its shape and size [12]. The lowest order plasmon resonance is an electric dipole in which the entire electron cloud of the nanoparticle oscillates coherently with the electric field of the incident light. Higher-order multipolar resonances such as that of an electric quadrupole or a magnetic dipole can also contribute to the scattering and absorption properties to varying degrees depending on the geometric and material attributes of the nanoparticle. These properties are well described by the Mie theory for small spherical nanoparticles, which gives the exact expressions of scattering and absorption cross sections from solving the Maxwell's equations [14, 15]. For larger spheres, electrodynamic corrections associated with enhanced radiative damping and depolarization across the volume of the nanoparticle must be included. This analysis has also been extended to spheroids [12]. However, for nanoparticles of other shapes, one must rely on numerical techniques such as discrete dipole approximation (DDA), the multiple multipole method [16], and FDTD simulations to model the optical properties.

1.3.3 Epsilon-near-zero (ENZ)

Materials can show some very interesting properties when their permittivity (ε) vanishes [17], which is also referred to as epsilon-near-zero. A vanishing permittivity also implies vanishing of the refractive index ($n = \sqrt{\mu\varepsilon}$; μ is the relative permeability of the material), divergence of wavelength ($= \lambda_0/n$; λ_0 is the wavelength in vacuum) and phase velocity ($= c/n$; c is the speed of light in vacuum), and negligible phase variation on propagation through the medium. The last feature

also means that space and time are decoupled within the medium, and that the field oscillates only in time, and not in space. Further, the electromagnetic boundary condition that requires the continuity of the longitudinal component of electric displacement field across an interface leads to a large field enhancement and localization within the medium at ENZ. The ENZ behavior occurs naturally close to absorption resonances where the zero-crossing of the real part of permittivity would occur from Kramers-Kronig relations. Examples include metals and doped semiconductors at frequencies close to their plasma frequency, and polar dielectrics close to their longitudinal optical phonon resonance [18]. Transparent conducting oxide(s) (TCO(s)) such as tin-doped indium oxide (ITO), aluminum-doped zinc oxide (AZO) and gallium-doped zinc oxide (GZO) are degenerately-doped semiconductors whose permittivity, like metals, is also given by the Drude model. The plasma frequency of TCO(s) lies at NIR frequencies, and can be tuned by varying the free carrier concentration through doping during fabrication or through electrical gating [19]. Metamaterials such as a metal-dielectric stack can also be designed to have an ENZ behavior at a specific spectral range [20–22]. However, this ENZ behavior is usually anisotropic.

Some exotic linear optical phenomena that can occur in the ENZ regime include tunneling of fields through subwavelength channels and arbitrary bends in a waveguide [23], enhanced directionality of emission [24, 25] and absorption [26], inhibition or enhancement of spontaneous emission depending on the medium dimensionality [27], and improved spatial coherence of thermal emission [28]. The vanishing of permittivity also leads to an enhancement of nonlinear optical

processes such as harmonic generation [29–31], frequency conversion [32, 33], optical rectification [34], and intensity-dependent change in the refractive index [35] that could even become comparable to the linear refractive index [6]. This enhanced nonlinear response can be partly attributed to the slight increase in the third-order susceptibility, and to the aforementioned giant field enhancement and localization within the material that occurs in this regime [8, 30]. Additionally, the vanishing of refractive index relaxes the phase-matching conditions that must be satisfied for an efficient nonlinear optical response [36, 37]. Specifically in TCO(s), the origin of large nonlinearity at ENZ has been explained to be due to Fermi-smearing. In this process, the electron distribution in the conduction band changes on excitation by an intense optical field at frequencies smaller than the band-gap. The non-parabolicity of the conduction band in these materials thus leads to an intensity-dependent change in the effective mass of the electrons, and consequently a change in the plasma frequency and in turn, of the permittivity [6].

1.3.4 Filamentation in Atomic Vapor

Self-action effects occur when an intense beam of light propagating through a medium modifies its own propagation through the nonlinear optical response of the medium [4]. These effects occur when the second-order nonlinear index of refraction n_2 is positive. The total refractive index n, which is given by the relation

$$n = n_0 + n_2 I, \tag{1.1}$$

with n_0 being the linear refractive index and I being the transverse intensity of the beam, is larger where the beam intensity is higher. Typical laser beams have a larger intensity at the center than in the periphery, and they induce a positive lens through this nonlinear response. The beam would come to a focus within the medium, or “self-focus", if its power is higher than the critical power for self-focusing P_{cr}, which is given by [38]

$$P_{\mathrm{cr}} = \alpha \frac{\lambda_0^2}{4\pi n_0 n_2}. \tag{1.2}$$

Here, the parameter α depends on the initial intensity distribution of the beam, and approximately equals 1.896 for a Gaussian beam. In the simplest case, wherein there is no absorption within the medium and only the third-order nonlinearity is present, beam diffraction is the only competing effect against self-focusing. When self-focusing is perfectly balanced by the spreading of the beam due to diffraction, the beam gets trapped into a single “filament" that can propagate for several Rayleigh ranges without diffracting. At very high powers, the self-focusing nonlinearity can also amplify wavefront perturbations on a beam through four-wave mixing that could lead to beam breakup, wherein the beam acquires a random intensity distribution with several filaments. This process has also been referred to as small-scale filamentation [39], or multiple filamentation [40] in literature.

Atomic vapors can have a very large nonlinear response close to a resonant optical transition that saturates at large enough intensities [4, 41]. At frequencies higher (lower) than the resonance frequency, n_2 is positive (negative) and self-focusing (self-defocusing) can occur [42]. The absorption can also be very large

close to the resonance, and can also saturate at large enough intensities. Hence, in intense beams propagating through atomic vapors, the absorption as well as the saturation of the nonlinear response counteract the effect of self-focusing along with the diffraction. The saturation of nonlinearity and absorption can be fully accounted for when modeling the nonlinear propagation of beams through atomic vapor as the exact expression for the total intensity-dependent susceptibility is known [4]. In the absence of Doppler broadening of the resonance, the total intensity dependent susceptibility is given by [4]

$$\chi = \frac{-\alpha_0(0)}{\omega_{ba}/c} \frac{\Delta T_2 - i}{1 + \Delta^2 T_2^2 + |E|^2/|E_s^0|^2}. \tag{1.3}$$

Here $\alpha_0(0)$ is the linear absorption coefficient at the resonance, ω_{ba} is the resonance frequency of the transition, Δ is the frequency detuning of the beam from the resonance, T_2 is the dephasing time of the transition dipole, and E_s^0 is the strength of the field that saturates the resonant transition.

2. Strongly Coupled Plasmon Polaritons in Bifilms of Gold and Epsilon-Near-Zero Materials

2.1 Introduction

Two harmonic oscillators become strongly coupled when they exchange energy faster than the rate at which energy decays from the system. The coupled system has eigenstates that are a hybrid of those of the two uncoupled oscillators, and which show a characteristic avoided crossing of their dispersion lines around the degeneracy point of the uncoupled oscillators [43, 44]. Strong coupling between dipolar oscillators and a cavity has been achieved previously either by reducing the cavity mode volume, or by enhancing the oscillator strength [44–52]. SPPs supported by a metal-dielectric interface also have small mode volumes that make them excellent candidates for strong coupling to other localized modes [44, 53, 54]. The LR-SPP modes supported by thin metallic films can propagate for hundreds of

microns while having a large field confinement along the metal-dielectric interface [3, 55, 56].

Thin films of TCO(s), such as ITO, also support polaritons. Close to their plasma frequency, the LR-SPP mode of very thin TCO films is modified such that it has a very large and localized longitudinal field component within the film, and, unlike the highly dispersive LR-SPP mode in metallic films, has a flat dispersion line rendering it non-propagative. This special mode is referred to as the “ENZ" mode [57]. It is a collective excitation of free electrons in the TCO film that is strongly absorptive. Despite the considerable recent interest in the unusual linear and nonlinear optical phenomena in the ENZ regime [6, 8, 17, 22, 29, 30, 35–37, 58–61] , the large absorption losses associated with most ENZ materials has limited the experimental studies so far to sub-wavelength-thick films. Metamaterial resonators strongly coupled to the ENZ mode of TCO and other doped semiconductor films can enhance the nonlinear response through local field enhancement [62–65]. However, these coupled systems are still limited by their subwavelength interaction lengths. Hence, it is interesting to explore structures that support hybrid modes formed by strong coupling between the ENZ mode and guided modes, such as polaritons. Previous demonstrations of strong coupling between polaritons and the ENZ mode have been performed with phonon polaritons [66], and with plasmon polaritons [67] at mid-infrared frequencies.

IHere, we propose a bifilm structure consisting of a gold film deposited on a thin ITO film backed by a float glass substrate. This structure supports guided modes at NIR frequencies. Since the plasma frequency of gold lies in the ultraviolet

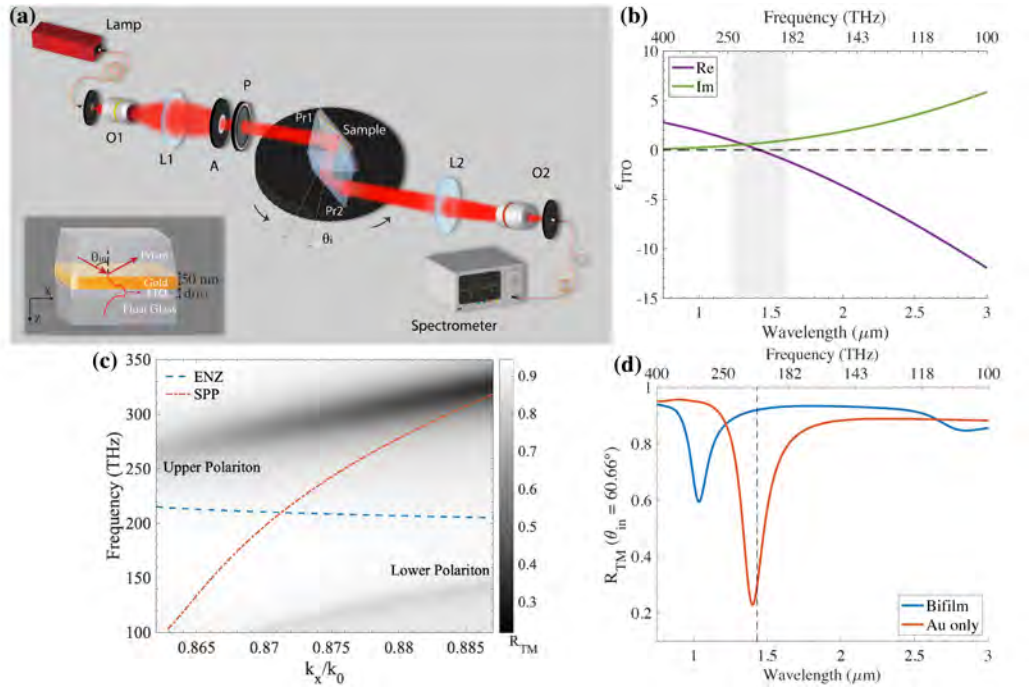

Figure 2.1: (a) Schematic of the experimental setup for measuring the reflectance maps using ATR spectroscopy in the Kretschmann-Raether [3] configuration. A 3D schematic of the sample is shown in the inset. (b) Permittivity spectrum of a representative ITO sample. The grayed region shows the absorption band of the ENZ mode. (c) Simulated reflectance map of TM-polarized light (R_{TM}) for a bifilm (inset in (a)) with 23-nm-thick film of the same ITO plotted against normalized wavevector ($k_N = k_x/k_0$; k_0 is the propagation constant within the prism) and frequency axes. The dispersion lines of the SPP mode (red, solid), and the ENZ mode (dashed, blue) are overlaid. (d) Linecut (blue) of the R_{TM} map in (b), and the R_{TM} spectrum of a standalone gold film (red) at an angle of incidence θ_{in} close to crossing of the SPP and the ENZ dispersion lines. The dashed black line indicates the ENZ frequency/wavelength.

region, the dispersion lines of the LR-SPP mode in the gold film and the ENZ mode in the ITO film cross around the ENZ region of ITO, which occurs at NIR frequencies. When placed in spatial proximity as in the bifilm structure [the inset in Fig. 2.1(a)], these constituent modes couple strongly in this ENZ region with a

strength dependent on their spatial overlap. The two hybrid modes thus formed have dispersion lines that show avoided (or anti) crossing, where they have at least an order of magnitude larger confinement in the ITO film than the LR-SPP mode in the gold film. Also, unlike the ENZ mode, they can propagate for several microns because of significantly lower losses. In section 2.2, we describe our experimental and simulation methods, and the results. We then examine the dependence of coupling strength of the constituent modes on the thickness of the ITO film in section 2.3, and show that ultra-strong coupling, wherein their coupling strength becomes comparable to the anti-crossing frequency [68, 69], can be achieved at certain thicknesses of the ITO film. Finally, we discuss the salient features of these hybrid polaritons such as propagation length, mode confinement, damping and field profiles in section 2.4.

2.2 Experiment and TMM simulations

Figure 2.1(c) shows an example of strong coupling behavior observed in the reflectance map R_{TM} of TM (or p)-polarized light obtained from TMM simulations of a representative bifilm made of a 50-nm-thick layer of gold and a 23-nm-thick layer of ITO. The permittivity ($\varepsilon_{\mathrm{ITO}}$) spectrum of ITO is shown in Fig. A.1(b). The permitivity of gold determined by Johnson and Christy [70] is used for all the calculations performed here. The hybrid polaritons are excited along the gold-ITO interface through use of a high-index N-SF11 prism in the Kretschmann-Raethar configuration [3, 9]. The dispersion of the coupling prism is excluded

in Fig. 2.1(c) by plotting the reflectance spectra in the normalized wavevector (k_x/k_0) and frequency (ν) space. The dispersion lines of the LR-SPP mode (red, dot-dashed), and the ENZ mode (blue, dashed) are obtained from the locus of minima of the reflectance map of a standalone gold film, and a standalone ITO film, respectively. The LR-SPP (just called SPP from now on for convenience) mode has a strongly wavevector dependent dispersion, while the ENZ mode has a flat dispersion pinned at the ENZ frequency. The two distinct branches of minima in the reflectance map correspond to the two hybrid modes of the bifilm, and they asymptotically approach the dispersion lines of the constituent SPP and ENZ modes away from their avoided crossing point.

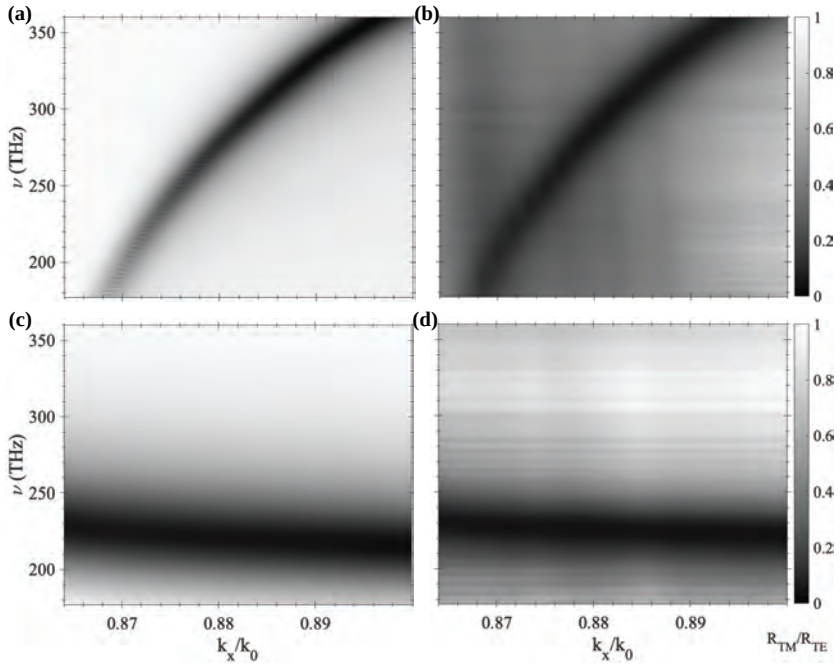

Figure 2.2: Reflectance maps of the standalone gold sample (top panels), and the standalone 23 nm thick ITO sample (bottom panels) obtained from TMM simulations (left), and measured experimentally (right).

We experimentally characterize the dispersion of bifilms through attenuated total reflection spectroscopy measurements. The fabrication procedure for these bifilms is described in appendix B.1. Figure 2.1(a) shows the schematic of the experimental setup used to measure the reflectance maps through attenuated total reflection spectroscopy. Broadband light from the halogen lamp is collimated using the objective O1. The exit pupil of the objective is imaged on the bifilm sample (cross-section shown in the inset) using the lens L1. The aperture A adjusts the spot size to avoid clipping the beam from the edges of the prisms. The thin film polarizer P transmits the TM-polarized component. The bifilm sample is kept in contact with an N-SF11 prism Pr1 with index-matching oil in between (Cargille series M 1.780). Another N-SF11 prism Pr2 redirects the reflected light from the diagonal face of the prism (and the sample) parallel to the incoming light. The prism and sample assembly is mounted on a rotation mount to vary the incidence angle on the sample. Another lens L2 images the sample onto the entrance pupil of a microscope objective O2, which couples the reflected light to a multi-mode fiber coupled spectrometer. We use an OSA (Agilent 86142A) to record the spectra from 600 nm to 1600 nm. We use an InGaAs spectrometer (customized SM304 from Spectral Products) to record the spectra from 1600 nm to 2300 nm. We take into account the shape of the blackbody spectrum of the lamp, the spectral response of the prisms and the oil, and the optical elements used in the setup by normalizing the TM-polarized reflectance spectrum from the sample at a particular incidence angle to the TE-polarized reflectance spectrum at the same angle. Before the spectral normalization, the detector noise in each spectrum is smoothed over first by using

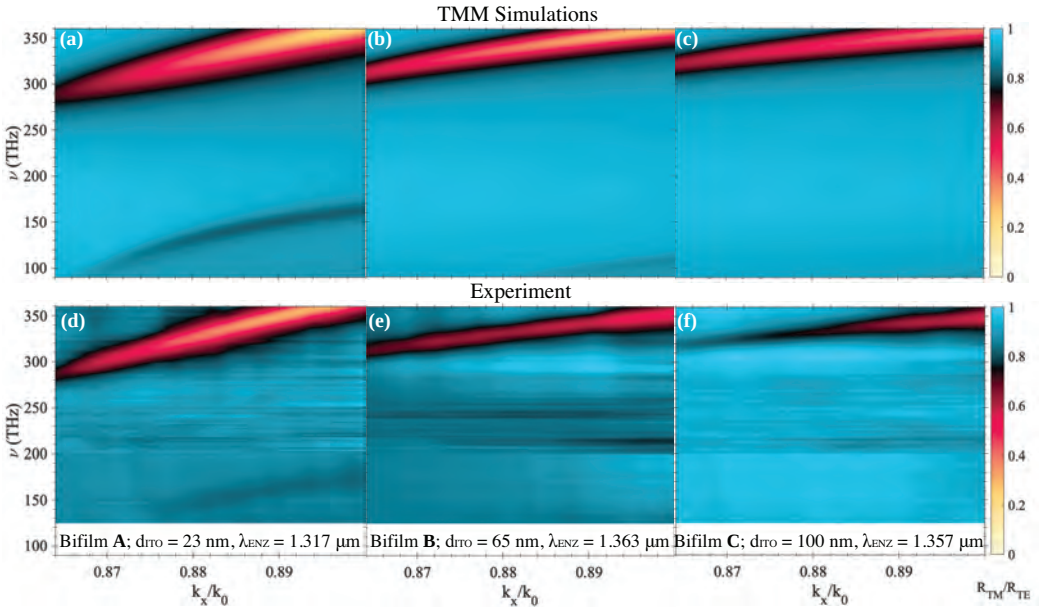

Figure 2.3: Simulated (top), and measured (bottom) reflectance maps of the three bifilm samples in the k_x/k_0-ν space. The TM-polarized reflectance spectra R_{TM} are normalized to the TE-polarized spectra R_{TE} at each incident wavevector to exclude measurement artifacts. The range of wavevectors is limited by the critical angle for the prism-substrate interface, and the maximum rotation of the prism-sample assembly possible without clipping the incoming field.

a Savtizky-Golay filter, and then by applying the wavelet transform.

The reflectance (R_{TM}/R_{TE}) maps of the standalone gold sample are shown in the top panels in Fig. 2.2, while the reflectance maps of the standalone 23-nm-thick ITO [permittivity spectrum shown in fig A.1(a)] sample are shown in the bottom panels. The simulated (measured) results are shown on the left (right) panel. As expected, the frequencies of the reflectance dips of the SPP mode in the standalone gold sample are strongly wavevector dependent, while the frequencies of the reflectance dips of the ENZ mode in the standalone ITO sample stay almost constant for all wavevectors. Figures 2.3(d)-(f) show the measured, and Fig. 2.3(a)-

(c) the simulated reflectance maps of three bifilm samples A, B and C, each with a 50-nm-thick gold film and ITO films with thicknesses (d_{ITO}) of 23 nm, 65 nm and 100 nm, respectively. The three ITO films have similar properties with their ENZ wavelengths at 1.317 μm, 1.363 μm and 1.357 μm, respectively. The permittivity spectra of the ITO films are shown in appendix A.1. We observe both the high frequency (upper), and the low frequency (lower) polariton branches in the measured (Fig. 2.3(d)) and the simulated (Fig. 2.3(a)) reflectance maps of the thinnest bifilm (A). The simulated maps of bifilms B and C show that the spectral separation between the two polariton branches, henceforth referred to as the “polariton band gap", increases with d_{ITO}.

2.2.1 The visibility of the lower polariton branch

We note that polaritons are said to be critically coupled when the coupling losses are balanced by the absorption losses [3]. The critical coupling condition at each frequency ν is given by the solutions to the characteristic equation in the complex wavevector k_x and real frequency ν space for which the $\mathrm{Im}[k_x]$ is minimized. These solutions depend on the geometrical parameters of the bifilm. The same set of parameters do not satisfy the critical coupling criterion for both the upper and the lower polariton simultaneously due to large polariton band gap. Consequently, while the upper polariton is coupled efficiently and has a prominent resonance dip, the lower polariton with its comparatively smaller resonance dip is not coupled as efficiently. This inefficient coupling and large absorption losses of the lower polariton contribute to its visibility being smaller than the upper polariton. For

bifilm C, the lower polariton branch is not visible in Fig. 2.3(c). However, it becomes more prominent if the absorption losses within ITO are reduced. We discuss the effect of losses on the visibility of the lower polariton branch below. The measured reflectance maps of bifilms B and C do not show the lower polariton branch as we are limited by the spectral range of our spectrometers and white light source. However, the measured, and the simulated maps for all three bifilms are in reasonable agreement in the spectral range shown here.

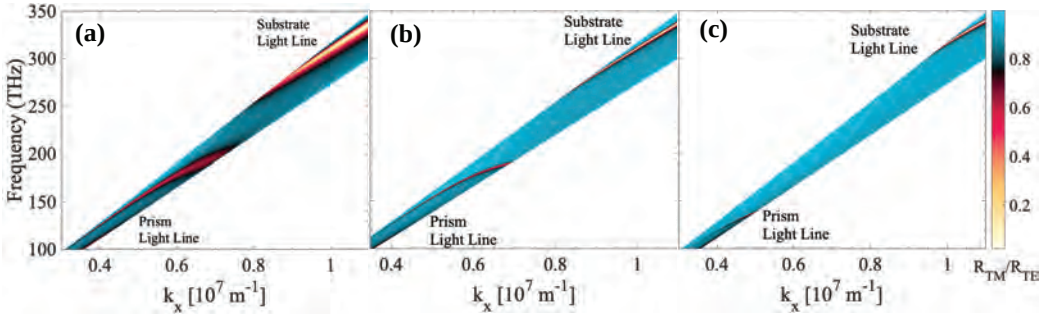

Figure 2.4: Reflectance map R_{TM}/R_{TE} obtained from TMM simulations in the un-normalized wavevector k_x and frequency space of (a) a bifilm with 35-nm-thick gold and 23-nm-thick ITO with the same permittivity as in bifilm A, and of (b) bifilm A, and (c) bifilm C with reduced losses in the ITO film. The spectra of ε_{ITO} used in (b) and (c) are shown in Figs. A.1(a) and A.1(c), respectively but with $\mathrm{Im}[\varepsilon_{ITO}]$ reduced by a factor of 10.

Figure 2.4(a) shows the reflectance map of a bifilm with a 35-nm-thick gold film and 23-nm-thick ITO film obtained from TMM simulations in the frequency ν and un-normalized wavevector k_x space. The wavevector k_x is defined such that $\mathrm{Re}[k_x(\omega)] = (\omega/c)\sin[\pi/4 + \arcsin(\sin\theta_i/n_p(\omega))]$, where $n_p(\omega)$ is the refractive index of the prism, and θ_i is the rotation angle of the prism-sample system [shown in Fig. 2.1(a)]. The permittivity of the ITO layer is taken to be the same as bifilm A.

Comparing Fig. 2.4(a) with the reflectance map of bifilm A in the k_x-ν space shown later in Fig. 2.5, we note that the choice of a thinner gold film in the former case leads to a better coupling efficiency to the lower polariton. However, the thinner gold film also leads to larger radiative damping of the upper polariton, which is evident in its broader spectral linewidth. Hence, the choice of a 50-nm-thick gold layer for our bifilms leads to efficient (inefficient) coupling to the upper (lower) polariton.

Large absorption losses within the ITO film also contribute to the smaller amplitude of the resonance dip for the lower polariton compared to the upper polariton. Figure 2.4(b) shows the reflectance map of bifilm A obtained from TMM simulations in the k_x-ν space, wherein the losses in the ITO film have been reduced by substituting the ITO permittivity $\varepsilon_{\mathrm{ITO}}$ to be $(\mathrm{Re}[\varepsilon_{\mathrm{ITO}}] + i\mathrm{Im}[\varepsilon_{\mathrm{ITO}}]/10)$ in the TMM calculation. The reduced losses in the ITO film lead to much sharper dips for both polariton branches when compared with the reflectance map calculated with the full permittivity of the ITO film $\varepsilon_{\mathrm{ITO}}$ [shown in Fig. 2.3(c)]. Additionally, the reduced losses in ITO result in a well-defined lower polariton branch that continues to exist until it approaches the prism light line. Figure 2.4(c) shows the reflectance map of bifilm C with similarly reduced losses in the ITO layer, and we see a well defined lower polariton branch that is pushed to smaller frequencies than for the thinner ITO in bifilm A. This lower polariton branch is not as clearly visible with the full ITO permittivity $\varepsilon_{\mathrm{ITO}}$. Hence, the losses in the ITO layer are responsible for increasing both the wavevector uncertainty, and the spectral linewidth of the lower polariton branch close to the avoided crossing region where the ENZ mode fraction

becomes increasingly significant. Both factors also contribute to the reduced visibility of the lower polariton branch in comparison with the upper polariton branch.

2.3 Analytical Model of the SPP-ENZ Hybridization

For an insight into the formation of these hybrid polaritons, we analytically model the bifilm as a system of two coupled harmonic oscillators that describe the constituent SPP and ENZ modes. With $\tilde{\omega}_{\mathrm{SPP}}(k_x)$ and $\tilde{\omega}_{\mathrm{ENZ}}(k_x)$ being the dispersion relations of the two oscillators in the complex angular frequency $\tilde{\omega}$ and real transverse wavevector k_x space, we write the interaction Hamiltonian of the coupled system in the rotating wave approximation as [2, 66]

$$\hat{H}(k_x) = \begin{bmatrix} \tilde{\omega}_{\mathrm{SPP}}(k_x) & g_R \\ g_R & \tilde{\omega}_{\mathrm{ENZ}}(k_x) \end{bmatrix}, \tag{2.1}$$

where g_R is the coupling strength, also known as the vacuum Rabi splitting. The complex frequency $\tilde{\omega}_l(k_x) = \omega_l(k_x) - i\gamma_l(k_x)$, where $l = \{\mathrm{SPP}, \mathrm{ENZ}\}$, ω_l is the resonance frequency of mode l at wavevector k_x and $\gamma_l(k_x)$ is the associated damping. The eigen-frequencies $\tilde{\omega}_{\mathrm{U,L}}(k_x)$ of $\hat{H}(k_x)$ (also known as the Hopfield or Hopfield-Bogliubov matrix [2, 66]) form the dispersion relations of the hybrid

modes, and are given by

$$\tilde{\omega}_{\mathrm{U,L}} = \frac{\tilde{\omega}_{\mathrm{SPP}} + \tilde{\omega}_{\mathrm{ENZ}} \pm \sqrt{(\tilde{\omega}_{\mathrm{SPP}} - \tilde{\omega}_{\mathrm{ENZ}})^2 + 4g_R^2}}{2}, \tag{2.2}$$

where the suffixes U and L denote the upper and lower polaritons, respectively. The eigenvectors of $\hat{H}(k_x)$ are also know as Hopfield coefficients, and their squared modulus denotes the relative mode fractions of the constituent SPP and ENZ modes in the hybrid polaritons at each k_x.

We obtain the dispersion lines of the hybrid polaritons in the bifilm, and the SPP mode in the complex frequency $\tilde{\omega}\,(=\omega_0 - i\gamma)$, real wavevector $\mathrm{Re}[k_x]$ space by fitting an asymmetric Lorentzian $f_{\mathrm{Re}[k_x]}(\omega)$ defined below, to the extinction $(1-R_{TM}/R_{TE})$ spectra at each $\mathrm{Re}[k_x]$ [71] using the nonlinear least-squares method

$$f_{\mathrm{Re[k_x]}}(\omega) = \frac{2A/\pi\gamma(\omega)}{1+[(\omega-\omega_0)/\gamma(\omega)]^2} + B + C\omega, \tag{2.3}$$

where

$$\gamma(\omega) = \frac{2\gamma_0}{1+e^{a(\omega-\omega_0)}}. \tag{2.4}$$

Here A is a fitting parameter that determines the peak of the extinction spectrum, and a is the asymmetry parameter. When a is zero, we recover the normal symmetric Lorentzian function with a full width at half maximum (FWHM) linewidth of $2\gamma_0$. The fit parameters B and C account for the frequency dependent linear distortion of the extinction spectra due to the dispersion of the prism.

From the dispersion lines of the SPP mode $\tilde{\omega}_{\mathrm{SPP}}(k_x)$, and the upper and the

lower hybrid polaritons $\tilde{\omega}_{\mathrm{U,L}}(k_x)$ calculated from their respective reflectance maps, we estimate the coupling strength g_R of the bifilm system by fitting the eigenvalues of the Hopfield-Bogliubov interaction Hamiltonian matrix [2], shown in Eq. (2.3), to the upper and the lower polariton dispersion lines

$$\tilde{\omega}_{\mathrm{U,L}} = \frac{\tilde{\omega}_{\mathrm{SPP}} + \tilde{\omega}_{\mathrm{ENZ}} \pm \sqrt{(\tilde{\omega}_{\mathrm{SPP}} - \tilde{\omega}_{\mathrm{ENZ}})^2 + 4g_R^2}}{2}. \tag{2.5}$$

We assume that the ENZ mode has a flat dispersion line given by

$$\tilde{\omega}_{\mathrm{ENZ}}(k_x) = \omega_{0,\mathrm{ENZ}} - i\gamma_{\mathrm{ITO}}/2, \tag{2.6}$$

where γ_{ITO} is the damping in the Drude permittivity model of ITO, and the resonance frequency $\omega_{0,\mathrm{ENZ}}$ is close to the ENZ frequency of ITO given by

$$\omega_{\mathrm{ENZ,ITO}} = \sqrt{\frac{\omega_P^2}{\varepsilon_\infty} - \gamma_{\mathrm{ITO}}^2}, \tag{2.7}$$

where γ_{ITO} is the damping in the Drude model of the permittivity of ITO, which is written as

$$\varepsilon_{\mathrm{ITO}}(\omega) = \varepsilon_\infty - \frac{\omega_p^2}{\omega(\omega + i\gamma_{\mathrm{ITO}})}. \tag{2.8}$$

Here, ε_∞ is the asymptotic value of permittivity for frequencies much larger than the ENZ frequency, ω_p is the plasma frequency, and we have neglected nonlocal contributions to $\varepsilon_{\mathrm{ITO}}(\omega)$ [72]. For the ITO in bifilm A, $\varepsilon_\infty = 3.901$, $\omega_p = 2.8533 \times 10^{15}\,\mathrm{rad\,s^{-1}}$, and $\gamma_{\mathrm{ITO}} = 2.116 \times 10^{14}\,\mathrm{rad\,s^{-1}}$. For the ITO in bifilm B,

$\varepsilon_\infty = 3.6914$, $\omega_p = 2.6667 \times 10^{15}\,\mathrm{rad\,s^{-1}}$, and $\gamma_{\mathrm{ITO}} = 1.193 \times 10^{14}\,\mathrm{rad\,s^{-1}}$. And for the ITO in bifilm C, $\varepsilon_\infty = 3.7359$, $\omega_p = 2.6948 \times 10^{15}\,\mathrm{rad\,s^{-1}}$, and $\gamma_{\mathrm{ITO}} = 1.289 \times 10^{14}\,\mathrm{rad\,s^{-1}}$.

We calculate g_R by performing a nonlinear least-squares fit of the hybrid polariton dispersion lines to their Hopfield model expressions in Eq. (2.5). We take $\omega_{0,\mathrm{ENZ}}$ to be an adjustable parameter in our fit, and not equal to $\omega_{\mathrm{ENZ,ITO}}$ as this assumption only holds true for an infinitesimally small thickness of the ITO film [57]. As the ITO thickness increases, the symmetric polariton mode within the ITO film transitions from an ENZ mode, which is asymptotically pinned to $\omega_{\mathrm{ENZ,ITO}}$, to a long-range surface plasmon polariton mode, whose dispersion line asymptotically approaches lower frequencies than $\omega_{\mathrm{ENZ,ITO}}$ for large wavevectors. We begin with $\omega_{0,\mathrm{ENZ}} = \omega_{\mathrm{ENZ,ITO}}$, and use the nonlinear least squares method to individually fit the dispersion lines of the upper and the lower polaritons to their analytical dispersion relations given in Eq. (2.2). If the difference between the two values of g_R that we obtain from the upper and the lower polariton fits is larger than 10%, we repeat the curve fit albeit with a slightly reduced value of $\omega_{0,\mathrm{ENZ}}$ until the difference in g_R obtained from both the upper and the lower polariton fits is minimized. The average of the two g_R values obtained after this optimization procedure is the final calculated value of the coupling strength of the hybrid polaritons, and the values themselves form the confidence interval of the fit.

Figure 2.5(b) shows the simulated dispersion lines of the hybrid polaritons of bifilm A (blue, solid) and their Hopfield model fits (red, dashed), and the dispersion lines of SPP (green, dot-dashed) and ENZ modes (purple, dot-dashed).

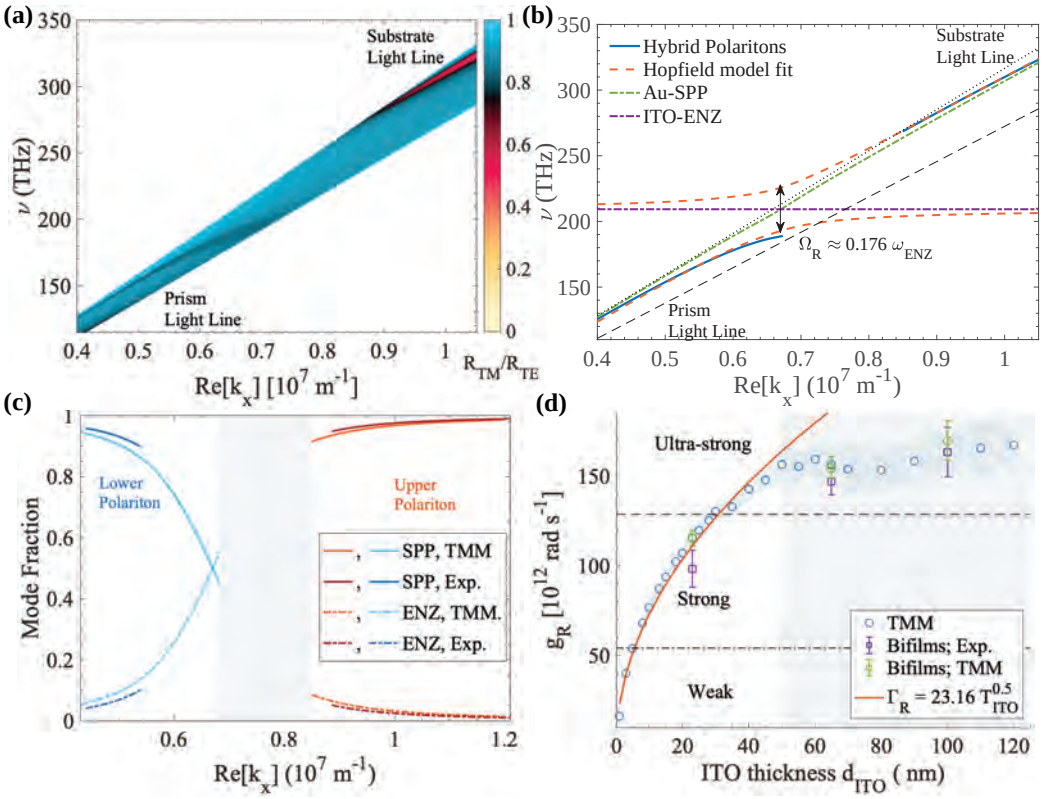

Figure 2.5: (a) Simulated reflectance map of bifilm A in k_x-ν space. (b) Dispersion lines of the SPP mode (green, dot-dashed), the ENZ mode (purple, dot-dashed), the hybrid polaritons in bifilm A (blue, solid) and their Hopfield model fits (red, dashed). (c) The SPP (solid) and ENZ (dot-dashed) mode fractions for the upper (red and maroon) and lower (cyan and blue) polaritons. The upper (lower) polariton is formed by a symmetric (antisymmetric) superposition of the constituent modes. (d) g_R for bifilms with various values of d_{ITO} estimated from the simulated (green circles) and measured (purple squares) reflectance maps of bifilms A, B and C; and the simulated reflectance maps of bifilms with $\varepsilon_{\mathrm{ITO}}$ assumed to be the same as in bifilm A (blue circles). The errorbars for estimated g_R from simulations for $d_{\mathrm{ITO}} < 80$ nm, and from measurements for bifilm A are given by the difference in g_R from fitting the upper and the lower polariton dispersion lines. The 95% confidence intervals for g_R estimated from fitting only the upper polariton dispersion line form the errorbars for estimated g_R from simulations for $d_{\mathrm{ITO}} \geq 80$ nm, and from measurements for bifilms B and C. The red line is the parabolic fit to g_R outside the gray region in which the Hopfield model yields large fitting errors.

The Hopfield fits plotted for all k_x agree reasonably well with the simulated bifilm dispersion, and they clearly show the avoided crossing. The estimated value of g_R for bifilm A from the fits is $115.5 \pm 4.3 \times 10^{12}\,\mathrm{rad\,s^{-1}}$, and being significantly larger than the average decay rate of the constituent modes γ_{avg} $[= (\gamma_{\mathrm{SPP}} + \gamma_{\mathrm{ENZ}})/2 \approx 54 \times 10^{12}\,\mathrm{rad\,s^{-1}}]$, clearly satisfies the strong coupling criterion. The polariton band gap $\Omega_R\,(= 2g_R)$ is approximately $0.176\,\omega_{0,\mathrm{ENZ}}$, which is close to the ultra-strong coupling threshold where $\Omega_R \geq 0.2\,\omega_{0,\mathrm{ENZ}}$ [68, 69]. Above this threshold, depolarization effects within the ITO film and the related counter-rotating terms – which are not included in our calculation of g_R – become significant [73]. We elaborate this point later in this section.

From the Hopfield fit to the upper polariton mode, we note that its avoided crossing is pushed to the left of the substrate light line due to the dispersion of the coupling prism, and is therefore not accessible. Hence, only its mostly SPP-like tail lies between the two light lines. The predominantly SPP-like nature of the upper polariton is also evident in its mode composition which, as shown in Fig. 2.5(c), has an SPP fraction larger than 0.9 throughout. We also note from Fig. 2.5(c) that the ENZ mode contribution for both hybrid polaritons increases closer to the avoided crossing. Comparing the simulated dispersion line of the lower polariton and its Hopfield fit in Fig. 2.5(b), we note that its dispersion line is not well-defined for wavevectors beyond the avoided crossing as a consequence of its largely ENZ-like nature at those wavevectors. Here, both the spectral linewidth and the wavevector uncertainty of the reflectance dip broaden as the absorption losses increase and the dispersion flattens [44, 45].

Since the spatial overlap between SPP and ENZ modes in the bifilm determines g_R (and Ω_R), it can be varied using the material and geometrical parameters of the ITO film. The SPP mode is confined to the gold-ITO interface with a long evanescent tail extending into the substrate, while the ENZ mode is mostly constant and localized to the ITO film. Hence, as we observe in Fig. 2.3, Ω_R initially increases with d_{ITO}. Figure 2.5(d) shows the estimated g_R for various values of d_{ITO}. For d_{ITO} smaller than 7 nm, g_R increases almost linearly but remains below the strong coupling threshold. Above this threshold, g_R is proportional to $\sqrt{d_{\mathrm{ITO}}}$ as shown by the fitted curve (red, solid), and exceeds the ultra-strong coupling threshold for d_{ITO} larger than 30 nm. The major factor determining this scaling is that the ENZ mode becomes more LR-SPP-like as d_{ITO} increases, and the E_z field within the ITO film is no longer constant [57]. Furthermore, the ENZ mode is a collective excitation of the free electrons within the ITO film with an oscillator strength f_{ENZ} that scales with d_{ITO}. Since g_R is proportional to $\sqrt{f_{\mathrm{ENZ}}}$ [44, 66], g_R should scale with $\sqrt{d_{\mathrm{ITO}}}$. For d_{ITO} larger than 45 nm, g_R saturates and deviates from the $\sqrt{d_{\mathrm{ITO}}}$ dependence as the ENZ mode transforms into an LR-SPP mode at these thicknesses, and its dispersion can no longer be approximated by a flat line given by Eq. (2.6). We have identified this range of d_{ITO} by a shaded gray region in Figure 2.5(d), and the values of g_R extracted from the analytical model in this region are not accurate, which is also reflected in the large fitting errors (blue shaded area) in this region. For d_{ITO} larger than 65 nm, the fields at the two interfaces of the ITO film also start to decouple, and the hybrid polaritons morph into polaritonic modes confined at these interfaces [66]. Thus, $d_{\mathrm{ITO}} \leq 45$

nm provides an upper limit to g_R that can be achieved with modes that inherit the desirable features of both the ENZ mode and the SPP mode.

For d_{ITO} larger than 80 nm, as a consequence of the large losses within the ITO layer, and inefficient excitation in our Kretschmann configuration, the spectral dips corresponding to the lower polariton branch become faint enough that it is not possible to perform the asymmetric Lorentzian fits to extract the dispersion line $\tilde{\omega}_L(k_x)$. Hence, we only plot the g_R corresponding to the upper polariton fit in Fig. 2.5(d) with $\omega_{0,\mathrm{ENZ}}$ taken to be the same as that obtained through optimization of the bifilm with d_{ITO} of 70 nm. The blue shaded region shows the 95% confidence interval of the fit parameter g_R. We also use just the upper polariton branch to estimate g_R for the measured reflectance spectra of bifilms B and C, as the lower polariton data is not available for these samples due to the limited spectral range of our source and spectrometers.

In ultra-strong coupling regime ($d > 30$ nm), the simple analytical (Hopfield) model for the hybrid polaritons based on two coupled harmonic oscillators is not accurate due to several underlying assumptions made by the model. For instance, the self-interaction term of the SPP and the ENZ modes, which is proportional to the square of their respective polarizations, is neglected in the interaction Hamiltonian [73]. In the complete interaction Hamiltonian written in the dipole gauge, this self-interaction term is responsible for the renormalization of the respective uncoupled mode frequencies. In the quantum-mechanical picture, this term corresponds to the $\mathbf{A}^2$ term of the interaction Hamiltonian, which also includes the counter-rotating terms that are neglected when making the rotating-wave approximation (RWA).

This self-interaction term leads to deviations from the curves obtained from the Hopfield model.

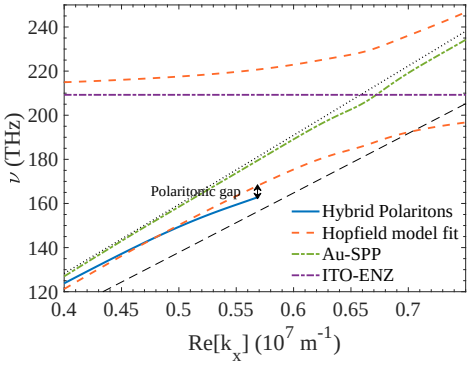

Figure 2.6: Dispersion lines of the hybrid polaritons for a bifilm with a 50 nm thick gold on a 40 nm thick ITO film (blue, solid), its Hopfield model fit (red, dashed), the SPP mode in the standalone 50 nm thick gold film (green, dot-dashed), and the ENZ mode in the 40 nm thick ITO film with permittivity shown in Fig. A.1(a). The black dashed and dotted lines are the prism and the substrate light lines, respectively.

For intersubband polaritons formed by ultra-strong coupling between a microcavity mode and the bound states in multiple quantum wells (which form a collective Berreman mode for a large enough number of quantum wells), it has been previously demonstrated that the low-energy polariton branch asymptotically approaches a smaller energy than the high-energy polariton close to the avoided-crossing [50]. As a consequence, the high reflectivity between the two energy asymptotes opens up a so-called “polaritonic gap" in the dispersion line of the intersubband polaritons. We observe a similar effect in the dispersion lines of our bifilms that support ultra-strongly coupled SPP and ENZ modes, that is for bifilms with $d_{\mathrm{ITO}} > 30$ nm. As shown in Fig. 2.6, the frequency asymptote of the

lower polariton (blue, solid) is smaller than the frequency at that specific transverse wavevector in the fitted dispersion line (red, dashed). The reflectance in this range of frequencies between the two frequency asymptotes, or in other words the polaritonic gap, is high. This polaritonic gap also implies a progressively worse agreement between the analytical dispersion model, and the actual dispersion of the hybrid polaritons for larger d_{ITO}. Hence, there is a larger difference in the values of g_R estimated from the upper, and from the lower polariton fit [shown by the blue shaded region in Fig. 2.5 (d)] in the ultra-strong coupling region.

2.4 The Characteristics of Hybrid Polaritons

The relevance of these hybrid polaritons for photonic applications can be examined through parameters such as their mode confinement, field enhancement, propagation lengths, and decay rates. Following the method described in appendix B of Ref. [74], we first develop an analytical dispersion model for the polaritons, and then use its solutions to calculate their field profiles, mode confinement and field enhancement. In short, we first assume an evanescent wave solution perpendicular to the interfaces of the bifilm. The electromagnetic continuity relations at the prism-gold, gold-ITO, and the ITO-substrate interfaces then yield a set of homogeneous equations for the field coefficients. The complex frequency $\tilde{\omega}$ that minimizes the determinant of the ill-conditioned coefficient matrix of these equations at each real-valued transverse wavevector k_x gives the analytical dispersion relation of the hybrid polaritons in the presence of only non-radiative losses [3]. We then calculate

the field distributions at points along the dispersion curve from the eigen-vectors of the coefficient matrix, which are obtained after singular value decomposition [75]. See appendix A.2 for details on the analytical dispersion model and the calculation of mode profiles. *We restrict our discussion from now on to bifilm A*. Appendices A.3 and A.4 have the details on the polaritons in bifilms B and C.

2.4.1 The Mode Profiles

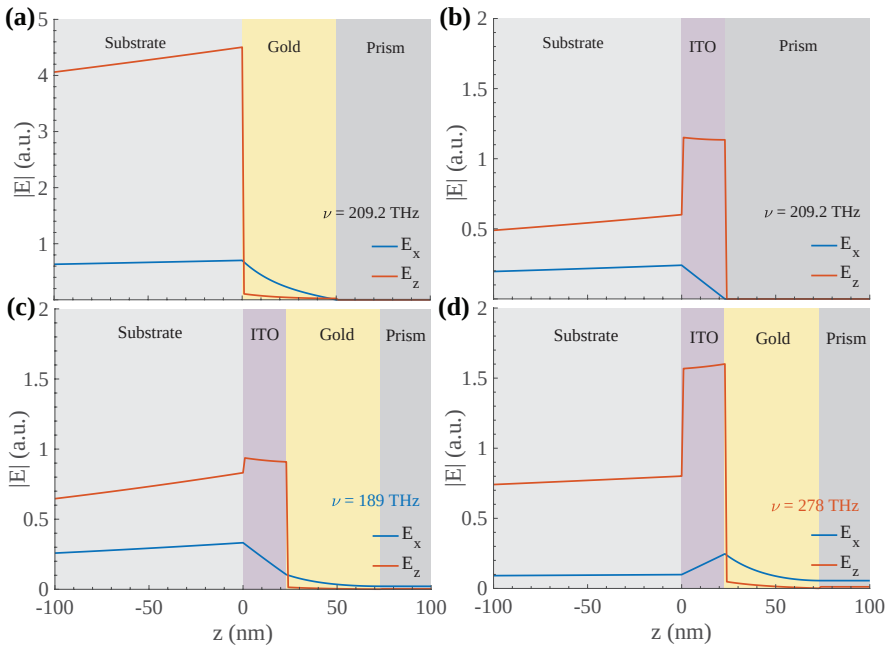

Figure 2.7: Electric field profiles of the longitudinal "z" (red) and the transverse "x" (blue) components of the (a) standalone LR-SPP mode in a 50 nm gold film, and the (b) standalone ENZ mode in a 23 nm ITO film at their point of degeneracy (where their respective dispersion lines cross). The electric field profiles of the (c) lower and the (d) upper polaritons for bifilm A (50 nm thick gold on 23 nm thick ITO) close to the avoided crossing region.

Figures 2.7 (a) and 2.7 (b) show the electric field profiles of the LR-SPP

mode in 50-nm-thick gold on float glass, and the ENZ mode in 23-nm thick-ITO [with the permittivity shown in Fig. A.1(a)] on glass, respectively at their point of degeneracy, or where their respective dispersion lines cross. As mentioned previously, the SPP mode is mostly confined at the gold-substrate interface, with a very small longitudinal field amplitude E_z in the gold layer. The ENZ mode, on the other hand, is tightly confined within the ITO film, where E_z is enhanced almost by a factor of three than at the ITO-substrate interface, and is largely constant within the film. Figures 2.7(c) and (d) show the electric field profiles of the lower and the upper polariton of bifilm A, respectively, close to the avoided crossing region, where both modes are maximally hybridized between the SPP mode and the ENZ mode. Accordingly, we see the characteristic features of both constituent modes in the field profiles of the hybrid modes. Hence, both modes have a large and almost constant E_z in the ITO film. On the other hand, E_x is enhanced along the gold-ITO interface for the upper polariton, and along the ITO-glass interface for the lower polariton. This difference emerges due to the fact that the upper (lower) polariton is formed by a symmetric (anti-symmetric) superposition of the SPP and the ENZ modes.

Figures 2.8(a) and (b) show the transverse $|E_x|$, and the longitudinal $|E_z|$ electric field profiles, respectively of the polaritons in bifilm A plotted at various k_x along their dispersion lines. From the continuity of the longitudinal component of the electric flux density D_z at the gold-ITO interface, we have $E_{\mathrm{z,ITO}} = (\varepsilon_{\mathrm{Au}}/\varepsilon_{\mathrm{ITO}})E_{\mathrm{z,Au}}$, where $E_{\mathrm{z,ITO}}$ ($E_{\mathrm{z,Au}}$) is the longitudinal electric field inside ITO (gold) at the interface, and $\varepsilon_{\mathrm{ITO}}$ ($\varepsilon_{\mathrm{Au}}$) is its permittivity. As $\varepsilon_{\mathrm{ITO}}$ vanishes close to the avoided

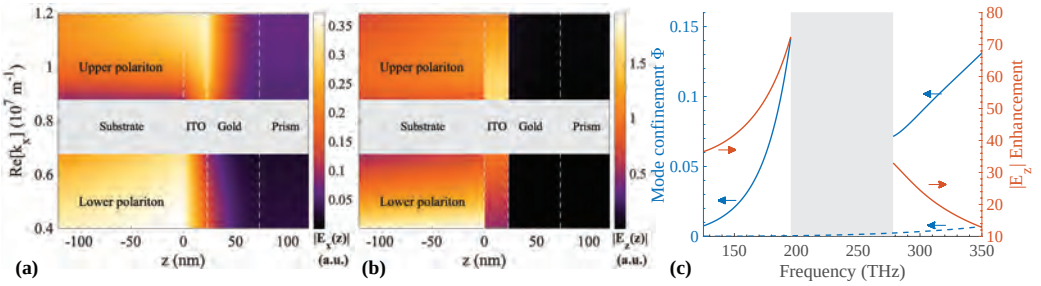

Figure 2.8: Profiles of (a) $|E_x|$ and (b) $|E_z|$ for bifilm A plotted along the dispersion lines of the hybrid polaritons. The polariton band gap is shown in gray, and the interfaces by the white dashed lines. (c) Mode confinement of the same hybrid polaritons (blue, solid) and the SPP mode (blue, dashed), and their longitudinal field enhancement in ITO with respect to the field in gold at the gold-ITO interface (red).

crossing, E_z is significantly enhanced within the ITO film and relayed from the gold-ITO interface to the substrate while maintaining its large amplitude [57, 76, 77]. Away from the avoided crossing, both polaritons become more SPP-like with a smaller E_z in ITO, and E_x confined along the ITO-substrate (gold-ITO) interface for the lower (upper) polariton. The hybrid nature of the modes is evident in the large amplitude of $|E_z|$ within ITO, and an enhanced $|E_x|$ at the edges of the ITO film.

Figure 2.8(c) shows the enhancement in E_z for the hybrid polaritons in bifilm A, and is defined as $|E_z|$ at the center of the ITO film normalized to the $|E_z|$ in gold near the gold-ITO interface (red, solid). We note that the lower (upper) polariton can have a field enhancement as large as $75\times$ ($32\times$) close to the avoided crossing. We now define the mode confinement Φ as follows [78]

$$\Phi = \frac{\int_d |E_z(z)H_y(z)|dz}{\int_{-\infty}^{\infty} |E_z(z)H_y(z)|dz}, \tag{2.9}$$

where [74] $H_y(z) = (\omega\varepsilon(z))/(\mu_0 c k_x)E_z(z)$ is the magnetic field, and d denotes the integration range of z. For the bifilm, we calculate Φ only within the ITO layer, whereas we calculate Φ within the gold layer for the standalone SPP mode, and within the ITO layer for the standalone ENZ mode. Figure 2.8(c) shows the variation of Φ for the polaritons in bifilm A (blue, solid), and the SPP mode in the standalone gold film (blue, dashed). We observe that although Φ for both hybrid polaritons is lower than the bare ENZ mode (≈ 0.3, not shown here), they substantially outperform the bare SPP mode throughout the spectral region of interest with values of Φ approaching 0.14 (0.075) close to avoided crossing for the lower (upper) polariton. This relaxation in mode confinement makes the hybrid polaritons less lossy compared to the ENZ mode, which is reflected in their reduced damping and enhanced propagation lengths.

2.4.2 The Damping and Propagation Lengths

To estimate the damping γ of the polaritons from the simulated and the measured reflectance maps, we fit the asymmetric Lorentzians defined in Eq. (2.3) to the spectral dips at each $\mathrm{Re}[k_x]$ in the reflectance maps. Figures 2.9(a) and (b) show representative fits to the extinction spectrum at the value of $\mathrm{Re}[k_x]$ stated in the inset for the lower and the upper polariton of bifilm A, respectively, along with the estimated values of the damping γ normalized to γ_{ITO} stated in the inset. To estimate the propagation lengths of the hybrid polaritons, and the SPP mode from their reflectance maps, we again perform a nonlinear least-squares fit of asymmetric Lorentzians of the following form to the extinction $(1 - R_{\mathrm{TM}}/R_{TE})$ wavevector

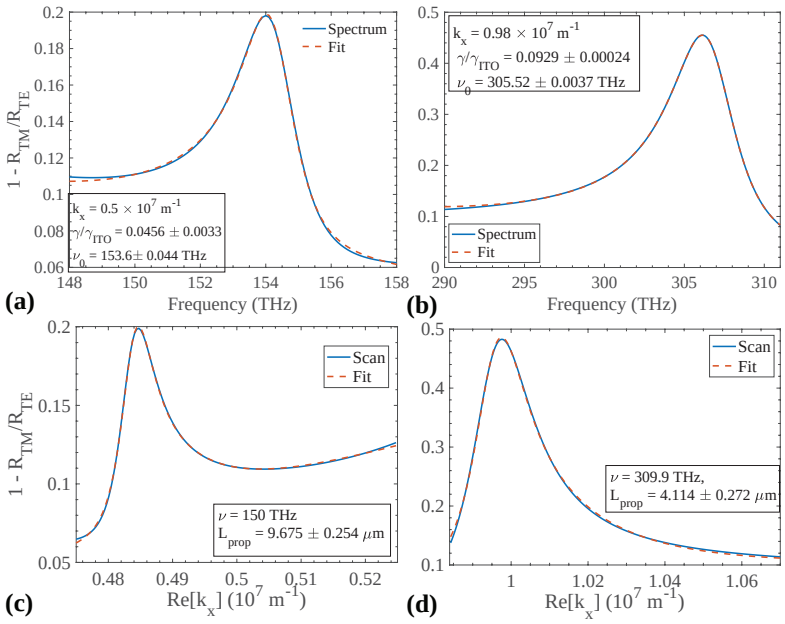

Figure 2.9: Asymmetric lorentzian fits (red, dashed) to the extinction ($(1 - R_{TM}/R_{TE})$) frequency spectrum (blue, solid) for the (a) lower and the (b) upper polariton at a certain $\mathrm{Re}[k_x]$, and to the extinction wavevector spectrum (blue, solid) at a certain frequency ν for the (c) lower and the (d) upper polariton. The 95 % confidence intervals of the estimated normalized damping γ/γ_{ITO} and the propagation lengths L_{prop} are stated in the inset of the top and the bottom panels, respectively along with the corresponding values of $\mathrm{Re}[k_x]$ (top) and ν(bottom) at which the spectra have been obtained.

scan at each frequency

$$f_\omega(k_x) = \frac{2C_1/\pi\sigma(k_x)}{1+[(k_x-k_{x0})/\sigma(k_x)]^2} + C_2 + C_3 k_x, \tag{2.10}$$

where

$$\sigma(k_x) = \frac{2\sigma_0}{1+e^{a(k_x-k_{x0})}}. \tag{2.11}$$

The fitting function is similar to the one assumed for extracting the decay rates γ_0 from the reflectance maps. The fit parameter k_{x0} calculated from the wavevector scans at various ω produces the dispersion line, albeit with back-bending present where relevant [44, 79]. On the other hand, the propagation length L_{prop} of the polariton is given by

$$L_{\text{prop}} = \frac{1}{2\sigma_0}. \tag{2.12}$$

Figures 2.9(c) and (d) show a representative example of the fits (red, dashed) to the simulated extinction scans (blue, solid) at two frequencies in the lower, and in the upper polariton branches of bifilm A, respectively. There is a reasonable agreement between the fitted curve, and the actual scan. To calculate L_{prop} of the hybrid polaritons from the analytical dispersion model, we solve the characteristic equation $|\det(L)| = 0$ in real frequency ω and complex wavevector k_x space. Thus, σ_0 at each frequency is directly obtained from the imaginary part of the k_x solution. Similarly, to estimate the damping γ of the hybrid polaritons from the analytical dispersion model, we solve the characteristic equation in real wavevector $\text{Re}[k_x]$ and complex frequency $\tilde{\omega}$ space. To calculate L_{prop} of the ENZ mode, we first extract the linewidth γ of the spectral dip from the reflectance maps shown in Figs. 2.2 (c) and (d). We then use the following relation from the supplement in Ref. [78] to calculate the propagation length

$$L_{\text{prop}} = \frac{d_{\text{ITO}}}{4} \frac{\omega^4 + \gamma^2\omega^2}{\omega_p^2 \gamma \omega}. \tag{2.13}$$

Figure 2.10(a) shows the damping γ ($= |\text{Im}[\tilde{\omega}]|$), and Figure 2.10(b) the propa-

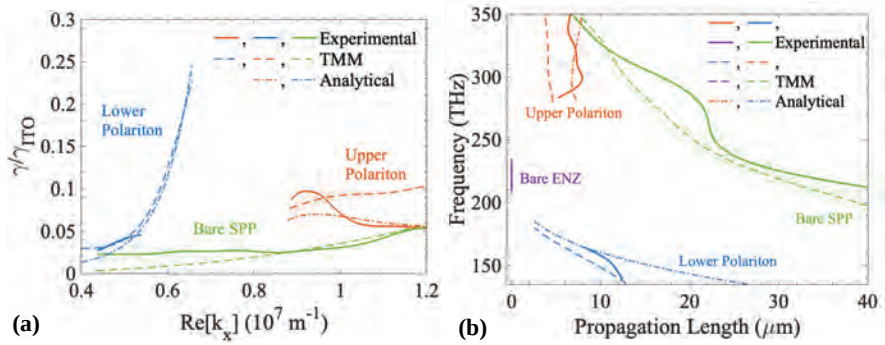

Figure 2.10: (a) Damping γ normalized to the decay constant in the Drude model of ITO γ_{ITO}, and the (b) propagation lengths of the of the upper (red), the lower (blue) polaritons of bifilm A, the SPP mode in an isolated 50-nm-thick gold film (green), and the ENZ mode in an isolated 23-nm-thick ITO film (purple). In (a) and (b), the dot-dashed lines are the solutions of the analytical dispersion relation, and the solid (experiment) and the dashed (TMM simulations) lines are the linewidths of the dips in the respective reflectance maps smoothed over their fitting errors (shaded areas around the lines).

gation lengths ($= 1/(2\mathrm{Im}[k_x])$) of the upper (red) and the lower (blue) polaritons of bifilm A, the SPP mode in the standalone gold film (green), and the ENZ mode in the standalone ITO film (purple). The estimated damping and propagation lengths in both the simulated (dashed) and the experimental (solid) datasets have a reasonable agreement in the presence of fitting errors, and differences between the simulated and experimental optical constants. The analytical results (dot-dashed) exclude radiative losses into the coupling prism [3]. The hybrid polaritons have a significantly lower damping throughout compared to the ENZ mode, which has a constant damping of $0.5\gamma_{ITO}$ [not shown in Figure 2.10(a)] [57]. Additionally, the lower (upper) polariton has a propagation length between 2–15 μm (4–8 μm) for bifilm A, which is significantly larger than the propagation length of the ENZ mode (≈ 0.08 μm for the 23-nm-thick ITO film). The damping (propagation length) of

the lower polariton is maximized (minimized) close to the avoided crossing, and approaches the values for the SPP mode away from it.

2.5 Conclusions

To summarize, we have proposed a bifilm structure consisting of a 50-nm-thick gold film deposited on a thin ITO film backed by a float glass substrate that supports hybrid polaritons formed by strong coupling between the SPP mode in the gold film and the ENZ mode in the ITO film at NIR frequencies. These polaritons have a much tighter mode confinement than the bare SPP mode, along with a propagation length of several microns in contrast to the non-propagating ENZ mode. The large mode confinement of these polaritons is accompanied by a significant enhancement in the longitudinal component of the electric field within the ITO film. The coupling between the constituent modes can be tuned through the thickness of the ITO layer, and can even approach the ultra-strong coupling regime at certain thicknesses.

A propagation length of several microns implies an interaction length of several wavelengths at these NIR frequencies. This large interaction length along with the tight mode confinement, and the large sub-ps nonlinear response of ITO in its ENZ region [6], make our device an ideal platform for electro-optical control of strong coupling [80], ultrafast switching [81], and studying giant ultrafast nonlinearities that do not rely on lossy optical resonances or require sophisticated fabrication techniques. The use of a prism for coupling to the polaritons can also be done away with through the use of appropriate grating couplers [10]. The ultrafast response

of ITO should also allow for the observation of effects due to time refraction and adiabatic frequency conversion [33, 82, 83], and exotic effects related to ultra-strong coupling phenomena, such as the dynamic Casimir effect [84].

3. Cooperative Radiative Broadening in a Dipolar Metasurface: “Weak Superradiance"

3.1 Introduction

Localized surface plasmon(s) (LSP(s)) supported by noble metal nanoparticles can lead to strong resonant scattering and absorption of light [3, 13]. A collection of these nanoparticles can be used to tailor the scattering and absorption of light at the nanoscale, which has been the subject of extensive research during the past decades for applications related to cloaking [85, 86], wavefront engineering [87–89], harmonic generation [90], all-optical switching [91, 92], and for the artificial engineering of optical properties such as permittivity and permeability [93–99]. As stated previously in chapter 1, the LSP(s) can behave like electric or magnetic dipoles, and can be modeled as classical harmonic oscillators [100]. Dimers of plasmonic nanoparticles can support coupled modes that have a broader spectral

linewidth than the linewidth of each nanoparticle in the dimer [101–106]. Linewidth broadening has also been observed in periodic arrays of subwavelength-size split-ring resonators [107–111] and rod nanoantennas [112], as well as three-dimensional arrangements of nanoparticles [113–116]. There are similarities in this regard with the well-known phenomenon of "superradiance", wherein cooperative behavior in a collection of N emitters can lead to broadening of the spectral linewidth by a factor of N [117, 118]. In the electric-dipole approximation, this behavior indicates the presence of a macroscopic dipole moment in the system equal to the sum of dipole moments of the individual emitters, which results from the collective radiative interactions between the emitters [117–121]. First predicted by Dicke in 1954 [117], superradiance has been demonstrated previously in quantum systems such as gases [122], atomic vapors [123], Rydberg atoms [124], Bose-Einstein condensates [125], trapped ions [126], superconducting qubits [127], Mössbauer nuclei [128] and color centers in diamond [129].

Although there are quantum features to superradiance, the accelerated radiative damping of a collection of mutually-coherent dipoles due to interaction with a common radiative field is essentially a classical effect. In some plasmonic systems, the linewidth broadening has either been explained by an enhanced scattering rate due to non-radiative near-field dipole-dipole coupling, [102–106, 109, 110] or by a retarded radiative interaction between the particles [111, 113]. On the other hand, in systems such as gold nanospheres trapped in a linear array by a tightly focussed laser beam [114], a plastic bead coated with gold nanospheres [115], and random aggregates of gold and silver nanospheres [116], the linear scaling of

linewidth of scattered light with the number of irradiated nanospheres has been phenomenologically associated with a corresponding increase in the radiative decay rate [114–116]. However, a detailed analysis of the emergence of the radiative linewidth dependence on the number of irradiated plasmonic nanoparticles has not yet been presented.

In this chapter, we describe our study of the collective behavior in a single array of identical plasmonic nanoparticles through experiment, FDTD simulations, and an analytical model. We show that the radiative linewidth of a planar array of nanoantennas is directly proportional to the effective number of nanoantennas, N_{eff}, contained within a circle of radius equal to the resonant optical wavelength, λ_0. In addition, we show that in the dipole approximation this linewidth dependence is due to the enhancement of the radiation reaction field of each nanoantenna by that of its neighbors in the array, and is, therefore, a cooperative effect. Finally, we draw a connection between the 'plasmonic superradiance' observed in our system and Dicke superradiance and argue that the plasmonic system is analogous to a system of weakly-excited emitters in the Dicke model. In section 3.2, we describe our experimental setup, and compare the measurements of the extinction spectra with the FDTD simulations. In section 3.3, we describe our analytical model and compare the calculated extinction spectra with the results from the simulations and the experiment. Lastly, in section 3.4, we discuss the scaling of the extinction linewidth with the lattice constant of the arrays.

3.2 Experiment and Numerical Analysis

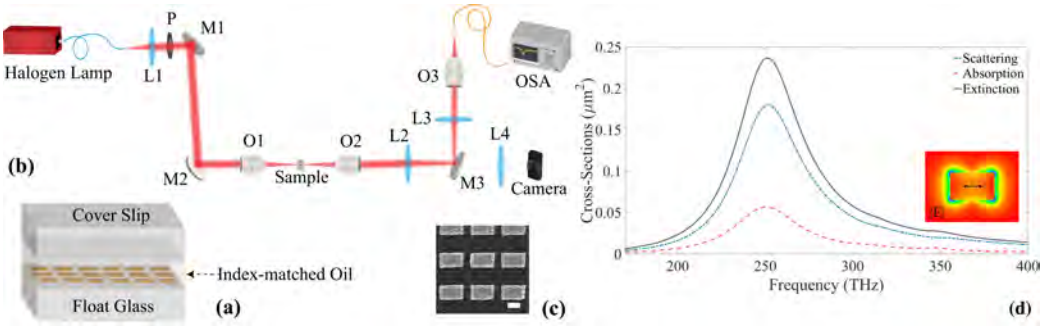

Figure 3.1: (a) Schematic of the experimental setup. The labels on the schematic are: collimating lens (L1), linear polarizer (P), microscope objectives, (O1: $\times 10$ and NA $= 0.25$, O2: $\times 4$ and NA $= 0.1$), imaging lenses (L2, L3, L4), OSA, folding mirrors (M1, M2), flip mirror (M3). (b) A cross-section view of the sample showing a nanoantenna array (gold bars). (c) Scanning electron micrograph of one of the fabricated arrays. The solid white bar in the lower right corner is 100 nm long for scaling. (d) Scattering (blue, dot-dashed), absorption (red, dashed) and extinction (gray, solid) cross-section spectra of a single nanorod obtained through FDTD simulations. The inset shows the electric field profile at the scattering resonance.

Fig. 3.1(a) shows a diagram of the structure under study, which is a planar square array of bar-shaped gold nanoantennas that are on average 185-nm-long, 105-nm-wide and 20-nm-thick, placed on a 1 mm thick BK7 (or float) glass substrate. The background medium is made symmetric by covering the sample with index-matched oil, which has the same permittivity as the substrate, followed by a float glass cover slip. The arrays are excited by normally incident broadband light, and we study the dependence of the linewidth of scattered light from the array as a function of the number density of nanoantennas, or equivalently, of the array's lattice constant, a. The dimensions of the nanoantenna are chosen such that the dominant damping mechanism is radiative, thereby allowing the observation of

variations in radiative linewidth simply by measuring the transmission spectrum of the array. This effect is evident in the scattering and absorption cross-sections of the nanoantenna calculated through FDTD simulations. Figure 3.1(d) shows the spectra of the scattering, absorption and extinction cross-sections of a a gold nanoantenna with the aforementioned dimensions calculated through FDTD simulations. The resonant scattering, which occurs at a wavelength (frequency) of 1181 nm (254 THz), is more than three times as strong as the absorption. The electric field profile at resonance shown in the inset of Fig. 3.1(d) also shows that a predominantly electric dipole mode is excited at the resonance.

We have fabricated eleven squared arrays of nanoantennas, with lattice constants ranging from 250 nm to 500 nm in steps of 25 nm, using electron beam lithography in a Raith Pioneer 30 kV e-beam system to form a patterned resist on a 1 mm thick float glass substrate. A gold film of thickness 20 nm is then deposited, and the resist removed by the process of lift-off, leaving behind the patterned gold on the substrate [130]. See appendix B.2 for more details on the fabrication. The size of each array is 200 μm $\times$ 200 μm. The scanning electron micrograph image in Fig. 3.1(c) shows a detail of one of the fabricated arrays.

The transmission spectra of the fabricated arrays are measured by transmission spectroscopy using the setup depicted schematically in Fig. 3.1(b). The normalized average transmission spectrum T of each array was obtained by taking the ratio of the transmission spectrum of each array to the transmission spectrum of the glass-oil assembly, with each spectrum averaged over three measurements. As the response of a single nanoantenna to an incident field can be described by contributions from

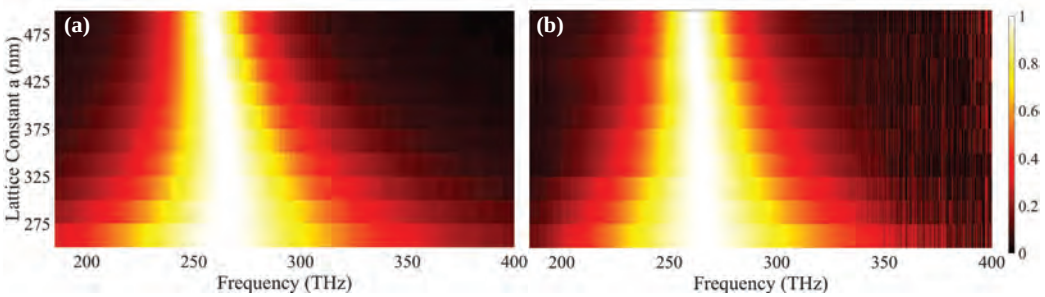

Figure 3.2: Extinction spectra of nanoantenna arrays of different lattice constants obtained from (a) FDTD simulations, and from (b) the experiment.

the excited multipoles [3], the collective response of nanoantennas in each array also consists of multipolar contributions. However, as mentioned previously, for the range of frequencies under consideration the dipole mode of the nanoantenna is dominant. Hence, the radiative decay rate of the collective dipolar mode of each array is given by the FWHM linewidth of the corresponding extinction spectrum, $(1-T)$.

In Figs. 3.2(a) and Fig. 3.2(b) we compare the extinction spectra of the nanoantenna arrays of different lattice constants obtained from FDTD simulations and from the experiment, respectively. For both the FDTD simulations shown here, and the analytical results discussed later, we use the permittivity data from Johnson and Christy for gold [70], and the refractive index data from the Schott optical glass datasheets [131] for the float glass. For the FDTD simulations, we apply periodic boundary conditions at the transverse boundaries of a single unit cell of the array. As a consequence, the uniformity of dimensions of the nanoantennas in each array was implicitly assumed. On the other hand, for the fabricated arrays, there are unavoidable inhomogeneities in the dimensions of the nanoantenna, which contribute

to inhomogeneous broadening. In addition, in the experiment the exciting field could have some obliquely incident components despite the use of objectives with low numerical apertures. These factors could explain the slight differences between the simulated and the measured spectra. However, both measured and simulated spectra show similar broadening of the extinction linewidth with decreasing array lattice constant, which is consistent with the expectation that increasing the number of dipoles within an optical wavelength broadens their radiative linewidth.

3.3 Analytical Model

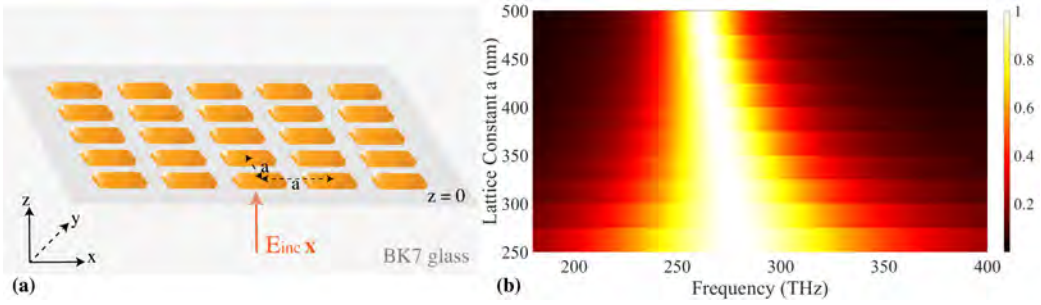

Figure 3.3: (a) Diagram of the nanoantenna array with a lattice constant a, and excited by a normally incident plane wave E_{inc}. (b) Analytically calculated extinction spectra for nanoarod arrays of various lattice constants.

For physical insight into the relation between the radiative linewidth and the lattice constant, we now introduce an analytic model to describe the scattered field from an array of nanoantennas. We approximate each nanoantenna as a point dipole of electric dipole moment p, and introduce the polarizability tensor $\overleftrightarrow{\alpha}_0$ in the electrostatic limit. For ease of analytical calculations, we model each nanoantenna

as an ellipsoid of same volume and aspect ratios as the nanorod, and assume the coordinate system to be aligned along the principal axes of the ellipsoid [see Fig. C.1(d)] The tensor $\overleftrightarrow{\alpha}_0$ is then represented by a diagonal matrix, and its elements are proportional to the volume of the ellipsoid. The diagonal elements, $\alpha_{0,\mathrm{ii}}$ for $i = \{x, y, z\}$, describe the response of the electric dipole excited along the corresponding axis, and depend on the exact shape and permittivities of the nanoantenna as well as the surrounding medium [see Eqs. (C.1)-(C.2) for an ellipsoid]. The implicit dependence of $\overleftrightarrow{\alpha}_0$ on the frequency ω includes the effects of material dispersion of both the nanoantenna and the surrounding medium. The resonance frequency ω_0 of the dipole is obtained from the condition $\mathrm{Re}[\alpha_{0,\mathrm{ii}}^{-1}(\omega_0)] = 0$. In addition, the damping of the dipole is purely non-radiative in the electrostatic limit, and the FWHM linewidth of the corresponding extinction spectrum [Eq. (C.5)] depends only on the material losses (characterized by $\mathrm{Im}[\alpha_{0,\mathrm{ii}}^{-1}]$).

We first consider an isolated ellipsoidal nanoantenna, excited by an incident field of frequency ω that has a value E_{inc} at the center of the nanoantenna. There are two features in the response that arise when we go beyond electrostatics. First, in the neighborhood of the nanoantenna there is a field contribution from the nanoantenna itself that is out of phase with its dipole moment, but proportional to it, and is responsible for radiation reaction. Second, if the volume V of the nanoantenna is not significantly smaller than λ_0^3, there is a part of the field from the nanoantenna which varies across the nanoantenna due to retardation. The effects due to these two features of the response on the electric dipole moment p of the nanoantenna induced can still be captured within a point dipole model, but with

the replacement of E_{inc} by a modified field E_{mod}. That is, we can write

$$p = \varepsilon_0 n^2 \overleftrightarrow{\alpha}_0 \cdot E_{\text{mod}}. \tag{3.1}$$

where

$$E_{\text{mod}} = E_{\text{inc}} + \frac{1}{4\pi\varepsilon_0}\frac{2}{3} i n \tilde{\omega}^3 p + \overleftrightarrow{\beta}_0 \cdot \frac{1}{\varepsilon_0 n^2} p. \tag{3.2}$$

Here n is the refractive index of the surrounding medium (here BK7 glass), and $\tilde{\omega} = \omega/c$. In Eq. (3.2), the second term on the right is the radiation reaction field from the nanoantenna itself, and the dyadic $\overleftrightarrow{\beta}_0$, sometimes referred to as the 'dynamic depolarization term', depends on the size and shape of the nanoantenna, is purely real, and is associated with the variation of the full electric field over the nanoantenna due to retardation [12, 132]. See appendix C for the expression of $\overleftrightarrow{\beta}_0$ for our ellipsoids.

The aforementioned electrodynamic contributions to the response of the nanoantenna to the incident field can alternately be captured by introducing a new polarizability $\overleftrightarrow{\alpha}$ that relates p to the incident field E_{inc} as follows [133]

$$p = \varepsilon_0 n^2 \overleftrightarrow{\alpha} \cdot E_{\text{inc}}, \tag{3.3}$$

where $\overleftrightarrow{\alpha}$ is also a diagonal matrix in the chosen coordinate system. From (3.1) and (3.3), and using the property that the diagonal matrices $\overleftrightarrow{\alpha}_0$ and $\overleftrightarrow{\alpha}$, and their

inverses, all commute with each other, we then write

$$\overleftrightarrow{\alpha}^{-1} \cdot E_{\text{mod}} = \overleftrightarrow{\alpha}_0^{-1} \cdot E_{\text{inc}}. \tag{3.4}$$

Then using Eqs. (3.2) and (3.3) in Eq. (3.4), we can write after some simplification

$$\overleftrightarrow{\alpha}^{-1} = \overleftrightarrow{\alpha}_0^{-1} - \frac{i}{6\pi}(n\tilde{\omega})^3 \overleftrightarrow{U} - \overleftrightarrow{\beta}_0, \tag{3.5}$$

where $\overleftrightarrow{U}$ is the unit dyadic. Recall that in general $\text{Im}[\overleftrightarrow{\alpha}_0^{-1}]$ describes nonradiative losses due to electron collisions within the nanoantenna, and free carrier absorption and interband transitions in the gold [100]. While the losses due to electron scattering are not relevant for the dimensions of the nanoantennas considered here, the losses due to bulk free-carrier absorption and interband transitions (the latter being negligible for our wavelengths) are captured by using the frequency-dependent complex dielectric constant for gold. In addition to these non-radiative losses, we can identify the radiation reaction term in (3.5) as describing radiative losses due to the scattering of the electromagnetic field from the nanonantenna. Both the radiative and non-radiative losses will broaden its extinction spectrum. The dynamic depolarization term, on the other hand, leads to a shift in the resonance frequency from its value in the electrostatic limit. We note that similar expressions for the dipolar polarizability of spheres and spheroids have been calculated previously from the modified long wavelength approximation (MLWA) [12] or from Padé approximations of Mie scattering coefficients [134].

We now consider a square lattice of these dipoles lying in the xy-plane. All the dipole moments in the array will be identical for a normally incident plane wave, and so we write

$$p = \varepsilon_0 n^2 \overleftrightarrow{\alpha}_0 \cdot E_{\text{tot}}, \tag{3.6}$$

where E_{tot} includes the field E_{mod}, given by (3.2), along with the field from the remaining nanoantennas in the array,

$$E_{\text{tot}} = E_{\text{inc}} + \frac{1}{4\pi\varepsilon_0}\frac{2}{3} i n \tilde{\omega}^3 p + (\overleftrightarrow{\beta}_0 + \overleftrightarrow{\beta}) \cdot \frac{1}{\varepsilon_0 n^2} p. \tag{3.7}$$

The dyadic $\overleftrightarrow{\beta}$ is the 'dynamic interaction constant' of the array [135], and is given by

$$\overleftrightarrow{\beta} = \sum_{R \neq 0} \overleftrightarrow{G}(-R), \tag{3.8}$$

with $\overleftrightarrow{G}$ being the periodic Green dyadic [136], such that $\overleftrightarrow{G}(-R) \cdot p$ represents the electric field at the origin due to a dipole moment p at a lattice site R. We note that $\text{Im}[\overleftrightarrow{\beta}]$ and $\text{Re}[\overleftrightarrow{\beta}]$ include the radiative and non-radiative near-field contributions at the origin from all the other nanoantennas in the array, respectively.

Similar to our model of an isolated nanoantenna, we now redefine the polarizability of each nanoantenna in the array with respect to the incident field as

$$p = \varepsilon_0 n^2 \overleftrightarrow{\alpha}_{\text{eff}} \cdot E_{\text{inc}}, \tag{3.9}$$

and we find that the effective polarizability $\overleftrightarrow{\alpha}_{\text{eff}}$ of a nanoantenna in a square array

is given by

$$\overleftrightarrow{\alpha}_{\text{eff}}^{-1} = \overleftrightarrow{\alpha}_{0}^{-1} - \frac{i}{6\pi}(n\tilde{\omega})^3 \overleftrightarrow{U} - (\overleftrightarrow{\beta}_0 + \overleftrightarrow{\beta}). \tag{3.10}$$

To calculate the the poorly convergent $\overleftrightarrow{\beta}$, we use the Poisson summation method followed by singularity cancellation discussed in Refs. [135, 136]. For the incident electric field polarized along the major axis of the nanoantenna (aligned with the x-axis, see diagram of the array and the excitation geometry in Fig. 3.3(a)), only the dipole along the x-axis is excited. Hence, the response of the array is given by the diagonal component of the effective polarizability $[\alpha_{\text{eff}}]_{\text{xx}}$. For our system as depicted in Fig. 3.3(a), the exact analytic result for $\text{Im}[\beta_{\text{xx}}]$, also known as the 'lattice sum', can be obtained from equations (76) and (110) in Swiecicki and Sipe [136], and is given by

$$\text{Im}[\beta_{\text{xx}}] = -\frac{1}{6\pi}(n\tilde{\omega})^3 + \frac{n\tilde{\omega}}{2a^2}. \tag{3.11}$$

In contrast, $\text{Re}[\beta_{\text{xx}}]$ does not have a closed-form expression, and is actually an infinite series [135, 137]. We numerically evaluate the series in our calculations by including as many terms required until convergence is achieved for the extinction spectrum. For our system, including the non-radiative contributions at the origin from a 100×100 array of dipoles is sufficient for $\text{Re}[\beta_{\text{xx}}]$ to converge.

From Eqs. (3.11) and (3.10), now we can write $[\alpha_{\text{eff}}]_{\text{xx}}$, while dropping the suffix xx, as

$$\alpha_{\text{eff}}^{-1} = \alpha_0^{-1} - \frac{i}{6\pi}(n\tilde{\omega})^3 N_{\text{eff}} - (\beta_0 + \text{Re}[\beta]), \tag{3.12}$$

where $N_{\text{eff}} = 3\lambda^2/4\pi n^2 a^2$ is the effective number of dipoles enclosed within a circle of radius equal to the wavelength in the background medium, λ/n. We note that the effective depolarization term of the dipole in the array, $\text{Re}[\alpha_{\text{eff}}^{-1}]$, is enhanced by the 'collective retardation' term, $\text{Re}[\beta]$, which is responsible for the shift in the resonance frequency (given by $\text{Re}[\alpha_{\text{eff}}^{-1}(\omega_0)] = 0$, or the maxima of the extinction spectra) for different arrays observed in Figs. 3.2(a) and 3.2(b). We also note from (3.12) that there are no collective contributions to the non-radiative losses due to absorption, which are once again represented by the term $\text{Im}[\alpha_0^{-1}]$. On the other hand, the radiative damping term has the form of the radiation-reaction term of N_{eff} dipoles. This collectively enhanced radiative damping is responsible for the observed linewidth broadening in Figs. 3.2(a) and 3.2(b). Finally, the transmittance T and reflectance R spectra of the array depend on $\alpha_{\text{eff}}(\omega)$ as follows [138]

$$\begin{aligned} R &= |r|^2 = \frac{(n\tilde{\omega})^2 |\alpha_{\text{eff}}|^2}{4a^4}, \\ T &= |t|^2 = 1 + R - \frac{n\tilde{\omega}}{a^2}\text{Im}[\alpha_{\text{eff}}]. \end{aligned} \tag{3.13}$$

Since the effective number of dipoles N_{eff} within a wavelength-sized area is proportional to a^{-2}, in the regime where scattering dominates absorption, the FWHM linewidth of the extinction spectrum $(1-T)$ should decrease according to a^{-2} as the lattice constant of the planar array is increased.

Figure 3.3(b) shows the analytically calculated extinction spectra of the equivalent ellipsoid arrays for various lattice constants. The dimensions of the ellipsoid (semi-principal axes of $a_e = 112$ nm, $b_e = 63.85$ nm, $c_e = 12.25$ nm) are chosen so

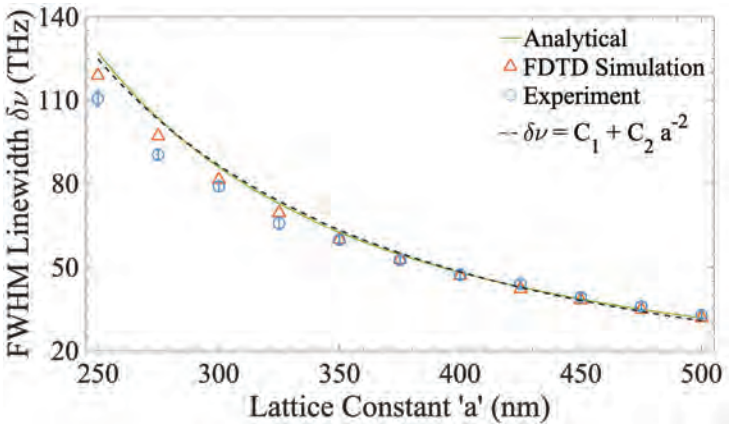

Figure 3.4: FWHM linewidths vs lattice constant of extinction spectra obtained from experiment (circles, blue), simulations (triangles, red) and analytical calculations (solid-green). The black-dashed curve represents the fitted curve $\delta\nu = C_1 + C_2 a^{-2}$ to the analytical data, where $C_1 = -0.1694$ THz and $C_2 = 7.73 \times 10^6$ THz nm^2.

as to have the closest agreement between the cross-section spectra of the ellipsoid calculated analytically through the use of Eqs. (C.5)-(C.7), and of the nanorod calculated through FDTD simulations. See appendix C for more details on this calculation. We note that the analytically calculated extinction spectra shown in Fig. 3.3(b) agree reasonably well with the corresponding measured and simulated extinction spectra shown in Fig. 3.2.

3.4 Results and Discussion

In Fig. 3.4 we show the dependence of the FWHM linewidths estimated from the measured, FDTD simulated, and analytically calculated extinction spectra on the lattice constant of the array a. For the datasets obtained from FDTD

simulations (red triangles) and the experiment (blue circles), only the linewidths of the spectra shown in Figs. 3.2(a) and 3.2(b) respectively are plotted in Fig. 3.4. For the analytical dataset, the extinction spectra of equivalent ellipsoid arrays were calculated for arrays with lattice constants varying from 250 nm to 500 nm in steps of 1 nm. The FWHM linewidth of these analytically calculated spectra are plotted in Fig. 3.4 as a continuous (green) line. The error bars on the experimental data indicate the experimental error in determining the FWHM from the OSA readout due to detector noise.

A simple expression for the dependence of the FWHM on the lattice constant is difficult to extract even for the analytic model, because the resonance frequency itself depends on the lattice constant a. However, for the form of the polarizability α_0 adopted (see appendix C), and recognizing that the shift of the resonant frequency due to the real part of β and the linewidth itself are reasonably small compared to the resonant frequency ω_0, a linewidth dependence of the form $\delta\nu = C_1 + C_2 a^{-2}$ can be expected, where C_1 captures the effects of absorption and $C_2 a^{-2}$ the effects of radiative broadening. The constants C_1 and C_2 are obtained by fitting the aforementioned curve to the analytical dataset. The fitted curve ($C_1 = -0.1694$ THz and and $C_2 = 7.73 \times 10^6$ THz nm^2) is shown as a dashed black line in Fig. 3.4, and we see a good agreement between the analytical dataset and the fitted curve. Comparing the numerical values of C_1 and C_2, we note that the term $C_2 a^{-2}$ has a significantly larger contribution to $\delta\nu$, thereby indicating that the radiative broadening effects dominate over those of absorption.

For lattice constants larger than about 375 nm there is an excellent quantitative

fit between experiment, FDTD simulation, and the analytic model. At smaller lattice constants we see that the results of the FDTD simulations differ from those of the analytic model. This may be in part due to the fact that the FDTD simulations were done for the actual array of rod-shaped nanoparticles, which includes contributions from all multipolar excitations of the nanoparticle as well as their interactions with the other nanoparticles in the array. In contrast, the analytic model relies on a fit to the response of an isolated nanoparticle with ellipsoidal shape, and the use of a point dipole approximation for calculating the interaction between the nanoparticles in the array. The validity of these features of the analytic model become questionable for very small lattice constants, giving a possible reason for the difference between the FDTD simulations and the analytic model for small values of a. We also see that at small lattice constants the experimental results differ from the results of the FDTD simulations, which may be due to inhomogeneities in the properties of the fabricated nanorods. The inevitable fabrication imperfections would contribute to some inhomogeneous broadening in the experimental case, which is not an issue in the analytical model as well as FDTD simulations due to our assumption of all the nanoantennas being identical. The effect of these inhomogeneities in the fabricated nanorods can be expected to have a larger effect at smaller lattice constants where the response of a given nanorod is more sensitive to the details of the near field from its neighbors, and thereby could also contribute to the mismatch between the experiment and the simulations for smaller lattice constants.

Nonetheless, within a reasonable margin of error our results indicate that the

observed N_{eff}-fold radiative linewidth broadening in the arrays of nanoantennas is a collective effect. We have also shown through the closed form expression in Eq. (3.12) of the imaginary part of the effective polarizability of each nanoantenna within the array that the observed N_{eff}-dependent linewidth scaling is because the radiation-reaction of the array is proportional to N_{eff}. In addition, since we have explicitly designed our nanoantennas to have a much larger scattering cross-section than the absorption cross-section, we conclude that the observed linewidth broadening is due to the interaction of the plasmonic scatterers with the common radiation field.

The scaling of the linewidth with the number density of dipoles indicates a connection with Dicke superradiance, where the interaction with the common radiation field is also the important physics. Dicke's treatment dealt with two-level systems [117]. While our plasmonic scatterers can be well described by a harmonic oscillator model, in general one would only expect a correspondence with two-level systems in the weak excitation limit. With that in mind we look at the first excited state in the Dicke model, which consists of a single excitation "shared" among the N two-level systems. The total dipole matrix element between this lowest excited state and the ground state is a factor of $\sqrt{N}$ larger than the dipole matrix element between the excited state and the ground state of a single two-level system, and so if the N two-level systems are confined within a wavelength of light the emission rate from this first excited state will be a factor of N larger than for a single excited two-level system, leading to a linewidth that is a factor of N times that for a single excited two-level system. This can be called "weak superradiance," to distinguish

it from the behavior of other excited states in the Dicke model that have much enhanced decay rates. In a scattering problem in the semiclassical approximation, where the radiation field is treated classically, it is the dipole moment between the ground state and the first excited state of the Dicke model that is relevant for weak enough incident fields. There again one finds a linewidth that is N times as large as would be seen if only a single two-level system were considered [133, 139–143]. Now if only the ground state and the first excited state are considered, then the Dicke model is essentially equivalent to a set of harmonic oscillators, since for the latter system the first excited state also consists of a single "shared" excitation, here shared between the harmonic oscillators. Thus we see that the behavior considered here for plasmonic oscillators mimics the corresponding behavior of two-level systems. And so whether considering plasmonic oscillators or two-level systems under weak excitation, for planar arrays of effective atoms the relevant N is the number of those atoms within a square wavelength of light.

3.5 Conclusion

To summarize, here we have shown that the linewidth of light scattered by a planar array of plasmonic nanoantennas scales linearly with the effective number of nanoantennas contained within an area equal to the square of the resonant optical wavelength. Through an analytical model, we have shown that this is a collective effect resulting from the enhancement of the radiation-reaction of a particular

nanoantenna by the radiation-reaction of all the other nanoantennas in the array, which in turns leads to an N_{eff}-fold enhancement of the radiative linewidth. In an effort to elucidate the relationship between the collective radiative behavior of plasmonic scatterers and the behavior of Dicke superradiance, we have also discussed the different radiative behaviors of plasmonic scatterers and dipolar emitters. We have argued that the collective radiative behavior of a system of plasmonic scatterers, and a corresponding system of 'weakly'-excited emitters (wherein only one emitter is initially excited on an average) are analogous. Accordingly, we have termed this effect 'weak-superradiance'. In the subsequent chapters, we will build upon the analytical model developed in this chapter to bi-layered and multi-layered structures made of dipolar arrays, and discuss the interesting linear optical properties of these structures.

4. Dark and Bright modes and their Coherent Control in Dipolar Metasurface Bilayers

4.1 Introduction

We now extend the analytical model developed in chapter 3 for a single dipolar nanoantenna array to a stack of two such arrays with a sub-wavelength separation between them. In a single array we have one collective mode with an enhanced radiative damping compared to an isolated dipole. For two such arrays, the strong radiative coupling between the arrays should lead to the emergence of hybrid modes with interesting scattering properties. Mode hybridization in a plasmonic dimer, where two identical nanoparticles are placed at a sub-wavelength separation, has been studied extensively [144–149]. These dimers can support “dark" modes that have a significant local field enhancement in their interstices. They are “dark" in the sense that, if the variation of the incident field over the dimer is neglected,

they cannot be excited because of their vanishing dipole moment. [144, 147, 148]. Dark modes in dimers can, however, be excited by linearly polarized light incident along the dimer axis, because of higher order multipole moments of the structure. The large field enhancement [150] and narrow absorption linewidths, which result because of the weak radiation from these higher order multipole moments, make these “bilayered" dimer structures a promising platform for nonlinear optical applications [92], including plasmonic nanolasers [151, 152]. The anti-parallel polarization distribution of these dark modes forms a quasi-current loop with an effective magnetic dipole, which can be a useful building block for an effective negative index material [153, 154]. Previous studies of cooperative modes in metasurface bilayers have been restricted to spherical or disc-shaped nanoparticles made of noble metals with resonances at visible or NIR frequencies [25, 155–158]. These nanoparticles have a low scattering efficiency due to their small dipolar polarizability [12, 15, 159, 160], and are also affected by the presence of multipolar modes and large absorption losses in most plasmonic materials due to interband transitions at ultraviolet frequencies.

In this chapter, we show that radiative coupling in this bilayer leads to the formation of bright (symmetric) and dark (anti-symmetric) modes [143], and discuss how the short-range non-radiative coupling shifts these resonances. We show that the “dark" modes can make a significant contribution to the optical response; although they are weakly driven, their weak radiation rate leads to significant excitation. We also discuss the selective excitation of these dark and bright modes by varying the relative phase between two equal intensity counter-

propagating fields. In section 4.2, we describe our analytical model for the bilayer with misalignments between the lattice points in the two arrays. We then also compare the reflectance and absorption spectra calculated from our analytical model with those obtained from FDTD simulations for both perfectly aligned and slightly misaligned bilayers. Finally, in section 4.3, we discuss the selective excitation of these modes through two equal intensity counter-propagating fields, which is also referred to as the coherent control of absorption or coherent perfect absorption (CPA) [161, 162].

4.2 Analytical Model

We now have two square arrays of dipolar nanoantennas with in-plane lattice constant of a that are separated by a sub-wavelength distance b. Figure 4.1 shows a diagram of the bilayer along with the assumed coordinate system. The first array is assumed to be in the $(z = -b/2)$ plane, and the second array in the $(z = b/2)$ plane. We again assume the incident wave to be a normally incident plane-wave polarized along the long axis of the nanoantenna $E_{\text{inc}} = E_{\text{inc}} e^{i(\tilde{\omega} n z - \omega t)} \hat{x}$, and make the point dipole approximation as in chapter 3.

4.2.1 Single nanoantenna array

The total electric field E_{tot} at each point dipole of dipole moment p in a single array is given by Eq. (3.7) derived in chapter 3, which we have restated below for

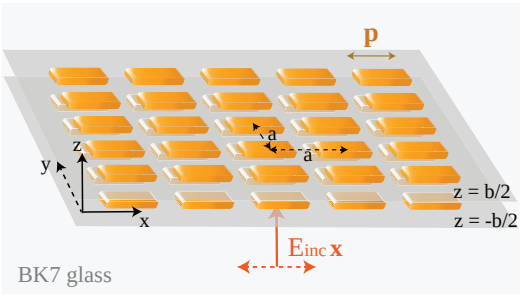

Figure 4.1: Diagram of the bilayered strucutre of two nanoantenna arrays spaced by a separation b, and excited by a normally incident plane wave E_{inc}.

convenience:

$$E_{\text{tot}} = E_{\text{inc}} + \frac{1}{4\pi\varepsilon_0}\frac{2}{3} in\tilde{\omega}^3 p + (\overleftrightarrow{\beta}_0 + \overleftrightarrow{\beta}) \cdot \frac{1}{\varepsilon_0 n^2} p, \tag{4.1}$$

where once again

$$p = \varepsilon_0 n^2 \overleftrightarrow{\alpha}_0 E_{\text{tot}}, \tag{4.2}$$

$\overleftrightarrow{\alpha}_0$ is the electrostatic polarizability of the nanoantenna, and the dyadics $\overleftrightarrow{\beta}_0$ and $\overleftrightarrow{\beta}$ account for the retardation over the volume of the nanoantenna, and the radiation reaction as well as retardation from all the other nanoantennas in the array, respectively.

The resonance frequency ω_0 in the electrostatic limit is once again given by the condition $\text{Re}[\alpha_{0,\text{ii}}^{-1}(\omega_0)] = 0$. We now define an effective polarizability $\overleftrightarrow{\alpha}_{\text{shift}}$ that includes the electrostatic response of each nanoantenna along with the resonance shifts due to the retardation contributions $\overleftrightarrow{\beta}_0$ and $\text{Re}[\overleftrightarrow{\beta}]$,

$$\overleftrightarrow{\alpha}_{\text{shift}}^{-1} = \overleftrightarrow{\alpha}_0^{-1} - \varepsilon_0 n^2 (\overleftrightarrow{\beta}_0 + \text{Re}[\overleftrightarrow{\beta}]). \tag{4.3}$$

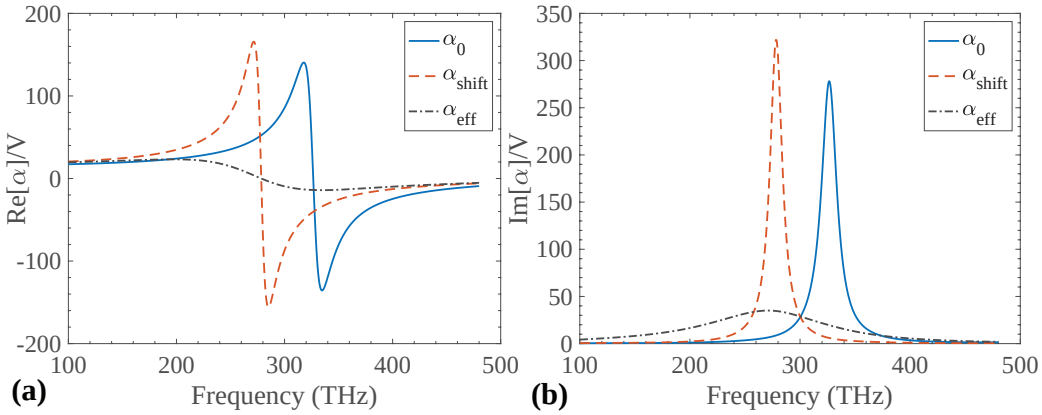

Figure 4.2: Spectra of the (a) real and (b) imaginary parts of polarizabilities normalized to the volume of a cuboidal gold nanoantenna (185 nm long, 105 nm wide and 20 nm thick, and embedded in BK7 glass) in the electrostatic limit (blue, solid), including only the retardation of the nanoantenna and the array (red, dashed), and including both retardation and radiation reaction of the nanoantenna and the array (black, dot-dashed). The nanoantenna polarizability model is taken to be the same as in [163], and the array lattice constant is assumed to be 250 nm.

The term $\mathrm{Im}[\overleftrightarrow{\alpha}_{\mathrm{shift}}^{-1}]$ is the same as $\mathrm{Im}[\overleftrightarrow{\alpha}_{0}^{-1}]$, which accounts for absorption losses in the nanoantenna. The term $\mathrm{Im}[\overleftrightarrow{\beta}]$ is the collective radiation reaction, and for the excitation geometry shown in Fig. 4.1, is given by Eq. (3.11), which we rewrite below for convenience

$$\mathrm{Im}[\beta_{\mathrm{xx}}] = -\frac{1}{6\pi}(n\tilde{\omega})^3 + \frac{n\tilde{\omega}}{2a^2}. \tag{4.4}$$

From Eqs. (4.2) - (4.4), we can write after some simplification

$$\alpha_{\mathrm{shift,xx}}^{-1} p_x = \varepsilon_0 n^2 \left(E_{\mathrm{inc}} + \frac{i\tilde{\omega}}{2\varepsilon_0 n a^2} p_x \right). \tag{4.5}$$

We drop the suffixes x from now on, and from Eq. (4.5) write

$$\alpha_{\text{eff}}^{-1} = \alpha_{\text{shift}}^{-1} - \frac{i\tilde{\omega}n}{2a^2}, \tag{4.6}$$

where α_{eff} has been defined in chapter 3 such that $p = \varepsilon_0 n^2 \alpha_{\text{eff}} E_{\text{inc}}$. Figure 4.2(a) and (b) show the spectra of the real and imaginary parts, respectively of α_0 (blue, solid), α_{shift} (red, dashed), and α_{eff} (black, dot-dashed) of a representative gold nanoantenna in a square lattice with lattice constant a of 250 nm. The nanoantenna parameters are taken to be the same as in chapter 3, and we keep a fixed at 250 nm in all the results presented here. As before, we also use the permittivity data from Johnson and Christy for gold [70], and the refractive index data from the Schott optical glass datasheets [131] for the float glass. We note from Fig. 4.2 that the effect of retardation is to shift the nanoantenna resonance, while the radiation reaction term contributes to its broadening.

We now define the polarization P of the nanoantenna array as the dipole moment per unit area, which is essentially the product of dipole moment p of a nanoantenna in the array and the number density of these nanoantennas (= $1/a^2$ for a square array with lattice constant a). So we write

$$P = \frac{\varepsilon_0 n^2 \alpha_{\text{eff}}}{a^2} E_{\text{inc}}. \tag{4.7}$$

The x component of the electric field from this lattice of electric dipoles at a position $(l_1 a + \Delta_x, l_2 a + \Delta_y, z)$, with (l_1, l_2) being the lattice indices in the xy-plane

and $\Delta_{x,y}$ being the displacements from the lattice points $(l_1 a, l_2 a)$, is given by

$$E_x(\mathbf{R}_l + \Delta, z) = \frac{i\tilde{\omega}}{2\varepsilon_0 n} P e^{i\tilde{\omega} n|z|} + \frac{\pi}{\varepsilon_0 a n^2} T_{xx}(\Delta, z) P, \tag{4.8}$$

where $\mathbf{R}_l = l_1 a\hat{\mathbf{x}} + l_2 a\hat{\mathbf{y}}$, and $\Delta = \Delta_x\hat{\mathbf{x}} + \Delta_y\hat{\mathbf{y}}$. The first term on the right is the long-range radiative field, whereas the second term is the short-range near-field that decays rapidly with z. See appendix D for the full derivation of Eq. (4.8), and the expression for $T_{xx}(\Delta, z)$.

4.2.2 The bilayered structure

We now consider the bilayered structure, wherein the two lattice planes are assumed to be laterally misaligned such that the lattice points in the second (first) plane are displaced by Δ ($-\Delta$) with respect to lattice points in the first (second) plane. The field at each dipole plane now includes not only the incident field E_{inc}, but also the radiated field and the near-field from the other plane. Hence, we can write the polarization of both dipole arrays as

$$P_{2,1} = \frac{\varepsilon_0 n^2 \alpha_{\text{eff}}}{a^2} \left[E_{\text{inc}} e^{\pm i\tilde{\omega} n b/2} + E_x(\pm\Delta, \pm b/2) \right], \tag{4.9}$$

where we consider the unit cell to be centered at the origin for simplicity. Multiplying both sides of Eqs. (4.9) by α_{eff}^{-1} and substituting Eq. (4.6), we get after some

simplification

$$\alpha_{\text{shift}}^{-1} P_{2,1} = \frac{\varepsilon_0 n^2}{a^2} E_{\text{inc}} e^{\pm i\tilde{\omega} nb/2} + \frac{i\tilde{\omega}}{2a^2}(P_{2,1} + P_{1,2} e^{i\tilde{\omega} nb}) \pm \frac{\pi}{a^3} T_{xx}(\Delta, b) P_{1,2}, \quad (4.10)$$

where we have used $T_{xx}(\Delta, b) = T_{xx}(-\Delta, -b)$. We then define $P_A = (P_1 + P_2)/2$ and $P_M = (P_2 - P_1)/2$ using Eq. (4.10), the first being the average of the plane polarizations, and the second half the difference between them. After some algebraic manipulation, we have

$$P_A = \frac{\varepsilon_0 n^2 \alpha_A}{a^2} E_{\text{inc}} \cos(\tilde{\omega} nb/2), \quad (4.11)$$

$$P_M = i\frac{\varepsilon_0 n^2 \alpha_M}{a^2} E_{\text{inc}} \sin(\tilde{\omega} nb/2), \quad (4.12)$$

where

$$\alpha_A^{-1} = \alpha_{\text{shift}}^{-1} + S(\Delta, b) - \frac{i\tilde{\omega} n}{a^2} \cos^2\left(\frac{\tilde{\omega} nb}{2}\right), \quad (4.13)$$

$$\alpha_M^{-1} = \alpha_{\text{shift}}^{-1} - S(\Delta, b) - \frac{i\tilde{\omega} n}{a^2} \sin^2\left(\frac{\tilde{\omega} nb}{2}\right), \quad (4.14)$$

and

$$S(\Delta, b) = \frac{\tilde{\omega} n}{2a^2} \sin(\tilde{\omega} nd) - \frac{\pi}{a^3} T_{xx}(\Delta, b). \quad (4.15)$$

The resonance frequency $\omega_A(\omega_M)$ of the $A(M)$ mode is given by the condition $\text{Re}[\alpha_{A,M}^{-1}] = \text{Re}[\alpha_{\text{shift}}^{-1}] \pm S(\Delta, b) = 0$. Hence, the purely real term $S(\Delta, b)$ leads to equal and opposite shifts in resonances for the A and M modes with respect to the resonance of a single layer. The terms $\text{Im}[\alpha_{\text{A,M}}^{-1}]$ include the absorption losses

$\mathrm{Im}[\alpha_{\mathrm{shift}}^{-1}]$, and the radiative damping terms given by the last terms on the right in Eqs. (4.13) and (4.14). For very small separations b, such that $\tilde{\omega}nb \ll 1$, the symmetric A mode has almost twice the radiative damping than a single layer. In contrast, the radiative damping of the anti-symmetric M mode is very small. For such small separations the A mode is a nominally bright mode with a wider linewidth than the single array, while the M mode is a nominally dark mode with a significantly narrower linewidth that in practice is limited by absorption losses within the nanoantenna. Hence, at the resonance of the M mode ($\mathrm{Re}[\alpha_{\mathrm{M}}^{-1}] = 0$), the polarizability α_M can be made to be significantly larger than α_{eff} with a careful choice of design parameters a and b. For this condition, the amplitude P_M of the nominally dark mode can be much larger than the amplitude P_A of the nominally bright mode, which essentially implies that the dipole moments of the nanoantennas in the different layers are mostly out of phase. We note that the retardation of the incident field between the two arrays is large enough to allow the excitation of the M mode at normal incidence for even perfectly aligned arrays [164].

Using $P_1 = P_A - P_M$ and $P_2 = P_A + P_M$, we calculate the expressions for the transmittance 'T', reflectance 'R' and absorbance 'A' of the bilayer. The forward propagating field from the bilayer at a distance $z \gg b/2$ is given by

$$E_{\mathrm{forward}}(z) = e^{i\tilde{\omega}nz}\left[E_{\mathrm{inc}} + \frac{i\tilde{\omega}}{2\varepsilon_0 n}(P_1 e^{i\tilde{\omega}nb/2} + P_2 e^{-i\tilde{\omega}nb/2})\right], \tag{4.16}$$

where the first term on the right is simply the retarded incident field, and the remaining terms are the long-range radiative fields from both nanoantenna arrays.

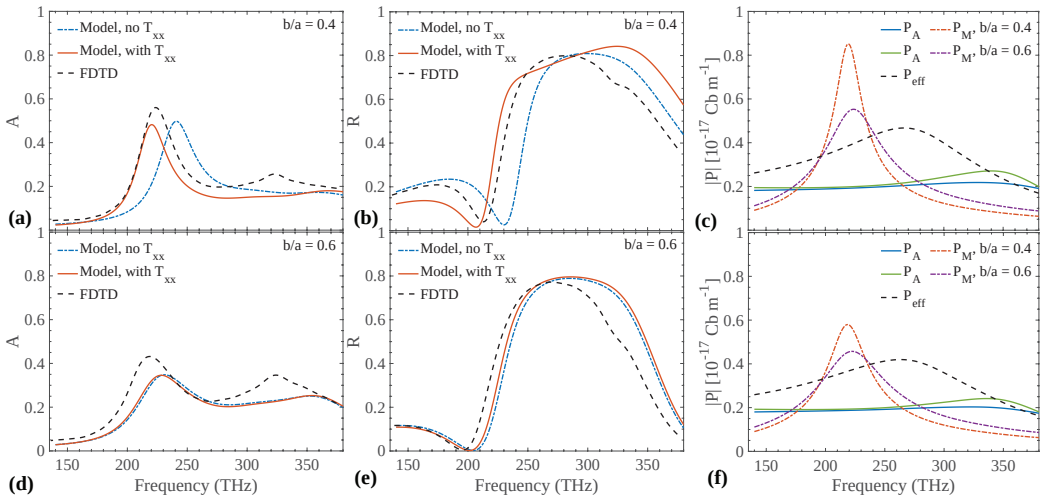

Figure 4.3: Absorption spectra of a bilayer structure with no misalignments between the layers, and (a) $b/a = 0.4$ and (d) $b/a = 0.6$ obtained from Eqs. (4.17) and (4.19) without (blue, dot-dashed) and with (red, solid) the near-field terms $T_{xx}(0,d)$. The black dashed lines are the respective absorption spectra obtained from FDTD simulations. The reflection spectra for the $b/a = 0.4$ and $b/a = 0.6$ structure are shown in panels (b) and (e), respectively. The polarization spectra of P_A (solid) and P_M (dot-dashed) for the two aforementioned bilayers without and with absorption losses in the nanoantennas are shown in panels (c) and (f), respectively along with the P_{eff} for a single nanoantenna plane (black, dashed) without and with the absorption losses.

Rewriting P_1 and P_2 in terms of P_A and P_M, and using Eqs. (4.11) and (4.12), we get after some simplification

$$t \equiv \frac{E_{\text{forward}}(z)}{E_{\text{inc}} e^{i\tilde{\omega}nz}} = 1 + \frac{i\tilde{\omega}n}{a^2}\left(\alpha_A \cos^2\frac{\tilde{\omega}nb}{2} + \alpha_M \sin^2\frac{\tilde{\omega}nd}{2}\right), \tag{4.17}$$

where t is the transmission coefficient, and $\mathrm{T} = |t|^2$ gives the transmittance. Similarly, the backward propagating reflected light from the bilayer at a distance

$z \ll -b/2$ is given by

$$E_{\text{backward}}(z) = \frac{i\tilde{\omega}}{2\varepsilon_0 n} e^{-i\tilde{\omega}nz}(P_1 e^{-i\tilde{\omega}nb/2} + P_2 e^{i\tilde{\omega}nb/2}). \tag{4.18}$$

Following a simplification procedure similar to that used in deriving Eq. (4.17), we can write

$$r \equiv \frac{E_{\text{backward}}(z)}{E_{\text{inc}} e^{-i\tilde{\omega}nz}} = \frac{i\tilde{\omega}n}{a^2}\left(\alpha_A \cos^2\frac{\tilde{\omega}nb}{2} - \alpha_M \sin^2\frac{\tilde{\omega}nb}{2}\right), \tag{4.19}$$

where r is the reflection coefficient, and the reflectance $\mathrm{R} = |r|^2$. The absorption is then given by $\mathrm{A} = 1 - \mathrm{R} - \mathrm{T}$.

Figures 4.3(a) and (d) show the absorption spectra of perfectly aligned bilayers ($\Delta = 0$), with relative separations b/a of 0.4 and 0.6, respectively. For both bilayers, there is a narrow absorption peak around 215 THz that, as we discuss later, corresponds to the resonance of the dark M mode. Including the $T_{xx}(0,b)$ terms in the analytical model redshifts this absorption peak, and results in a better agreement between the analytically calculated spectra and the FDTD simulations. The dip in the reflectance spectrum, shown in panels 4.3(b) and (e), occurs at the spectral overlap of the bright A mode and the dark M mode. The reflectance spectrum is largely flat between this dip until 320 THz, with an average reflectance of 80%, and essentially forms a stop band. The broad absorption resonance of the A mode can be observed in the analytical spectra beyond 350 THz, and blueshifts as b is reduced. In the FDTD result, an additional absorption peak around 320 THz is due to the electric quadrupolar mode of the nanoantenna (see appendix C), and

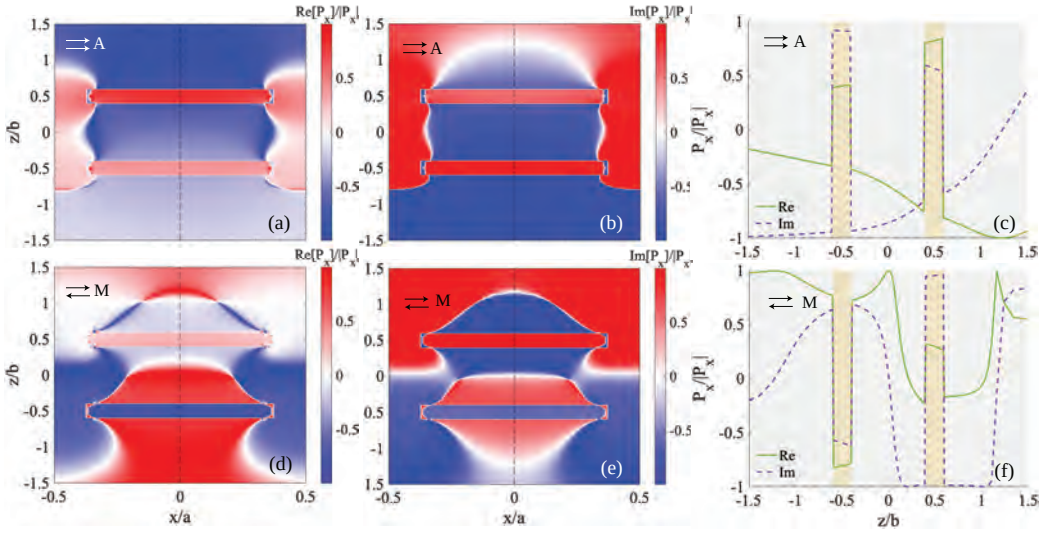

Figure 4.4: Normalized real (left panels) and imaginary (middle panels) parts of the field polarization $P_x(x,z) = \varepsilon_0 \varepsilon_r(x,z) E_x(x,z)/a^2$ in a single unit cell of a bilayer structure with $b/a = 0.4$ in the xz-plane. The field distribution E_x is obtained from FDTD simulations, and ε_r is the relative permittivity of the medium at a point (x,z). The top (bottom) panels show the polarization distributions at the resonance of the A (M) mode. The panels on the right show linecuts of the respective modes along the z-axis (black dotted lines in the left and middle planels), or $P_x(0,z)/|P_x(0,z)|$. The yellow shaded regions represent the z locations of the nanoantennas.

overshadows the absorption peak of the A mode for both bilayers. Ignoring this multipolar contribution at frequencies larger than 320 THz, our dipolar analytical model is able to largely reproduce the results from the full-wave FDTD simulations with a reasonable accuracy.

Figures 4.3(c) and (f) show the spectra of P_A (solid) and P_M (dot-dashed) of the two bilayers without and with the absorption losses, respectively. The polarization spectra of a single nanoantenna array P_{eff} (black, dashed) without and with the absorption losses are shown in the respective panels. The absorption losses are excluded by replacing $\alpha_{\text{shift}}^{-1}$ by $\text{Re}[\alpha_{\text{shift}}^{-1}]$ in Eq. (4.6), which, as observed

in Fig. 4.3(c), leads to narrower resonances throughout. However, for a single array the collective radiation reaction of the array is significantly larger than the absorption losses. Hence, ignoring the absorption losses leads to a barely perceptible narrowing of the spectrum of P_{eff}. For the bilayer, the P_A and P_M modes have equal and opposite resonance shifts with respect to the resonance of P_{eff}. The resonance linewidth of (dark) P_M is also much narrower than (bright) P_A, and P_M is significantly larger than both P_A and P_{eff} at its resonance even with the absorption losses. Figure 4.4 shows the normalized field polarization ($P_x = \varepsilon_0 \varepsilon_r E_x / a^2$) at the resonances of the A (top) and M (bottom) modes in the xz-plane of a single unit cell of the bilayer with $b/a = 0.4$. Here ε_r is the relative permittivity at a given location, and E_x is the local field obtained from FDTD simulations. Consistent with our predictions, we observe that for the A (M) mode, P_x within both nanoantennas has the same (opposite) phase. The large field enhancements at the corners of the nanoantennas are due to the large field gradient at these metallic corners, also known as the “lightning rod" effect [165, 166].

We now consider the effect of misalignments between the layers, which is a typical fabrication error in multilayered metasurfaces. Figure 4.5 compares the reflectance spectra of bilayers (a) without and (b) with misalignments [$\{\Delta_x, \Delta_y\} = \{0.2a, 0.2a\}$] for various separations b/a between the layers indicated in the legend. The solid lines are the reflectance spectra obtained from the analytical model, while the dashed lines are obtained from FDTD simulations. We note that the positions of the reflectance dip in the simulated and the analytically calculated spectra for both perfectly aligned and misaligned structures agree reasonably well with an

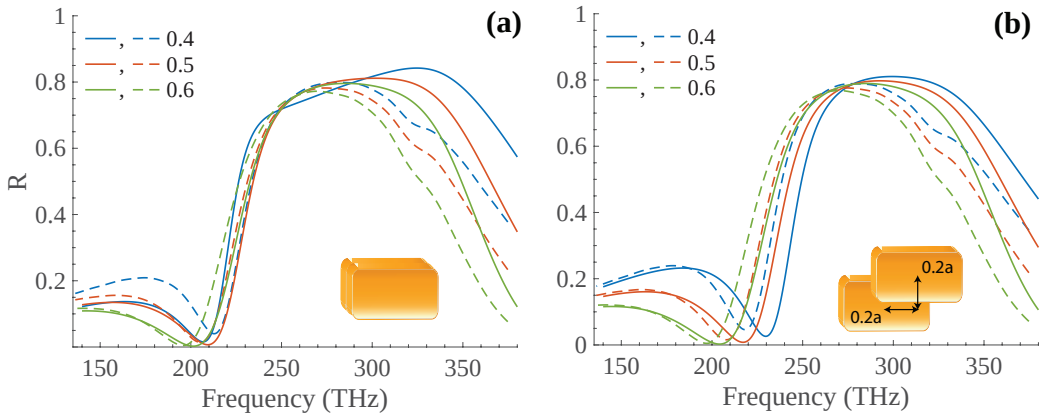

Figure 4.5: Reflectance spectra of (a) perfectly aligned, and (b) misaligned bilayers with $\{\Delta_x, \Delta_y\} = \{0.2a, 0.2a\}$ with various separations b/a shown in the legend. The solid reflectance curves were calculated using the full analytical model with the near-field terms $T_{xx}(0.2a, 0.2a, b)$, and the dashed curves were obtained from FDTD simulations.

accuracy larger than 95%. Additionally, the effect of misalignments becomes more pronounced as separation between the layers is reduced. This effect is not surprising, as the $T_{xx}(\Delta, b)$ terms that lead to retardation induced resonance shifts in both P_A and P_M get larger as b is reduced, and are sensitive to lattice misalignments. For the smallest separation considered here, this misalignment-induced resonance shift is as large as 12 THz (or about 75 nm). Hence, along with b and a, the lattice misalignments $\{\Delta_x, \Delta_y\}$ are another set of parameters that can be used for designing broadband spectral filters.

4.3 Coherent perfect absorption

Our analysis so far has been restricted to a single incident field on the bilayers, which behaves as a one port system. We now consider the situation when the bilayers are excited by two counter-propagating fields $E_1 e^{i(\tilde{\omega}nz-\omega t)}\hat{x}$ and $E_2 e^{-i(\tilde{\omega}nz+\omega t)}\hat{x}$, which is essentially a two port scenario. Both the phases and the amplitudes of the incident fields $E_{1,2}$ now constitute another set of parameters for the coherent control of scattering and absorption of light [161, 162, 167, 168]. We note that even with misalignments, the bilayers are symmetric with respect to the direction of excitation under normal incidence, which is also evident in the relation $T_{xx}(\Delta, b) = T_{xx}(-\Delta, -b)$. Accordingly, we define a 2×2 symmetric scattering matrix S_{scat} that relates the vector of incoming fields $[E_2\,, E_1]^T$ to the outgoing fields $[E_2^-\,, E_1^-]^T$ as

$$\begin{bmatrix} E_2^- \\ E_1^- \end{bmatrix} = S_{\text{scat}} \begin{bmatrix} E_2 \\ E_1 \end{bmatrix} = \begin{bmatrix} r & t \\ t & r \end{bmatrix} \begin{bmatrix} E_2 \\ E_1 \end{bmatrix}, \tag{4.20}$$

where r and t are the transmission and reflection coefficients that have been defined in Eqs. (4.17) and (4.19), respectively.

For the specific set of input fields where there are no outgoing fields, i.e. $[E_2^-\,, E_1^-]^T$ is a null vector, the incoming radiation is converted to trapped radiation that dissipates non-radiatively within the system. This effect has been referred to as coherent perfect absorption (CPA), and is the time-reversed counterpart of laser action [161, 162, 168]. Setting $[E_2^-\,, E_1^-]^T$ to a null vector in Eq. (4.20) leads

to the condition that for a non-trivial solution of Eq. (4.20) to exist: $|\det(\mathrm{S}_{\mathrm{scat}})|$ approaches zero, or $|r^2 - t^2| \approx 0$. The symmetric solution $(r+t) \approx 0$ corresponds to the eigenvector $[E_2\,,E_1]^T = [1\,,1]^T$, which implies that the CPA condition is satisfied when $E_2 = E_1$. Similarly, the anti-symmetric solution $(r-t) \approx 0$ corresponds to the eigenvector $[E_2\,,E_1]^T = [1\,,-1]^T$, or the CPA condition is satisfied when $E_2 = -E_1$. We also note that it is not possible to satisfy either of the CPA conditions with a single array of dipolar nanoparticles that is not backed by a reflector [169].

From Eqs. (4.17) and (4.19), we write the anti-symmetric CPA condition as

$$r - t = -\left(1 + \frac{2in\tilde{\omega}}{a^2}\alpha_M \sin^2\frac{\tilde{\omega}nb}{2}\right) = 0, \tag{4.21}$$

which on using Eq. (4.14) simplifies to

$$\alpha_{\mathrm{shift}}^{-1} - S + \frac{in\tilde{\omega}}{a^2}\sin^2\frac{\tilde{\omega}nb}{2} = 0. \tag{4.22}$$

At the resonance of the M mode, $\mathrm{Re}[\alpha_{\mathrm{shift}}^{-1}] - S = 0$. Recalling that $\mathrm{Im}[\alpha_{\mathrm{shift}}^{-1}] = \mathrm{Im}[\alpha_0^{-1}]$, and that $\mathrm{Im}[\alpha_0^{-1}](= -\mathrm{Im}[\alpha_0]/|\alpha_0|^2)$ is negative, we get the following simplified anti-symmetric CPA condition at the resonance of the M mode

$$|\mathrm{Im}[\alpha_0^{-1}]| = \frac{n\tilde{\omega}}{a^2}\sin^2\frac{\tilde{\omega}nb}{2}. \tag{4.23}$$

Similarly, the simplified symmetric CPA condition at the resonance of the A mode

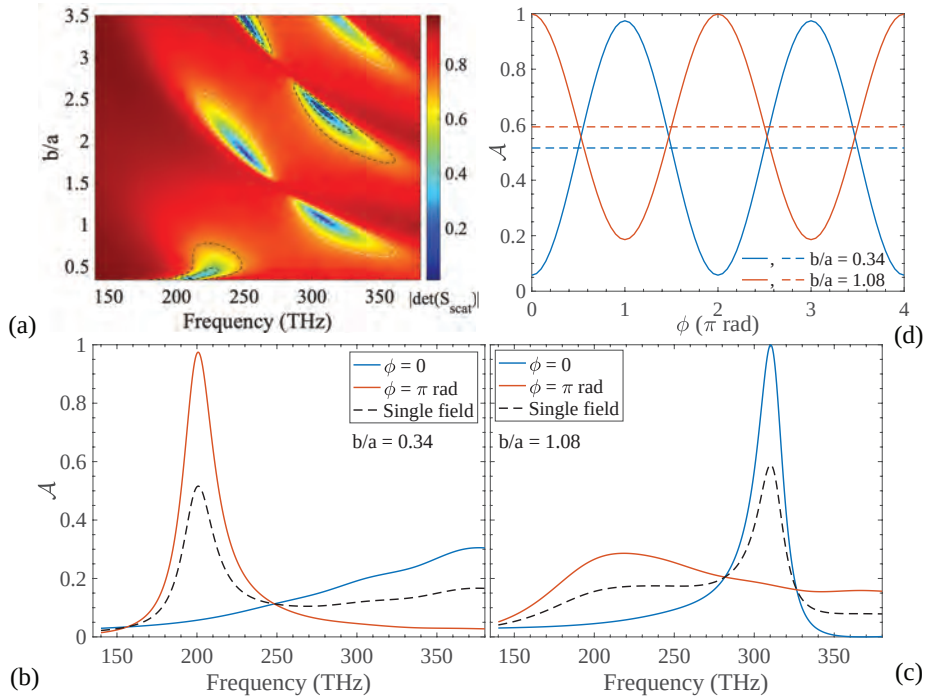

Figure 4.6: (a) Spectra of $|\det(\mathrm{S}_{\mathrm{scat}})|$ for various separations b of perfectly aligned bilayers. Absorption spectra of a bilayer with (b) $b/a = 0.34$, and (c) $b/a = 1.08$ for a single normally incident field (black, dashed), and two counter-propagating normally incident fields with equal amplitude and same phase (blue) and opposite phase (red). (d) The joint absorption $\mathscr{A}$ as the phase difference ϕ between the two fields $E_{1,2}$ is varied (solid lines) for bilayers with $b/a = 0.34$ (blue) and $b/a = 1.08$. The respective maximum single incident field absorption values are shown by dashed lines.

can be written as

$$|\mathrm{Im}[\alpha_0^{-1}]| = \frac{n\tilde{\omega}}{a^2}\cos^2\frac{\tilde{\omega}nb}{2}. \tag{4.24}$$

The CPA conditions given by Eqs. (4.23) and (4.24) can also be interpreted as critical coupling conditions to the M and the A mode of the bilayer, respectively, wherein the absorption losses are balanced by radiative coupling losses to the respective mode. For very small separations between the bilayers, such that

$\tilde{\omega}nb \ll 1$, the right-hand side of Eq. (4.23) becomes proportional to $(b/a)^2$, while the right-hand side of Eq. (4.24) becomes proportional to $1/a^2$. For the nanoantenna arrays with significantly larger collective radiation reaction than absorption, it is straightforward to see that the anti-symmetric, and not the symmetric, CPA condition given by Eq. (4.23) should hold true when $\tilde{\omega}nb \ll 1$. Figure 4.6(a) shows the spectra of $|\det(\mathrm{S_{scat}})|$ for various separations b/a of perfectly aligned bilayers. The minima, indicated by the blue regions in the plot, indicate the separations b/a where the CPA conditions are satisfied for a particular range of frequencies. The black (white) contours identify the anti-symmetric (symmetric) sets of CPA solutions. We note that the variation of $|\det(\mathrm{S_{scat}})|$ shown in Fig. 4.6(a) is very similar to the variation of the absorption spectra of a perfect absorber consisting of a single dipolar metasurface backed by a reflector [169].

As a metric for CPA, we define the joint absorption $\mathscr{A}$ [162] as follows:

$$\mathscr{A} = 1 - \frac{|E_1^-|^2 + |E_2^-|^2}{|E_1|^2 + |E_2|^2}. \tag{4.25}$$

Specifically for equal amplitude fields with a phase difference of ϕ, or $E_2 = E_1 e^{i\phi}$, from Eq. (4.20) we get, after some simplification,

$$\mathscr{A} = 1 - |r|^2 - |t|^2 - (r^* t + r t^*)\cos\phi. \tag{4.26}$$

The spectra of $\mathscr{A}$ for symmetric ($\phi = 0$, solid blue) and anti-symmetric ($\phi = \pi$ rad, solid red) excitation, and the absorption spectrum A for a single incident field (dashed black) are shown in Figs. 4.6(b) and 4.6(c) for two perfectly aligned

bilayers with separations b/a of 0.34 and 1.08, respectively. As shown in Fig. 4.6(a), the separation b/a of 0.34 (1.08) satisfies the anti-symmetric (symmetric) CPA condition. Accordingly, the joint absorption $\mathscr{A}$ in Fig. 4.6(b) approaches unity for anti-symmetric excitation (red) at the resonance of the M mode, and is significantly smaller than the absorption A for single incident field around the resonance of the A mode. On the other hand, $\mathscr{A}$ under symmetric excitation (blue) is almost twice the absorption A for single field excitation around the resonance of the A mode, and is significantly smaller than the corresponding single field absorption around the resonance of the M mode. The opposite trend holds true for the bilayer that satisfies the symmetric CPA conditions shown in Fig. 4.6(c) as the symmetric (anti-symmetric) mode becomes the dark (bright) mode for this bilayer.

Thus the excitation by two counter-propagating fields of equal intensity is a way of mode-matching the incident fields to either the bright mode or the dark mode by adjusting the relative phase of the fields. Figure 4.6(d) shows the variation with respect to the relative phase ϕ of $\mathscr{A}$ at the single field absorption resonance frequency of the two bilayers shown in Figs. 4.6(b) (blue, solid) and 4.6(c), respectively. The maximum variation in $\mathscr{A}$ achievable at the CPA condition is given by the magnitude of the difference in $\mathscr{A}$ for in-phase ($\phi = 0$) and out-of-phase ($\phi = \pi$) excitation after substituting the CPA conditions $r = \pm t$ in Eq. (4.26). After some simplification, we get the maximum achievable variation in $\mathscr{A}$ to be approximately $4R$, with R being the reflectance of the bilayer for a single incident field. We observe a variation in $\mathscr{A}$ as large as 0.9 for $b/a = 0.34$, and 0.82 for $b/a = 1.08$ at the respective CPA frequency. These estimated values of the variation in $\mathscr{A}$ are

close to the values of $4R$ for the respective bilayers with a single field excitation. This property makes these bilayers useful for applications such as all-optical modulation and switching without the need of any optical nonlinearity. The relative phase dependent absorption also implies that the bilayer essentially behaves as an absorptive interferometer at the CPA point, and has applications in areas such as pattern recognition [170, 171].

4.4 Conclusions

To summarize, we have extended our analytical model for a single dipolar nanoantenna array to bilayers of two such arrays. Through this model, as well as full-wave FDTD simulations, we have studied the formation of dark and bright modes in these bilayers. We have discussed how the radiative coupling between the layers leads to resonance shifts as well as linewidth variations, wherein the bright (dark) mode has a larger (smaller) radiative damping than the single layer. The dark mode with its large polarization amplitude can make a significant contribution to the optical response of the system. The extended analytical model now also accounts for near-field interactions between the two arrays, and can model the scattering and absorption behavior of the bilayer structure with a reasonable accuracy, including the effects of misalignments between the two layers. Finally, we have shown that these dark and bright modes can be selectively excited through two equal intensity counter-propagating fields by varying the relative phase between them. And so the scattering and absorption behavior of these bilayers can be coherently controlled.

5. Linear Optical Properties of Metacrystals of Dipolar Nanoantennas

5.1 Introduction

Natural materials typically have refractive indices that vary between 1-4 at optical and NIR frequencies. In the absence of a magnetic response, the refractive index of a medium scales with the product of the number density and the electric dipole polarizability of each atom through the Lorentz-Lorenz equation [172], with the assumption that the medium surrounding an atom can be modeled as a smooth dielectric while ignoring the granularity of the neighboring atoms [173]. Hence, the possible values of the atomic number densities and transition dipole moments in natural media determine the upper limit to the off-resonance refractive index. On resonance, various line broadening mechanisms also limit the maximum index. We note, however, that an individual atom does interact very strongly with light, which

is evidenced by an atom's scattering cross-section being several orders of magnitude larger than its physical size [174]. Even still, the refractive indices observed in dense atomic ensembles saturate to be of the order of unity. This saturation has been explained to be fundamentally electrodynamic in origin, wherein multiple scattering and near-field effects in the ensemble contribute to inhomogeneous broadening of the atomic resonance [173]. Artificially structured (meta-)materials can be used to further engineer the refractive index, or equivalently, the material permittivity and permeability. Large positive refractive indices are desirable for developing high numerical aperture optics for imaging, solar concentrators [175] and immersion lithography [176], and to enhance the radiative decay rate of emitters [177]. The nonlinear optical response also increases with the linear refractive index as per Miller's rule [4]. On the other end, near-zero [8, 17] and negative indices [178] also enable some very exotic linear and nonlinear optical phenomena.

The real part of permittivity can diverge in arrays of perfectly conducting spheres for packing fractions larger than 0.3 [179]. At optical frequencies, the gap plasmon modes in closely-packed gold nanoparticles can have highly localized electric field in the interstices leading to an enhancement of the overall polarization, which also enhances the effective permittivity, and in turn, the refractive index [25, 157, 180–184]. However, the overall nanoparticle size should be smaller than the skin depth in order to ensure that the reduction in permeability due to their diamagnetic response is negligible. A maximum refractive index of 5.4 has been recently reported for large superlattices of gold spheres with sub-nanometer gaps [184]. Such closely-packed crystals of plasmonic nanoparticles also interact

very strongly with light, and can even show evidence of deep strong light-matter coupling with the dispersion curves of the crystals's polariton modes showing a vacuum Rabi split approaching $1.8\times$ the isolated nanoparticle's plasmon resonance [185]. Octave-wide photonic band gaps can also form in plasmonic meta-crystals for lattice separations approaching the Bragg condition due to purely radiative coupling between the nanoparticles [186]. The metal volume fraction in these meta-crystals are small enough that their optical behavior can be modeled through the use of effective medium theories such as the Maxwell Garnett model [155, 187, 188]. These meta-crystals can also support collective Bloch modes that have a transparency window within the band gap due to the vanishing dipole moment, and are localized throughout the crystal volume [189].

In this chapter, we generalize our analytical model from chapters 3 and 4 to a three-dimensional meta-crystal formed by multiple layers of dipolar nanoantenna arrays. We first derive closed-form expressions for the dipole moment of a nanoantenna in the crystal on excitation with a plane wave incident normally on the interface of the crystal. We then derive the expressions for the effective "microscopic" refractive index, reflectance and transmittance of a semi-infinite meta-crystal and a thin meta-film, and calculate these optical parameters using the same design parameters assumed in chapters 3 and 4. For our chosen material and geometric parameters, we observe a maximum effective refractive index ≈ 4 along with an octave-wide photonic stop band at NIR frequencies. We find that the reflectance and transmittance of the example meta-films calculated using our analytical model agree reasonably well with those calculated through full wave FDTD

simulations with significantly reduced computational requirements. Our model is thus considerably advantageous for exploring the huge structural and material parameter space for the rational design of 3D-metacrystals, and complements the existing effective medium theories in the regime of larger metal volume fractions where they are less accurate [190].

To model the linear optical properties of a meta-crystal formed by dipolar nanoantennas, we utilize the microscopic theory of plane-wise summation method first discussed by Mahan and Obermeir [191] in the context of calculating the reflectivity of normally incident light from a semi-infinite crystal of dipoles, which was later extended by Philpott to oblique incidences and to thin films [192]. In this method, at first, the dipole-dipole interaction over all atoms in each plane J parallel to the interface of the crystal are summed up to yield the in-plane polarization P_J. The inter-plane interaction terms – both near and far-field – then yield coupled equations for P_J and the vector potential A_J. The solutions of these coupled equations are the various normal “polariton" modes supported by the bulk crystal with their own microscopic propagation constants and effective refractive indices. For N inter-plane interaction terms that contribute to P_J, there are $N+1$ polariton modes required to satisfy the boundary conditions at each interface. Hence, for the situation where we only account for the nearest neighbor inter-plane coupling, or when $N=1$ and is a realistic approximation for our system parameters, there will be two polariton modes supported by the crystal. Of these two modes, one of them will have a negative real part of the effective index implying the presence of an effective local magnetic response with a net negative permeability [193],

and a much larger imaginary part of the effective index implying its evanescent nature. Spatial dispersion also arises in our system as the field varies on the scale of the lattice constant of the crystal, and the dipole-dipole interaction terms throughout the crystal must be included to calculate the effective polarizability of an individual atom within the crystal [191]. While this behavior has been called non-local [191, 192], Sipe and Kranendonk [143] have clarified that all the spatially dispersive contributions to the field at any point within the crystal can be included in the local field, and that the local susceptibility would remain independent of the wavevector. Hence, this spatially dispersive behavior is essentially local. In section 5.2, we first extend our analytical model from previous chapters to a semi-infinite meta-crystal formed by stacking an infinite number of dipolar arrays. In section 5.2.1, we derive the optical properties of the meta-crystal assuming no near-field coupling between the planes, which we refer to as “scenario one" throughout. In section 5.2.2, we perform these derivations assuming that only the nearest neighbor near-field coupling, which we refer to as “scenario two" throughout. Then in sections 5.3.1-5.3.2, we derive the expressions for the optical properties of a meta-film formed by stacking a finite number of dipolar arrays in scenario one and scenario two, respectively. Lastly, we compare the reflectance and transmittance spectra calculated using these expressions of representative meta-films with the spectra obtained from FDTD simulations.

5.2 Semi-Infinite Meta-crystal

The first system under study consists of planar square arrays of gold nanoantennas with an in-plane lattice constant of a stacked in a semi-infinite meta-crystal and surrounded by a homogeneous dielectric of refractive index n assumed to be the same as that of BK7 glass. The separation between the arrays is denoted by b. Both a and b are sub-wavelength in the spectral range of interest. Figure 5.1 shows a representative diagram of the system along with the orientation of the coordinate axes and the exciting plane wave. The permittivity data for gold is taken from Johnson and Christy [70], and the refractive index data for BK7 glass is taken from the Schott optical glass datasheets [131]. The nanoantenna parameters are assumed to be the same as in our previous works [163, 194].The lattice planes are placed at $z_J = Jb$, with J being an integer varying from 1 to ∞. The incident field on the stack is assumed to have the form $E_0 e^{i(\tilde{\omega} nz - \omega t)}\hat{x}$. We model the electrodynamic response of nanoantennas as point electric dipoles, wherein each nanoantenna in the plane J has a dipole moment p_J, and is excited by the retarded incident field $E_0 e^{i(\tilde{\omega} nJb - \omega t)}\hat{x}$, the field from all the dipoles within plane J, and the radiative and near-field contributions from all the other dipole planes. We also assume that the lattice points in all the planes are in perfect alignment.

For the x-polarized incident field, the x-polarized component of p_J is given by

$$p_J = \varepsilon_0 n^2 \alpha_{\text{atom}} E(J), \tag{5.1}$$

where we have dropped the suffixes for convenience. Here, α_{atom} is the effec-

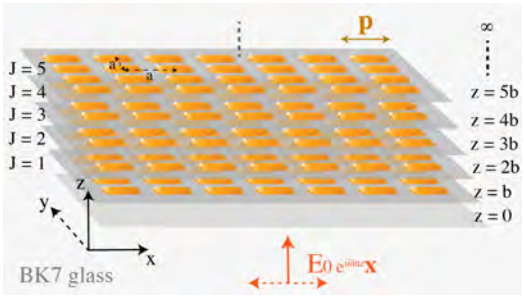

Figure 5.1: Diagram showing the semi-infinite meta-crystal formed by stacked layers of nanoantenna arrays excited by a normally incident plane wave E_0 polarized along the length of the nanoantenna. The in-plane lattice constant for each array is a, whereas the separation between each layer is b.

tive electrostatic polarizability of the nanoantenna including the effect of field retardation over its volume,

$$E(J) = E_0 e^{i\phi J} + \frac{i\phi}{2\varepsilon_0 a^2 b n^2} \sum_{K=1}^{\infty} e^{i\phi|J-K|} p_K + L(J), \tag{5.2}$$

with

$$\phi = \tilde{\omega} n b, \tag{5.3}$$

and

$$L(J) = \frac{\pi}{\varepsilon_0 a^3 n^2} \sum_{K=1}^{\infty} \mathrm{T}(|z_J - z_K|) p_K, \tag{5.4}$$

and $\mathrm{T}(|z_J - z_K|$ (see Eq. (E.1.1.6) of Appendix E.1 for the expression) denotes the near-field contribution at plane K from the dipoles in the plane J assuming perfect alignment between the lattices in the two planes. We solve this system of coupled equations for two specific scenarios:

1. *Each plane is only radiatively coupled to all the other planes*: Here, only the

in-plane non-radiative coupling term $T(0)$ survives in Eq. (5.3), which gives us

$$L(J) = \frac{\pi}{\varepsilon_0 a^3 n^2} T(0) p_J = \frac{1}{\varepsilon_0 a^2 b n^2} s_0 p_J, \tag{5.5}$$

where

$$s_0 = \frac{\pi b T(0)}{a}. \tag{5.6}$$

So each dipole plane essentially behaves as a continuous current sheet, and the exact transverse arrangement of the lattice planes in the meta-crystal is immaterial to its overall optical response. Additionally, there is no distinction between a surface plane and a bulk plane, and p_J is proportional only to the total electric field in plane J, which also implies that there is no spatial dispersion.

2. *Each plane is radiatively coupled to all the other planes and non-radiatively coupled to its nearest-neighboring planes*: For the bulk planes (or $J > 1$), the near-field contribution $L(J)$ is

$$L(J) = \frac{\pi}{\varepsilon_0 a^3 n^2} [T(0) p_J + T(b) p_{J+1} + T(-b) p_{J-1}] = \frac{1}{\varepsilon_0 a^2 b n^2} [s_0 p_J + s_1 (p_{J+1} + p_{J-1})], \tag{5.7}$$

where we have used $T(b) = T(-b)$, and defined

$$s_1 = \frac{\pi b T(b)}{a}. \tag{5.8}$$

For the plane at the surface ($J = 1$) of a semi-infinite meta-crystal, only the

plane at $J = 2$ contributes to the near-field. So we have

$$L(1) = \frac{1}{\varepsilon_0 a^2 b n^2}[s_0 p_1 + s_1 p_2]. \tag{5.9}$$

For the meta-film, which we study later, we have another surface at $L = N$ for which only the plane at $J = N - 1$ contributes to the near-field. So we have

$$L(N) = \frac{1}{\varepsilon_0 a^2 b n^2}[s_0 p_N + s_1 p_{N-1}]. \tag{5.10}$$

We do have spatial dispersion in this scenario as p_J depends on the total electric field in not only the J-th planes, but also the adjacent planes.

For the plane wave excitation considered here, we assume the normal mode solutions to Eq. (5.1) to have the form of a single plane wave (scenario one), or a superposition of two plane waves (scenario two) with complex effective refractive index(ices). We first determine the dispersion relation of these effective indices from Eq. (5.1). We then determine the modal amplitudes from the boundary conditions at the interface, and hence p_J, from which we determine the reflectance of the meta-crystal. *We also note that these effective indices are microscopic indices that relate the polarization and electric field at each lattice point within the meta-crystal. In the continuum limit, wherein* $\phi \ll 1$ *and the granularity of the meta-crystal can be ignored, these microscopic indices would approach the macroscopic refractive indices that would relate the macroscopic versions of the polarization within the medium and the electric field.*

5.2.1 Scenario One: No Near-Field Coupling Between the Dipole Planes

We assume the solution for Eq. (5.1) to have the form of a plane wave as follows

$$p_J = \mathscr{P} e^{in_0\phi J}, \tag{5.11}$$

where the amplitude $\mathscr{P}$ and the refractive index enhancement n_0 are to be determined. We call n_0 the index enhancement as the total refractive index n_{eff} would be the product of the background substrate's index n and the enhancement n_0, or $n_{\text{eff}} = nn_0$. See appendix E.2 for justification. Substituting Eqs. (5.6) and (5.11) in (5.2), we get after simplification (detailed in appendix E.3)

$$\begin{aligned} E(J) = e^{i\phi J}\left(E_0 + \frac{i\phi\mathscr{P}}{2\varepsilon_0 a^2 b n^2 (e^{-i(n_0-1)\phi}-1)}\right) + \\ + \frac{\mathscr{P}e^{in_0\phi J}}{\varepsilon_0 a^2 b n^2}\left(\frac{\phi\sin\phi/4}{\sin^2\frac{n_0\phi}{2} - \sin^2\frac{\phi}{2}}\right) + \frac{s_0\mathscr{P}e^{in_0\phi J}}{\varepsilon_0 a^2 b n^2}. \end{aligned} \tag{5.12}$$

Here, the first term on the right with the phase term evolving as $e^{i\phi J}$ is the plane wave propagating within the crystal with the same phase velocity as in the background substrate ($= c/n$). The second and third terms on the right contribute to the plane wave that propagates within the meta-crystal with a new effective phase

velocity ($= c/(nn_0)$). Now from Eqs. (5.1), (5.11) and (5.12), we have

$$\begin{aligned}\mathscr{P}e^{in_0\phi J} = \varepsilon_0 n^2 \alpha_{\text{atom}} e^{i\phi J}\left(E_0 + \frac{i\phi\,\mathscr{P}}{2\varepsilon_0 a^2 b n^2 (e^{-i(n_0-1)\phi}-1)}\right) + \\ + \mathscr{P}e^{in_0\phi J}\frac{\alpha_{\text{atom}}}{a^2 b}\left(\frac{\phi\sin\phi/4}{\sin^2\frac{n_0\phi}{2}-\sin^2\frac{\phi}{2}} + s_0\right).\end{aligned} \tag{5.13}$$

Comparing the coefficients of the exponential terms on both sides, we note that the coefficient of $e^{i\phi J}$ should vanish. So we have

$$E_0 + \frac{i\phi\,\mathscr{P}}{2\varepsilon_0 a^2 b n^2 (e^{-i(n_0-1)\phi}-1)} = 0, \tag{5.14}$$

which means that the incident field within the crystal is canceled out by a component of the field form the induced dipoles within the crystal. Eq. (5.14) is thus the microscopic analog of the Ewald-Oseen extinction theorem [1], from which we also get the expression for the dipole amplitude $\mathscr{P}$ as

$$\mathscr{P} = \frac{2i\varepsilon_0 a^2 n}{\tilde{\omega}}(e^{-i(n_0-1)\phi}-1)E_0. \tag{5.15}$$

Dispersion Relations for n_0

Now, comparing the coefficients of $e^{in_0\phi J}$, we get the dispersion relation for n_0 as

$$1 - \frac{\alpha_{\text{atom}}}{a^2 b}\left(\frac{\phi\sin\phi/4}{\sin^2\frac{n_0\phi}{2}-\sin^2\frac{\phi}{2}} + s_0\right) = 0, \tag{5.16}$$

which can also be written as

$$\frac{\sin^2\frac{n_0\phi}{2}-\sin^2\frac{\phi}{2}}{\phi\sin\phi/4}=\frac{\frac{\alpha_{\text{atom}}}{a^2b}}{1-s_0\frac{\alpha_{\text{atom}}}{a^2b}}. \tag{5.17}$$

Eq. (5.17) is analogous to the Lorentz-Lorenz equation [1] that has to be solved to yield n_0. In appendix E.4, we show that this solution for n_0 is given by

$$n_0=\frac{1}{\phi}\text{sgn}[\text{Im}(\text{Arccos}\,Z_0)]\text{Arccos}\,Z_0, \tag{5.18}$$

where

$$Z_0=\cos\phi+\frac{\phi\sin\phi}{4\xi}, \tag{5.19a}$$

$$\xi=-a^2b\left[\alpha_{\text{atom}}^{-1}-\frac{1}{a^2b}s_0\right]. \tag{5.19b}$$

Now the polarization P_J of the J-th dipole plane, defined as the product of the dipole moment p_J and the number density of nanoantennas in the plane ($=1/a^2$), is given by

$$P_J=\frac{p_J}{a^2}=\frac{\mathscr{P}}{a^2}e^{in_0\phi J}. \tag{5.20}$$

Reflectance from the Meta-crystal

The reflected field E_R at a plane z, where $z < 0$ is given by the sum of the fields radiated by all the dipole planes. So we write [172]

$$E_R(z) = \frac{i\tilde{\omega}}{2\varepsilon_0 n}\sum_{K=1}^{\infty} P_K e^{i\tilde{\omega}n|z-z_K|} = \frac{i\tilde{\omega}}{2\varepsilon_0 n}\sum_{K=1}^{\infty} P_K e^{-i\tilde{\omega}nz} e^{i\tilde{\omega}nbK}. \tag{5.21}$$

Substituting Eq. (5.20) in (5.21) and simplifying, we get

$$E_R(z) = \frac{i\tilde{\omega}}{2\varepsilon_0 a^2 n}\mathscr{P} e^{-i\tilde{\omega}nz}\sum_{K=1}^{\infty} e^{i(n_0+1)\phi K} = \frac{i\tilde{\omega}}{2\varepsilon_0 a^2 n}\mathscr{P} e^{-i\tilde{\omega}nz}\frac{1}{e^{-i(n_0+1)\phi}-1}. \tag{5.22}$$

Now, using Eq. (5.15) in (5.22), we get

$$E_R(z) = -e^{-i\tilde{\omega}nz}\frac{e^{-i(n_0-1)\phi}-1}{e^{-i(n_0+1)\phi}-1}E_0, \tag{5.23}$$

which gives us the reflectance from the meta-crystal as

$$R = \left|\frac{E_R(z)}{E_0 e^{-i\tilde{\omega}nz}}\right|^2 = \left|\frac{e^{-i(n_0-1)\phi}-1}{e^{-i(n_0+1)\phi}-1}\right|^2. \tag{5.24}$$

5.2.2 Scenario Two: Nearest-Neighbor Near-Field Coupling Between the Dipole Planes

We now have two polariton solutions that are plane wave-like and propagate with their own complex propagation constants and refractive indices. Hence, we define

$$p_J = \sum_{\alpha=1}^{2} \mathscr{P}_\alpha e^{in_\alpha \phi J}, \tag{5.25}$$

where $\mathscr{P}_{\alpha=1,2}$ are the dipole amplitudes, and $n_{\alpha=1,2}$ the refractive index enhancements of the two polariton modes that need to be determined. Also, the effective indices of the two modes are $n_{\text{eff}_{\alpha=1,2}} = nn_{\alpha=1,2}$. As before, we substitute Eq. (5.25) in (5.2) and after some simplification (see appendix E.3), we get

$$\begin{aligned} E(J) = e^{i\phi J}\left(E_0 + \frac{1}{2\varepsilon_0 a^2 b n^2}\sum_{\alpha=1}^{2}\mathscr{P}_\alpha \frac{i\phi}{e^{-i(n_\alpha-1)\phi}-1}\right) + \\ + \sum_{\alpha=1}^{2}\mathscr{P}_\alpha \frac{e^{in_\alpha\phi J}}{\varepsilon_0 a^2 b n^2}\left(\frac{\phi\sin\phi/4}{\sin^2\frac{n_\alpha\phi}{2}-\sin^2\frac{\phi}{2}}\right) + L(J), \end{aligned} \tag{5.26}$$

where $L(J)$ is given by Eqs. (5.7)-(5.9). Once again, using Eqs. (5.1), (5.25) and (5.26), we have

$$\begin{aligned} \sum_{\alpha=1}^{2}\mathscr{P}_\alpha e^{in_\alpha\phi J} = \varepsilon_0 n^2 \alpha_{\text{atom}} e^{i\phi J}\left(E_0 + \frac{1}{2\varepsilon_0 a^2 b n^2}\sum_{\alpha=1}^{2}\mathscr{P}_\alpha \frac{i\phi}{e^{-i(n_\alpha-1)\phi}-1}\right) + \\ + \varepsilon_0 n^2 \alpha_{\text{atom}} \sum_{\alpha=1}^{2}\mathscr{P}_\alpha \frac{e^{in_\alpha\phi J}}{\varepsilon_0 a^2 b n^2}\left(\frac{\phi\sin\phi/4}{\sin^2\frac{n_\alpha\phi}{2}-\sin^2\frac{\phi}{2}}\right) + \varepsilon_0 n^2 \alpha_{\text{atom}} L(J). \end{aligned} \tag{5.27}$$

The second and third terms on the right have phase factors that evolve with $e^{in_\alpha \phi J}$ as on the left side of the equation. However, the first term on the right has the phase factor that evolves with $e^{i\phi J}$ as for a plane wave propagating in the background substrate. Hence, its coefficient should disappear, which again gives us the microscopic analog to the Ewald-Oseen extinction theorem [1] as

$$E_0 + \frac{1}{2\varepsilon_0 a^2 b n^2} \sum_{\alpha=1}^{2} \mathscr{P}_\alpha \frac{i\phi}{e^{-i(n_\alpha - 1)\phi} - 1} = 0. \tag{5.28}$$

From the rest of the terms in Eq. (5.27) we get

$$\sum_{\alpha=1}^{2} \mathscr{P}_\alpha e^{in_\alpha \phi J} = \frac{\alpha_{\text{atom}}}{a^2 b} \sum_{\alpha=1}^{2} \mathscr{P}_\alpha e^{in_\alpha \phi J} \left(\frac{\phi \sin \phi / 4}{\sin^2 \frac{n_\alpha \phi}{2} - \sin^2 \frac{\phi}{2}} \right) + \varepsilon_0 n^2 \alpha_{\text{atom}} L(J). \tag{5.29}$$

Dispersion Relations for $n_{\alpha=1,2}$

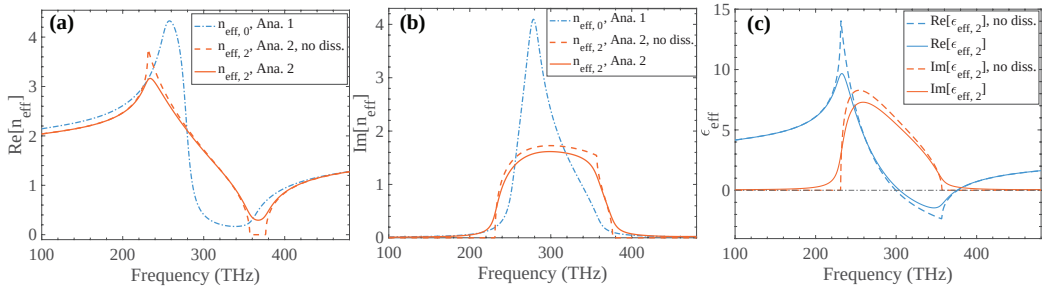

Figure 5.2: The spectra of (a) real and (b) imaginary components of effective refractive indices of metacrystal A ($a = 250$ nm, $d = 110$ nm) calculated analytically in scenario one ($n_{\text{eff},0} = nn_0$, blue, dot dashed) and in scenario two ($n_{\text{eff},2} = nn_2$, red, solid). The red dashed lines show the effective indices in scenario two with dissipation excluded. (c) The spectra of real (blue) and imaginary (red) parts of the permittivity of metacrystal A with (solid) and without (dashed) dissipation.

To get the dispersion relations for $n_{\alpha=1,2}$, we consider Eq. (5.29) for the planes in the bulk, or $J > 1$. Hence, substituting Eq. (5.7) in (5.29), we get

$$\sum_{\alpha=1}^{2} \mathscr{P}_\alpha e^{in_\alpha \phi J}\left(1-\frac{\alpha_{\text{atom}}}{a^2 b}\frac{\phi\sin\phi/4}{\sin^2\frac{n_\alpha\phi}{2}-\sin^2\frac{\phi}{2}}\right)-\frac{\alpha_{\text{atom}}}{a^2 b}[s_0 p_J + s_1(p_{J-1}+p_{J+1})]=0. \tag{5.30}$$

Then, using Eq. (5.25) in (5.30) we get

$$\sum_{\alpha=1}^{2} \mathscr{P}_\alpha e^{in_\alpha \phi J}\left(1-\frac{\alpha_{\text{atom}}}{a^2 b}\frac{\phi\sin\phi/4}{\sin^2\frac{n_\alpha\phi}{2}-\sin^2\frac{\phi}{2}}-\frac{\alpha_{\text{atom}}}{a^2 b}[s_0 + s_1(e^{-in_\alpha\phi}+e^{in_\alpha\phi})]\right)=0, \tag{5.31}$$

which can only be satisfied if the following relation holds true

$$1-\frac{\alpha_{\text{atom}}}{a^2 b}\frac{\phi\sin\phi/4}{\sin^2\frac{n_\alpha\phi}{2}-\sin^2\frac{\phi}{2}}-\frac{\alpha_{\text{atom}}}{a^2 b}[s_0 + s_1(e^{-in_\alpha\phi}+e^{in_\alpha\phi})]=0. \tag{5.32}$$

Eq. (5.32) is the dispersion relation for $n_{\alpha=1,2}$, which can also be written as

$$\frac{\sin^2\frac{n_\alpha\phi}{2}-\sin^2\frac{\phi}{2}}{\phi\sin\phi/4}=\frac{\frac{\alpha_{\text{atom}}}{a^2 b}}{1-\frac{\alpha_{\text{atom}}}{a^2 b}(s_0+2s_1\cos n_\alpha\phi)}. \tag{5.33}$$

The two solutions n_α to the above dispersion relation are given by (see appendix E.4)

$$n_\alpha = \frac{1}{\phi}\text{sgn}[\text{Im}(\text{Arccos}\, Z_\alpha)]\text{Arccos}\, Z_\alpha, \tag{5.34}$$

where

$$Z_\alpha = \frac{(4s_1\cos^2\frac{\phi}{2} - \xi) \pm \sqrt{(4s_1\sin^2\frac{\phi}{2} - \xi)^2 + 4s_1\phi\sin\phi}}{4s_1}, \tag{5.35a}$$

$$\xi = -a^2 b\left[\alpha_{\text{atom}}^{-1} - \frac{1}{a^2 b}(s_0 + 2s_1)\right]. \tag{5.35b}$$

From here on, we refer to the index for which the numerator in Z_α is summed with the subscript "1" (as n_1 and $n_{\text{eff},1}$ as the case maybe), and the index for which the numerator in Z_α is the difference of the two terms with the subscript "2" (as n_2 and $n_{\text{eff},2}$). The dispersion of $n_{\text{eff},2}$ will be qualitatively similar to that of $n_{\text{eff},0}$ in scenario one. The polariton "1" will have a larger $\text{Im}[n_{\text{eff},\alpha}]$, and consequently higher losses. We also note that α_{atom} is in general complex due to absorption losses (or dissipative damping) within the nanoantenna that are proportional to $\text{Im}[\alpha_{\text{atom}}^{-1}]$. The radiative and non-radiative interactions between the nanoantennas are included in the s_0 and s_1 terms, respectively. So we can calculate the parameters of an "ideal" meta-crystal in which there are no dissipation losses by setting $\text{Im}[\alpha_{\text{atom}}^{-1}] \to 0$ in the calculation of indices n_α.

Figs. 5.2(a) and (b) show the spectra of the real and imaginary parts of the effective refractive indices $n_{\text{eff},0}$ (blue, dot-dashed) and $n_{\text{eff},2}$ (red, solid) for a meta-crystal with lattice parameters $a = 250$ nm and $b = 110$ nm, which from here on we refer to as the meta-crystal "A". Comparing the spectra for both indices, we note that the effect of the nearest-neighbor interaction (the s_1 dependent terms in the dispersion relation) is to not only shift the polariton resonance, but also lead to additional damping. This damping is quite evident in a significant broadening

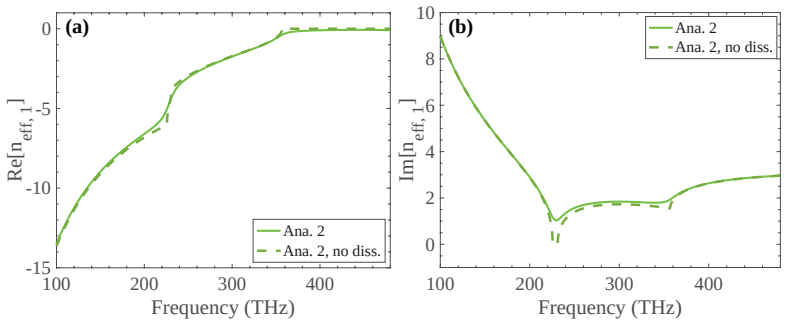

Figure 5.3: The spectra of (a) real and (b) imaginary components of effective refractive indices of metacrystal A ($a = 250$ nm, $d = 110$ nm) calculated analytically in scenario two (($n_{\text{eff},1} = nn_1$) with (solid) and without (dashed) dissipation.

of the resonance, which also consequently reduces the maximum achievable on-resonance refractive index from ≈ 4.32 to ≈ 3.14. In red dashed lines, we show the spectra of $n_{\text{eff},2}$ calculated with the dissipative damping ignored. Unsurprisingly, the exclusion of dissipation losses in the nanoantennas causes the resonant features in both the real and imaginary indices to become slightly sharper. The maximum on-resonance refractive index achievable for this “ideal" meta-crystal is ≈ 3.76 for the chosen lattice parameters. The enhancement of refractive index over that of the background substrate, which has refractive index of 1.51, is also present off-resonance at lower frequencies where the effective index levels off to ≈ 2 for all three cases shown. We also show in Fig. 5.3 the spectra of the real (left) and imaginary (right) parts of $n_{\text{eff},1}$ with (solid) and without (dashed) dissipation. The dispersion line of this polariton mode is quite different from both $n_{\text{eff},0}$ and $n_{\text{eff},2}$, and as evidenced by the much larger value of its imaginary part throughout, is also lossier than its counterpart. We also note that, unlike $n_{\text{eff},2}$, the real part of $n_{\text{eff},1}$ is negative throughout, which indicates that this polariton mode has an associated

effective negative permeability. This result is not surprising even if we have only included the electric dipolar response of each nanoantenna in our model as the near-field coupling between the arrays could support anti-symmetric modes that can form current loops with an effective magnetic response locally [193]. Indeed the dark mode of the bilayered structure discussed in chapter 4 is an anti-symmetric mode.

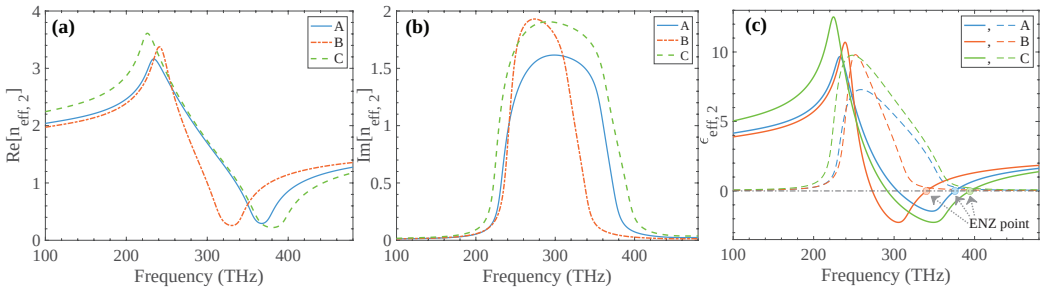

Figure 5.4: The spectra of (a) real and (b) imaginary parts of effective refractive indices, and the (c) real (solid) and imaginary (dashed) components of the effective permittivities of metacrystal **A** ($a = 250$ nm, $b = 110$ nm), **B** ($a = 250$ nm, $b = 150$ nm), and **C** ($a = 220$ nm, $b = 110$ nm) calculated analytically in scenario two.

Fig. 5.2(c) shows the spectra of the real (blue) and imaginary (red) parts of effective permittivity $\varepsilon_{\text{eff},2}(= n^2_{\text{eff},2})$ calculated with (solid) and without (dashed) dissipation for meta-crystal A. The effect of dissipation is once again evident in widening of the much sharper resonant features present for the ideal meta-crystal without any dissipation. Additionally, the meta-crystal behaves as a lossy dielectric through most of the spectral range where $\text{Re}[\varepsilon_{\text{eff},2}] > 0$ except in the frequency range 300-376 THz where the behavior is metallic with $\text{Re}[\varepsilon_{\text{eff},2}] < 0$. The existence of a negative permittivity regime for the meta-crystal is not surprising

as the system under study shares similarities with hyperbolic metamaterials [195]. However, a full exploration of this aspect is beyond the scope of this work. We further note the presence of an epsilon-near-zero (ENZ) point at 376.5 THz where $\varepsilon_{\text{eff},2} = 0 + 0.264i$, and the effective refractive index is $0.393 + 0.337i$, which has interesting implications for the various exotic optical phenomena that are possible in this regime [8, 17].

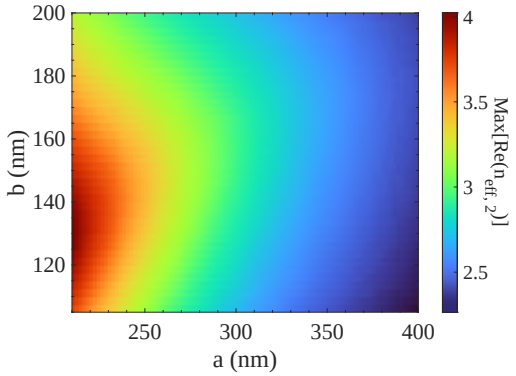

Figure 5.5: The variation of the maximum of real part of effective refractive index $n_{\text{eff},2}$ with lattice parameters a and b.

For the same nanoantenna design, the polariton dispersion can still be engineered through the appropriate choice of lattice parameters a and b. The radiative coupling between nanoantennas broadens the polariton resonance while cooperatively enhancing the dipole moment of each nanoantenna within the crystal. On the other hand, as shown earlier in Fig. 5.2, the near-field coupling between the planes leads to additional non-radiative damping and broadening of the polariton resonance that reduces the maxima of both the real and imaginary parts of the index. Hence, with regards to achieving the maximum possible refractive index

in these meta-crystals, radiative and near-field interactions are competing effects. In Fig. 5.4, we compare the spectra of the real (left panel) and imaginary (middle panel) parts of the effective index $n_{\text{eff},2}$ of meta-crystals with three different lattice parameters: A with $a = 250$ nm and $b = 110$ nm (blue, solid), B with $a = 250$ nm and $b = 150$ nm (red, dot-dashed), and C with $a = 220$ nm and $b = 110$ nm (green, dashed). Of the three configurations, C has the largest number density of nanoantennas ($= \frac{1}{a^2 b}$), and hence the highest radiative coupling between the nanoantennas and the highest near-field coupling between the planes. Consequently, the maxima of real and imaginary parts of the refractive index are the highest for this configuration along with the widest resonance bandwidth. On the other hand, configuration B has the smallest number density and the largest separation between the planes. So even though the radiative coupling between the nanoantennas is reduced, the effect of smaller interplane near-field coupling than in configuration A leads to further narrowing of the resonance linewidth, which leads to a comparatively larger effective index.

In Fig. 5.5, we show the variation of the maximum of $\text{Re}[n_{\text{eff},2}]$ with the lattice parameters a and b. Reducing the in-plane lattice constant a increases the maximum achievable index monotonically due to in-plane radiative coupling that increases with $1/a^2$ [163]. However, the maximum index does not increase monotonically with inter-plane separation b due to the aforementioned counteracting contributions from the inter-plane near-field coupling. The *maximum achievable refractive index of* ≈ 4.02 *at 1312 nm* occurs for the lattice parameters $a = 210$ nm and $b = 130$ nm with the same nanoantenna design parameters. For in-plane (interplane) lattice

constants below 210 nm (100 nm), the shape-dependent near-field interactions become significant enough that we cannot use the current point dipole model without further corrections. So we set $a = 210$ nm and $b = 105$ nm as the lower limits for our parameter sweep. Also,for $b > 200$ nm, we start to satisfy the Bragg criterion ($b = \lambda/4n$) in the spectral range under study. So we set the upper limit of for b as 200 nm. For $b > 200$ nm, another high reflectance stop band appears at the higher frequencies and redshifts with increasing b. At $b = 350$ nm, the Bragg condition and the polariton resonance overlap, which leads to an even wider stop band with a spectral shape that has been previously reported in Refs. [186, 189]. See appendix E.10 for further discussion and plots of the spectra. Lastly, in Fig. 5.4(c), we show the spectra of effective permittivity for the three meta-crystal configurations. The variation of resonance linewidth and the maximum permittvity is similar to that of the indices. The key takeaway here is that the choice of lattice parameters can be used to tune the ENZ point and the negative permittivity regime for the meta-crystal.

Reflectance from the Meta-crystal

To determine the dipole amplitudes $\mathscr{P}_\alpha$, we use the boundary conditions at the surface $(J = 1)$ and the extinction relation (5.28). Substituting $J = 1$ in Eq. (5.31), we get

$$\sum_{\alpha=1}^{2} \mathscr{P}_\alpha e^{in_\alpha\phi}\left(1 - \frac{\alpha_{\text{atom}}}{a^2 b}\frac{\phi\sin\phi/4}{\sin^2\frac{n_\alpha\phi}{2} - \sin^2\frac{\phi}{2}} - \frac{\alpha_{\text{atom}}}{a^2 b}[s_0 + s_1(e^{-in_\alpha\phi} + e^{in_\alpha\phi})]\right) = 0, \tag{5.36}$$

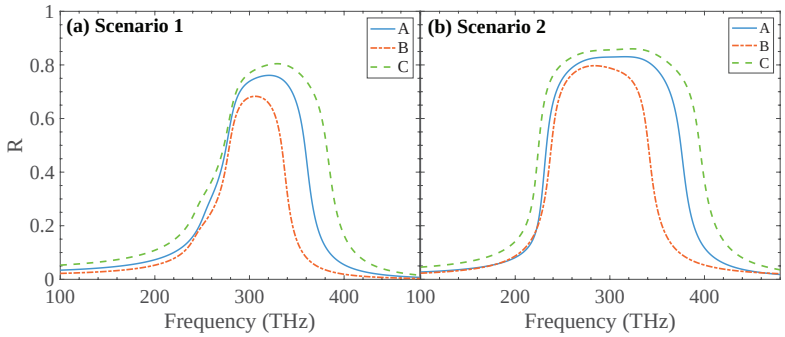

Figure 5.6: The reflectance spectra of meta-crystals A (blue, solid), B (red, dot-dashed) and C (green, dashed) calculated using the analytical model in scenario (a) one and (b) two, respectively.

Also, substituting $J = 1$ in (5.29) and using Eq. (5.9) for $L(1)$, we get

$$\sum_{\alpha=1}^{2} \mathscr{P}_\alpha e^{in_\alpha\phi}\left(1 - \frac{\alpha_{\text{atom}}}{a^2 b}\frac{\phi\sin\phi/4}{\sin^2\frac{n_\alpha\phi}{2} - \sin^2\frac{\phi}{2}} - \frac{\alpha_{\text{atom}}}{a^2 b}[s_0 + s_1 e^{in_\alpha\phi)}]\right) = 0. \quad (5.37)$$

For both Eqs. (5.36) and (5.37) to hold true, we must have

$$\sum_{\alpha=1}^{2} \mathscr{P}_\alpha = 0. \quad (5.38)$$

The above boundary condition relating the polarization amplitudes of the two polaritons is analogous to the Dirichlet additional boundary conditions (abc) introduced by Pekar in the context of describing propagation of light in crystals close to strong exciton resonances where the macroscopic polarization is spatially dispersive [196]. These abc enforce the disappearance of macroscopic polarization due to the two polaritons excited within the crystal at the crystal boundary.

Now solving Eqs. (5.28) and (5.38) together (see appendix E.5), we get the

dipole amplitudes $\mathscr{P}_\alpha$ as follows

$$\mathscr{P}_1 = \frac{2i\varepsilon_0 a^2 n}{\tilde{\omega}} \left(\frac{(e^{-i(n_1-1)\phi}-1)(e^{-i(n_2-1)\phi}-1)}{(e^{-i(n_2-1)\phi}-e^{-i(n_1-1)\phi})} \right) E_0, \tag{5.39a}$$

$$\mathscr{P}_2 = -\frac{2i\varepsilon_0 a^2 n}{\tilde{\omega}} \left(\frac{(e^{-i(n_1-1)\phi}-1)(e^{-i(n_2-1)\phi}-1)}{(e^{-i(n_2-1)\phi}-e^{-i(n_1-1)\phi})} \right) E_0. \tag{5.39b}$$

We now follow similar steps as in scenario one (see appendix E.5) to calculate the reflected field now that p_J is determined, and we get

$$R = \left| \frac{(e^{-i(n_1-1)\phi}-1)(e^{-i(n_2-1)\phi}-1)}{(e^{-i(n_1+1)\phi}-1)(e^{-i(n_2+1)\phi}-1)} \right|^2. \tag{5.40}$$

Fig. 5.6 compares the reflectance spectra of the meta-crystals A (blue, solid), B (red, dot-dashed) and C (green, dashed) calculated with (right) and without (left) including the nearest-neighbor near-field coupling. A large on-resonance index contrast between the surrounding medium and the meta-crystal leads to a very high reflectance. This region of high reflectance is essentially *a photonic stop band that spans almost an octave* for the three meta-crystals under consideration. We note that this stop band is qualitatively different from the photonic band gap in (plasmonic) photonic crystals as the interplane spacing b considered here is smaller than the Bragg criterion ($nb < \lambda_0/4$, where $\lambda_0 \approx 1\,\mu$m and $n = 1.51$ for BK7 glass) [186, 188]. The stop band here depends on the characteristics of the polariton mode(s) excited in the volume of the meta-crystal instead of arising from interference at the Bragg condition as in a photonic crystal. Further, comparing the reflectances in both scenarios, we note that the effect of nearest-neighbor interplane

near-field coupling is to broaden the stop band, which is consistent with its effect on broadening the spectrum of $n_{\text{eff},2}$ shown earlier in Fig. 5.2. However, the overall increase in the reflectance in scenario two cannot be understood from the behavior of $n_{\text{eff},2}$ versus $n_{\text{eff},0}$ as the contribution from the polariton "1" must also be taken into consideration at the interface, which can also be noted from the expression for R in Eq. (5.40). From Fig. 5.3, we see that polariton "1" has a large negative $\text{Re}[n_{\text{eff},1}]$ along with a large positive $\text{Im}[n_{\text{eff},1}]$, and hence has an even larger index contrast with the surrounding medium than polariton "2". Hence, we observe a further enhancement of the reflectance in scenario two over scenario one.

5.3 N-Layered Meta-Film

When now consider a thin film comprised of N dipolar planes with the same transverse and longitudinal lattice constants as the semi-infinite meta-crystal. Fig. 5.7 shows a diagram of the meta-film and the excitation geometry. The planes are located at $z = b$, $z = 2b$ and so on until $z = Nb$. The dipole moment in the J-th layer is again given by Eq. (5.1), where $E(J)$ now becomes

$$E(J) = E_0 e^{i\phi J} + \frac{i\phi}{2\varepsilon_0 a^2 b n^2} \sum_{K=1}^{N} e^{i\phi|J-K|} p_K + L(J). \tag{5.41}$$

The effective refractive index, being a bulk parameter, should remain the same for the meta-film and the semi-infinite meta-crystal. However, in contrast to the meta-crystal, the meta-film has an additional interface or surface layer, which mod-

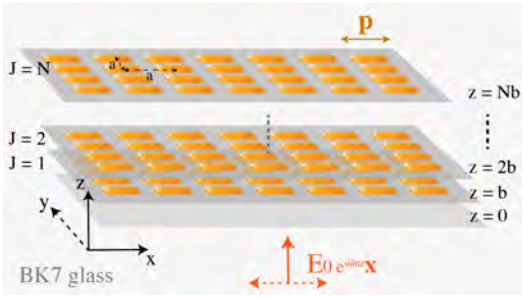

Figure 5.7: Diagram showing the meta-film with N stacked layers of nanoantenna arrays. The excitation configuration, and the material and geometric parameters are taken to be the same as for the semi-infinite meta-crystal.

ifies the fields at each plane. The reflections from an additional boundary should cause the reflectance spectrum to exhibit additional features. Also, analogous to thin dielectric films, we will now have transmission through the meta-film.

5.3.1 Meta-film Scenario One: No Near-Field Coupling Between the Dipole Planes

From Eqs. (5.1), (5.6) and (5.41), the dipole moment p_J is given by

$$p_J = \varepsilon_0 n^2 \alpha_{\text{atom}} \left(E_0 e^{i\phi J} + iC \sum_{K=1}^{N} e^{i\phi|J-K|} p_K + \frac{1}{\varepsilon_0 n^2 a^2 b} s_0 p_J \right), \tag{5.42}$$

where $C = \frac{\phi}{2\varepsilon_0 a^2 b n^2}$. We now define

$$\alpha_{s_0} = \frac{\alpha_{\text{atom}}}{1 - \frac{\alpha_{\text{atom}}}{a^2 b} s_0}, \tag{5.43}$$

to write Eq. (5.41) in a simpler form and also reference the incident field with respect to half longitudinal lattice spacing before the first plane, or to the position $z = b/2$, or

$$E_I = E_0 e^{\frac{1}{2}i\phi}, \tag{5.44}$$

and

$$p_J = \varepsilon_0 n^2 \alpha_{s_0} E_J = \varepsilon_0 n^2 \alpha_{s_0} \left(E_I e^{i\phi\left(J-\frac{1}{2}\right)} + iC \sum_{K=1}^{N} e^{i\phi|J-K|} p_K \right), \tag{5.45}$$

where E_J is the electric field at $z = Jb$. The polariton solutions will still be characterized by a single effective refractive index as in the semi-infinite crystal. However, due to the additional boundary in a thin film, we will now have both forward and backward propagating polaritons. So we assume solutions for p_J of the form

$$p_J = A_0' e^{i\Phi_0(J-\frac{1}{2})} + B_0' e^{-i\Phi_0\left(J-\frac{1}{2}\right)}, \tag{5.46}$$

where the phase Φ_0 ($= n_0\phi$, with $n_0 n$ being the effective refractive index) and the coefficients A_0' and B_0' have to be determined.

Dispersion Relations for n_0

Doing the sums in Eq. (5.42), we get (see appendix E.6)

$$\begin{aligned} p_J = \varepsilon_0 n^2 \alpha_{s_0} \Bigg[& e^{i\phi\left(J-\frac{1}{2}\right)} \left(iA_0' C \frac{e^{-\frac{1}{2}i(\phi-\Phi_0)}}{1-e^{-i(\phi-\Phi_0)}} + iB_0' C \frac{e^{-\frac{1}{2}i(\phi+\Phi_0)}}{1-e^{-i(\phi+\Phi_0)}} + E_I \right) \\ & + e^{-i\phi J} \left(iA_0' e^{-\frac{1}{2}i\Phi_0} C \frac{e^{i(\phi+\Phi_0)N}}{1-e^{-i(\phi+\Phi_0)}} + iB_0' e^{\frac{1}{2}i\Phi_0} C \frac{e^{i(\phi-\Phi_0)N}}{1-e^{-i(\phi-\Phi_0)}} \right) \\ & + e^{i\Phi_0(J-\frac{1}{2})} \left(-iA_0' C \frac{1}{1-e^{-i(\phi-\Phi_0)}} - iA_0' C \frac{1}{1-e^{-i(\phi+\Phi_0)}} + iA_0' C \right) \\ & + e^{-i\Phi_0(J-\frac{1}{2})} \left(-iB_0' C \frac{1}{1-e^{-i(\phi+\Phi_0)}} - iB_0' C \frac{1}{1-e^{-i(\phi-\Phi_0)}} + iB_0' C \right) \Bigg]. \end{aligned} \tag{5.47}$$

For both Eqs. (5.46) and (5.47) to be true, the following must be satisfied

$$iA_0' C \frac{e^{-\frac{1}{2}i(\phi-\Phi_0)}}{1-e^{-i(\phi-\Phi_0)}} + iB_0' C \frac{e^{-\frac{1}{2}i(\phi+\Phi_0)}}{1-e^{-i(\phi+\Phi_0)}} + E_I = 0, \tag{5.48a}$$

$$iA_0' e^{-\frac{1}{2}i\Phi_0} C \frac{e^{i(\phi+\Phi_0)N}}{1-e^{-i(\phi+\Phi_0)}} + iB_0' e^{\frac{1}{2}i\Phi_0} C \frac{e^{i(\phi-\Phi_0)N}}{1-e^{-i(\phi-\Phi_0)}} = 0, \tag{5.48b}$$

$$\varepsilon_0 n^2 \alpha_{s_0} \left(-iA_0' C \frac{1}{1-e^{-i(\phi-\Phi_0)}} - iA_0' C \frac{1}{1-e^{-i(\phi+\Phi_0)}} + iA_0' C \right) = A_0', \tag{5.48c}$$

$$\varepsilon_0 n^2 \alpha_{s_0} \left(-iB_0' C \frac{1}{1-e^{-i(\phi+\Phi_0)}} - iB_0' C \frac{1}{1-e^{-i(\phi-\Phi_0)}} + iB_0' C \right) = B_0'. \tag{5.48d}$$

Similar to the meta-crystal, Eq. (5.48a) signifies that the incident field E_I interferes destructively with the fields from dipoles within the film that propagate with the same phase velocity as the incident field in the surrounding medium ($= c/n$). Eq. (5.48b) signifies that the backward propagating fields from all the dipoles in the meta-film that propagate with the same phase velocity as in the surrounding

medium should also vanish. Thus, the only surviving fields at each plane J will be the forward and backward propagating polaritons introduced in Eq. (5.46). Eqs. (5.48c) and (5.48d)) are the same, and can be simplified (see appendix E.7) to give

$$\frac{\sin^2\frac{\Phi_0}{2}-\sin^2\frac{\phi}{2}}{\phi\sin\phi/4}=\frac{\alpha_{s_0}}{a^2b}=\frac{\frac{\alpha_{\text{atom}}}{a^2b}}{1-\frac{\alpha_{\text{atom}}}{a^2b}s_0}\equiv\chi_0, \tag{5.49}$$

which is the dispersion relation for n_0 that we obtained earlier in Eq. (5.17).

Fields at the Plane $z = Jb$

We now determine the amplitudes of forward (A'_0) and backward (B'_0) propagating modes. From Eq. (5.48b), we have

$$\frac{B'_0}{A'_0}=e^{2iN\Phi_0}\left(\frac{e^{-i\phi}-e^{-i\Phi_0}}{1-e^{-i(\phi+\Phi_0)}}\right). \tag{5.50}$$

And from Eqs. (5.45) and (5.46), we have

$$E_J=E_J^+ + E_J^-=\frac{A'_0}{\varepsilon_0 n^2\alpha_{s_0}}e^{i\Phi_0(J-\frac{1}{2})}+\frac{B'_0}{\varepsilon_0 n^2\alpha_{s_0}}e^{-i\Phi_0(J-\frac{1}{2})}, \tag{5.51}$$

where E_J^+ (E_J^-) denote the forward (backward) propagating polariton fields. We can define the meta-film boundaries to be between $z = b/2$ and $z = (N+1/2)b$ even though the surface planes are located at $z = b$ and $z = Nb$. Then we have from Eq. (5.51)

$$\frac{E^-_{N+\frac{1}{2}}}{E^+_{N+\frac{1}{2}}}=\frac{B'_0}{A'_0}e^{-i2N\Phi_0}, \tag{5.52}$$

and using Eq. (5.50), we get

$$\frac{E^{-}_{N+\frac{1}{2}}}{E^{+}_{N+\frac{1}{2}}} = \frac{e^{-i\phi} - e^{-i\Phi_0}}{1 - e^{-i(\phi+\Phi_0)}} \equiv r_{10,0}, \tag{5.53}$$

where we have introduced $r_{10,0}$ as the effective Fresnel reflection coefficient from the surrounding medium into the meta-film. The field inside the film at the interface $z = b/2$ can be obtained from Eq. (5.51) as

$$E_{\frac{1}{2}} = \frac{A'_0}{\varepsilon_0 n^2 \alpha_{s_0}} + \frac{B'_0}{\varepsilon_0 n^2 \alpha_{s_0}} = \mathscr{E}_+ + \mathscr{E}_-, \tag{5.54}$$

where $\mathscr{E}_+ = \frac{A'_0}{\varepsilon_0 n^2 \alpha_{s_0}}$ and $\mathscr{E}_- = \frac{B'_0}{\varepsilon_0 n^2 \alpha_{s_0}}$.

Now using Eqs. (5.50) and (5.53), we can simplify (5.48a) as

$$E_I = -iA'_0 C \left(\frac{e^{-\frac{1}{2}i(\phi-\Phi_0)}}{1 - e^{-i(\phi-\Phi_0)}} + r_{10,0} e^{i2N\Phi_0} \frac{e^{-\frac{1}{2}i(\phi+\Phi_0)}}{1 - e^{-i(\phi+\Phi_0)}} \right), \tag{5.55}$$

or

$$E_I = -iA'_0 C \frac{e^{-\frac{1}{2}i(\phi-\Phi_0)}}{1 - e^{-i(\phi-\Phi_0)}} (1 - r^2_{10,0} e^{i2N\Phi_0}). \tag{5.56}$$

Using Eqs. (5.54) in (5.56), we have

$$E_I = -i\varepsilon_0 n^2 \alpha_{s_0} C \frac{e^{-\frac{1}{2}i(\phi-\Phi_0)}}{1 - e^{-i(\phi-\Phi_0)}} (1 - r^2_{10,0} e^{i2N\Phi_0}) \mathscr{E}_+. \tag{5.57}$$

In appendix E.7, we show that

$$i\varepsilon_0 n^2 \alpha_{s_0} C = \frac{(1-e^{-i(\phi-\Phi_0)})(1-e^{-i(\phi-\Phi_0)})}{e^{-2i\phi}-1}, \tag{5.58}$$

which we substitute in Eq. (5.57) to get

$$E_I = \mathscr{E}_+ \frac{1-e^{-i(\phi+\Phi_0)}}{(1-e^{-2i\phi})e^{\frac{1}{2}i(\phi-\Phi_0)}}(1-r_{10,0}^2 e^{i2N\Phi_0}) = \frac{1}{t_{01,0}}(1-r_{10,0}^2 e^{i2N\Phi_0})\mathscr{E}_+, \tag{5.59}$$

where

$$t_{01,0} \equiv \frac{(1-e^{-2i\phi})e^{\frac{1}{2}(\phi-\Phi_0)}}{1-e^{-i(\phi+\Phi_0)}}. \tag{5.60}$$

Here, we have introduced $t_{01,0}$ as the effective transmission coefficient into the meta-film from the surrounding medium. Now going back to Eq. (5.51), we have

$$E_J = \mathscr{E}_+ \left(e^{i\Phi_0(J-\frac{1}{2})} + \frac{B_0'}{A_0'} e^{-i\Phi_0(J-\frac{1}{2})} \right), \tag{5.61}$$

and using Eqs. (5.53) and (5.59) we get

$$E_J = \frac{t_{01,0}}{1-r_{10,0}^2 e^{2iN\Phi_0}} \left(e^{i\Phi_0(J-\frac{1}{2})} + r_{10,0} e^{2iN\Phi_0} e^{-i\Phi_0(J-\frac{1}{2})} \right) E_I. \tag{5.62}$$

So we have determined the expression for the electric field at plane $z = Jb$.

Transmittance and Reflectance from the Meta-film

The transmitted field E_T through the meta-film is the forward propagating field plane wave at a plane $z > Nb$. We assume $z = (N+\frac{1}{2})b$, and we write from

Eq. (5.45)

$$E_T = E_{N+\frac{1}{2}} = E_I e^{i\phi N} + iC \sum_{K=1}^{N} e^{i\phi(N+\frac{1}{2}-K)} p_K, \tag{5.63}$$

which on further simplification (see appendix E.8) gives us

$$E_T = \frac{t_{01,0} t_{10,0} e^{iN\Phi_0}}{1 - r_{10,0}^2 e^{2iN\Phi_0}} E_I. \tag{5.64}$$

Here we have defined

$$t_{10,0} \equiv \frac{(1 - e^{-2i\Phi_0}) e^{\frac{1}{2}i(\Phi_0 - \phi)}}{1 - e^{-i(\phi+\Phi_0)}} \tag{5.65}$$

as the effective Fresnel transmission coefficient from the meta-film to the surrounding medium with the following relation holding true as in continuum electrodynamics

$$1 - r_{10,0}^2 = t_{10,0} t_{01,0}. \tag{5.66}$$

Hence, the effective transmittance of the meta-film is

$$T = \left| \frac{E_T}{E_I} \right|^2 = \left| \frac{t_{01,0} t_{10,0} e^{iN\Phi_0}}{1 - r_{10,0}^2 e^{2iN\Phi_0}} \right|^2. \tag{5.67}$$

The reflected field E_R is similarly given by the backward propagating wave from the film at the plane $z < b$. Assuming $z = \frac{b}{2}$, we have

$$E_R = iC \sum_{K=1}^{N} e^{i\phi(K-\frac{1}{2})} p_K, \tag{5.68}$$

which we can write after further simplification (see appendix E.9) as

$$E_R = \frac{r_{01,0} + r_{10,0}e^{2iN\Phi_0}}{1 - r_{10,0}^2 e^{2iN\Phi_0}} E_I = \left(r_{01,0} + \frac{t_{01,0}r_{10,0}t_{10,0}e^{2iN\Phi_0}}{1 - r_{10,0}^2 e^{2iN\Phi_0}} \right) E_I. \tag{5.69}$$

Here we have defined

$$r_{01,0} = -r_{10,0} \tag{5.70}$$

as the effective Fresnel reflection coefficient from the meta-film into the surrounding medium. Hence the effective reflectance of the meta-film is given by

$$R = \left| \frac{E_R}{E_I} \right|^2 = \left| r_{01,0} + \frac{t_{01,0}r_{10,0}t_{10,0}e^{2iN\Phi_0}}{1 - r_{10,0}^2 e^{2iN\Phi_0}} \right|^2. \tag{5.71}$$

5.3.2 Meta-film Scenario Two: Nearest-Neighbor Near-Field Coupling Between the Planes

From Eqs. (5.1), (5.7) and (5.41), the dipole moment p_J can be written as

$$p_J = \varepsilon_0 n^2 \alpha_{\text{atom}} E(J) = \varepsilon_0 n^2 \alpha_{\text{atom}} \left[E_I e^{i\phi(J-\frac{1}{2})} + iC \sum_{K=1}^{N} e^{i\phi|J-K|} p_K + L(J) \right], \tag{5.72}$$

where we have once again referenced the incident field as in Eq. (5.44). We will again have two polariton solutions, as in the semi-infinite meta-crystal, each with forward and backward propagating components due to the additional boundary in

the meta-film. So we assume

$$p_J = \sum_{\alpha=1}^{2} (A'_\alpha e^{i\Phi_\alpha(J-\frac{1}{2})} + B'_\alpha e^{-i\Phi_\alpha(J-\frac{1}{2})}), \tag{5.73}$$

where the phases $\Phi_{\alpha=1,2}$ ($= n_{\alpha=1,2}\phi$), with nn_α being the effective refractive indices of the two polariton solutions), and the amplitudes $A'_{\alpha=1,2}$ and $B'_{\alpha=1,2}$ are to be determined.

Dispersion Relations for n_α

Doing the sums in Eq.(5.72) (see appendix E.6), we get

$$\begin{aligned}
p_J = \varepsilon_0 n^2 \alpha_{\text{atom}} \Bigg[& e^{i\phi(J-\frac{1}{2})} \left\{ E_I + \sum_{\alpha=1}^{2} \left(iA'_\alpha C \frac{e^{-i\frac{1}{2}(\phi-\Phi_\alpha)}}{1-e^{-i(\phi-\Phi_\alpha)}} + iB'_\alpha C \frac{e^{-i\frac{1}{2}(\phi+\Phi_\alpha)}}{1-e^{-i(\phi+\Phi_\alpha)}} \right) \right\} + \\
& + e^{-i\phi J} \sum_{\alpha=1}^{2} \left(iA'_\alpha C e^{-\frac{1}{2}i\Phi_\alpha} \frac{e^{i(\phi+\Phi_\alpha)N}}{1-e^{-i(\phi+\Phi_\alpha)}} + iB'_\alpha C^{\frac{1}{2}i\Phi_\alpha} \frac{e^{i(\phi-\Phi_\alpha)N}}{1-e^{-i(\phi-\Phi_\alpha)}} \right) + \\
& + \sum_{\alpha=1}^{2} \Bigg\{ e^{i\Phi_\alpha(J-\frac{1}{2})} \left(-iA'_\alpha C \frac{1}{1-e^{-i(\phi-\Phi_\alpha)}} - iA'_\alpha C \frac{1}{1-e^{-i(\phi+\Phi_\alpha)}} + iA'_\alpha C \right) + \\
& + e^{-i\Phi_\alpha(J-\frac{1}{2})} \left(-iB'_\alpha C \frac{1}{1-e^{-i(\phi+\Phi_\alpha)}} - iB'_\alpha C \frac{1}{1-e^{-i(\phi-\Phi_\alpha)}} + iB'_\alpha C \right) \Bigg\} + L(J) \Bigg],
\end{aligned} \tag{5.74}$$

where

$$L(J)=\begin{cases} \frac{1}{\varepsilon_0 n^2 a^2 b}\sum_{\alpha=1}^{2}[\{A'_\alpha e^{i\Phi_\alpha(J-\frac{1}{2})}+B'_\alpha e^{-i\Phi_\alpha(J-\frac{1}{2})}\}\cdot \\ \cdot\{s_0+s_1(e^{i\Phi_\alpha}+e^{-i\Phi_\alpha})\}], \text{ if } 1<J<N, \\ \frac{1}{\varepsilon_0 n^2 a^2 b}\sum_{\alpha=1}^{2}[A'_\alpha e^{i\frac{\Phi_\alpha}{2}}(s_0+s_1e^{i\Phi_\alpha})+B'_\alpha e^{-i\frac{\Phi_\alpha}{2}}(s_0+s_1e^{-i\Phi_\alpha})], \text{ if } J=1, \\ \frac{1}{\varepsilon_0 n^2 a^2 b}\sum_{\alpha=1}^{2}[A'_\alpha e^{i\Phi_\alpha(N-\frac{1}{2})}(s_0+s_1e^{-i\Phi_\alpha})+B'_\alpha e^{-i\Phi_\alpha(N-\frac{1}{2})}(s_0+s_1e^{i\Phi_\alpha})], \text{ if } J=N. \end{cases} \tag{5.75}$$

To get the dispersion relations for n_α, we use the expression for p_J in the bulk, or when $1<J<N$. Substituting Eq. (5.75) in (5.74) and combining the terms with the same J dependence, we have

$$\begin{aligned} p_J = \varepsilon_0 n^2 \alpha_{\text{atom}} \Bigg[& e^{i\phi(J-\frac{1}{2})}\Bigg\{E_I+\sum_{\alpha=1}^{2}\left(iA'_\alpha C\frac{e^{-i\frac{1}{2}(\phi-\Phi_\alpha)}}{1-e^{-i(\phi-\Phi_\alpha)}}+iB'_\alpha C\frac{e^{-i\frac{1}{2}(\phi+\Phi_\alpha)}}{1-e^{-i(\phi+\Phi_\alpha)}}\right)\Bigg\}+ \\ & +e^{-i\phi J}\sum_{\alpha=1}^{2}\left(iA'_\alpha Ce^{-\frac{1}{2}i\Phi_\alpha}\frac{e^{i(\phi+\Phi_\alpha)N}}{1-e^{-i(\phi+\Phi_\alpha)}}+iB'_\alpha Ce^{\frac{1}{2}i\Phi_\alpha}\frac{e^{i(\phi-\Phi_\alpha)N}}{1-e^{-i(\phi-\Phi_\alpha)}}\right)+ \\ & +\sum_{\alpha=1}^{2}\Bigg\{e^{i\Phi_\alpha(J-\frac{1}{2})}\Bigg(-iA'_\alpha C\frac{1}{1-e^{-i(\phi-\Phi_\alpha)}}-iA'_\alpha C\frac{1}{1-e^{-i(\phi+\Phi_\alpha)}}+iA'_\alpha C+ \\ & +\frac{A'_\alpha}{\varepsilon_0 n^2 a^2 b}\left(s_0+s_1(e^{i\Phi_\alpha}+e^{-i\Phi_\alpha})\right)\Bigg)+e^{-i\Phi_\alpha(J-\frac{1}{2})}\Bigg(-iB'_\alpha C\frac{1}{1-e^{-i(\phi+\Phi_\alpha)}}- \\ & -iB'_\alpha C\frac{1}{1-e^{-i(\phi-\Phi_\alpha)}}+iB'_\alpha C+\frac{B'_\alpha}{\varepsilon_0 n^2 a^2 b}\left(s_0+s_1(e^{i\Phi_\alpha}+e^{-i\Phi_\alpha})\right)\Bigg)\Bigg\}\Bigg]. \end{aligned} \tag{5.76}$$

Comparing the coefficients of the exponentials in Eqs. (5.73) and (5.76), we get

$$E_I + iC\sum_{\alpha=1}^{2}\left(A'_\alpha \frac{e^{-i\frac{1}{2}(\phi-\Phi_\alpha)}}{1-e^{-i(\phi-\Phi_\alpha)}} + B'_\alpha \frac{e^{-i\frac{1}{2}(\phi+\Phi_\alpha)}}{1-e^{-i(\phi+\Phi_\alpha)}}\right) = 0, \tag{5.77a}$$

$$iC\sum_{\alpha=1}^{2}\left(A'_\alpha e^{-\frac{1}{2}i\Phi_\alpha} \frac{e^{i(\phi+\Phi_\alpha)N}}{1-e^{-i(\phi+\Phi_\alpha)}} + B'_\alpha e^{\frac{1}{2}i\Phi_\alpha} \frac{e^{i(\phi-\Phi_\alpha)N}}{1-e^{-i(\phi-\Phi_\alpha)}}\right) = 0, \tag{5.77b}$$

$$\begin{aligned}&\sum_{\alpha=1}^{2} A'_\alpha e^{i\Phi_\alpha(J-\frac{1}{2})}\left[iC\left(1-\frac{1}{1-e^{-i(\phi-\Phi_\alpha)}}-\frac{1}{1-e^{-i(\phi+\Phi_\alpha)}}\right)+\right.\\ &\left.+\frac{1}{\varepsilon_0 n^2 a^2 b}\left(s_0+s_1(e^{i\Phi_\alpha}+e^{-i\Phi_\alpha})\right)-\frac{1}{\varepsilon_0 n^2 \alpha_{\text{atom}}}\right]=0,\end{aligned} \tag{5.77c}$$

$$\begin{aligned}&\sum_{\alpha=1}^{2} B'_\alpha e^{-i\Phi_\alpha(J-\frac{1}{2})}\left[iC\left(1-\frac{1}{1-e^{-i(\phi-\Phi_\alpha)}}-\frac{1}{1-e^{-i(\phi+\Phi_\alpha)}}\right)+\right.\\ &\left.+\frac{1}{\varepsilon_0 n^2 a^2 b}\left(s_0+s_1(e^{i\Phi_\alpha}+e^{-i\Phi_\alpha})\right)-\frac{1}{\varepsilon_0 n^2 \alpha_{\text{atom}}}\right]=0.\end{aligned} \tag{5.77d}$$

For both Eqs. (5.77c) and (5.77d) to be satisfied, we must have

$$\begin{aligned}&iC\left(1-\frac{1}{1-e^{-i(\phi-\Phi_\alpha)}}-\frac{1}{1-e^{-i(\phi+\Phi_\alpha)}}\right)+\\ &+\frac{1}{\varepsilon_0 n^2 a^2 b}\left(s_0+s_1(e^{i\Phi_\alpha}+e^{-i\Phi_\alpha})\right)-\frac{1}{\varepsilon_0 n^2 \alpha_{\text{atom}}}=0,\end{aligned} \tag{5.78}$$

which simplifies to (see appendix E.7)

$$\frac{\sin^2\frac{\Phi_\alpha}{2}-\sin^2\frac{\phi}{2}}{\phi\sin\phi/4} = \frac{\frac{\alpha_{\text{atom}}}{a^2 b}}{1-\frac{\alpha_{\text{atom}}}{a^2 b}(s_0+2s_1\cos\Phi_\alpha)} \equiv \chi_\alpha, \tag{5.79}$$

which is again the same dispersion relation that we obtained earlier for the polaritons in a semi-infinite meta-crystal. The solutions for $\Phi_\alpha = (\phi n_\alpha)$ are then given

by Eqs. (5.34)-(5.35). This result is not surprising as the presence of an additional boundary for a meta-film should not affect the mode dispersion in the bulk.

Fields at the Plane $z = Jb$

We now calculate the four mode amplitudes A'_α and B'_α. Of the four equations required to calculate these amplitudes, Eqs. (5.77a) and (5.77b) are the first two. The remaining two equations are obtained by applying the boundary conditions at $J = 1$ and $J = N$ to the expression for p_J in Eq. (5.74).As before, Eq. (5.77a) implies that the forward propagating incident field E_I vanishes within the meta-film due to radiative contributions from all the dipoles within the film. Eq. (5.77b) then implies that all backward propagating fields from the dipoles within the meta-film with the same phase velocity as in the surrounding medium $(= c/n)$ also vanish.

From Eq. (5.77b) we have

$$\sum_{\alpha=1}^{2} A'_\alpha \frac{e^{i\Phi_\alpha(N+\frac{1}{2})}}{1-e^{-i(\phi+\Phi_\alpha)}} \left\{ 1 + \frac{B'_\alpha}{A'_\alpha} e^{-2i\Phi_\alpha(N-\frac{1}{2})} \left(\frac{1-e^{-i(\phi+\Phi_\alpha)}}{1-e^{-i(\phi-\Phi_\alpha)}} \right) \right\} = 0. \tag{5.80}$$

So the coefficients of the exponentials $e^{i\Phi_\alpha(N+\frac{1}{2})}$ should vanish on both sides, which gives us

$$1 + \frac{B'_\alpha}{A'_\alpha} e^{-2i\Phi_\alpha(N-\frac{1}{2})} \left(\frac{1-e^{-i(\phi+\Phi_\alpha)}}{1-e^{-i(\phi-\Phi_\alpha)}} \right) = 0. \tag{5.81}$$

We can then write

$$\frac{B'_\alpha}{A'_\alpha} = r_{10,\alpha} e^{2iN\Phi_\alpha}, \tag{5.82}$$

where we have introduced $r_{10,\alpha}$ as the effective Fresnel reflection coefficient from the meta-film to the surrounding medium for the polariton mode α, which is given by

$$r_{10,\alpha} = \frac{e^{-i\phi} - e^{-i\Phi_\alpha}}{1 - e^{-i(\phi+\Phi_\alpha)}}. \tag{5.83}$$

Now from Eqs. (5.72) and (5.73), we have

$$E(J) = \sum_{\alpha=1}^{2} (E^{+}_{J,\alpha} + E^{-}_{J,\alpha}) = \sum_{\alpha=1}^{2} \left(\frac{A'_\alpha}{\varepsilon_0 n^2 \alpha_{\text{atom}}} e^{i\Phi_\alpha (J-\frac{1}{2})} + \frac{B'_\alpha}{\varepsilon_0 n^2 \alpha_{\text{atom}}} e^{-i\Phi_\alpha (J-\frac{1}{2})} \right), \tag{5.84}$$

where $E^{+}_{J,\alpha}$ ($E^{-}_{J,\alpha}$) is the forward (backward) propagating polariton mode α. Also, we define

$$E^{\pm}_{J} = \sum_{\alpha=1}^{2} E^{\pm}_{J,\alpha}. \tag{5.85}$$

As in scenario one, we define the field just inside the first boundary of the meta-film at $z = \frac{b}{2}$ as

$$\mathscr{E}_{+} = E^{+}_{\frac{1}{2}} = \frac{1}{\varepsilon_0 n^2 \alpha_{\text{atom}}} \sum_{\alpha=1}^{2} A'_\alpha. \tag{5.86}$$

Now we consider the dipole moments at the boundary layers $J = 1$ and $J = N$. For

the first boundary ($J = 1$), we get from Eqs. (5.74) and (5.75)

$$
\begin{aligned}
p_1 &= \sum_{\alpha=1}^{2} (A'_\alpha e^{i\frac{\Phi_\alpha}{2}} + B'_\alpha e^{-i\frac{\Phi_\alpha}{2}}) \\
&= \varepsilon_0 n^2 \alpha_{\text{atom}} \left[e^{i\phi\frac{1}{2}} \left\{ E_I + \sum_{\alpha=1}^{2} \left(iA'_\alpha C \frac{e^{-i\frac{1}{2}(\phi-\Phi_\alpha)}}{1-e^{-i(\phi-\Phi_\alpha)}} + iB'_\alpha C \frac{e^{-i\frac{1}{2}(\phi+\Phi_\alpha)}}{1-e^{-i(\phi+\Phi_\alpha)}} \right) \right\} + \right. \\
&+ e^{-i\phi} \sum_{\alpha=1}^{2} \left(iA'_\alpha C e^{-\frac{1}{2}i\Phi_\alpha} \frac{e^{i(\phi+\Phi_\alpha)N}}{1-e^{-i(\phi+\Phi_\alpha)}} + iB'_\alpha C e^{\frac{1}{2}i\Phi_\alpha} \frac{e^{i(\phi-\Phi_\alpha)N}}{1-e^{-i(\phi-\Phi_\alpha)}} \right) + \\
&+ \sum_{\alpha=1}^{2} \left\{ e^{i\frac{\Phi_\alpha}{2}} \left(-iA'_\alpha C \frac{1}{1-e^{-i(\phi-\Phi_\alpha)}} - iA'_\alpha C \frac{1}{1-e^{-i(\phi+\Phi_\alpha)}} + iA'_\alpha C + \right. \right. \\
&+ \left. \frac{A'_\alpha}{\varepsilon_0 n^2 a^2 b} \left(s_0 + s_1 e^{i\Phi_\alpha}\right) \right) + e^{-i\frac{\Phi_\alpha}{2}} \left(-iB'_\alpha C \frac{1}{1-e^{-i(\phi+\Phi_\alpha)}} - \right. \\
&\left. \left. \left. - iB'_\alpha C \frac{1}{1-e^{-i(\phi-\Phi_\alpha)}} + iB'_\alpha C + \frac{B'_\alpha}{\varepsilon_0 n^2 a^2 b} \left(s_0 + s_1 e^{-i\Phi_\alpha}\right) \right) \right\} \right].
\end{aligned}
\tag{5.87}
$$

Comparing the coefficients of $e^{\pm i\frac{\Phi_\alpha}{2}}$ on both sides of Eq. (5.87), we get the following equations

$$
\begin{aligned}
&\sum_{\alpha=1}^{2} A'_\alpha e^{i\frac{\Phi_\alpha}{2}} \left[iC \left(1 - \frac{1}{1-e^{-i(\phi-\Phi_\alpha)}} - \frac{1}{1-e^{-i(\phi+\Phi_\alpha)}} \right) + \right. \\
&\left. + \frac{1}{\varepsilon_0 n^2 a^2 b} \left(s_0 + s_1 e^{i\Phi_\alpha}\right) - \frac{1}{\varepsilon_0 n^2 \alpha_{\text{atom}}} \right] = 0,
\end{aligned}
\tag{5.88a}
$$

$$
\begin{aligned}
&\sum_{\alpha=1}^{2} B'_\alpha e^{-i\frac{\Phi_\alpha}{2}} \left[iC \left(1 - \frac{1}{1-e^{-i(\phi-\Phi_\alpha)}} - \frac{1}{1-e^{-i(\phi+\Phi_\alpha)}} \right) + \right. \\
&\left. + \frac{1}{\varepsilon_0 n^2 a^2 b} \left(s_0 + s_1 e^{-i\Phi_\alpha}\right) - \frac{1}{\varepsilon_0 n^2 \alpha_{\text{atom}}} \right] = 0.
\end{aligned}
\tag{5.88b}
$$

Now the Eqs. (5.77c) and (5.77d) also hold true for $J = 1$, which gives us

$$\sum_{\alpha=1}^{2} A'_\alpha e^{i\frac{\Phi_\alpha}{2}} \left[iC\left(1 - \frac{1}{1-e^{-i(\phi-\Phi_\alpha)}} - \frac{1}{1-e^{-i(\phi+\Phi_\alpha)}}\right) + \right.$$
$$\left. + \frac{1}{\varepsilon_0 n^2 a^2 b}\left(s_0 + s_1(e^{i\Phi_\alpha} + e^{-i\Phi_\alpha})\right) - \frac{1}{\varepsilon_0 n^2 \alpha_{\text{atom}}}\right] = 0, \tag{5.89a}$$

$$\sum_{\alpha=1}^{2} B'_\alpha e^{-i\frac{\Phi_\alpha}{2}} \left[iC\left(1 - \frac{1}{1-e^{-i(\phi-\Phi_\alpha)}} - \frac{1}{1-e^{-i(\phi+\Phi_\alpha)}}\right) + \right.$$
$$\left. + \frac{1}{\varepsilon_0 n^2 a^2 b}\left(s_0 + s_1(e^{i\Phi_\alpha} + e^{-i\Phi_\alpha})\right) - \frac{1}{\varepsilon_0 n^2 \alpha_{\text{atom}}}\right] = 0. \tag{5.89b}$$

So from Eqs. (5.88a) and (5.89a), and then from Eqs. (5.88b) and (5.89b), we have

$$\sum_{\alpha=1}^{2} A'_\alpha e^{-i\frac{\Phi_\alpha}{2}} = 0, \tag{5.90a}$$

$$\sum_{\alpha=1}^{2} B'_\alpha e^{i\frac{\Phi_\alpha}{2}} = 0. \tag{5.90b}$$

Solving Eqs. (5.86) and (5.90a) together, we get

$$A'_1 = a_1 \varepsilon_0 n^2 \alpha_{\text{atom}} \mathscr{E}_+; a_1 = \frac{1}{1 - e^{-\frac{i}{2}(\Phi_1 - \Phi_2)}} \tag{5.91a}$$

$$A'_2 = a_2 \varepsilon_0 n^2 \alpha_{\text{atom}} \mathscr{E}_+; a_2 = 1 - a_1. \tag{5.91b}$$

So with Eqs. (5.82) and (5.91), we know A'_α and B'_α in terms of $\mathscr{E}_+$. To now obtain

$\mathscr{E}_+$ in terms of the known incident field E_I, we rewrite Eq. (5.77a) as

$$\begin{aligned} E_I &= -iC\sum_{\alpha=1}^{2} A'_\alpha \frac{e^{-i\frac{1}{2}(\phi-\Phi_\alpha)}}{1-e^{-i(\phi-\Phi_\alpha)}}\left(1+\frac{B'_\alpha}{A'_\alpha}e^{-i\Phi_\alpha}\frac{1-e^{-i(\phi-\Phi_\alpha)}}{1-e^{-i(\phi+\Phi_\alpha)}}\right) \\ &= -iC\sum_{\alpha=1}^{2} A'_\alpha \frac{e^{-i\frac{1}{2}(\phi-\Phi_\alpha)}}{1-e^{-i(\phi-\Phi_\alpha)}}\left(1+r_{10,\alpha}e^{i2N\Phi_\alpha}\frac{e^{-i\Phi_\alpha}-e^{-i\phi}}{1-e^{-i(\phi+\Phi_\alpha)}}\right) \\ &= -iC\sum_{\alpha=1}^{2} A'_\alpha \frac{e^{-i\frac{1}{2}(\phi-\Phi_\alpha)}}{1-e^{-i(\phi-\Phi_\alpha)}}\left(1-r_{10,\alpha}^2 e^{i2N\Phi_\alpha}\right), \end{aligned} \tag{5.92}$$

where we have used Eqs. (5.82) and (5.83) in the second and third steps. Now substituting Eqs. (5.91) above, we get

$$\begin{aligned} E_I = -\frac{iC\varepsilon_0 n^2\alpha_{\text{atom}}\mathscr{E}_+}{1-e^{-\frac{i}{2}(\Phi_1-\Phi_2)}}\Bigg[&\frac{e^{-i\frac{1}{2}(\phi-\Phi_1)}}{1-e^{-i(\phi-\Phi_1)}}\left(1-r_{10,1}^2e^{i2N\Phi_1}\right)- \\ -&\frac{e^{-i\frac{1}{2}(\Phi_1-\Phi_2)}e^{-i\frac{1}{2}(\phi-\Phi_2)}}{1-e^{-i(\phi-\Phi_2)}}\left(1-r_{10,2}^2e^{i2N\Phi_2}\right)\Bigg]. \end{aligned} \tag{5.93}$$

We also have (see appendix E.7)

$$iC\varepsilon_0 n^2\alpha_{\text{atom}} = \frac{\alpha_{\text{atom}}}{a^2 b\chi_\alpha}\frac{(1-e^{-i(\phi-\Phi_\alpha)})(1-e^{-i(\phi+\Phi_\alpha)})}{e^{-2i\phi}-1}, \tag{5.94}$$

where χ_α has been defined previously in Eq. (5.79). So from Eqs. (5.94) in (5.93),

we get

$$E_I = \mathscr{E}_+ \Bigg[\Big(\frac{\alpha_{\text{atom}}}{a^2 b \chi_1}\Big) \Bigg(\frac{1}{1-e^{-\frac{i}{2}(\Phi_1-\Phi_2)}}\Bigg) \frac{e^{-\frac{i}{2}(\phi-\Phi_1)}(1-e^{-i(\phi+\Phi_1)})}{1-e^{-2i\phi}} \Big(1-r_{10,1}^2 e^{i2N\Phi_1}\Big) + \\ + \Big(\frac{\alpha_{\text{atom}}}{a^2 b \chi_2}\Big) \Bigg(\frac{-e^{-\frac{i}{2}(\Phi_1-\Phi_2)}}{1-e^{-\frac{i}{2}(\Phi_1-\Phi_2)}}\Bigg) \frac{e^{-\frac{i}{2}(\phi-\Phi_2)}(1-e^{-i(\phi+\Phi_2)})}{1-e^{-2i\phi}} \Big(1-r_{10,2}^2 e^{i2N\Phi_2}\Big) \Bigg]. \tag{5.95}$$

Now we define the effective Fresnel transmission coefficients for the polariton α from the surrounding medium into the meta-film as

$$t_{01,\alpha} = t'_{01,\alpha} \frac{(1-e^{-2i\phi}) e^{\frac{i}{2}(\phi-\Phi_\alpha)}}{1-e^{-i(\phi+\Phi_\alpha)}}, \tag{5.96}$$

with

$$t'_{01,\alpha} = \Bigg(\frac{\alpha_{\text{atom}} a_\alpha}{a^2 b \chi_\alpha}\Bigg)^{-1}, \tag{5.97}$$

and a_α has been introduced previously in Eqs. (5.91). We can then rewrite Eq.(5.95) in a more straightforward form as

$$E_I = \sum_{\alpha=1}^{2} \mathscr{E}_{+,\alpha}, \tag{5.98}$$

where

$$\mathscr{E}_{+,\alpha} = \frac{1}{t_{01,\alpha}} (1 - r_{10,\alpha}^2 e^{i2N\Phi_\alpha}) \mathscr{E}_+. \tag{5.99}$$

We note the similarities in the expressions for E_I obtained for scenario one (Eq. (5.59)) and those obtained for scenario two (Eqs. (5.98)-(5.99)). Of course in

scenario two, we must sum up the field contributions from both polariton modes in the film in contrast to scenario one, wherein we only have the one polariton mode.

We now go back to the expression for $E(J)$ in Eq. (5.85), and we have

$$E(J) = \frac{1}{\varepsilon_0 n^2 \alpha_{\text{atom}}} \sum_{\alpha=1}^{2} A'_\alpha \left(e^{i\Phi_\alpha(J-\frac{1}{2})} + \frac{B'_\alpha}{A'_\alpha} e^{-i\Phi_\alpha(J-\frac{1}{2})} \right). \tag{5.100}$$

Then using Eqs. (5.82) and (5.91) above, we get

$$E(J) = \mathscr{E}_+ \sum_{\alpha=1}^{2} a_\alpha [e^{i\Phi_\alpha(J-\frac{1}{2})} + r_{10,\alpha} e^{i2N\Phi_\alpha} e^{-i\Phi_\alpha(J-\frac{1}{2})}]. \tag{5.101}$$

And finally, using Eqs. (5.98)-(5.99) above, we get the final expression for the electric field in plane J as

$$E(J) = E_I \frac{\sum_{\alpha=1}^{2} a_\alpha [e^{i\Phi_\alpha(J-\frac{1}{2})} + r_{10,\alpha} e^{i2N\Phi_\alpha} e^{-i\Phi_\alpha(J-\frac{1}{2})}]}{\sum_{\alpha=1}^{2} \frac{1}{t_{01,\alpha}} (1 - r_{10,\alpha}^2 e^{i2N\Phi_\alpha})}. \tag{5.102}$$

We also then have the expression for the dipole moment p_J as

$$p_J = \varepsilon_0 n^2 \alpha_{\text{atom}} E_I \frac{\sum_{\alpha=1}^{2} a_\alpha [e^{i\Phi_\alpha(J-\frac{1}{2})} + r_{10,\alpha} e^{i2N\Phi_\alpha} e^{-i\Phi_\alpha(J-\frac{1}{2})}]}{\sum_{\alpha=1}^{2} \frac{1}{t_{01,\alpha}} (1 - r_{10,\alpha}^2 e^{i2N\Phi_\alpha})}. \tag{5.103}$$

Transmittance and Reflectance from the Meta-film

The transmitted field $E_T(z)$ through the meta-film is the sum of the incident field and the forward propagating radiative contributions from all the dipole planes at a

plane $z > Nb$. So we write

$$E_T(z) = E_I e^{-i\frac{\phi}{2}} e^{i\tilde{\omega}nz} + iC \sum_{J=1}^{N} e^{i\tilde{\omega}n(z-bJ)} p_J, \tag{5.104}$$

where p_J is given by Eq. (5.103). The above expression simplifies to (see appendix E.8)

$$E_T(z) = -iCe^{-i\frac{\phi}{2}} e^{i\tilde{\omega}nz} \sum_{\alpha=1}^{2} A'_\alpha \frac{e^{-\frac{i}{2}(\phi-\Phi_\alpha)}}{1-e^{-i(\phi-\Phi_\alpha)}} e^{-iN(\phi-\Phi_\alpha)}(1-r_{10,\alpha}^2). \tag{5.105}$$

Now from an earlier expression for E_I in Eq.(5.92), we can write the transmittance as

$$T = \left| \frac{E_T}{E_I e^{-i\frac{\phi}{2}} e^{i\tilde{\omega}nz}} \right|^2 = \left| \frac{\sum_{\alpha=1}^{2} A'_\alpha \frac{e^{-\frac{i}{2}(\phi-\Phi_\alpha)}}{1-e^{-i(\phi-\Phi_\alpha)}} e^{-iN(\phi-\Phi_\alpha)}(1-r_{10,\alpha}^2)}{\sum_{\alpha=1}^{2} A'_\alpha \frac{e^{-\frac{i}{2}(\phi-\Phi_\alpha)}}{1-e^{-i(\phi-\Phi_\alpha)}} \left(1-r_{10,\alpha}^2 e^{i2N\Phi_\alpha}\right)} \right|^2, \tag{5.106}$$

or

$$T = \left| \frac{\sum_{\alpha=1}^{2} a_\alpha \frac{e^{-i(\phi-\Phi_\alpha)(N+\frac{1}{2})}}{1-e^{-i(\phi-\Phi_\alpha)}} t_{10,\alpha} t_{01,\alpha}}{\sum_{\alpha=1}^{2} a_\alpha \frac{e^{-\frac{i}{2}(\phi-\Phi_\alpha)}}{1-e^{-i(\phi-\Phi_\alpha)}} \left(1-r_{10,\alpha}^2 e^{i2N\Phi_\alpha}\right)} \right|^2, \tag{5.107}$$

where we have used Eqs. (5.91), and introduced the effective Fresnel transmission coefficient for the polariton α from the meta-film into the surrounding medium as

$$t_{10,\alpha} = \frac{1}{t'_{01,\alpha}} \frac{(1-e^{-2i\Phi_\alpha}) e^{\frac{i}{2}(\Phi_\alpha-\phi)}}{1-e^{-i(\phi-\Phi_\alpha)}}, \tag{5.108}$$

and $t'_{01,\alpha}$ has been defined earlier in Eq. (5.97).

The reflected field $E_R(z)$ from the meta-film is the sum of backward propagating

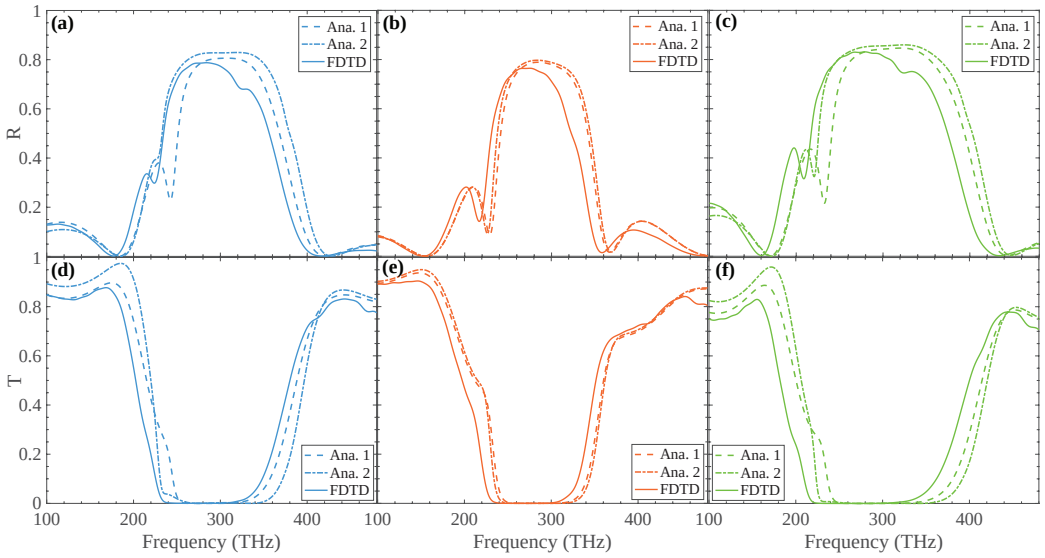

Figure 5.8: Reflectance (top) and transmittance (bottom) spectra of a meta-film of **N = 3** dipole planes with the design parameters taken to be the same as for meta-crystal A ($a = 250$ nm, $b = 110$ nm, left), meta-crystal B ($a = 250$ nm, $b = 150$ nm, middle) and meta-crystal C ($a = 220$ nm, $b = 110$ nm, right). The dashed (dot-dashed) lines are the spectra calculated from the analytical model in scenario one (two) and the solid lines show the spectra obtained from FDTD simulations.

radiative fields from all the planes within the meta-film at a plane $z < 0$. So we have

$$E_R(z) = iC \sum_{J=1}^{N} e^{-i\tilde{\omega}n(z-bJ)} p_J = iCe^{-i\tilde{\omega}nz} \sum_{J=1}^{N} e^{i\phi J} p_J. \tag{5.109}$$

Using Eq. (5.103) above, we get

$$E_R(z) = \frac{iC\varepsilon_0 n^2 \alpha_{\text{atom}} E_I e^{-i\tilde{\omega}nz} \sum_{\alpha=1}^{2} a_\alpha e^{i\phi J} \left[e^{i\Phi_\alpha (J-\frac{1}{2})} + r_{10,\alpha} e^{i2N\Phi_\alpha} e^{-i\Phi_\alpha (J-\frac{1}{2})} \right]}{\sum_{\alpha=1}^{2} \frac{1}{t_{01,\alpha}} (1 - r_{10,\alpha}^2 e^{i2N\Phi_\alpha})}, \tag{5.110}$$

which simplifies to (see appendix E.9)

$$E_R(z) = -\frac{iC\varepsilon_0 n^2 \alpha_{\text{atom}} E_I e^{-i\tilde{\omega}nz} \sum_{\alpha=1}^{2} a_\alpha \frac{e^{i\frac{\Phi_\alpha}{2}}}{1-e^{-i(\phi-\Phi_\alpha)}} [r_{01,\alpha} + r_{10,\alpha} e^{i2N\Phi_\alpha}]}{\sum_{\alpha=1}^{2} \frac{1}{t_{01,\alpha}} (1 - r_{10,\alpha}^2 e^{i2N\Phi_\alpha})}. \tag{5.111}$$

Here we have defined as in scenario one

$$r_{01,\alpha} = -r_{10,\alpha}, \tag{5.112}$$

which is the effective Fresnel reflection coefficient for the polariton mode α from the meta-film into the surrounding medium. Now using the definition of C introduced earlier in Eq. (5.42), we finally have the expression for the reflectance as

$$R = \left| \frac{E_R(z)}{E_I e^{-i\tilde{\omega}nz}} \right|^2 = \left| \frac{\frac{i\phi}{2} \frac{\alpha_{\text{atom}}}{a^2 b} \sum_{\alpha=1}^{2} a_\alpha \frac{e^{i\frac{\Phi_\alpha}{2}}}{1-e^{-i(\phi-\Phi_\alpha)}} [r_{01,\alpha} + r_{10,\alpha} e^{i2N\Phi_\alpha}]}{\sum_{\alpha=1}^{2} \frac{1}{t_{01,\alpha}} (1 - r_{10,\alpha}^2 e^{i2N\Phi_\alpha})} \right|^2, \tag{5.113}$$

Lastly, the effective Fresnel coefficients defined for each polariton mode (Eqs. (5.112), (5.108), (5.96), and (5.83)) also satisfy the relation from continuum electrodynamics

$$1 - r_{10,\alpha}^2 = t_{10,\alpha} t_{01,\alpha}. \tag{5.114}$$

The expressions for R and T of the meta-film obtained so far in both scenarios share similarities with the corresponding expressions for a dielectric film of thickness Nb. While the similarity for scenario one, in which we have a single polariton

mode excited within the meta-film, is explicit, the corresponding expressions for scenario two are a bit more complicated due to the excitation of two polariton modes. For a meta-crystal with a single interface, only the effective indices of the media at the interface determine R and T, which is also evident in the expression for R of a meta-crystal derived previously. For the meta-film, as is also evident from their expressions, these quantities will also depend on the effective thickness Nb. To recall, the reflectance of a normally incident field at wavelength λ_0 from a dielectric film has extrema when the optical thickness of the film is either an odd multiple of $\lambda_0/4$, or a multiple of $\lambda_0/2$ [1]. Hence, given the highly dispersive and broadband spectra of the polariton indices of our meta-crystals, there should be multiple extrema in the reflectance spectra depending on the number of planes N in the meta-film apart from the uniform stop-band observed for the meta-crystals in Fig. 5.6.

In Fig. 5.8, we show the reflectance (top panels) and transmittance (bottom panels) spectra of meta-films consisting of 3 dipole planes and with lattice parameters taken to be the same as those for the meta-crystals A (left panels), B (middle panels) and C (right panels). The spectra calculated using the analytical model in scenario one (two) are shown as dashed (dot-dashed lines). To compare the accuracy of our analytical models, we also show the results from finite-difference time-domain (FDTD) simulations (solid lines) of the meta-films to the corresponding panels. For $N = 3$, we only have one “bulk" plane in the center, and the other two planes form the interfaces. In contrast to the corresponding reflectance spectra of the semi-infinite meta-crystals shown in Fig. 5.6, we note the presence of more ripples

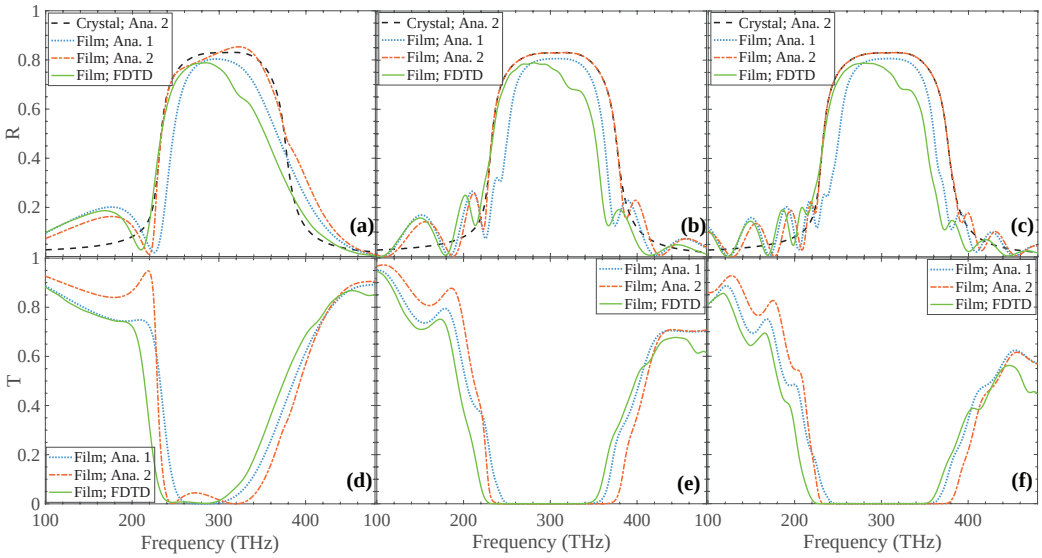

Figure 5.9: Reflectance (top) and transmittance (bottom) spectra of a meta-film of **two** (left), **six** (middle) and **ten** (right) dipole planes with the design parameters taken to be the same as for meta-crystal A ($a = 250$ nm, $b = 110$ nm). The solid green lines show the spectra obtained from FDTD simulations, and the dotted blue and dot-dashed red lines show the spectra calculated using the analytical model in scenario one and two, respectively. The black dashed lines in the top panels show the reflectance from a semi-infinite meta-crystal with the same lattice parameters as the meta-film calculated using the analytical model in scenario two.

in the wings of the stop band, which occur when the aforementioned conditions for the reflectance extrema are met. Also, while the maximum reflectance reaches approximately 0.8 within the stop band, the transmittance becomes negligibly small. Of course, this reflectance maxima is limited by absorption losses or dissipation within the nanoantennas. The spectra obtained from FDTD simulations show a better agreement with the spectra calculated using the analytical model in scenario two at the lower frequencies. Hence, including only the nearest-neighbor near-field coupling between the planes is sufficient to calculate the optical response of these

meta-films through our analytical model. At higher frequencies, the disagreement of both analytical models with the FDTD results is likely due to contributions from the quadrupolar mode of the nanoantenna, whose resonance frequency is around 320 THz. These higher-order multipole contributions are of course not accounted for in our point dipole approximation for the nanoantennas.

In Fig. 5.9, we show the reflectance (top panels) and transmittance (bottom panels) spectra of meta-film A consisting of two (left), six (middle) and ten (right) dipole planes. The reflectance spectrum of the semi-infinite meta-crystal (black, dashed) is also shown for comparison. The addition of more planes, and hence increasing thickness of the meta-film, leads to more ripples in the wings of the stop band as the condition for the extrema of reflectance is satisfied at more frequencies for thicker films. Also, the reflectance spectra of the meta-film (red, dot-dashed) and the semi-infinite meta-crystal (black, dashed) have increasingly better agreement within the stop band even with six dipole planes. The inclusion of more dipole planes also widens the transmittance dip due to enhanced absorption in the wings of the stop band.

The widening of the transmittance dip is even more evident in Fig. 5.10(b), where we show the transmittance spectra of meta-film A with 20 (blue), 50 (red), 100 (green) and 400 (purple) planes. With 400 planes, we have negligible transmittance for most of the spectral range under consideration. The reflectance of these “thick" meta-films (shown in Fig. 5.10(a)) is also negligible in the wings of the stop band, and the reduction in transmittance with increasing number of planes is due to the enhanced absorption ($A = 1 - R - T$) in the wings as shown

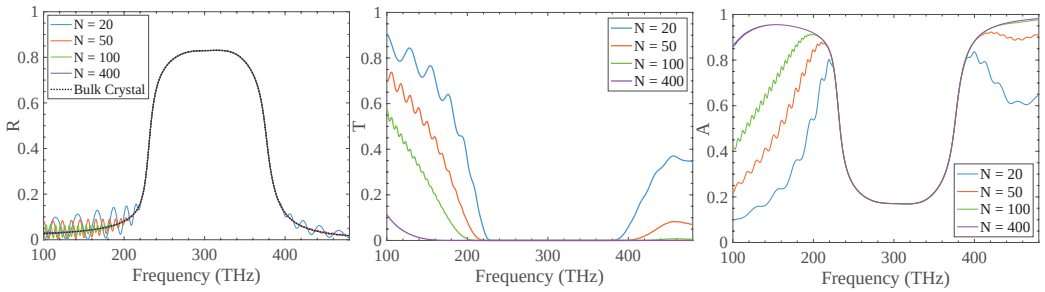

Figure 5.10: (a) Reflectance, (b) transmittance and (c) absorption spectra of a meta-film of N dipole planes (solid lines) indicated in the legend calculated using the analytical model in scenario two assuming the same lattice parameters as for meta-crystal A ($a = 250$ nm, $b = 110$ nm). The dotted black line on the left shows the reflectance of a semi-infinite meta-crystal with the same lattice parameters as the meta-films calculated using the analytical model in scenario two.

in Fig. 5.10(c). Also from Fig. 5.9, we note that the number of ripples in the wings of the reflectance stop band increase with the number of dipole planes while also decreasing in amplitude. For 400 dipole planes, the reflectance spectra of the meta-film and the semi-infinite meta-crystal are indistinguishable. We only show the results from the analytical model in scenario two in Fig. 5.10 as the FDTD simulations become computationally very intensive for such a large number of planes. As an aside, the home-developed MATLAB code for the analytical model can perform these calculations for arbitrarily large number of planes in less than a second on a laptop computer. This computational advantage offered by our analytical model makes it a convenient tool to sweep the already huge material and structural parameter space for rationally designing 3D-metamaterials.

5.4 Conclusions and Future Work

To summarize, we have studied the linear optical properties of a meta-crystal made of dipolar plasmonic nanoantennas with sub-wavelength lattice constants by describing the propagation of a normally incident field through the meta-crystal in terms of polaritons induced by the field within the meta-crystal. We have derived closed-form expressions for the microscopic effective refractive index of these polaritons for two specific scenarios: (1) when there is no near-field coupling between the planes of nanoantenna arrays in the meta-crystal, and (2) when there is nearest-neighbor near-field coupling between the planes. We have also derived the expressions for quantities such as reflectance and transmittance for a semi-infinite meta-crystal and a meta-film consisting of a few planes of nanoantenna arrays. We have also compared the reflectance and transmittance spectra of meta-films consisting of 3-10 planes of nanoantenna arrays calculated using our analytical model with the results from finite-difference time-domain simulations, and found that the results from our model and the full-wave numerical simulations agree reasonably well. The meta-films in our study can support an octave-wide photonic stop band at near-infrared frequencies, and have a maximum effective refractive index of 4 at these frequencies. The stop band also has a range of frequencies where the effective permittivity is either negative or vanishes. The use of our model to calculate the optical properties of meta-crystals provides a significant computational advantage for the rational design of these 3D-metamaterials in the regime where effective medium theories become less accurate. Our model can be

used to perform large sweeps of the structural and material parameter space where the traditional numerical tools such as FDTD and finite element method (FEM) become unwieldy. The latter numerical tools can then be used to finesse the design to account for fabrication tolerances.

As in our previous study [194], the choice of material and structural parameters in our study are based on our previous successful demonstration for a single nanoantenna array and our in-house fabrication capabilities. These parameters can be chosen as per the requirement, and allow for a wide range of tunability for the aforementioned optical properties. Our model can be further generalized to include oblique incidence of the incoming field, higher-order multipoles in the nanoantennas, and misalignments and rotations of the lattices. This more general model would allow for greater flexibility in the choice of materials and shapes for the nanoantennas, as well as lattice structures. In particular, we could model the optical properties of meta-crystals made of dielectric nanoparticles that have the advantage of significantly smaller dissipation compared to plasmonic nanoparticles. More interesting lattice structures such as Moiré lattices [197] and lattice defects [198, 199] can also be modeled with this generalized model. Extending the model to oblique incidences would also enable the calculation of dispersion curves for the meta-crystals, and provide more insight into the stop band. The anisotropic octave-wide stop band of these meta-crystals with a large (≈ 0.85) and nearly flat reflectance spectrum has potential applications for devices such as broadband notch filters, mirrors and polarizers. Introducing defects in the meta-crystal should also enable realizing wavguides and nanocavities for controlling spontaneous emission

[200, 201], realizing nanolasers [202, 203], nonlinear optics and cavity quantum electrodynamics [204].

Future efforts for experimentally characterizing the optical properties of these plasmonic meta-films and then to possibly utilize them for nanophotonic applications require fast and efficient methods for fabricating several layers of nanoantenna arrays while maintaining the orientation and alignment of the nanoantennas in each layer. The conventional lithographic methods for fabricating 3D plasmonic metamaterials are cumbersome [205]. These top-down techniques involve layer-by-layer electron beam lithography followed by metal evaporation and lift-off and subsequent deposition of dielectric spacers [186, 206]. There are also bottom-up techniques such as colloidal self-assembly [207–211] that can be used to fabricate large “superlattices" of nanoparticles with areas approaching 1 cm^2 [184]. Colloidal self-assembly involves slow evaporation of a colloidal solution of nanoparticles leading to the agglomeration of similarly-sized nanoparticles into ordered superlattices governed by van der Waals and electrostatic forces, and by entropy [207]. The inter-particle spacing is usually controlled through the choice of appropriate ligands such as various polymers and proteins [212]. DNA strands offer a lot of versatility as ligands due to the controllable strengths of hydroden bonding in their base pairings [211]. Highly-ordered 3D arrangements of plasmonic nanoparticles can be self-assembled by functionalizing individual nanoparticles with specific DNA strands [213, 214], or on templates formed by DNA strands [215]. In interfacial self-assembly, thin films of nanoparticles can assemble at the liquid-air or liquid-liquid interfaces and then transferred to the appropriate substrate through

the use of the Langmuir-Blodgett technique [216, 217]. In short, these techniques are encouraging developments towards efficient and fast fabrication of plasmonic meta-films.

6. Controlling Nonlinear Rogue Wave Formation Using the Coherence Length of Phase Noise

6.1 Introduction

The formation of rare but extreme (or “rogue") amplitude waves in optical [218–223], microwave [224], and hydrodynamic systems [225] have attracted considerable recent interest [226–228]. A random phase fluctuation with sufficient strength imposed on an optical field can develop on propagation into network-like intensity patterns that are commonly referred to as “caustics" [220, 223, 229]. Light can concentrate very tightly in caustics, which facilitates rogue wave formation and leads to long-tailed statistics for the intensity and non-Rayleigh statistics for the amplitude. Rogue waves in linear systems can develop through the constructive interference of several waves with random phases and amplitudes [230], or through the directional focusing of these waves [231]. Speckle formation in optical sys-

tems is also a linear phenomenon, and a fully developed speckle field has circular Gaussian statistics with a Rayleigh distribution of the amplitude [232]. Long-tailed intensity statistics in linear systems can occur due to multiple scattering through a medium [233], due to the spatial inhomogeneity-induced clustering of speckles with different grain sizes [234], and through the redistribution of energy among several speckle grains in the farfield due to higher-order correlations encoded onto the field [235].

The presence of nonlinearity in an optical system can considerably influence the formation of rogue waves. Rogue events have been observed during supercontinuum generation in nonlinear fiber-optics systems and are the result of collisions between “breather" solitons formed by nonlinear amplification of modulational instability in the system [218, 227, 236, 237]. Rogue waves can also form in spatially extended nonlinear systems either by means of self-focusing seeded by wavefront perturbations on the field [221, 223, 238] or by hypercycle amplification after the breaking of spatial symmetry in optical cavities [239]. Small scale filamentation is another phenomenon that occurs when a large self-focusing nonlinearity amplifies angular spectral sidebands through four-wave mixing, leading to the formation of several localized structures called “filaments" such that each filament has the same (critical) power P_{cr} [4, 240]. Rogue waves can also form in a beam undergoing small-scale filamentation when filaments merge because of medium inhomogeneities [240]. A self-focusing nonlinearity can enhance rogue wave formation in laser beams containing weak phase noise [223]. However, a non-uniform polarization structure on the beam can suppress rogue waves under

certain conditions [241]. Rogue waves are more likely to form in speckle patterns of a particular coherence length propagating through a photorefractive crystal due to the saturation of nonlinearity once a rogue feature reaches a certain minimum width [222]. Light scattered through a medium with tailored disorder can also show a similar enhancement of rogue wave formation at a particular coherence length of the disorder [242].

Here, we study how the transverse spatial coherence length of phase noise affects rogue wave formation in the presence of a self-focusing nonlinearity. We measure the intensity statistics of the beam after it propagates through a hot rubidium vapor cell for various coherence lengths (or grain sizes) of the phase noise and various beam powers. We observe that the intensity statistics have a diminished sensitivity to nonlinearity when the coherence length of the phase noise is much smaller than the beam width. We also study the mechanism behind this effect through numerical simulations of nonlinear beam propagation. Our simulations show that small-grained phase noise induces the redistribution of beam power into multiple filaments of reduced intensity, thereby limiting the maximum intensity in a rogue feature relative to the background. Our study complements Refs. [222, 223, 241], and is relevant for the development of better optical power limiters, and for probing a turbulent medium and mitigating its effect on the propagation of intense laser beams. In section 6.2, we describe our experimental setup and the results of our measurements of the intensity statistics. In section 6.3, we describe our numerical simulations of the propagation dynamics of the beam within the medium to understand the interaction between phase noise of various coherence

lengths and self-focusing nonlinearity of the medium that leads to rogue wave formation. Then in section 6.4, we discuss the results of these simulations for beams of various powers and added phase noise of different coherence lengths.

6.2 Experiment

Figure 6.1(a) shows the schematic of our experimental setup. Our saturable nonlinear medium is a cell containing natural abundance rubidium. We heat the cell to 115 °C, and blue detune our laser source by 600 MHz above the ^{87}Rb D_2 $F = 1 \rightarrow F' = 2$ transition in order to have a self-focusing nonlinear response. A horizontally polarized beam from our laser source diffracts from a phase grating impressed on a spatial light modulator (SLM1) and forms a Gaussian beam of diameter 2.5 mm (D_0) in the first diffractive order. We isolate this diffractive order by letting the light propagate over 2 m, and add a conjugate defocus on SLM1 to compensate for the accumulated defocus on the beam. Both SLM1 and SLM2 are liquid-crystal-on-silicon (LCOS) phase only SLMs from Hamamatsu that have identical resolution (600×800) and pixel size (20 μm). SLM2 adds a random phase mask with a spatial coherence length L_{coh} and a maximum amplitude of π rad onto the beam. To determine the random phase mask, we generate a 600×800 matrix of uniformly distributed random numbers between 0 and 1, and apply to this salt-and-pepper noise matrix a Gaussian filter of width $1/L_{\text{coh}}$ defined below

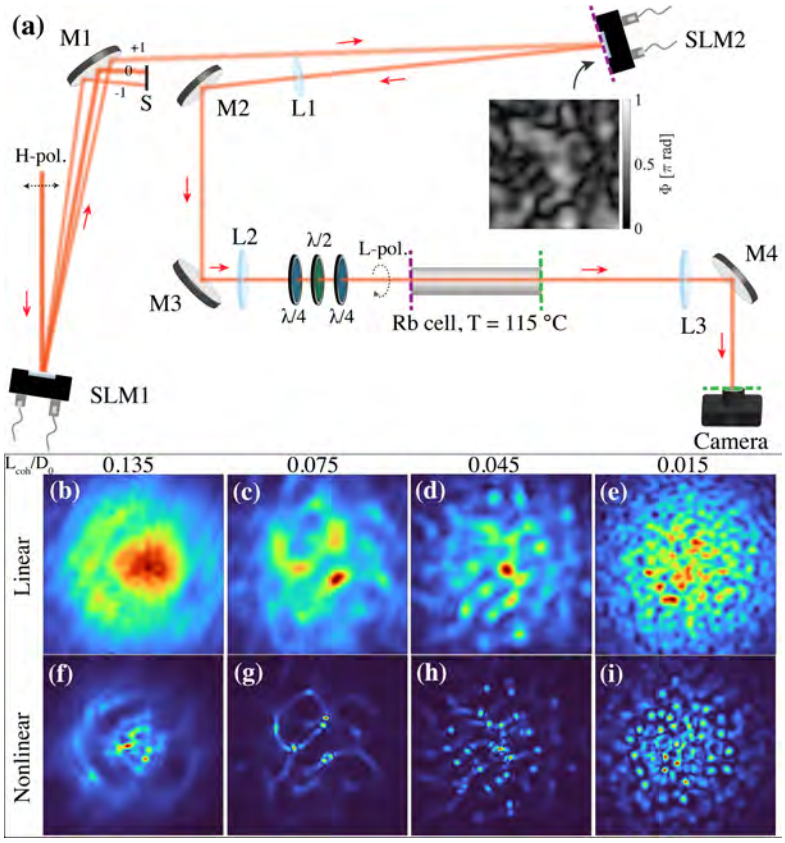

Figure 6.1: (a) Schematic of the experimental setup. H-polarized light from a tunable diode laser is diffracted by a phase-only grating on SLM1 forming a Gaussian beam of diameter D_0 (to $1/e^2$ values of the intensity) in the first diffractive order. SLM2 adds a random phase mask (example shown in the inset) with coherence length L_{coh} and amplitude of π rad on the beam. SLM2 is then imaged using lenses L1 and L2 onto the entrance facet (purple dashed line) of a 7.5 cm-long rubidium cell heated to 115 ℃ . The output facet (green dashed line) of the cell is then imaged by lens L3 onto the image plane of the camera. Measured caustic patterns formed by noisy beams with L_{coh}/D_0 of (b, f) 0.135, (c, g) 0.075, (d, h) 0.045, and (e, i) 0.015, after linear (top), and nonlinear (bottom) propagation through the cell are also shown. The beam power at the input of the cell (P_{in}) was 90 mW for the nonlinear results. The focal lengths of the lenses L1, L2 and L3 are 1 m, 75 cm and 30 cm, respectively.

[243], which acts as a blur

$$G(k_x, k_y) = \frac{L_{\text{coh}}^2}{2\pi} \exp\big[-\frac{k_x^2 + k_y^2}{2} L_{\text{coh}}^2\big]. \tag{6.1}$$

We then multiply the matrix by π so that the maximum phase amplitude of the added phase noise is π rad. Limiting the maximum phase amplitude to π rad ensures, as we show later, that the caustics formed after purely linear propagation through the cell are weak enough to not yield long-tailed intensity statistics [223]. The lenses L1 and L2 image the active area of SLM2 onto the entrance facet of the rubidium cell. The waveplates before the cell convert the polarization of the beam to left-handed circular to match the handedness of the σ_+ atomic transition. The lens L3 images the output facet of the cell onto the image plane of the camera, which records the intensity at the cell output.

Figures 6.1(b)-(e) show the recorded output intensity distributions after linear propagation through the cell for representative phase masks with L_{coh}/D_0 of 0.135, 0.075, 0.045, and 0.015, respectively. For all linear measurements, we increase the value of detuning from 600 MHz to 65.04 GHz and fix input beam power P_{in} to 4 mW. As shown in Figs. 6.1(b)-(e), the added phase noise leads to redistribution of the beam intensity upon linear propagation, but is weak enough that no sharp caustics are formed. As we decrease the L_{coh}/D_0 of noise (left to right), more "hotspots" are formed in the beam such that the intensity corresponding to the smallest L_{coh}/D_0 [Fig. 6.1 (e)] becomes more granular. Figures 6.1(f)-(i) show the recorded intensities for the same phase masks as in the top panels (b)-(e), but with

the nonlinearity turned on by changing the detuning to 600 MHz, and the beam power P_{in} to 90 mW. The nonlinearity sharpens the hotspots formed during linear propagation while preserving their underlying structure [223].

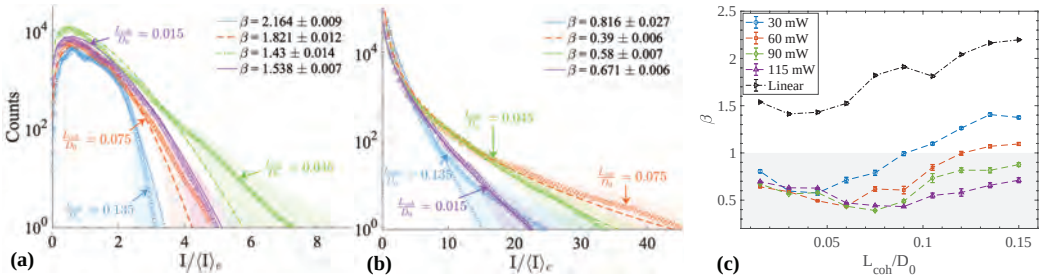

Figure 6.2: (a) Measured intensity histograms (markers), and their respective Weibull distribution fits (lines) after (a) linear, and (b) nonlinear propagation through the rubidium cell for L_{coh}/D_0 of 0.135 (blue, solid), 0.075 (red, dot-dashed), 0.045 (green, dashed), and 0.015 (purple, dotted). The value of P_{in} for the nonlinear datasets is 90 mW. The shaded regions around the respective plot markers represent the uncertainty of counts in the corresponding bins. The value of the parameter β for each fit is stated in the legend. (c) The variation of β with L_{coh}/D_0 for linear measurements (black triangles), and nonlinear measurements with P_{in} of 30 mW (blue circles), 60 mW (red squares), 90 mW (green diamonds), and 115 mW (purple triangles). The gray shaded region indicates the range of β corresponding to long-tailed intensity statistics.

To quantify the intensity statistics, we record output intensity patterns for an ensemble of 500 random phase masks with the same L_{coh}. We acquire these intensity datasets for nonlinear propagation through the cell at various incident beam powers P_{in} (30 mW, 60 mW, 90 mW, and 115 mW) and various L_{coh} values (varied from 50 μm to 450 μm). We also record datasets for linear propagation through the cell. These intensity histograms $N_H(I_N)$ are well described by a Weibull

distribution defined as follows [244]

$$N_H(I_N) = N_{\text{total}} \frac{\beta}{\alpha} \left(\frac{I_N}{\alpha} \right)^{\beta-1} \exp\left[- \left(\frac{I_N}{\alpha} \right)^{\beta} \right], \tag{6.2}$$

where $I_N = I/\langle I \rangle_e$ is the beam intensity normalized to the ensemble average of intensities in the entire dataset $\langle I \rangle_e$, N_{total} is the total number of counts in the dataset, and the parameters α and β are the scale and shape parameters of the distribution, respectively. Fully developed speckle patterns have an exponential distribution of intensities [245] and correspond to the scenario when $\beta = 1$. Long-tailed statistics have values of β smaller than 1 with caustic formation and rogue wave behavior becoming more likely with smaller values of β. We estimate β for our measured intensity histograms by performing maximum likelihood estimation (MLE) fits to the Weibull distribution followed by Monte-Carlo simulations to obtain the uncertainties of the fit parameters.

Figures 6.2(a) and (b) show the measured intensity statistics along with their respective Weibull distribution fits for linear and nonlinear propagation through the rubidium cell, respectively, for L_{coh}/D_0 of 0.135 (blue circles and dotted line), 0.075 (red diamonds and dashed line), 0.045 (green squares and dot-dashed line), and 0.015 (purple triangles and solid line). The input beam power P_{in} for the nonlinear datasets in Fig. 6.2(b) is 90 mW. The values of β estimated from the fits to each dataset are indicated in the legend. The nonlinear datasets in Fig. 6.2(b) show long-tailed statistics throughout, which is also manifested in the smaller estimated values of β for all L_{coh}/D_0 compared to the linear datasets in Fig. 6.2(a).

Additionally, we note that phase noise of smaller L_{coh}/D_0 has a wider angular spectral bandwidth [see Fig. F.2 in appendix F.2]. This broadband noise seed should cause further broadening of the angular spectrum of the beam through four-wave mixing and lead to sharper caustics and longer-tailed intensity statistics. However, we do not observe a monotonic increase in the “tailiness" of intensity statistics as L_{coh}/D_0 is reduced in Fig. 6.2(b), which is also reflected in the associated values of β given in the legend. Instead, β is minimized for L_{coh}/D_0 of 0.075, and its distribution is the most long tailed.

Figure 6.2(c) shows the variation of β with L_{coh}/D_0 for linear measurements (black triangles) and nonlinear measurements with P_{in} of 30 mW (blue circles), 60 mW (red squares), 90 mW (green diamonds), and 115 mW (purple triangles). The shaded gray region represents the region where $\beta < 1$ and rogue wave behavior is likely. As also shown in Fig. 6.2(a), $\beta > 1$ for purely linear propagation for all values of L_{coh}/D_0 considered here and we do not observe either rogue wave behavior or the formation of a fully developed speckle pattern. The reasons for this result are: (i) The propagation distance (length of the cell) is short enough to be in the Fresnel region of the incident beam. Consequently, the number of scattering centers on the phase mask contributing to the field at any point on the observation plane is small enough for the central limit theorem to not be valid in a random walk statistical model of the field, which leads to non-Gaussian field statistics [246]. This argument is especially true for larger values of L_{coh}/D_0 for which there are fewer scattering centers for the input beam. (ii) The maximum phase amplitude of the added phase noise is π, and hence small enough to not lead

to strong focusing into sharp caustics after propagation through the cell [223]. The value of β for nonlinear measurements is smaller than β for linear measurements for all L_{coh}/D_0, which is consistent with the aforementioned increase in sharpness of caustics due to nonlinearity. The noteworthy feature, however, is that for nonlinear measurements, β is significantly more sensitive to the beam power P_{in} when L_{coh}/D_0 is larger than 0.075 than it is for smaller L_{coh}/D_0. This diminished sensitivity of the broadening of angular spectrum of the beam to nonlinearity when seeded by broadband phase noise shares similarities with the reduced effect of nonlinearity on the broadening of the modulational instability spectrum in an optical fiber for a low amplitude partially coherent broadband seed [247]. We further explore this observed phenomenon through numerical simulations.

6.3 Numerical Modeling

The propagation of a field $E(r,t) = E(x,y)e^{i(kz-\omega t)}\hat{e_L} + \text{c.c.}$ through a spatially extended nonlinear medium, such as our rubidium cell, can be described by the (2+1)-D nonlinear Schrödinger equation (NLSE) [4] given below

$$\frac{\partial E}{\partial z} - \frac{i}{2k}\nabla_{\perp}^2 E = \frac{ik}{2\varepsilon_0}P, \tag{6.3}$$

where $E(x,y)$ is the field envelope, ω is the angular frequency of the laser, k is the wave number, $\nabla_{\perp}^2 = \partial^2/\partial x^2 + \partial^2/\partial y^2$ is the transverse Laplacian, $P = \varepsilon_0\chi(E)E$ is the atomic polarization, and $\chi(E)$ is the total atomic susceptibility that includes

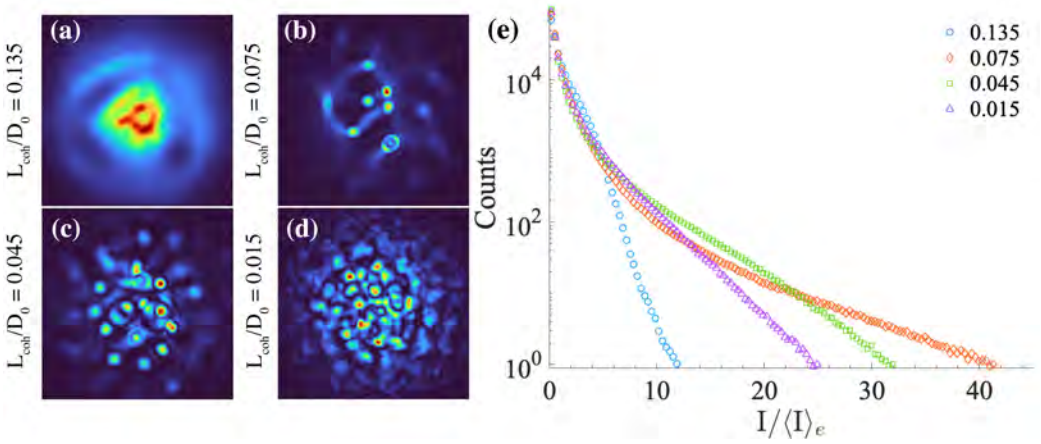

Figure 6.3: (a) Simulated caustic patterns at the output of the cell for P_{in} of 90 mW, and L_{coh}/D_0 of (a) 0.135, (b) 0.075, (c) 0.045, and (d) 0.015. The phase masks used for these calculations were the same as the ones used in the experiment to capture the caustic patterns shown in Figs. 6.1(b)-(e). (e) Simulated intensity statistics for P_{in} of 90 mW, and L_{coh}/D_0 of 0.135 (blue circles), 0.075 (red diamonds), 0.045 (green squares), and 0.015 (purple triangles).

the linear as well as all orders of nonlinear response [4]. In our calculation of total susceptibility, we include the contributions from all the D2 transitions of rubidium. See appendix F.1 for more details. We use the split-step Fourier method [248] to solve Eq. (6.3), and obtain the field at any location (x, y, z) within the rubidium cell. We use Fresnel propagation for all linear propagation calculations [249]. For all simulations, we assume a transverse resolution of 2048 $\times$ 2048 pixels, a pixel size of 4.89 μm, and a longitudinal step size of 0.5 mm. We account for the slight longitudinal misalignment in our experimental setup by assuming that the beam waist is located 6 mm before the cell and add 1 cm of linear propagation after the cell.

Figures 6.3(a)-(d) show the simulated output intensities for the same set of

phase masks used in the experiment that were used for the measured output intensities shown in Figs. 6.1(f)-(i). We also include an amplitude mask on the Gaussian beam to match the intensity of the Gaussian beam in our experiment [see Fig. 6.4(a)]. The simulated intensities in Figs. 6.3(a)-(d), and the measured intensities in Figs. 6.1(f)-(i) have very similar underlying intensity structures and sharpness of caustic features. Figure 6.3(e) shows the simulated intensity statistics for P_{in} of 90 mW, and L_{coh}/D_0 of 0.135 (blue circles), 0.075 (red diamonds), 0.045 (green squares), and 0.015 (purple triangles). We use 200 realizations of random phase masks of a particular L_{coh}/D_0 to calculate these intensity statistics. The simulated statistics show a good qualitative agreement with the measured statistics shown in Fig. 6.2(b) for the same set of parameters, and in both scenarios, the histogram corresponding to L_{coh}/D_0 of 0.075 is the most long tailed. We emphasize that we do not expect a complete agreement between our measurements and numerical simulations due to several contributing factors, such as nonlocality in the nonlinear response of rubidium vapor [250], temperature variation within the cell leading to a spatial variation in the nonlinear susceptibility, aberrations in the imaging optics and the windows of the cell, and the pixel size of SLMs. Furthermore, the reinforcing nature of the self-focusing nonlinearity implies that our system is highly sensitive to any noise present in the experiment, which is difficult to account for in our simplified numerical model completely. However, the good qualitative agreement between our measurements and simulations allows us to study and draw reasonable conclusions about the propagation dynamics of the beam within the cell.

6.4 Discussion

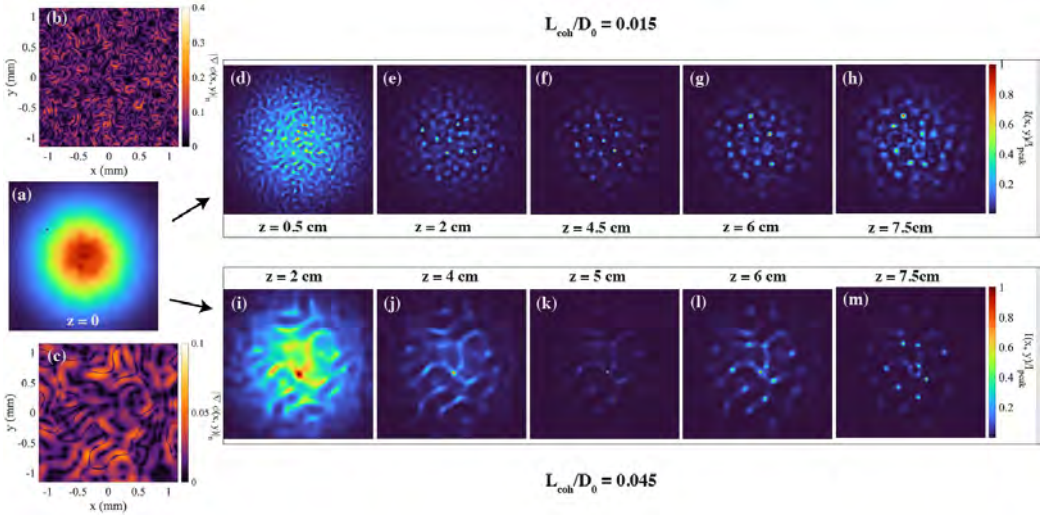

Figure 6.4: (a) Input Gaussian beam intensity. Phase gradient map $|\nabla\phi(x,y)|$ for a sample mask with L_{coh}/D_0 of (b) 0.015 and (c) 0.045. The top panels (d)-(h) show the beam intensity at various propagation distances z within the cell for the phase gradient map shown in (b), and the bottom panels (i)-(m) show the beam intensity at various z for the phase gradient map shown in (c). The beam power P_{in} is 90 mW throughout. The intensity distributions in all panels are normalized with respect to the maximum intensity in the respective frames.

To understand the interplay between phase noise induced distortion of the beam and the self-focusing nonlinearity, we use our simplified numerical model to study the nonlinear propagation dynamics through the cell. Our use of the numerical model to understand the propagation dynamics is motivated by the fact that we cannot experimentally image the beam inside the nonlinear medium. Figure 6.4(a) shows the intensity of the input Gaussian beam generated in our setup, which we also assume as the input intensity in our numerical simulations. We select one realization of the random phase masks of a particular coherence

length, and monitor the intensity profiles at various distances z within the rubidium cell calculated through numerical simulations. Figures 6.4(b) and (c) show the phase gradient maps $|\nabla\phi(x,y)|$ of one realization of the phase masks of coherence lengths L_{coh}/D_0 of 0.015 and 0.045, respectively. The top panels (d)-(h) show the normalized intensities of the beam at various propagation distances z stated in the panel label for the phase gradient map shown in Fig. 6.4(b). Similarly, the bottom panels (i)-(m) show the normalized intensities of the beam at various z for the phase gradient map shown in Fig. 6.4(c).

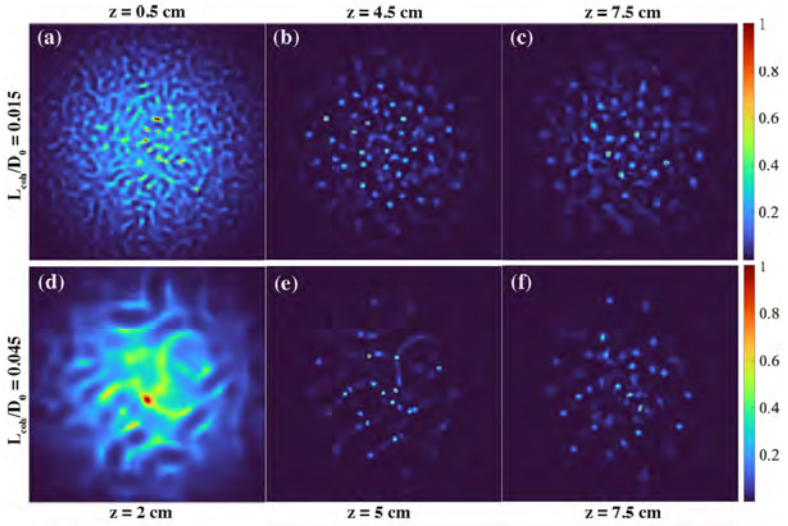

Figure 6.5: The top panels (a)-(c) show the beam intensity at various propagation distances z within the cell for the phase gradient map shown in Fig. 6.4(b), and the bottom panels (d)-(f) show the beam intensity at various z for the phase gradient map shown in Fig. 6.4(c). The beam power P_{in} is 180 mW throughout. The intensity distributions in all panels are normalized with respect to the maximum intensity in the respective frames.

As shown in Figs. 6.4(d) and (i), the beam at first reorganizes by focusing along the minima of the respective phase gradient maps. This initial reorganization

occurs at smaller z for phase noise of smaller grain size. The intensity hotspots on this reorganized beam then continue to self focus until at least one of the hotspots reaches the size of a filament that has a FWHM size Δr of $25 \pm 2.5 \mu$m as shown in Figs. 6.4(f) and (k). With the field being very concentrated in a small number of hotspots, the intensity contrast in this plane is very large. A Gaussian beam of width Δr and an average power of 1.4 mW (say, P_{cr}) forms a self-trapped filament that propagates for at least 1.3 cm in the rubidium vapor without any change in its width before diverging due to absorption and diffraction. The collapse of the filament is also limited by absorption, saturation of the nonlinearity, and non-paraxiality [251]. For L_{coh}/D_0 of 0.015, multiple filaments of width Δr are formed at $z = 4.5$ cm, and each filament has power smaller than P_{cr} required for forming a self-trapped filament that can propagate for several cm. Hence, these filaments diffract within a few mm as the other hotspots also self-focus and subsequently diffract. Around $z = 6$ cm, absorption losses reduce the effect of nonlinearity, and the filaments start to diverge. Figures 6.5 (a)-(c) show the beam evolution through the cell for the same phase gradient map as shown in Fig. 6.4(b), but at a beam power P_{in} of 180 mW. Similarly, Figs. 6.5(d)-(f) show the beam evolution for the phase gradient map as shown in Fig. 6.4(c), and at a beam power P_{in} of 180 mW. Comparing Fig. 6.4(d) with Fig. 6.5(a), and Fig. 6.4(e) with Fig. 6.5(d), we note that the initial beam reorganization stage involving focusing along the minima of the respective phase gradients remains similar despite the higher power. Comparing Fig. 6.4(f) with Fig. 6.5(b), and Fig. 6.4(k) with Fig. 6.5(e), we note that the larger beam power gets distributed into several more filaments along the same underlying caustic pattern.

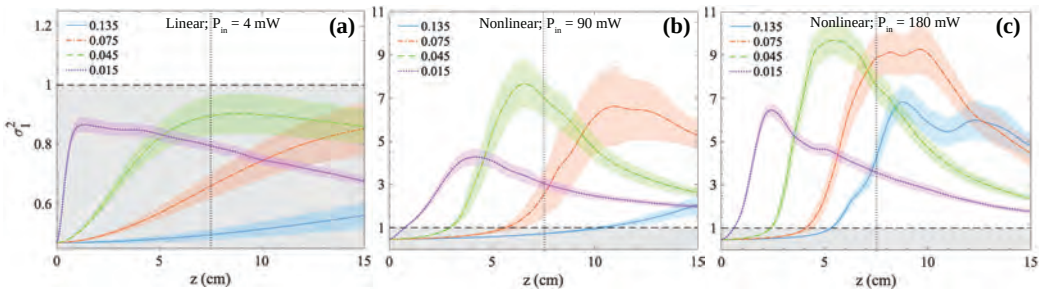

Figure 6.6: The evolution of the scintillation index σ_I^2 with propagation distance z as predicted by our numerical model under (a) linear, and under (b), (c) nonlinear propagation with P_{in} of 90 mW and 180 mW, respectively. The legend shows the values of L_{coh}/D_0 of the random phase mask added to the beam. The dashed black line indicates the threshold above which long-tailed intensity statistics start to emerge.

To quantify the propagation dynamics, we use the scintillation index σ_I^2 as a metric for the intensity contrast within the beam (or in other words, the sharpness of the caustics) and monitor its variation with propagation distance z. We also extend the length of the nonlinear medium to 15 cm in order to include the stage where diffraction starts to dominate the propagation dynamics for all values of L_{coh}/D_0 of the phase noise. The quantity σ_I^2 is the normalized variance of intensity defined as [252, 253]

$$\sigma_I^2 = \frac{\langle I^2 \rangle - \langle I \rangle^2}{\langle I \rangle^2}. \tag{6.4}$$

Here, $\langle \cdots \rangle$ denotes the transverse spatial average over the entire field. Fully developed speckle patterns have a σ_I^2 of unity, while caustics with large intensity fluctuations in the transverse plane have σ_I^2 larger than unity. Also referred in the literature as the intensity "contrast" [229, 246], the scintillation index has been used as a metric to identify the onset of branched flow – another instance

of caustic formation due to the focusing of waves propagating through media with correlated disorder [253, 254], and to characterize irradiance fluctuations in waves propagating through turbulence [229, 252, 255]. Figure 6.6(a) shows the evolution of σ_I^2 for a noisy Gaussian beam with L_{coh}/D_0 of 0.135 (blue, solid), 0.075 (red, dot-dashed), 0.045 (green, dashed), and 0.015 (purple, dotted) during linear propagation. The black horizontal dashed line indicates the threshold value of σ_I^2 above which sharp caustics characterized by larger fluctuations in intensity than a Gaussian speckle are observed. For a specific set of input parameters (P_{in} and L_{coh}), we average σ_I^2 at each z over 100 different phase masks. This averaged σ_I^2 is represented by the lines, and the shaded regions around the lines represent its standard deviation. Figures 6.6(b) and (c) show the evolution of σ_I^2 with z for nonlinear propagation with P_{in} of 90 mW and 180 mW, respectively, and the same set of values of L_{coh}/D_0 as in Fig. 6.6(a).

For purely linear propagation, we note that in all of the scenarios shown in Figs. 6.6(a)-(c), σ_I^2 at first increases with z, and then peaks as the phase noise on the beam morphs into intensity distortion. This rate of increase in σ_I^2 depends strongly on the grain size of the phase noise, as well as the nonlinearity. As also discussed previously in Refs. [229, 246], we observe in Fig. 6.6(a) that σ_I^2 initially increases with z until it reaches a maximum when the various “facets" or grains of the added phase noise on the beam initially come to a focus along the minima of their gradients to form hotspots. When the grain size of the noise is much smaller than the beam diameter (such as when $L_{\text{coh}}/D_0 = 0.015$), the phase variations occur over a smaller area within the beam and so the phase gradients are larger

and more densely packed [see Fig. 6.4(b)]. In the absence of nonlinearity, these hotspots then diverge, thereby causing σ_I^2 to decrease with z. As the grain size of phase noise becomes larger, the phase gradients decrease in magnitude and become less densely packed [see Fig. 6.4(c)], which leads to fewer grains within the beam that focus into hotspots at larger z.

In the presence of nonlinearity, σ_I^2 increases beyond unity as the hotspots continue to self-focus and maximizes. When the hotspots focus down to the size of a self-trapped filament of width Δr, σ_I^2 is maximized as the beam has the highest intensity contrast at this stage of propagation. Filaments of the same width but smaller power than $P_{\rm cr}$ diverge more quickly, while those with power larger than $P_{\rm cr}$ undergo multiple self-focusing and defocusing cycles depending on their power [251]. For $P_{\rm in}$ of 90 mW and $L_{\rm coh}/D_0$ of 0.015, more than two filaments of size Δr are formed when σ_I^2 is maximized such that the power in each filament is smaller than 0.9 mW [see Fig. 6.4(f)]. In contrast, for $P_{\rm in}$ of 90 mW, and $L_{\rm coh}/D_0 \geq 0.045$, a single filament of size Δr with average power larger than 1 mW is formed when σ_I^2 is maximized [see Fig. 6.4(k)]. As shown in Fig. 6.6(b), this sharper intensity contrast between the “rogue" filaments and the background intensity in the beam for $L_{\rm coh}/D_0 \geq 0.045$ results in a higher peak of σ_I^2 for these cases than when $L_{\rm coh}/D_0 \leq 0.045$. When $P_{\rm in}$ is increased to 180 mW, the caustics become even sharper, and more filaments of size Δr are formed when σ_I^2 is maximized, which, as shown in Fig. 6.6(c), occurs at even smaller z for all cases. For $L_{\rm coh}/D_0$ of 0.015 (≥ 0.045), the average power in each filament is smaller (larger) than 1.4 mW [see Fig. 6.5]. Hence, for noisy beams with $L_{\rm coh}/D_0 \geq 0.045$, the propagation after the

initial peak of σ_I^2 is followed by another cycle of self-focusing of filaments and subsequently, by diffraction. Nevertheless, even at such large beam powers, the small-grained phase noise seeds the formation of several filaments each containing less than $P_{\rm cr}$ power. This phenomenon limits the maximum intensity in a rogue feature and the tailiness of the intensity statistics. Finally, we note that σ_I^2 for $L_{\rm coh}/D_0 < 0.045$ ($L_{\rm coh}/D_0 \geq 0.045$) has little (large) variation between $P_{\rm in}$ of 90 mW and 180 mW at $z = 7.5$ cm, or the length of the cell (dotted vertical line in Figs. 6.6(b) and (c)). This result is a consequence of the initial beam reorganization followed by self-focusing cycle(s) occurring at shorter z as the phase noise becomes more granular, and is consistent with the diminished sensitivity of the likelihood of rogue wave formation to nonlinearity observed experimentally.

6.5 Conclusion

In summary, we have shown that the grain size of phase noise on a laser beam can be used to control rogue wave formation in media with a self-focusing nonlinearity. The likelihood of rogue wave formation is minimally affected by nonlinearity when the coherence length of phase noise is much smaller than the beam diameter. Our numerical simulations show that small-grained phase noise causes the beam power to be redistributed into multiple filaments rather than a single filament, which is formed when the phase noise has a longer correlation length. This redistribution of beam power into several filaments of smaller intensity limits the maximum intensity in rogue features relative to the background. Understanding the role of

nonlinearity in amplifying the phase noise-induced intensity fluctuations on a field could be helpful in devising efficient mechanisms to mitigate these fluctuations for intense structured light propagating through a turbulent medium [256, 257], and developing efficient radiance limiters using saturable nonlinear media [39].

7. Summary and Outlook

The interaction of light with matter is fundamental to a wide variety of known phenomena. In this thesis, we have studied light-matter interaction in three different systems. In chapter 2, we have described a bifilm of sub-wavelength-thick gold and ITO films that support hybrid polariton modes that are formed by strong coupling between the LR-SPP mode in the gold film and the ENZ mode in the ITO film. We have performed linear characterization of these modes through experiment, TMM simulations, and an analytical model, and shown that they are not only strongly confined within the ITO film, but can also propagate for several wavelengths. These modes, with their relatively long propagation lengths and reasonably large mode confinements, have properties that make them favorable for nonlinear optical applications in the ENZ regime. The experimental effort for performing nonlinear characterization of these modes is currently underway within our research group. The first set of experiments in this effort involves performing intensity-dependent attenuated total reflection spectroscopy measurements with a single incident pump beam at frequencies along the dispersion curves of the two hybrid polaritons. The second set of experiments involves degenerate as well as non-degenerate pump-

probe measurements of the temporal dynamics of the nonlinear response of these polaritons. The latter experiment is relevant as ITO has a sub-ps nonlinear response at ENZ frequencies [6], and understanding the temporal response of these hybrid SPP-ENZ modes is relevant for applications such as ultrafast switching.

In chapter 3, we showed through experiment, FDTD simulations and an analytical model that the extinction linewidth of a planar array of dipolar nanoantennas is proportional to the number density of the nanoantennas in the array. In chapter 4, we extended our analytical model to a bilayer of two such arrays separated by a sub-wavelength distance and showed the existence of a bright mode with twice the extinction linewidth of a single array, and a dark mode with a significantly smaller linewidth. We also showed that these modes can be selectively excited by adjusting the relative phase of two equal intensity counter-propagating incident fields on the bilayer. In chapter 5, we further extended our analytical model to a meta-crystal formed by stacking several such arrays, and found that we could have a maximum effective refractive index of 4 with an octave wide photonic stop band at near-infrared frequencies. Our analytical model is another useful tool in the electrodynamic simulations of metamaterials as it can be used to perform broadband sweeps over several material and geometric design parameters much more quickly than full wave analysis such as FDTD and FEM. It can also be further generalized to account for multipolar contributions and lattice rotations and misalignments for more design flexibility. With regards to the experimental characterization of these meta-films, we currently have ongoing efforts with collaborators in the Boyd group at the University of Ottawa to fabricate these meta-films. The

lithographic fabrication of these multilayered structures is unsurprisingly proving to be challenging. The measurement of transmittance and reflectance spectra at normal incidence of these meta-films once fabricated can be done through the use of the experimental setup shown in Fig. 3.1.

Finally, in chapter 6, we experimentally showed that the likelihood of rogue wave formation in a laser beam in the presence of a saturable self-focusing nonlinearity depends on the coherence length of phase noise added to the beam. The likelihood of rogue wave formation is much less sensitive to change in laser power when the coherence length is significantly smaller than the beam diameter, or the phase noise is more granular. As a followup, we currently have experimental efforts underway in the group to test whether a smaller coherence length also reduces the focussability of the beam at high powers, and hence its tendency to cause optical damage. In these measurements, the intensity statistics will be measured in both the image plane and the focal plane of the rubidium cell. Preliminary numerical simulations already show that the maximum intensity at the focal plane saturates as the laser power is increased due to a degradation of the beam quality when the added phase noise is very granular. A worsening beam quality at the focal spot at higher powers implies a reduced likelihood of optical damage at these powers. Hence, performing these followup measurements would directly inform future efforts towards the development of radiance limiters [39].

Bibliography

[1] Max Born and Emil Wolf. *Principles of optics: electromagnetic theory of propagation, interference and diffraction of light*. Elsevier, 2013.

[2] JJ Hopfield. "Theory of the contribution of excitons to the complex dielectric constant of crystals". In: *Physical Review* 112.5 (1958), p. 1555. URL: https://doi.org/10.1103/PhysRev.112.1555.

[3] Lukas Novotny and Bert Hecht. *Principles of nano-optics*. Cambridge university press, 2012. URL: https://doi.org/10.1017/CBO9780511794193.

[4] Robert W Boyd. *Nonlinear optics*. 4th ed. Academic press, 2020. URL: https://doi.org/10.1016/C2015-0-05510-1.

[5] Robert R Alfano and SL Shapiro. "Observation of self-phase modulation and small-scale filaments in crystals and glasses". In: *Physical Review Letters* 24.11 (1970), p. 592. URL: https://doi.org/10.1103/PhysRevLett.24.592.

[6] M Zahirul Alam et al. "Large optical nonlinearity of indium tin oxide in its epsilon-near-zero region". In: *Science* 0330.6287 (2016), pp. 0-5. URL: http://dx.doi.org/10.1126/science.aae0330%7B%5C%%7D5Cn.

[7] Orad Reshef et al. "Beyond the perturbative description of the nonlinear optical response of low-index materials". In: *Optics letters* 42.16 (2017), pp. 3225–3228. URL: https://doi.org/10.1364/OL.42.003225.

[8] Orad Reshef et al. "Nonlinear optical effects in epsilon-near-zero media". In: *Nature Reviews Materials* 4.8 (2019), pp. 535–551. URL: https://doi.org/10.1038/s41578-019-0120-5.

[9] Erwin Kretschmann. "The determination of the optical constants of metals by excitation of surface plasmons". In: *Zeitschrift für Physik A Hadrons and nuclei* 241 (1971), pp. 313–324.

[10] Heinz Raether. "Surface plasmons on smooth surfaces". In: *Surface plasmons on smooth and rough surfaces and on gratings*. Springer, 1988, pp. 4–39.

[11] Pierre Berini. "Long-range surface plasmon polaritons". In: *Advances in optics and photonics* 1.3 (2009), pp. 484–588. URL: https://doi.org/10.1364/AOP.1.000484.

[12] K Lance Kelly et al. "The optical properties of metal nanoparticles: the influence of size, shape, and dielectric environment". In: *The Journal of Physical Chemistry B* 107.3 (2003), pp. 668–677. URL: https://doi.org/10.1021/jp026731y.

[13] Eliza Hutter and Janos H Fendler. "Exploitation of localized surface plasmon resonance". In: *Advanced materials* 16.19 (2004), pp. 1685–1706. URL: https://doi.org/10.1002/adma.200400271.

[14] Julius Adams Stratton. *Electromagnetic theory*. Vol. 33. John Wiley & Sons, 2007.

[15] Craig F Bohren and Donald R Huffman. *Absorption and scattering of light by small particles*. John Wiley & Sons, 2008. URL: https://doi.org/10.1002/9783527618156.

[16] Esteban Moreno et al. "Multiple multipole method with automatic multipole setting applied to the simulation of surface plasmons in metallic nanostructures". In: *JOSA A* 19.1 (2002), pp. 101–111. URL: https://doi.org/10.1364/JOSAA.19.000101.

[17] Iñigo Liberal and Nader Engheta. "Near-zero refractive index photonics". In: *Nature Photonics* 11.3 (2017), pp. 149–158.

[18] Mark Fox. *Optical properties of solids*. 2002.

[19] Eyal Feigenbaum, Kenneth Diest, and Harry A Atwater. "Unity-order index change in transparent conducting oxides at visible frequencies". In: *Nano letters* 10.6 (2010), pp. 2111–2116. URL: https://doi.org/10.1021/nl1006307.

[20] Nick N Lepeshkin et al. "Enhanced nonlinear optical response of one-dimensional metal-dielectric photonic crystals". In: *Physical review letters* 93.12 (2004), p. 123902. URL: https://doi.org/10.1103/PhysRevLett.93.123902.

[21] RJ Pollard et al. "Optical nonlocalities and additional waves in epsilon-near-zero metamaterials". In: *Physical review letters* 102.12 (2009), p. 127405. URL: https://doi.org/10.1103/PhysRevLett.102.127405.

[22] Sisira Suresh et al. "Enhanced nonlinear optical responses of layered epsilon-near-zero metamaterials at visible frequencies". In: *Acs Photonics* 8.1 (2020), pp. 125–129. URL: https://doi.org/10.1021/acsphotonics.0c01178.

[23] Mário Silveirinha and Nader Engheta. "Tunneling of electromagnetic energy through subwavelength channels and bends using ε-near-zero materials". In: *Physical review letters* 97.15 (2006), p. 157403. URL: https://doi.org/10.1103/PhysRevLett.97.157403.

[24] Andrea Alu et al. "Epsilon-near-zero metamaterials and electromagnetic sources: Tailoring the radiation phase pattern". In: *Physical review B* 75.15 (2007), p. 155410. URL: https://doi.org/10.1103/PhysRevB.75.155410.

[25] Reehyang Kim et al. "Metal nanoparticle array as a tunable refractive index material over broad visible and infrared wavelengths". In: *ACS Photonics* 5.4 (2018), pp. 1188–1195. URL: https://doi.org/10.1021/acsphotonics.7b01497.

[26] Ting S Luk et al. "Directional perfect absorption using deep subwavelength low-permittivity films". In: *Physical Review B* 90.8 (2014), p. 085411. URL: https://doi.org/10.1103/PhysRevB.90.085411.

[27] Michaël Lobet et al. "Fundamental radiative processes in near-zero-index media of various dimensionalities". In: *ACS Photonics* 7.8 (2020), pp. 1965–1970. URL: https://doi.org/10.1021/acsphotonics.0c00782.

[28] Iñigo Liberal and Nader Engheta. "Manipulating thermal emission with spatially static fluctuating fields in arbitrarily shaped epsilon-near-zero bodies". In: *Proceedings of the National Academy of Sciences* 115.12 (2018), pp. 2878–2883. URL: https://doi.org/10.1073/pnas.1718264115.

[29] Ting S Luk et al. "Enhanced third harmonic generation from the epsilon-near-zero modes of ultrathin films". In: *App. Phys. Lett.* 106.15 (2015), p. 151103. URL: https://doi.org/10.1063/1.4917457.

[30] Antonio Capretti et al. “Comparative Study of Second-Harmonic Generation from Epsilon-Near-Zero Indium Tin Oxide and Titanium Nitride Nanolayers Excited in the Near-Infrared Spectral Range”. In: *ACS Photonics* 2.11 (2015). DOI: 10.1021/acsphotonics.5b00355, pp. 1584–1591.

[31] Antonio Capretti et al. “Enhanced third-harmonic generation in Si-compatible epsilon-near-zero indium tin oxide nanolayers”. In: *Optics letters* 40.7 (2015), pp. 1500–1503. URL: https://doi.org/10.1364/OL.40.001500.

[32] Matteo Clerici et al. “Controlling hybrid nonlinearities in transparent conducting oxides via two-colour excitation”. In: *Nature communications* 8.1 (2017), p. 15829. URL: https://doi.org/10.1038/ncomms15829.

[33] Yiyu Zhou et al. “Broadband frequency translation through time refraction in an epsilon-near-zero material”. In: *Nat. Comm.* 11.1 (Dec. 2020), p. 2180. URL: http://dx.doi.org/10.1038/s41467-020-15682-2.

[34] Wenhe Jia et al. “Broadband terahertz wave generation from an epsilon-near-zero material”. In: *Light: Science & Applications* 10.1 (2021), p. 11. URL: https://doi.org/10.1038/s41377-020-00452-y.

[35] Lucia Caspani et al. “Enhanced nonlinear refractive index in ϵ-near-zero materials”. In: *Phys. Rev. Lett.* 116.23 (2016), p. 233901. URL: https://doi.org/10.1103/PhysRevLett.116.233901.

[36] Haim Suchowski et al. “Phase mismatch–free nonlinear propagation in optical zero-index materials”. In: *Science* 342.6163 (2013), pp. 1223–1226. URL: https://doi.org/10.1126/science.1244303.

[37] Justin R Gagnon et al. “Relaxed phase-matching constraints in zero-index waveguides”. In: *Phys. Rev. Lett.* 128.20 (2022), p. 203902. URL: https://doi.org/10.1103/PhysRevLett.128.203902.

[38] Gadi Fibich and Alexander L Gaeta. “Critical power for self-focusing in bulk media and in hollow waveguides”. In: *Optics letters* 25.5 (2000), pp. 335–337. URL: https://doi.org/10.1364/OL.25.000335.

[39] A. Schweinsberg, J.W. Kuper, and R.W. Boyd. “Loss of spatial coherence and limiting of focal plane intensity by small-scale laser-beam filamentation”. In: *Phys. Rev. A* 84 (5 Nov. 2011), p. 053837. URL: https://link.aps.org/doi/10.1103/PhysRevA.84.053837.

[40] L Bergé et al. “Multiple filamentation of terawatt laser pulses in air”. In: *Physical Review Letters* 92.22 (2004), p. 225002. URL: https://doi.org/10.1103/PhysRevLett.92.225002.

[41] Petros Zerom and Robert W Boyd. “Self-focusing, conical emission, and other self-action effects in atomic vapors”. In: *Self-focusing: Past and Present: Fundamentals and Prospects*. Springer, 2009, pp. 231–251.

[42] PL Kelley. “Self-focusing of optical beams”. In: *Physical Review Letters* 15.26 (1965), p. 1005. URL: https://doi.org/10.1103/PhysRevLett.15.1005.

[43] Lukas Novotny. “Strong coupling, energy splitting, and level crossings: A classical perspective”. In: *Am. J. Phys.* 78.11 (2010), pp. 1199–1202. URL: https://doi.org/10.1119/1.3471177.

[44] Päivi Törmä and William L Barnes. “Strong coupling between surface plasmon polaritons and emitters: a review”. In: *Rep. Prog. Phys.* 78.1 (2014), p. 013901. URL: https://doi.org/10.1088/0034-4885/78/1/013901.

[45] V. M. Agranovich, M. Litinskaia, and D. G. Lidzey. “Cavity polaritons in microcavities containing disordered organic semiconductors”. In: *Phys. Rev. B* 67 (8 Feb. 2003), p. 085311. URL: https://doi.org/10.1103/PhysRevB.67.085311.

[46] Tomoyuki Yoshie et al. “Vacuum Rabi splitting with a single quantum dot in a photonic crystal nanocavity”. In: *Nature* 432.7014 (2004), pp. 200–203. URL: https://doi.org/10.1038/nature03119.

[47] J Pelal Reithmaier et al. “Strong coupling in a single quantum dot–semiconductor microcavity system”. In: *Nature* 432.7014 (2004), pp. 197–200. URL: https://doi.org/10.1038/nature02969.

[48] Ralf Ameling and Harald Giessen. “Cavity plasmonics: large normal mode splitting of electric and magnetic particle plasmons induced by a photonic microcavity”. In: *Nano Lett.* 10.11 (2010), pp. 4394–4398. URL: https://doi.org/10.1021/nl1019408.

[49] David J Shelton et al. “Strong coupling between nanoscale metamaterials and phonons”. In: *Nano Lett.* 11.5 (2011), pp. 2104–2108. URL: https://doi.org/10.1021/nl200689z.

[50] B Askenazi et al. "Ultra-strong light–matter coupling for designer Reststrahlen band". In: *New J. Phys.* 16.4 (2014), p. 043029. URL: https://doi.org/10.1088/1367-2630/16/4/043029.

[51] Daehan Yoo et al. "Ultrastrong plasmon–phonon coupling via epsilon-near-zero nanocavities". In: *Nat. Phot.* (2020). DOI: 10.1038/s41566-020-00731-5. URL: https://doi.org/10.1038/s41566-020-00731-5.

[52] Denis G Baranov et al. "Ultrastrong coupling between nanoparticle plasmons and cavity photons at ambient conditions". In: *Nat. Comm.* 11.1 (2020). DOI: 10.1038/s41467-020-16524-x. URL: https://doi.org/10.1038/s41467-020-16524-x.

[53] Kotni Santhosh et al. "Vacuum Rabi splitting in a plasmonic cavity at the single quantum emitter limit". In: *Nat. Comm.* 7.1 (2016), pp. 1–5. URL: https://doi.org/10.1038/ncomms11823.

[54] Haixu Leng et al. "Strong coupling and induced transparency at room temperature with single quantum dots and gap plasmons". In: *Nat. Comm.* 9.1 (2018), pp. 1–7. URL: https://doi.org/10.1038/s41467-018-06450-4.

[55] Pierre Berini. "Plasmon-polariton waves guided by thin lossy metal films of finite width: Bound modes of asymmetric structures". In: *Phys. Rev. B* 63.12 (2001). DOI: 10.1103/PhysRevB.63.125417. URL: https://doi.org/10.1103/PhysRevB.63.125417.

[56] Stefan A Maier. "Plasmonic field enhancement and SERS in the effective mode volume picture". In: *Opt. Exp.* 14.5 (2006). DOI: 10.1364/OE.14.001957, p. 1957. URL: https://doi.org/10.1364/OE.14.001957.

[57] Salvatore Campione, Igal Brener, and Francois Marquier. "Theory of epsilon-near-zero modes in ultrathin films". In: *Phys. Rev. B* 91.12 (2015). DOI: 10.1103/PhysRevB.91.121408, p. 121408. URL: https://journals.aps.org/prb/pdf/10.1103/PhysRevB.91.121408.

[58] Wenjun Wang et al. "Second harmonic generation investigation of indium tin oxide thin films". In: *Thin Solid Films* 365.1 (2000), pp. 116–118. URL: https://doi.org/10.1016/S0040-6090(00)00649-0.

[59] Yuanmu Yang et al. "High-harmonic generation from an epsilon-near-zero material". In: *Nat. Phys.* 15.10 (2019), pp. 1022–1026. URL: https://doi.org/10.1038/s41567-019-0584-7.

[60] Raktim Sarma et al. “Strong Coupling in All-Dielectric Intersubband Polaritonic Metasurfaces”. In: *Nano Lett.* (2020). DOI: 10.1021/acs.nanolett.0c03744. URL: https://dx.doi.org/10.1021/acs.nanolett.0c03744.

[61] Junhong Deng et al. “Giant enhancement of second-order nonlinearity of epsilon-near-zero medium by a plasmonic metasurface”. In: *Nano Lett.* 20.7 (2020), pp. 5421–5427. URL: https://doi.org/10.1021/acs.nanolett.0c01810.

[62] Young Chul Jun et al. “Epsilon-near-zero strong coupling in metamaterial-semiconductor hybrid structures”. In: *Nano Lett.* 13.11 (2013). DOI: 10.1021/nl402939t, pp. 5391–5396. URL: https://doi.org/10.1021/nl402939t.

[63] Salvatore Campione et al. “Near-infrared strong coupling between metamaterials and epsilon-near-zero modes in degenerately doped semiconductor nanolayers”. In: *ACS Photonics* 3.2 (2016), pp. 293–297. URL: https://doi.org/10.1021/acsphotonics.5b00663.

[64] M Zahirul Alam et al. “Large optical nonlinearity of nanoantennas coupled to an epsilon-near-zero material”. In: *Nature Photonics* 12.2 (2018), pp. 79–83. URL: https://doi.org/10.1038/s41566-017-0089-9.

[65] Kuidong Wang et al. “Large Optical Nonlinearity of Dielectric Nanocavity-Assisted Mie Resonances Strongly Coupled to an Epsilon-near-Zero Mode”. In: *Nano Lett.* 22.2 (2022), pp. 702–709. URL: https://doi.org/10.1021/acs.nanolett.1c03876.

[66] Nikolai Christian Passler et al. “Strong Coupling of Epsilon-Near-Zero Phonon Polaritons in Polar Dielectric Heterostructures”. In: *Nano Lett.* 18.7 (July 2018). DOI: 10.1021/acs.nanolett.8b01273, pp. 4285–4292.

[67] Evan L. Runnerstrom et al. “Polaritonic Hybrid-Epsilon-near-Zero Modes: Beating the Plasmonic Confinement vs Propagation-Length Trade-Off with Doped Cadmium Oxide Bilayers”. In: *Nano Lett.* 19.2 (2019). DOI: 10.1021/acs.nanolett.8b04182, pp. 948–957. URL: https://doi.org/10.1021/acs.nanolett.8b04182.

[68] P Forn-Díaz et al. “Ultrastrong coupling regimes of light-matter interaction”. In: *Rev. Mod. Phys.* 91.2 (2019). DOI: 10.1103/RevModPhys.91.025005. URL: https://doi.org/10.1103/RevModPhys.91.025005.

[69] Anton Frisk Kockum et al. “Ultrastrong coupling between light and matter”. In: *Nat. Rev. Phys.* 1.1 (2019). DOI: 10.1038/s42254-018-0006-2, pp. 19–40. URL: https://doi.org/10.1038/s42254-018-0006-2.

[70] Peter B Johnson and R-WJPrB Christy. “Optical constants of the noble metals”. In: *Physical review B* 6.12 (1972), p. 4370. URL: https://doi.org/10.1103/PhysRevB.6.4370.

[71] Aaron L Stancik and Eric B Brauns. “A simple asymmetric lineshape for fitting infrared absorption spectra”. In: *Vibrational Spectroscopy* 47.1 (2008). DOI: 10.1016/j.vibspec.2008.02.009, pp. 66–69.

[72] Domenico De Ceglia et al. “Viscoelastic optical nonlocality of low-loss epsilon-near-zero nanofilms”. In: *Sci. Rep.* 8.1 (2018), pp. 1–11. URL: https://doi.org/10.1038/s41598-018-27655-z.

[73] Yanko Todorov et al. “Ultrastrong light-matter coupling regime with polariton dots”. In: *Phys. Rev. Lett.* 105.19 (2010), p. 196402. URL: https://doi.org/10.1103/PhysRevLett.105.196402.

[74] Jennifer Anne Dionne. “Flatland photonics: circumventing diffraction with planar plasmonic architectures”. 162–174. PhD thesis. California Institute of Technology, 2009, pp. 162–174.

[75] William H Press et al. “Numerical recipes in C++”. In: *The art of scientific computing* 2 (1992), p. 1002.

[76] Simon Vassant et al. “Berreman mode and epsilon near zero mode”. In: *Opt. Exp.* 20.21 (2012), p. 23971. URL: https://doi.org/10.1364/OE.20.023971.

[77] Salvatore Campione et al. “Epsilon-near-zero modes for tailored light-matter interaction”. In: *Phys. Rev. Appl.* 4.4 (2015). DOI: 10.1103/PhysRevApplied.4.044011. URL: https://journals.aps.org/prapplied/pdf/10.1103/PhysRevApplied.4.044011.

[78] Evan L Runnerstrom et al. “Polaritonic Hybrid-Epsilon-near-Zero Modes: Beating the Plasmonic Confinement vs Propagation-Length Trade-Off with Doped Cadmium Oxide Bilayers”. In: *Nano Lett.* 19.2 (2019). DOI: 10.1021/acs.nanolett.8b04182, pp. 948–957.

[79] A Archambault et al. “Surface plasmon Fourier optics”. In: *Phys. Rev. B* 79.19 (2009). DOI: 10.1103/PhysRevB.79.195414. URL: https://doi.org/10.1103/PhysRevB.79.195414.

[80] Dipa Ghindani et al. “Gate Tunable Coupling of Epsilon-Near-Zero and Plasmonic Modes”. In: *Adv. Opt. Mater.* 9.22 (2021), p. 2100800. URL: https://doi.org/10.1002/adom.202100800.

[81] Kevin F MacDonald et al. “Ultrafast active plasmonics”. In: *Nat. Phot.* 3.1 (2009), pp. 55–58. URL: https://doi.org/10.1038/nphoton.2008.249.

[82] Cong Liu et al. “Photon Acceleration Using a Time-Varying Epsilon-near-Zero Metasurface”. In: *ACS Photonics* 8.3 (2021), pp. 716–720. URL: https://doi.org/10.1021/acsphotonics.0c01929.

[83] Kai Pang et al. “Adiabatic Frequency Conversion Using a Time-Varying Epsilon-Near-Zero Metasurface”. In: *Nano Lett.* 21.14 (2021), pp. 5907–5913. URL: https://doi.org/10.1021/acs.nanolett.1c00550.

[84] Astrid Lambrecht. “Electromagnetic pulses from an oscillating high-finesse cavity: possible signatures for dynamic Casimir effect experiments”. In: *J. Opt. B: Quantum Semiclassical Opt.* 7.3 (2005), S3. URL: https://doi.org/10.1088/1464-4266/7/3/001.

[85] Wenshan Cai et al. “Optical cloaking with metamaterials”. In: *Nature photonics* 1.4 (2007), pp. 224–227. URL: https://doi.org/10.1038/nphoton.2007.28.

[86] Xingjie Ni et al. “An ultrathin invisibility skin cloak for visible light”. In: *Science* 349.6254 (2015), pp. 1310–1314. URL: https://doi.org/10.1126/science.aac9411.

[87] Nanfang Yu et al. “Light propagation with phase discontinuities: generalized laws of reflection and refraction”. In: *Science* 334.6054 (2011), pp. 333–337. URL: https://doi.org/10.1126/science.1210713.

[88] Shulin Sun et al. “Gradient-index meta-surfaces as a bridge linking propagating waves and surface waves”. In: *Nature materials* 11.5 (2012), pp. 426–431. URL: https://doi.org/10.1038/nmat3292.

[89] Xingjie Ni, Alexander V Kildishev, and Vladimir M Shalaev. “Metasurface holograms for visible light”. In: *Nature communications* 4.1 (2013), pp. 1–6. URL: https://doi.org/10.1038/ncomms3807.

[90] Matthias W Klein et al. “Second-harmonic generation from magnetic metamaterials”. In: *Science* 313.5786 (2006), pp. 502–504. URL: https://doi.org/10.1126/science.1129198.

[91] Gregory A Wurtz et al. "Designed ultrafast optical nonlinearity in a plasmonic nanorod metamaterial enhanced by nonlocality". In: *Nature nanotechnology* 6.2 (2011), pp. 107–111. URL: https://doi.org/10.1038/nnano.2010.278.

[92] Martti Kauranen and Anatoly V Zayats. "Nonlinear plasmonics". In: *Nature photonics* 6.11 (2012), pp. 737–748. URL: https://doi.org/10.1038/nphoton.2012.244.

[93] Costas M Soukoulis and Martin Wegener. "Past achievements and future challenges in the development of three-dimensional photonic metamaterials". In: *Nature photonics* 5.9 (2011), pp. 523–530. URL: https://doi.org/10.1038/nphoton.2011.154.

[94] Nanfang Yu and Federico Capasso. "Flat optics with designer metasurfaces". In: *Nature materials* 13.2 (2014), pp. 139–150. URL: https://doi.org/10.1038/nmat3839.

[95] Nina Meinzer, William L Barnes, and Ian R Hooper. "Plasmonic meta-atoms and metasurfaces". In: *Nature photonics* 8.12 (2014), pp. 889–898. URL: https://doi.org/10.1038/nphoton.2014.247.

[96] Hui-Hsin Hsiao, Cheng Hung Chu, and Din Ping Tsai. "Fundamentals and applications of metasurfaces". In: *Small Methods* 1.4 (2017), p. 1600064. URL: https://doi.org/10.1002/smtd.201600064.

[97] Guixin Li, Shuang Zhang, and Thomas Zentgraf. "Nonlinear photonic metasurfaces". In: *Nature Reviews Materials* 2.5 (2017), pp. 1–14. URL: https://doi.org/10.1038/natrevmats.2017.10.

[98] Patrice Genevet et al. "Recent advances in planar optics: from plasmonic to dielectric metasurfaces". In: *Optica* 4.1 (2017), pp. 139–152. URL: https://doi.org/10.1364/OPTICA.4.000139.

[99] Vasyl G Kravets et al. "Plasmonic surface lattice resonances: a review of properties and applications". In: *Chemical reviews* 118.12 (2018), pp. 5912–5951. URL: https://doi.org/10.1021/acs.chemrev.8b00243.

[100] U. Kreibig and M. Vollmer. *Optical Properties of Metal Clusters*. Vol. 25. Berlin: Springer, 1995.

[101] P.K. Jain, W. Huang, and M. El-Sayed. "On the Universal Scaling Behavior of the Distance Decay of Plasmon Coupling in Metal Nanoparticle Pairs: A Plasmon Ruler Equation". In: *Nano Letters* 7.7 (2007), pp. 2080–2088. URL: http://dx.doi.org/10.1021/nl071008a.

[102] C. Dahmen, B. Schmidt, and G. von Plessen. "Radiation Damping in Metal Nanoparticle Pairs". In: *Nano Letters* 7.2 (2007), pp. 318–322. URL: http://dx.doi.org/10.1021/nl062377u.

[103] F. Hao et al. "Symmetry Breaking in Plasmonic Nanocavities: Subradiant LSPR Sensing and a Tunable Fano Resonance". In: *Nano Letters* 8.11 (2008). PMID: 18831572, pp. 3983–3988. URL: http://dx.doi.org/10.1021/nl802509r.

[104] Y. Sonnefraud et al. "Experimental Realization of Subradiant, Superradiant, and Fano Resonances in Ring/Disk Plasmonic Nanocavities". In: *ACS Nano* 4.3 (2010). PMID: 20155967, pp. 1664–1670. URL: http://dx.doi.org/10.1021/nn901580r.

[105] O. L. Muskens et al. "Optical scattering resonances of single and coupled dimer plasmonic nanoantennas". In: *Opt. Express* 15.26 (Dec. 2007), pp. 17736–17746. URL: http://www.opticsexpress.org/abstract.cfm?URI=oe-15-26-17736.

[106] P. Olk et al. "Distance Dependent Spectral Tuning of Two Coupled Metal Nanoparticles". In: *Nano Letters* 8.4 (2008), pp. 1174–1178.

[107] S. Linden et al. "Magnetic Response of Metamaterials at 100 Terahertz". In: *Science* 306.5700 (2004), pp. 1351–1353. URL: http://www.sciencemag.org/content/306/5700/1351.abstract.

[108] C. Rockstuhl et al. "Resonances of split-ring resonator metamaterials in the near infrared". English. In: *Applied Physics B* 84.1-2 (2006), pp. 219–227. URL: http://dx.doi.org/10.1007/s00340-006-2205-2.

[109] P. Lunnemann, I. Sersic, and A. F. Koenderink. "Optical properties of two-dimensional magnetoelectric point scattering lattices". In: *Phys. Rev. B* 88 (24 Dec. 2013), p. 245109. URL: http://link.aps.org/doi/10.1103/PhysRevB.88.245109.

[110] I. Sersic et al. "Electric and Magnetic Dipole Coupling in Near-Infrared Split-Ring Metamaterial Arrays". In: *Phys. Rev. Lett.* 103 (21 Nov. 2009), p. 213902. URL: http://link.aps.org/doi/10.1103/PhysRevLett.103.213902.

[111] M. Decker et al. "Retarded long-range interaction in split-ring-resonator square arrays". In: *Phys. Rev. B* 84 (8 Aug. 2011), p. 085416. URL: http://link.aps.org/doi/10.1103/PhysRevB.84.085416.

[112] B. S. Simpkins et al. "Pitch-dependent resonances and near-field coupling in infrared nanoantenna arrays". In: *Opt. Express* 20.25 (Dec. 2012), pp. 27725–27739. URL: http://www.opticsexpress.org/abstract.cfm?URI=oe-20-25-27725.

[113] R. Taubert et al. "From Near-Field to Far-Field Coupling in the Third Dimension: Retarded Interaction of Particle Plasmons". In: *Nano Letters* 11.10 (2011). PMID: 21879724, pp. 4421–4424. URL: http://dx.doi.org/10.1021/nl202606g.

[114] T. Iida. "Control of Plasmonic Superradiance in Metallic Nanoparticle Assembly by Light-Induced Force and Fluctuations". In: *The Journal of Physical Chemistry Letters* 3.3 (2012). PMID: 26285847, pp. 332–336. URL: http://dx.doi.org/10.1021/jz2014924.

[115] S. Tokonami et al. "Multipole Superradiance from Densely Assembled Metallic Nanoparticles". In: *The Journal of Physical Chemistry C* 117.29 (2013), pp. 15247–15252. URL: http://dx.doi.org/10.1021/jp4028244.

[116] M. Tamura et al. "Stochastic approach to simulation of evaporation-triggered multiple self-assembly of mixed metal nanoparticles and their variable superradiance". In: *Applied Physics Letters* 112.3 (2018), p. 033106.

[117] R. H. Dicke. "Coherence in Spontaneous Radiation Processes". In: *Phys. Rev.* 93 (1 Jan. 1954), pp. 99–110. URL: http://link.aps.org/doi/10.1103/PhysRev.93.99.

[118] N. E. Rehler and J. H. Eberly. "Superradiance". In: *Phys. Rev. A* 3 (5 May 1971), pp. 1735–1751. URL: http://link.aps.org/doi/10.1103/PhysRevA.3.1735.

[119] R. Bonifacio and L. A. Lugiato. "Cooperative radiation processes in two-level systems: Superfluorescence". In: *Phys. Rev. A* 11 (5 May 1975), pp. 1507–1521. URL: http://link.aps.org/doi/10.1103/PhysRevA.11.1507.

[120] M. Gross and S. Haroche. "Superradiance: An essay on the theory of collective spontaneous emission". In: *Physics Reports* 93.5 (1982), pp. 301–396. URL: http://www.sciencedirect.com/science/article/pii/0370157382901028.

[121] A. V. Andreev, V. I. Emel'yanov, and Y. A. Il'inski. "Collective spontaneous emission (Dicke superradiance)". In: *Soviet Physics Uspekhi* 23.8 (1980), p. 493. URL: http://stacks.iop.org/0038-5670/23/i=8/a=R04.

[122] N. Skribanowitz et al. "Observation of Dicke superradiance in optically pumped HF gas". In: *Phys. Rev. Lett.* 30 (8 Feb. 1973), pp. 309–312. URL: http://link.aps.org/doi/10.1103/PhysRevLett.30.309.

[123] M. Gross et al. "Observation of Near-Infrared Dicke Superradiance on Cascading Transitions in Atomic Sodium". In: *Phys. Rev. Lett.* 36 (17 Apr. 1976), pp. 1035–1038. URL: http://link.aps.org/doi/10.1103/PhysRevLett.36.1035.

[124] M. Gross et al. "Maser Oscillation and Microwave Superradiance in Small Systems of Rydberg Atoms". In: *Phys. Rev. Lett.* 43 (5 July 1979), pp. 343–346. URL: http://link.aps.org/doi/10.1103/PhysRevLett.43.343.

[125] S. Inouye et al. "Superradiant Rayleigh Scattering from a Bose-Einstein Condensate". In: *Science* 285.5427 (1999), pp. 571–574. URL: http://www.sciencemag.org/content/285/5427/571.abstract.

[126] R. G. DeVoe and R. G. Brewer. "Observation of Superradiant and Subradiant Spontaneous Emission of Two Trapped Ions". In: *Phys. Rev. Lett.* 76 (12 Mar. 1996), pp. 2049–2052. URL: http://link.aps.org/doi/10.1103/PhysRevLett.76.2049.

[127] J. A. Mlynek et al. "Observation of Dicke superradiance for two artificial atoms in a cavity with high decay rate". In: *Nat Commun* 5 (Nov. 2014). URL: http://dx.doi.org/10.1038/ncomms6186.

[128] M. O. Scully. "Collective Lamb Shift in Single Photon Dicke Superradiance". In: *Phys. Rev. Lett.* 102 (14 Apr. 2009), p. 143601. URL: http://link.aps.org/doi/10.1103/PhysRevLett.102.143601.

[129] A. Angerer et al. "Superradiant emission from colour centres in diamond". In: *Nature Physics* (2018), p. 1.

[130] K. M. Awan. "Fabrication of III-V Integrated Photonic Devices". PhD thesis. Université d'Ottawa/University of Ottawa, 2018.

[131] *Schott optical glass datasheets*. https://refractiveindex.info/download/data/2017/schott_2017-01-20.pdf. URL: https://refractiveindex.info/download/data/2017/schott_2017-01-20.pdf.

[132] M. Meier, P. F. Liao, and A. Wokaun. "Enhanced fields on rough surfaces: dipolar interactions among particles of sizes exceeding the Rayleigh limit". In: *J. Opt. Soc. Am. B* 2.6 (June 1985), pp. 931–949. URL: http://josab.osa.org/abstract.cfm?URI=josab-2-6-931.

[133] J.E. Sipe and J. Van Kranendonk. "Macroscopic electromagnetic theory of resonant dielectrics". In: *Physical Review A* 9.5 (1974), p. 1806.

[134] D. Tzarouchis and A. Sihvola. "Light scattering by a dielectric sphere: perspectives on the Mie resonances". In: *Applied Sciences* 8.2 (2018), p. 184.

[135] P. A. Belov and C. R. Simovski. "Homogenization of electromagnetic crystals formed by uniaxial resonant scatterers". In: *Phys. Rev. E* 72 (2 Aug. 2005), p. 026615. URL: http://link.aps.org/doi/10.1103/PhysRevE.72.026615.

[136] Sylvia D Swiecicki and JE Sipe. "Periodic Green functions for 2D magneto-electric quadrupolar arrays: explicitly satisfying the optical theorem". In: *Journal of Optics* 19.9 (2017), p. 095006.

[137] Aaron D Scher and Edward F Kuester. "Extracting the bulk effective parameters of a metamaterial via the scattering from a single planar array of particles". In: *Metamaterials* 3.1 (2009), pp. 44–55. URL: https://doi.org/10.1016/j.metmat.2009.02.001.

[138] S. Tretyakov. *Analytical modeling in applied electromagnetics*. Artech House, 2003.

[139] A. A. Svidzinsky, J. T. Chang, and M. O. Scully. "Cooperative spontaneous emission of N atoms: Many-body eigenstates, the effect of virtual Lamb shift processes, and analogy with radiation of N classical oscillators". In: *Physical Review A* 81.5 (2010), p. 053821.

[140] JH Eberly. "Emission of one photon in an electric dipole transition of one among N atoms". In: *Journal of Physics B: Atomic, Molecular and Optical Physics* 39.15 (2006), S599.

[141] J. Ruostekoski and J. Javanainen. "Quantum field theory of cooperative atom response: Low light intensity". In: *Physical Review A* 55.1 (1997), p. 513.

[142] H. Freedhoff and J. Van Kranendonk. "Theory of coherent resonant absorption and emission at infrared and optical frequencies". In: *Canadian Journal of Physics* 45.5 (1967), pp. 1833–1859.

[143] JE Sipe and J Van Kranendonk. "Energy band models for spatially dispersive dielectric media". In: *Canadian Journal of Physics* 53.19 (1975), pp. 2095–2122. URL: https://doi.org/10.1139/p75-260.

[144] Peter Nordlander et al. "Plasmon hybridization in nanoparticle dimers". In: *Nano letters* 4.5 (2004), pp. 899–903. URL: https://doi.org/10.1021/nl049681c.

[145] Alexandre Dmitriev et al. "Gold–silica–gold nanosandwiches: tunable bimodal plasmonic resonators". In: *Small* 3.2 (2007), pp. 294–299. URL: https://doi.org/10.1002/smll.200600409.

[146] Alison M Funston et al. "Plasmon coupling of gold nanorods at short distances and in different geometries". In: *Nano letters* 9.4 (2009), pp. 1651–1658. URL: https://doi.org/10.1021/nl900034v.

[147] Naomi J Halas et al. "Plasmons in strongly coupled metallic nanostructures". In: *Chemical reviews* 111.6 (2011), pp. 3913–3961. URL: https://doi.org/10.1021/cr200061k.

[148] DE Gómez et al. "The dark side of plasmonics". In: *Nano letters* 13.8 (2013), pp. 3722–3728. URL: https://doi.org/10.1021/nl401656e.

[149] Steven J Barrow et al. "Mapping bright and dark modes in gold nanoparticle chains using electron energy loss spectroscopy". In: *Nano letters* 14.7 (2014), pp. 3799–3808. URL: https://doi.org/10.1021/nl5009053.

[150] Yun-Chorng Chang et al. "Observation of absorption-dominated bonding dark plasmon mode from metal–insulator–metal nanodisk arrays fabricated by nanospherical-lens lithography". In: *ACS nano* 6.4 (2012), pp. 3390–3396. URL: https://doi.org/10.1021/nn300420x.

[151] MA Noginov et al. "Demonstration of a spaser-based nanolaser". In: *Nature* 460.7259 (2009), pp. 1110–1112. URL: https://doi.org/10.1038/nature08318.

[152] Rupert F Oulton et al. "Plasmon lasers at deep subwavelength scale". In: *Nature* 461.7264 (2009), pp. 629–632. URL: https://doi.org/10.1038/nature08364.

[153] Tavakol Pakizeh et al. "Magnetic-field enhancement in gold nanosandwiches". In: *Optics Express* 14.18 (2006), pp. 8240–8246. URL: https://doi.org/10.1364/OE.14.008240.

[154] Ruggero Verre et al. "Optical magnetism and plasmonic Fano resonances in metal–insulator–metal oligomers". In: *Nano letters* 15.3 (2015), pp. 1952–1958. URL: https://doi.org/10.1021/nl504802r.

[155] Michael B Ross, Chad A Mirkin, and George C Schatz. "Optical properties of one-, two-, and three-dimensional arrays of plasmonic nanostructures". In: *The journal of physical chemistry C* 120.2 (2016), pp. 816–830. URL: https://doi.org/10.1021/acs.jpcc.5b10800.

[156] Niclas S Mueller et al. "Dark interlayer plasmons in colloidal gold nanoparticle bi-and few-layers". In: *ACS photonics* 5.10 (2018), pp. 3962–3969. URL: https://doi.org/10.1021/acsphotonics.8b00898.

[157] Bruno GM Vieira et al. "Plasmonic properties of close-packed metallic nanoparticle mono-and bilayers". In: *The Journal of Physical Chemistry C* 123.29 (2019), pp. 17951–17960. URL: https://doi.org/10.1021/acs.jpcc.9b03859.

[158] Dominik Hoeing et al. "Dark plasmon modes for efficient hot electron generation in multilayers of gold nanoparticles". In: *Journal of Chemical Physics* 152.6 (Feb. 2020), p. 064710. URL: http://aip.scitation.org/doi/10.1063/1.5131696.

[159] Lukas Novotny. "Effective wavelength scaling for optical antennas". In: *Physical review letters* 98.26 (2007), p. 266802. URL: https://doi.org/10.1103/PhysRevLett.98.266802.

[160] Igor Zoric et al. "Gold, platinum, and aluminum nanodisk plasmons: material independence, subradiance, and damping mechanisms". In: *ACS nano* 5.4 (2011), pp. 2535–2546. URL: https://doi.org/10.1021/nn102166t.

[161] YD Chong et al. "Coherent perfect absorbers: time-reversed lasers". In: *Physical review letters* 105.5 (2010), p. 053901. URL: https://doi.org/10.1103/PhysRevLett.105.053901.

[162] Alex Krasnok and Andrea Alú. "Coherent control of light scattering". In: *arXiv preprint arXiv:1904.11384* (2019). URL: https://doi.org/10.48550/arXiv.1904.11384.

[163] Saumya Choudhary et al. "Weak superradiance in arrays of plasmonic nanoantennas". In: *Phys. Rev. A* 100 (4 Oct. 2019), p. 043814. URL: https://link.aps.org/doi/10.1103/PhysRevA.100.043814.

[164] André Christ et al. "Symmetry breaking in a plasmonic metamaterial at optical wavelength". In: *Nano letters* 8.8 (2008), pp. 2171–2175. URL: https://doi.org/10.1021/nl0805559.

[165] Alessandro Alabastri et al. "Extraordinary light-induced local angular momentum near metallic nanoparticles". In: *ACS nano* 10.4 (2016), pp. 4835–4846. URL: https://doi.org/10.1021/acsnano.6b01851.

[166] Mattin Urbieta et al. "Atomic-scale lightning rod effect in plasmonic picocavities: A classical view to a quantum effect". In: *ACS nano* 12.1 (2018), pp. 585–595. URL: https://doi.org/10.1021/acsnano.7b07401.

[167] Jianfa Zhang, Kevin F MacDonald, and Nikolay I Zheludev. "Controlling light-with-light without nonlinearity". In: *Light: Science & Applications* 1.7 (2012), e18–e18. URL: https://doi.org/10.1038/lsa.2012.18.

[168] Wei Tan et al. "Selective coherent perfect absorption of subradiant mode in ultrathin bi-layer metamaterials via antisymmetric excitation". In: *Applied Physics Letters* 110.18 (2017), p. 181111. URL: https://doi.org/10.1063/1.4983087.

[169] Rasoul Alaee, Mohammad Albooyeh, and Carsten Rockstuhl. "Theory of metasurface based perfect absorbers". In: *Journal of Physics D: Applied Physics* 50.50 (2017), p. 503002. URL: https://doi.org/10.1088/1361-6463/aa94a8.

[170] Wenjie Wan et al. "Time-reversed lasing and interferometric control of absorption". In: *Science* 331.6019 (2011), pp. 889–892. URL: https://doi.org/10.1126/science.1200735.

[171] Denis G Baranov et al. "Coherent perfect absorbers: linear control of light with light". In: *Nature Reviews Materials* 2.12 (2017), pp. 1–14. URL: https://doi.org/10.1038/natrevmats.2017.64.

[172] John David Jackson. *Classical electrodynamics*. American Association of Physics Teachers, 1999.

[173] Francesco Andreoli et al. "Maximum refractive index of an atomic medium". In: *Physical Review X* 11.1 (2021), p. 011026. URL: https://doi.org/10.1103/PhysRevX.11.011026.

[174] Claude Cohen-Tannoudji, Jacques Dupont-Roc, and Gilbert Grynberg. *Atom-photon interactions: basic processes and applications*. John Wiley & Sons, 1998.

[175] G Smestad et al. "The thermodynamic limits of light concentrators". In: *Solar Energy Materials* 21.2-3 (1990), pp. 99–111. URL: https://doi.org/10.1016/0165-1633(90)90047-5.

[176] John H Burnett et al. "High-index optical materials for 193nm immersion lithography". In: *Optical Microlithography XIX* 6154 (2006), pp. 445–456. URL: https://doi.org/10.1117/12.656901.

[177] Ksenia Dolgaleva, Robert W Boyd, and Peter W Milonni. "Influence of local-field effects on the radiative lifetime of liquid suspensions of Nd: YAG nanoparticles". In: *JOSA B* 24.3 (2007), pp. 516–521. URL: https://doi.org/10.1364/JOSAB.24.000516.

[178] David R Smith, John B Pendry, and Mike CK Wiltshire. "Metamaterials and negative refractive index". In: *science* 305.5685 (2004), pp. 788–792.

[179] DR McKenzie and RC McPhedran. "Exact modelling of cubic lattice permittivity and conductivity". In: *Nature* 265.5590 (1977), pp. 128–129. URL: https://doi.org/10.1038/265128a0.

[180] Xingzhan Wei et al. "A high refractive index metamaterial at visible frequencies formed by stacked cut-wire plasmonic structures". In: *Applied Physics Letters* 97.1 (2010). URL: https://doi.org/10.1063/1.3453477.

[181] Seungwoo Lee. "Colloidal superlattices for unnaturally high-index metamaterials at broadband optical frequencies". In: *Optics Express* 23.22 (2015), pp. 28170–28181. URL: https://doi.org/10.1364/OE.23.028170.

[182] Taeyong Chang et al. "Broadband giant-refractive-index material based on mesoscopic space-filling curves". In: *Nature communications* 7.1 (2016), p. 12661. URL: https://doi.org/10.1038/ncomms12661.

[183] Ji-Hyeok Huh, Jaewon Lee, and Seungwoo Lee. "Soft plasmonic assemblies exhibiting unnaturally high refractive index". In: *Nano Letters* 20.7 (2020), pp. 4768–4774. URL: https://doi.org/10.1021/acs.nanolett.0c00422.

[184] Bin Lu et al. "Tunable Subnanometer Gaps in Self-Assembled Monolayer Gold Nanoparticle Superlattices Enabling Strong Plasmonic Field Confinement". In: *ACS nano* 13.17 (2023), pp. 12774–12787. URL: https://doi.org/10.1021/acsnano.3c03804.

[185] Niclas S Mueller et al. "Deep strong light–matter coupling in plasmonic nanoparticle crystals". In: *Nature* 583.7818 (2020), pp. 780–784. URL: https://doi.org/10.1038/s41586-020-2508-1.

[186] Richard Taubert et al. "Octave-wide photonic band gap in three-dimensional plasmonic Bragg structures and limitations of radiative coupling". In: *Nature communications* 3.1 (2012), p. 691. URL: https://doi.org/10.1038/ncomms1694.

[187] Vadim A Markel. "Introduction to the Maxwell Garnett approximation: tutorial". In: *JOSA A* 33.7 (2016), pp. 1244–1256. URL: https://doi.org/10.1364/JOSAA.33.001244.

[188] Lin Sun et al. "Design principles for photonic crystals based on plasmonic nanoparticle superlattices". In: *Proceedings of the National Academy of Sciences* 115.28 (2018), pp. 7242–7247. URL: https://doi.org/10.1073/pnas.1800106115.

[189] Danielle Ben-Haim and Tal Ellenbogen. "Optical Anomalies due to Volume Collective Modes of Plasmonic Metamaterials". In: *Laser & Photonics Reviews* 17.4 (2023), p. 2200671. URL: https://doi.org/10.1002/lpor.202200671.

[190] Michael B Ross et al. "Defect tolerance and the effect of structural inhomogeneity in plasmonic DNA-nanoparticle superlattices". In: *Proceedings of the National Academy of Sciences* 112.33 (2015), pp. 10292–10297.

[191] GD Mahan and Gustav Obermair. "Polaritons at surfaces". In: *Physical Review* 183.3 (1969), p. 834. URL: https://doi.org/10.1103/PhysRev.183.834.

[192] Michael R Philpott. "Effect of spatial dispersion on the S-polarized optical properties of a slab dielectric". In: *The Journal of Chemical Physics* 60.6 (1974), pp. 2520–2529. URL: https://doi.org/10.1063/1.1681392.

[193] Hsiao-Kuan Yuan et al. "A negative permeability material at red light". In: *Optics Express* 15.3 (2007), pp. 1076–1083. URL: https://doi.org/10.1364/OE.15.001076.

[194] Saumya Choudhary, Robert W. Boyd, and J. E. Sipe. "Dark and bright modes, and their coherent control in dipolar metasurface bilayers". In: *Phys. Rev. A* 107 (2 Feb. 2023), p. 023521. URL: https://link.aps.org/doi/10.1103/PhysRevA.107.023521.

[195] Alexander Poddubny et al. "Hyperbolic metamaterials". In: *Nature photonics* 7.12 (2013), pp. 948–957. URL: https://doi.org/10.1038/nphoton.2013.243.

[196] SI Pekar. "The theory of electromagnetic waves in a crystal in which excitons are produced". In: *Sov. Phys. JETP* 6.33 (1958), p. 4.

[197] Jun Guan et al. "Far-field coupling between moiré photonic lattices". In: *Nature nanotechnology* (2023), pp. 1–7. URL: https://doi.org/10.1038/s41565-023-01320-7.

[198] Amit M Lakhani et al. "Plasmonic crystal defect nanolaser". In: *Optics Express* 19.19 (2011), pp. 18237–18245. URL: https://doi.org/10.1364/OE.19.018237.

[199] Hikaru Saito et al. "Emergence of point defect states in a plasmonic crystal". In: *Physical Review B* 100.24 (2019), p. 245402. URL: https://doi.org/10.1103/PhysRevB.100.245402.

[200] Susumu Noda, Masayuki Fujita, and Takashi Asano. "Spontaneous-emission control by photonic crystals and nanocavities". In: *Nature photonics* 1.8 (2007), pp. 449–458. URL: https://doi.org/10.1038/nphoton.2007.141.

[201] Aleksandr Vaskin et al. "Light-emitting metasurfaces". In: *Nanophotonics* 8.7 (2019), pp. 1151–1198. URL: https://doi.org/10.1515/nanoph-2019-0110.

[202] Wei Zhou et al. "Lasing action in strongly coupled plasmonic nanocavity arrays". In: *Nature nanotechnology* 8.7 (2013), pp. 506–511. URL: https://doi.org/10.1038/nnano.2013.99.

[203] A Hinke Schokker and A Femius Koenderink. "Lasing at the band edges of plasmonic lattices". In: *Physical Review B* 90.15 (2014), p. 155452. URL: https://doi.org/10.1103/PhysRevB.90.155452.

[204] Oluwafemi S Ojambati et al. "Quantum electrodynamics at room temperature coupling a single vibrating molecule with a plasmonic nanocavity". In: *Nature communications* 10.1 (2019), p. 1049. URL: https://doi.org/10.1038/s41467-019-08611-5.

[205] Muamer Kadic et al. “3D metamaterials”. In: *Nature Reviews Physics* 1.3 (2019), pp. 198–210. URL: https://doi.org/10.1038/s42254-018-0018-y.

[206] Na Liu et al. “Three-dimensional photonic metamaterials at optical frequencies”. In: *Nature materials* 7.1 (2008), pp. 31–37. URL: https://doi.org/10.1038/nmat2072.

[207] Dmitri V Talapin. “LEGO materials”. In: *Acs Nano* 2.6 (2008), pp. 1097–1100. URL: https://doi.org/10.1021/nn8003179.

[208] Andrea R Tao et al. “Self-organized silver nanoparticles for three-dimensional plasmonic crystals”. In: *Nano letters* 8.11 (2008), pp. 4033–4038. URL: https://doi.org/10.1021/nl802877h.

[209] Angang Dong et al. “Binary nanocrystal superlattice membranes self-assembled at the liquid–air interface”. In: *Nature* 466.7305 (2010), pp. 474–477. URL: https://doi.org/10.1038/nature09188.

[210] Michael A Boles, Michael Engel, and Dmitri V Talapin. “Self-assembly of colloidal nanocrystals: From intricate structures to functional materials”. In: *Chemical reviews* 116.18 (2016), pp. 11220–11289. URL: https://doi.org/10.1021/acs.chemrev.6b00196.

[211] Shawn J Tan et al. “Building plasmonic nanostructures with DNA”. In: *Nature nanotechnology* 6.5 (2011), pp. 268–276. URL: https://doi.org/10.1038/nnano.2011.49.

[212] Martin Mayer et al. “Colloidal Self-Assembly Concepts for Plasmonic Metasurfaces”. In: *Advanced Optical Materials* 7.1 (2019), p. 1800564. URL: https://doi.org/10.1002/adom.201800564.

[213] Sung Yong Park et al. “DNA-programmable nanoparticle crystallization”. In: *Nature* 451.7178 (2008), pp. 553–556. URL: https://doi.org/10.1038/nature06508.

[214] Dmytro Nykypanchuk et al. “DNA-guided crystallization of colloidal nanoparticles”. In: *Nature* 451.7178 (2008), pp. 549–552.

[215] Jaswinder Sharma et al. “DNA-templated self-assembly of two-dimensional and periodical gold nanoparticle arrays”. In: *Angewandte Chemie* 118.5 (2006), pp. 744–749. URL: https://doi.org/10.1002/ange.200503208.

[216] Karen Geisel, Walter Richtering, and Lucio Isa. "Highly ordered 2D microgel arrays: compression versus self-assembly". In: *Soft Matter* 10.40 (2014), pp. 7968–7976.

[217] Liping Song et al. "Instant interfacial self-assembly for homogeneous nanoparticle monolayer enabled conformal "lift-on" thin film technology". In: *Science Advances* 7.52 (2021), eabk2852.

[218] D R Solli et al. "Optical rogue waves". In: *Nature* 450.7172 (2007), pp. 1054–1057. URL: https://doi.org/10.1038/nature06402.

[219] Changxu Liu et al. "Triggering extreme events at the nanoscale in photonic seas". In: *Nature Physics* 11.4 (2015), pp. 358–363. URL: https://doi.org/10.1038/nphys3263.

[220] Amaury Mathis et al. "Caustics and rogue waves in an optical sea". In: *Sci. Rep.* 5 (Aug. 2015). URL: https://doi.org/10.1038/srep12822.

[221] D Pierangeli et al. "Spatial rogue waves in photorefractive ferroelectrics". In: *Phys. Rev. Lett.* 115.9 (2015), p. 093901. URL: https://doi.org/10.1103/PhysRevLett.115.093901.

[222] D Pierangeli et al. "Enhancing optical extreme events through input wave disorder". In: *Phys. Rev. A* 94.6 (2016), p. 063833. URL: https://doi.org/10.1103/PhysRevA.94.063833.

[223] Akbar Safari et al. "Generation of Caustics and Rogue Waves from Nonlinear Instability". In: *Phys. Rev. Lett.* 119.20 (2017), pp. 1–5. URL: https://doi.org/10.1103/PhysRevLett.119.203901.

[224] R Höhmann et al. "Freak waves in the linear regime: A microwave study". In: *Phys. Rev. Lett.* 104.9 (2010), p. 093901. URL: https://doi.org/10.1103/PhysRevLett.104.093901.

[225] Henri Degueldre et al. "Random focusing of tsunami waves". In: *Nat. Phys.* 12.3 (2016), pp. 259–262. URL: https://doi.org/10.1038/nphys3557.

[226] Miguel Onorato et al. "Rogue waves and their generating mechanisms in different physical contexts". In: *Physics Reports* 528.2 (2013), pp. 47–89. URL: https://doi.org/10.1016/j.physrep.2013.03.001.

[227] John M Dudley et al. "Instabilities, breathers and rogue waves in optics". In: *Nat. Phot.* 8.10 (2014), pp. 755–764. URL: https://doi.org/10.1038/nphoton.2014.220.

[228] John M Dudley et al. "Rogue waves and analogies in optics and oceanography". In: *Nat. Rev. Phys.* 1.11 (2019), pp. 675–689. URL: https://doi.org/10.1038/s42254-019-0100-0.

[229] G Parry et al. "Focussing by a random phase screen". In: *Optics Communications* 22.2 (1977), pp. 195–201. URL: https://doi.org/10.1016/0030-4018(77)90018-9.

[230] Michael Selwyn Longuet-Higgins. "The statistical analysis of a random, moving surface". In: *Philosophical Transactions of the Royal Society of London. Series A, Mathematical and Physical Sciences* 249.966 (1957), pp. 321–387. URL: https://doi.org/10.1098/rsta.1957.0002.

[231] Christophe Fochesato, Stéphan Grilli, and Frédéric Dias. "Numerical modeling of extreme rogue waves generated by directional energy focusing". In: *Wave motion* 44.5 (2007), pp. 395–416. URL: https://doi.org/10.1016/j.wavemoti.2007.01.003.

[232] Joseph W Goodman. "Some fundamental properties of speckle". In: *J. Opt. Soc. Am.* 66.11 (1976), pp. 1145–1150. URL: https://doi.org/10.1364/JOSA.66.001145.

[233] Th M Nieuwenhuizen and MCW Van Rossum. "Intensity distributions of waves transmitted through a multiple scattering medium". In: *Phys. Rev. Lett.* 74.14 (1995), p. 2674. URL: https://doi.org/10.1103/PhysRevLett.74.2674.

[234] F T Arecchi et al. "Granularity and inhomogeneity are the joint generators of optical rogue waves". In: *Phys. Rev. Lett.* 106.15 (2011). URL: https://doi.org/10.1103/PhysRevLett.106.153901.

[235] Yaron Bromberg and Hui Cao. "Generating non-Rayleigh speckles with tailored intensity statistics". In: *Phys. Rev. Lett.* 112.21 (2014), p. 213904. URL: https://doi.org/10.1103/PhysRevLett.112.213904.

[236] Pierre Walczak, Stéphane Randoux, and Pierre Suret. "Optical rogue waves in integrable turbulence". In: *Phys. Rev. Lett.* 114.14 (2015), p. 143903. URL: https://doi.org/10.1103/PhysRevLett.114.143903.

[237] Mikko Närhi et al. "Real-time measurements of spontaneous breathers and rogue wave events in optical fibre modulation instability". In: *Nat. Comm.* 7.1 (2016), pp. 1–9. URL: https://doi.org/10.1038/ncomms13675.

[238] Miguel Onorato, Alfred Richard Osborne, and Mariana Serio. "Modulational instability in crossing sea states: A possible mechanism for the formation of freak waves". In: *Phys. Rev. Lett.* 96.1 (2006), p. 014503. URL: https://doi.org/10.1103/PhysRevLett.96.014503.

[239] A Montina et al. "Non-Gaussian statistics and extreme waves in a nonlinear optical cavity". In: *Phys. Rev. Lett.* 103.17 (2009). URL: https://doi.org/10.1103/PhysRevLett.103.173901.

[240] Simon Birkholz et al. "Spatiotemporal rogue events in optical multiple filamentation". In: *Phys. Rev. Lett.* 111.24 (2013), p. 243903. URL: https://doi.org/10.1103/PhysRevLett.111.243903.

[241] A. Nicholas Black et al. "Suppression of Nonlinear Optical Rogue Wave Formation Using Polarization-Structured Beams". In: *Phys. Rev. Lett.* 129 (13 Sept. 2022), p. 133902. URL: https://link.aps.org/doi/10.1103/PhysRevLett.129.133902.

[242] Alessandro Zannotti, Daniel Ehrmanntraut, and Cornelia Denz. "Enhanced optical rogue waves by scattering caustic networks in tailored disorder". In: *Nonlinear Optics*. Optical Society of America. 2019, NW3B–2. URL: https://doi.org/10.1364/NLO.2019.NW3B.2.

[243] Tomohiro Shirai, Olga Korotkova, and Emil Wolf. "A method of generating electromagnetic Gaussian Schell-model beams". In: *Journal of Optics A: Pure and Applied Optics* 7.5 (2005), p. 232. URL: https://doi.org/10.1088/1464-4258/7/5/004.

[244] W. Weibull. "A statistical distribution function of wide applicability". In: *J. Appl. Mech.* 18 (1951), pp. 293–297. URL: https://cir.nii.ac.jp/crid/1571980074030266112.

[245] Joseph W Goodman. *Speckle phenomena in optics: theory and applications*. Roberts and Company Publishers, 2007. URL: https://spie.org/Publications/Book/2548482?SSO=1.

[246] Eo Jakeman. "Speckle statistics with a small number of scatterers". In: *Optical Engineering* 23.4 (1984), pp. 453–461. URL: https://doi.org/10.1117/12.7973317.

[247] Duc Minh Nguyen et al. "Incoherent resonant seeding of modulation instability in optical fiber". In: *Optics letters* 38.24 (2013), pp. 5338–5341. URL: https://doi.org/10.1364/OL.38.005338.

[248] Govind Agrawal. *Nonlinear Fiber Optics*. 5th ed. Academic Press, 2013. URL: https://www.elsevier.com/books/nonlinear-fiber-optics/agrawal/978-0-12-397023-7.

[249] Joseph W. Goodman. *Introduction to Fourier optics*. 3rd ed. Roberts & Co., 2005. URL: https://www.macmillanlearning.com/college/us/product/Introduction-to-Fourier-Optics/p/1319119166.

[250] Dieter Suter and Tilo Blasberg. "Stabilization of transverse solitary waves by a nonlocal response of the nonlinear medium". In: *Phys. Rev. A* 48.6 (1993), p. 4583. URL: https://doi.org/10.1103/PhysRevA.48.4583.

[251] MDand Feit and JA Fleck. "Beam nonparaxiality, filament formation, and beam breakup in the self-focusing of optical beams". In: *J. Opt. Soc. Am. B* 5.3 (1988), pp. 633–640. URL: https://doi.org/10.1364/JOSAB.5.000633.

[252] Larry C Andrews et al. "Theory of optical scintillation". In: *JOSA A* 16.6 (1999), pp. 1417–1429. URL: https://doi.org/10.1364/JOSAA.16.001417.

[253] Sonja Barkhofen et al. "Experimental observation of a fundamental length scale of waves in random media". In: *Physical Review Letters* 111.18 (2013), p. 183902. URL: https://doi.org/10.1103/PhysRevLett.111.183902.

[254] Anatoly Patsyk et al. "Observation of branched flow of light". In: *Nature* 583.7814 (2020), pp. 60–65. URL: https://doi.org/10.1038/s41586-020-2376-8.

[255] Greg Gbur. "Partially coherent beam propagation in atmospheric turbulence [Invited]". In: *J. Opt. Soc. Am. A* 31.9 (2014), p. 2038. URL: http://dx.doi.org/10.1364/JOSAA.31.002038.

[256] Mitchell A Cox et al. "Structured light in turbulence". In: *IEEE Journal of Selected Topics in Quantum Electronics* 27.2 (2020), pp. 1–21. URL: https://doi.org/10.1109/JSTQE.2020.3023790.

[257] Richard J Watkins et al. "Experimental probing of turbulence using a continuous spectrum of asymmetric OAM beams". In: *Opt. Exp.* 28.2 (2020), pp. 924–935. URL: https://doi.org/10.1364/OE.380405.

[258] H. Kuwata et al. "Resonant light scattering from metal nanoparticles: Practical analysis beyond Rayleigh approximation". In: *Applied physics letters* 83.22 (2003), pp. 4625–4627.

[259] S. Zou, N. Janel, and G. C. Schatz. "Silver nanoparticle array structures that produce remarkably narrow plasmon lineshapes". In: *The Journal of Chemical Physics* 120.23 (2004), pp. 10871–10875. URL: http://scitation.aip.org/content/aip/journal/jcp/120/23/10.1063/1.1760740.

[260] Jarkko J Saarinen and JE Sipe. "A Green function approach to surface optics in anisotropic media". In: *Journal of Modern Optics* 55.1 (2008), pp. 13–32. URL: https://doi.org/10.1080/09500340701248383.

[261] Akbar Safari. "Resonant Light-Matter Interaction for Enhanced Control of Exotic Propagation of Light". PhD thesis. Université d'Ottawa/University of Ottawa, 2019. URL: http://dx.doi.org/10.20381/ruor-23306.

[262] Daniel A Steck. "Rubidium 85 and 87 d line data". In: *http://steck. us/alkalidata. Revision* 2.2 (2009), p. 12.

[263] Rodney Loudon. *The quantum theory of light*. 3rd ed. OUP Oxford, 2000. URL: https://global.oup.com/academic/product/the-quantum-theory-of-light-9780198501763?cc=us%5C&lang=en%5C&.

[264] Paul Siddons et al. "Absolute absorption on rubidium D lines: comparison between theory and experiment". In: *Journal of Physics B: Atomic, Molecular and Optical Physics* 41.15 (2008), p. 155004. URL: https://doi.org/10.1088/0953-4075/41/15/155004.

A. Supplementary Materials for Chapter 2

A.1 Permittivity of indium tin oxide used in the bifilm samples

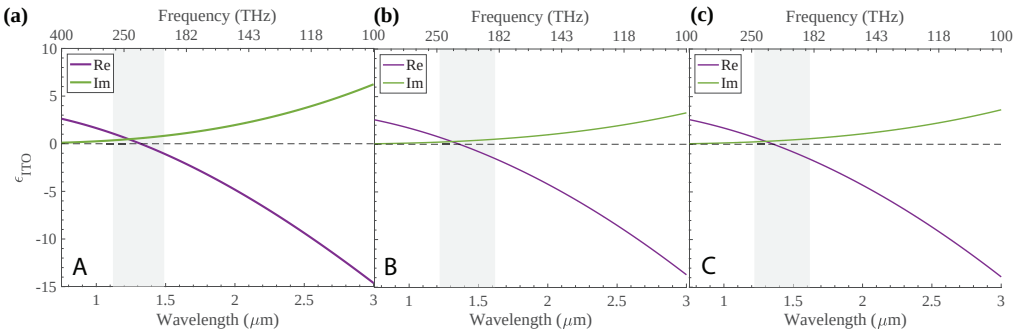

Figure A.1: Spectra of the real (purple) and the imaginary (green) parts of the permittivity of ITO in bifilm samples (a) A, (b) B and (c) C, respectively. The gray region denotes the ENZ spectral region.

Figure A.1 shows the spectra of the real (purple) and the imaginary (green) parts of the permittivies of the ITO samples used in bifilms A (a), B (b) and C (c), respectively. The Re$[\varepsilon]$ approaches zero at a frequency (wavelength) of 227.79 THz (1.317 μm) for sample A, 220.08 THz (1.363 μm) for sample B, and 220.94 THz (1.357 μm) for sample C.

A.2 The Analytical Dispersion Model for Polaritons

We follow the method described in the appendix B of Ref. [74] to analytically model the dispersion relations of the hybrid polaritons from which we also calculate the field profiles, the mode confinement, field enhancement and the damping and propagation lengths in the absence of radiative losses. In our coordinate system, shown in the inset of Figure 1(c) of the main text, the polaritons propagate parallel to the interfaces of the layered films, which we assume to be aligned along the x-axis. The films themselves are arranged along the z-axis with the substrate-ITO interface located at $z = 0$, the ITO-gold interface at $z = d_{\mathrm{ITO}}$, and the gold-prism interface at $z = d_{\mathrm{ITO}} + 50$ nm.The TM-polarized guided solutions in each layer of this multi-layered plasmonic structure are evanescent wave-like, and can be written as

$$E_{xl} = e^{ik_x x}(a_l e^{k_{zl} z} + b_l e^{-k_{zl} z}), \tag{A.1}$$

$$E_{zl} = \left(\frac{ik_x}{k_{zl}}\right) e^{ik_x x}(-a_l e^{k_{zl} z} + b_l e^{-k_{zl} z}), \tag{A.2}$$

$$E_y = 0, \tag{A.3}$$

where $l = \{s, i, a, p\}$ is the index for the substrate, ITO, gold and prism layers, respectively, in this multi-layered structure; k_x is the transverse wavevector; a_l and b_l are the coefficients of the forward and backward propagating solutions within the layer that are determined by the field continuity relations, and k_{zl} is the longitudinal wavevector given by

$$k_{zl}^2 = k_x^2 - \left(\frac{\omega}{c}\right)^2 \varepsilon_l, \tag{A.4}$$

with ε_l being the permittivity of the layer l. The continuity of E_{xl} and $D_{zl} (= \varepsilon_l E_{zl})$ at each interface leads to a set of 8 linear homogeneous equations for the 8 field coefficients $C^T = \{a_s, b_s, a_i, b_i, a_a, b_a, a_p, b_p\}$ at each k_x. In matrix form, the set of equations can be written as

$$LC = 0, \tag{A.5}$$

where L is given by

$$L = \begin{bmatrix} 0 & 1 & 0 & 0 & 0 & 0 & 0 & 0 \\ 1 & 1 & -1 & -1 & 0 & 0 & 0 & 0 \\ -\varepsilon_p k_{za} & \varepsilon_p k_{za} & \varepsilon_a k_{zp} & -\varepsilon_a k_{zp} & 0 & 0 & 0 & 0 \\ 0 & 0 & e^{k_{za} d_{\mathrm{Au}}} & e^{-k_{za} d_{\mathrm{Au}}} & -e^{k_{zi} d_{\mathrm{Au}}} & -e^{-k_{zi} d_{\mathrm{Au}}} & 0 & 0 \\ 0 & 0 & -\varepsilon_a k_{zi} e^{k_{za} d_{\mathrm{Au}}} & \varepsilon_a k_{zi} e^{-k_{za} d_{\mathrm{Au}}} & \varepsilon_i k_{za} e^{k_{zi} d_{\mathrm{Au}}} & -\varepsilon_i k_{za} e^{-k_{zi} d_{\mathrm{Au}}} & 0 & 0 \\ 0 & 0 & 0 & 0 & e^{k_{zi} d_{\mathrm{Au,ITO}}} & e^{-k_{zi} T_{\mathrm{Au,ITO}}} & -e^{k_{zs} d_{\mathrm{Au,ITO}}} & -e^{-k_{zs} d_{\mathrm{Au,ITO}}} \\ 0 & 0 & 0 & 0 & -\varepsilon_i k_{zs} e^{k_{zi} d_{\mathrm{Au,ITO}}} & \varepsilon_i k_{zs} e^{-k_{zi} d_{\mathrm{Au,ITO}}} & \varepsilon_s k_{zi} e^{k_{zs} d_{\mathrm{Au,ITO}}} & -\varepsilon_s k_{zi} e^{-k_{zs} d_{\mathrm{Au,ITO}}} \\ 0 & 0 & 0 & 0 & 0 & 0 & 1 & 0 \end{bmatrix}, \tag{A.6}$$

with $d_{\mathrm{Au,ITO}} = d_{\mathrm{Au}} + d_{\mathrm{ITO}}$, and d_{Au} is the thickness of the gold layer (fixed at 50 nm throughout). A non-trivial solution of the equation (A.6) exists only when $|\det(\mathrm{L})| = 0$, which gives the characteristic equation of the bifilm. One can also obtain the characteristic equation, and the dispersion lines by searching for the poles of the reflection coefficient of the bifilm [3]. To obtain the dispersion lines of the structure, we work in either the complex frequency $\tilde{\omega}$ and real transverse wavevector $\mathrm{Re}[k_x]$ space, or in the real frequency ω and complex wavevector k_x space, and search for the minima of $|\det(L)|$. We use the former solution space for the calculation of mode profiles, field enhancement and mode confinement, and the latter for the calculation of the propagation lengths of the hybrid polaritons. In both scenarios, we first find the minima of $|\det(L)|$ for real frequency ω and $\mathrm{Re}[k_x]$ for the situation where we ignore the losses in both the gold and the ITO layer by using only the real part of their permittivities in the $|\det(L)|$ function. We then use these $\{\omega, \mathrm{Re}[k_x]\}$ solutions as the initial conditions while searching for the minima of $|\det(L)|$ in the $\{\tilde{\omega}, \mathrm{Re}[k_x]\}$ space or the $\{\omega, k_x\}$ space, for which we use the Nelder-Mead method [74]. We use MATLAB for all these calculations, and its built-in function `fminsearch` for the minima search.

Figure A.2 compares the dispersion lines (real frequency and wavevector) of bifilm A calculated by curve-fitting asymmetric Lorentzians to the spectral minima at each $\mathrm{Re}[\mathrm{k_x}]$ in its TMM reflactance map (blue, solid line), and the analytically calculated dispersion line (red dots). We find a very close agreement in the dispersion lines calculated from the two methods, which verifies our analytical dispersion model, and our subsequent calculations from the model.

A.3 The calculation of mode profiles

To calculate the mode profiles of the hybrid polaritons, we need the coefficient vector C, which lies in the null space of the ill-conditioned matrix L. Hence, we

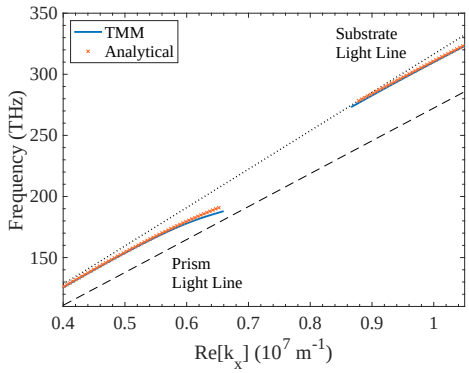

Figure A.2: Dispersion line of bifilm A obtained from the TMM reflectance map (blue, solid), and from the analytical dispersion model (red crosses).

first perform a singular value decomposition (SVD) of L at a point $\{\tilde{\omega}, \mathrm{Re}[k_x]\}$ of the dispersion line, which yields a unitary matrix U whose columns are the left singular vectors, a diagonal matrix S whose elements are the singular values of the L, and a unitary matrix V whose columns are the right singular vectors. The column of V that corresponds to the diagonal element in S that has the smallest singular value is the coefficient vector C. We susbtitute these coefficients in the equations (A.1)-(A.3) to get the electric field distributions of the hybrid polaritons at each point $\{\tilde{\omega}, \mathrm{Re}[k_x]\}$ on the dispersion line. To calculate the electric field profiles of the standalone samples (gold film on float glass substrate, and the ITO film on the float glass substrate), we follow the same procedure used for the hybrid modes detailed above, but with the required changes in the characteristic equation, and the coefficient vector C, which now has only 6 elements.

A.3.1 Mode profiles of Bifilms with $d_{\mathrm{ITO}} \geq 65$ nm

Figures A.3(a) and A.3(b) show the electric field profiles of the LR-SPP mode in 50-nm-thick gold film on float glass, and the "ENZ" mode in a 65-nm-thick ITO film on float glass with the same permittivity as in Fig. 2.7(b), respectively at their point of degeneracy. We see that for this thicker ITO film, the "ENZ" mode starts to resemble the SPP mode so that the fields are now confined along the ITO-substrate interface, and E_z is no longer strongly enhanced within the ITO film. For the bifilm comprising the 50-nm-thick gold on 65-nm-thick ITO, the electric field of the hybrid polaritons within the ITO film starts to decouple between the two ITO interfaces, as seen in the electric field profiles of the upper and the lower

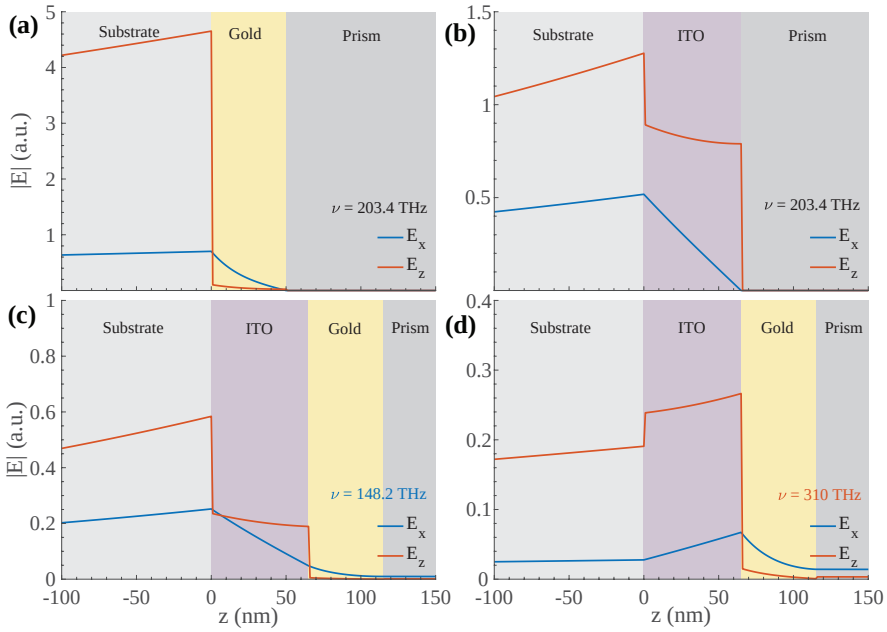

Figure A.3: Electric field profiles of the longitudinal "z" (red) and the transverse "x" (blue) components of the (a) standalone LR-SPP mode in a 50 nm gold film, and the (b) standalone ENZ mode in a 65 nm ITO film at their point of degeneracy (where their respective dispersion lines cross). The electric field profiles of the (c) lower and the (d) upper polaritons of the bifilm with 50 nm thick gold on 65 nm thick ITO close to the avoided crossing region.

polariton close to the avoided crossing region shown in Figures A.3(c) and A.3(d), respectively. Both E_x and E_z for the upper (lower) polariton are enhanced along the gold-ITO (ITO-substrate) interface.

For even thicker ITO films, the "ENZ" mode becomes even more SPP-like in nature. As shown in Figure A.4(b), both E_z and E_x components of the "ENZ" mode for a 100-nm-thick ITO film are confined along the ITO-substrate interface. For the bifilm comprising this 100-nm-thick ITO film, the hybrid polaritons clearly evolve into two interface polaritons, with the upper polariton confined along the gold-ITO interface, and the lower polariton confined along the ITO-substrate interface. We can also understand this effect from the behavior of ITO in the spectral range under consideration. ITO behaves like a dielectric for frequencies larger than $\omega_{\mathrm{ENZ,ITO}}$ with a refractive index approaching the float glass substrate for the range of frequencies where the upper polariton exists. Hence, this 100-nm-thick ITO

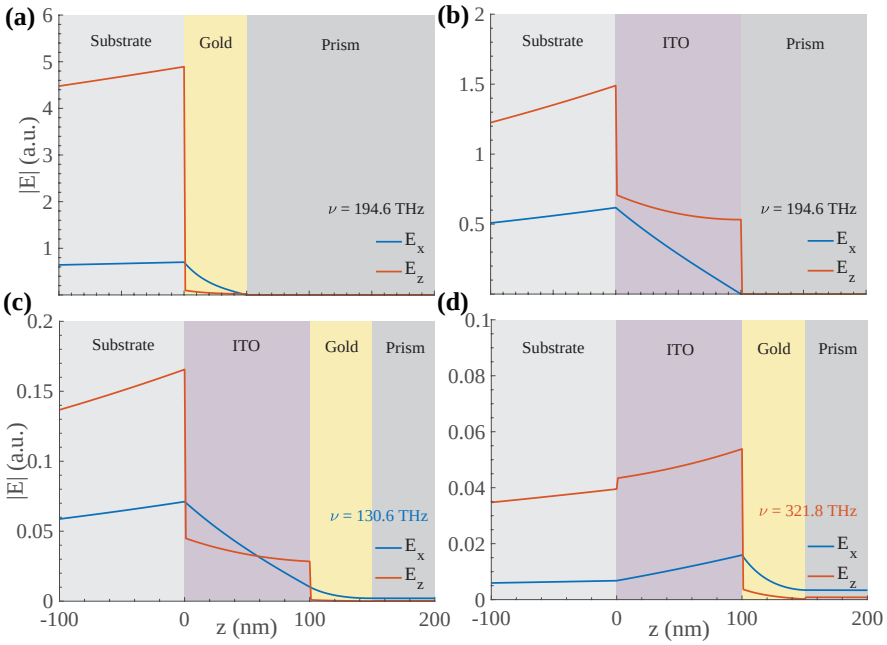

Figure A.4: Electric field profiles of the longitudinal "z" (red) and the transverse "x" (blue) components of the (a) standalone LR-SPP mode in a 50 nm gold film, and the (b) standalone ENZ mode in a 100 nm ITO film at their point of degeneracy (where their respective dispersion lines cross). The electric field profiles of the (c) lower and the (d) upper polaritons of the bifilm with 50 nm thick gold on 100 nm thick ITO close to the avoided crossing region.

layer behaves like a dielectric boundary for the gold film, and leads to a plasmon polariton confined along the gold-ITO interface. For the range of frequencies corresponding to the lower polariton, the ITO response is metal-like. Hence, for these frequencies, the entire bifilm behaves as a thick metal film that supports a long range polariton along the ITO-substrate interface. For such bifilms, the field enhancement within the ITO layer is significantly lower than for the bifilms with a thinner ITO layer. Hence, even though the coupling strength of the SPP and the ENZ modes for such bifilms is strong enough to be classified as being in the ultra-strong coupling region, increasing the thickness of the ITO layer in the bifilm beyond 65 nm does not offer much practical advantage in terms of applications pertaining to accessing the giant nonlinear response of ITO in a guided wave geometry.

A.4 The properties of the upper polariton in bifilms B and C

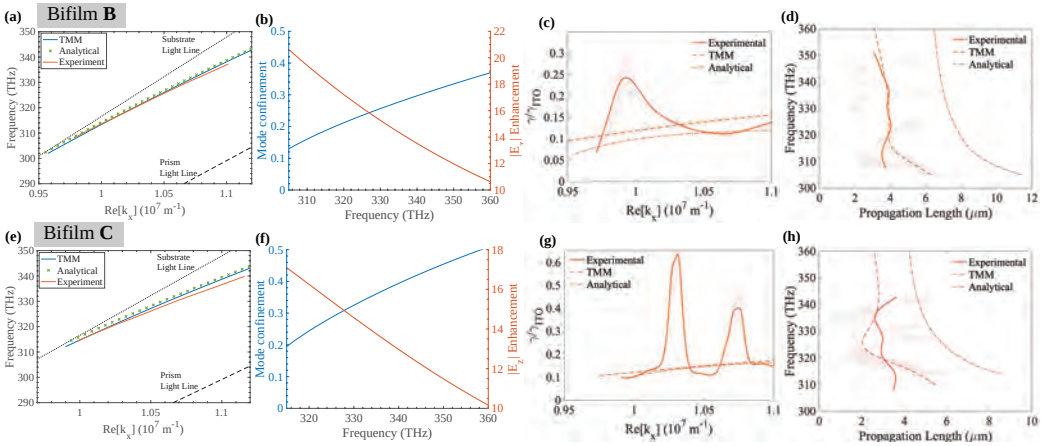

Figure A.5: Dispersion lines of the upper polariton of bifilms (a) B and (e) C obtained from TMM simulations (blue, solid), experimental measurements (red, solid), and the analytical model (green crosses). Mode confinement (blue) and the longitudinal field enhancement (red) of the upper polariton in bifilms (b) B and (f) C. The damping γ (normalized to the damping in the Drude permittivity model of the corresponding ITO layer) of the upper polariton in bifilms (c) B and (g) C obtained from the experimental measurements (solid), TMM simulations (dashed), and the analytical model (dot-dashed). The propagation length of the upper polariton in bifilms (d) B and (h) C obtained from the experimental measurements (solid), TMM simulations (dashed), and the analytical model (dot-dashed). The lines representing the simulated, and the measured results in panels (c), (d), (g) and (h) are the smoothened parameters extracted through curve-fitting to the respective datasets to account for fitting errors – and measurement errors in the case of experiment – represented by the red shaded regions around the lines.

Figures A.5(a) and (e) show the dispersion lines of the upper polariton in bifilms B and C, respectively. The blue (red) solid lines represent the results from TMM simulations (experimental measurements) in both panels, and are obtained as before by fitting asymmetric Lorentzians to the corresponding reflectance maps. The green crosses in both panels represent the results from the analytical dispersion model, and are the real part of the complex $\tilde{\omega}$ that minimize the $|\det(L)|$ given in Eq. (A.6) at each real wavevector $\mathrm{Re}[k_x]$. The dispersion lines obtained form

TMM simulations are in almost perfect agreement with those obtained from the analytical model. The slight differences observed in the experimentally measured dispersion lines with the simulations and the analytical model could be attributed to several factors. First, there could be possible differences in the permittivity values of gold and ITO in the fabricated bifilms and the permittivity values assumed in the simulations, and in the analytical model. Second, the measurement errors, as well as the errors in curve fitting to the measured reflectance maps for the parameter extraction could also contribute to the slight differences.

Figures A.5(b) and (f) show the mode confinement (blue, left axis), and the longitudinal field enhancement (red, right axis) within the ITO layer for the upper polariton of bifims B and C, respectively. These quantities are calculated from the mode profiles of the upper polariton (calculated using the method described in section S6) for both bifilms using the definitions of the quantities given in the main text. The upper polariton of bifilm B has slightly larger mode confinement than the upper polariton in bifilm A [Fig. 2.8(c)] at frequencies close to the band edge of bifilm B (around 0.093 and 0.13 for bifilms A and B, respectively). However, the slope of the confinement curve is steeper for bifilm B than for bifilm A, and becomes as large as 0.4 for bifilm B away from the polariton band edge, which is more than thrice the confinement at that particular frequency (350 THz) for the upper polariton in bifilm A. The mode confinement of the upper polariton in bifilm C is even larger than the upper polariton in bifilm B throughout spectral range with a maximum value close to 0.5. This trend is in agreement with the transition of the hybrid polaritons to interface polaritons for larger thicknesses of the ITO layer discussed previously in section A.3. At the “bluer" frequencies, where ITO behaves as a dielectric, the (upper polariton) becomes more confined along the gold-ITO interface for both bifilms B and C. This confinement is even larger for bifilm C where the ENZ mode in the 100 nm-thick-ITO layer is even more LR-SPP-like than the ENZ mode in the 65 nm-thick-ITO layer in bifilm B.

On the other hand, the longitudinal field enhancement of the upper polariton in bifilm A is larger than both bifilms B and C throughout the spectral range under consideration. The maximum field enhancement for the upper polariton in bifilm A $\approx 32\times$ at the band edge of bifilm A, whereas it is $\approx 20\times$ and $\approx 17\times$ at the band edges of bifilms B and C, respectively. A larger field enhancement would be more desirable for enhancing the nonlinear optical response for certain applications. The larger mode confinements of the upper polaritons in bifilms B and C in comparison to the polariton in bifilm A also reflects in their smaller propagation lengths and larger damping. The simulated as well as the measured propagation lengths for the upper polaritons in both bifilms B and C is between 2-4 μm, whereas the

corresponding lengths for bifilm A is between 4-8 μm. On the other hand, the simulated and the measured damping rates of the upper polaritons in both bifilms B and C is larger than $0.1\gamma_{\mathrm{ITO}}$, while the damping rate for the upper polariton in bifilm A is lower than $0.1\gamma_{\mathrm{ITO}}$ throughout.

B. Fabrication Details for the Bi-film and the Nanoantenna Arrays

B.1 The Gold-ITO Bifilms

The 50-nm-thick gold layer over the commercial ITO samples was deposited using the thermal evaporation technique. The samples were cleaned using acetone and extreme sonication followed by isopropyl alcohol (IPA) and extreme sonication to remove most of the contamination over the surface that could lead to the undesired scattering of the surface waves. A thermal source was then used to evaporate the gold at a constant rate until a 50-nm-thick layer of gold accumulated over the samples under a high vacuum. No adhesion layer was used between the gold layer and the substrate.

B.2 The Nanoantenna Arrays

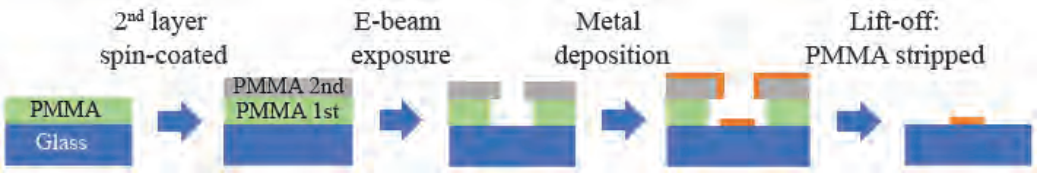

Figure B.1: Flow diagram depicting the fabrication process of the nanoantenna arrays.

Fig. B.1 shows a flow diagram of the fabrication process of our nanoantenna arrays. As a first step, a 2 cm $\times$ 2 cm chip was diced from a fused silica wafer.

This chip was then cleaned through the use of acetone and IPA, followed by blow-drying with nitrogen. A 2% wt. polymethyl methacrylate (PMMA) in anisole solution (molecular weight of 450,000) was used as the bottom resist layer. The chip was then spin-coated with the bottom resist at 5000 rpm for 60 seconds with an acceleration of 300 rps, and then baked at 180°C for 30 minutes, thereby producing a 50-nm-thick bottom resist layer. Similarly, a 2% wt. PMMA in anisole solution (molecular weight of 950,000) was used as the top resist layer. This top layer was spin-coated at 7000 rpm for 60 seconds, with an acceleration of 300 rps, thereby producing a 25-nm-thick top resist layer. A non-conductive substrate, such as silica, can result in charge buildup during E-beam exposure (commonly termed as charging). To avoid this charging effect during E-beam lithography of our plasmonic nanostructures, *espacer*, a water-soluble conductive polymer solution, was spin-coated at 2500 rpm for 25 seconds with an acceleration of 300 rps. The plasmonic nanostructures were then patterned using 30-kV Raith E-beam lithography system (CRPuO, uOttawa) with a dose of 550 mC/cm^2. After the patterning, the samples were rinsed in de-ionized water to remove the espacer layer, and post-baked on a hot plate at 80°C for 1 hour. The resist was then developed for 2 minutes in 3:1 MIBK-IPA (Methyl Isobutyl Ketone-Isopropyl Alcohol) mixture at 20°C, followed by an IPA rinse. With the PMMA bi-layer pattern prepared, metallization was carried out by thermal evaporation of 20-nm-thick gold layer through the use of an Angstrom Nexdep evaporator. As a final step in the fabrication, acetone was used to lift-off of the PMMA.

C. Analytical Model of a Single Nanorod

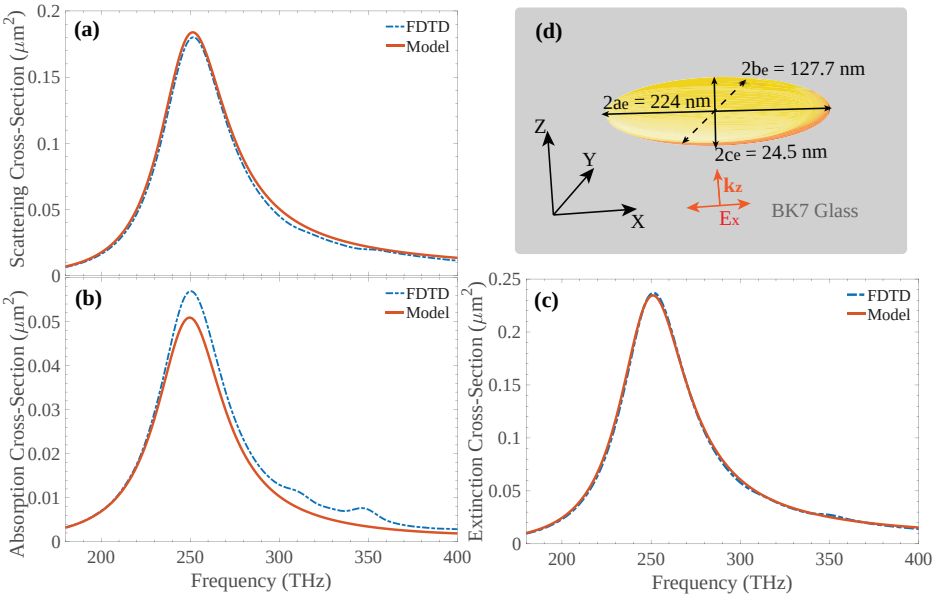

Figure C.1: (a) Scattering, (b) absorption, and (c) extinction cross-section spectra of a single nanorod obtained from FDTD simulations (blue, dot-dashed), and of the equivalent ellipsoid calculated analytically (red, solid). (d) Diagram showing the dimensions of the equivalent ellipsoid and the excitation geometry.

From the electrostatic model for dipole polarizability of an ellipsoid of semi-axes lengths a_e, b_e and c_e, we have the following expression [15]

$$\alpha_{0,ii} = V\left(L_i + \frac{\varepsilon}{\varepsilon_1 - \varepsilon}\right)^{-1}, \tag{C.1}$$

where $i = x,y,z$, $V = 4\pi a_e b_e c_e/3$ is the volume of the ellipsoid, ε_1 and ε are the

material permittivity of the ellipsoid (gold) and of the surrounding medium (BK7 glass) respectively. L_i is the shape-parameter (or the depolarization factor) given by

$$L_i = \frac{a_e b_e c_e}{2} \int_0^\infty \frac{dq}{f(q)(q+d_i^2)}, \tag{C.2}$$

with $d_i = \{a_e, b_e, c_e\}$ for $i = \{x, y, z\}$, and $f(q) = \sqrt{(q+a_e^2)(q+b_e^2)(q+c_e^2)}$. The optical constants of gold (for ε_1) were taken from Johnson and Christy [70], and the permittivity of the BK7 glass (ε_m) from [131]. The only damping mechanism in this limit arises from the material response, which is independent of the dimensions of the ellipsoid. For ellipsoids of volumes as large as the nanorod (185 nm long, 105 nm wide and 20 nm thick), radiative damping becomes a significant contribution to the linewidth, along with the non-radiative damping due to the material response. In addition, retardation effects come into play, which lead to a shift in the resonance frequency. These effects are not accounted for in the electrostatic polarizability model. Kuwata et al. [258] provide an empirical model for an arbitrary shaped nanoparticle that takes into account retardation as well as the radiation reaction by approximating the total polarizability as

$$\alpha_{ii}^{-1} \approx \alpha_{0,ii}^{-1} - i\frac{(n\tilde{\omega})^3}{6\pi} - \beta_{0,ii}, \tag{C.3}$$

$$\beta_{0,ii} = -\frac{A(L_i)}{V}(n\tilde{\omega}d_i)^2 - \frac{B(L_i)}{V}(n\tilde{\omega}d_i)^4, \tag{C.4}$$

where $\tilde{\omega} = \omega/c$, and n is the refractive index of the surrounding medium. The second term on the right in Eq. (C.3) accounts for the radiation-reaction, while the $\beta_{0,ii}$ term is an empirical term that accounts for retardation. $A(L_i)$ and $B(L_i)$ are polynomials of the shape-parameter L_i. The specific form of the polynomials depends on the geometry of the nanoparticles under consideration and does not depend on the material being considered. The resonance condition is met when the real part of the right hand side of Eq. (C.3) vanishes. In addition, from Eqs. (C.1) and (C.3), we see that a larger volume of the ellipsoid leads to larger radiative damping (and hence larger spectral linewidth), as well as a red-shift in the resonance [12, 259].

The cross-sections of the ellipsoid are given by (assuming $i = x$ and dropping

the suffixes)

$$C_{\text{ext}} = n\tilde{\omega}\,\text{Im}[\alpha], \tag{C.5}$$

$$C_{\text{scat}} = \frac{(n\tilde{\omega})^4}{6\pi}|\alpha|^2, \tag{C.6}$$

$$C_{\text{abs}} = C_{\text{ext}} - C_{\text{scat}}, \tag{C.7}$$

Kuwata et al. [258] provide the polynomials $A(L)$ and $B(L)$ for spheroids of aspect ratios larger than 3.8. However, for the aspect ratios of the nanorods that we have considered, the polynomials given in [258] do not yield correct results. In order to obtain the correct form of the polynomials specific to our case, we compare the cross-section spectra of ellipsoids of different dimensions simulated in FDTD with the cross-section spectra corresponding to ellipsoid polarizability given by Eqs. (C.5)-(C.7) while assuming different forms of the polynomials $A(L)$ and $B(L)$. The closest agreement between the FDTD simulations and the analytical model were found for $A(L) = -0.4915L - 1.046L^2 + 0.8481L^3$ and dropping the term associated with the polynomial $B(L)$.

The dimensions of the ellipsoid with scattering and extinction spectra in closest agreement with the corresponding spectra of an isolated nanorod are: $a_e = 112$ nm, $b_e = 63.85$ nm, $c_e = 12.25$ nm. Figure C.1 (a), (b) and (c) compare the spectra of the scattering, absorption, and extinction cross-sections, respectively, of the nanorod obtained from FDTD (blue, dot-dashed), and of the equivalent ellipsoid calculated analytically. We see that the extinction and the scattering cross-section spectra of the nanorod and the equivalent ellipsoid agree reasonably well. However, there are additional features are present at the frequencies higher than the absorption resonance for the nanorod, but not for the ellipsoid. These additional features are due to contributions from multipolar resonances of the nanorod, with the prominent bump around 350 THz due to the electric quadrupolar component. Since the analytical results calculated everywhere in this work only include the electric dipole contributions from the equivalent ellipsoid, we see some disagreements between the analytically calculated spectra and the spectra obtained from FDTD simulations in the frequency range 280-380 THz for the single, bi-, and multi-layered nanoantenna arrays.

D. Electric field from a 2D Lattice of Identical Electric Dipoles

Here we present the derivation of Eq. (4.8), which is the electric field at a given point in space from a square lattice of identical electric dipoles of dipole moment p located in the xy-plane. We consider fields at a fixed frequency ω, or

$$E(r,t) = E(r)e^{-i\omega t} + \text{c.c.}, \tag{D.1}$$

and assuming a source polarization $P(r)$ in a background medium of refractive index n, we have [260]

$$P(R;z) = \int \frac{d\kappa}{(2\pi)^2} P(\kappa;z)e^{i\kappa\cdot R}, \tag{D.2}$$

$$E(R;z) = \int \frac{d\kappa}{(2\pi)^2} E(\kappa;z)e^{i\kappa\cdot R}, \tag{D.3}$$

where $P(r) = P(R;z)$, $\kappa = (\kappa_x, \kappa_y)$, and

$$E(\kappa;z) = \int G(\kappa;z-z')\cdot P(\kappa;z')dz', \tag{D.4}$$

with $G(\kappa;z)$ being the Green's function given by

$$\begin{aligned} G(\kappa;z) = {} & \frac{i\tilde{\omega}^2}{2\varepsilon_0 w}(\hat{s}\hat{s} + \hat{p}_+\hat{p}_+)\theta(z-z')e^{iw(z-z')} \\ & + \frac{i\tilde{\omega}^2}{2\varepsilon_0 w}(\hat{s}\hat{s} + \hat{p}_-\hat{p}_-)\theta(z'-z)e^{-iw(z-z')} - \frac{\hat{z}\hat{z}}{2\varepsilon_0 n^2}\delta(z-z'). \end{aligned} \tag{D.5}$$

Here $\theta(z)$ is the Heaviside step function,

$$w = \sqrt{\tilde{\omega}^2 n^2 - \kappa^2},$$

and

$$\hat{s} = \hat{\kappa} \times \hat{z}$$
$$\hat{p}_{\pm} = \frac{\kappa \hat{z} \mp w \hat{\kappa}}{\tilde{\omega} n},$$

with $\kappa = |\kappa|$. We assume the lattice positions of the nanoantenna array to be

$$R_l = l_x a \hat{x} + l_y a \hat{y},$$

with a being the lattice constant; l denotes (l_x, l_y), where l_x and l_y are integers. The reciprocal lattice vectors are then given by

$$K_m = \frac{2\pi}{a} m_x \hat{x} + \frac{2\pi}{a} m_y \hat{y}, \tag{D.6}$$

where m denotes (m_x, m_y), with m_x and m_y integers. The relation $e^{iK_m \cdot R_l} = 1$ holds for any R_l and any K_m

In the point dipole approximation, the polarization $P(R;z)$ and $P(\kappa;z)$ of the plane of dipoles can be written as

$$P(R;z) = \delta(z) \sum_l p \delta(R - R_l), \tag{D.7}$$

$$P(\kappa;z) = \delta(z) p \sum_l e^{-i\kappa \cdot R_l}. \tag{D.8}$$

Substituting Eq. (D.8) in (D.4), we get after some simplification

$$E(\kappa;z) = \frac{i\tilde{\omega}^2}{2\varepsilon_0 w} (\hat{s}\hat{s} + \hat{p}_{\pm}\hat{p}_{\pm}) \cdot p \sum_l e^{-i\kappa \cdot R_l} e^{iw|z|}. \tag{D.9}$$

Then using Eqs. (D.9) and (D.3), we get

$$E(R;z) = \frac{i\tilde{\omega}^2}{2\varepsilon_0} \int \frac{d\kappa}{(2\pi)^2 w} (\hat{s}\hat{s} + \hat{p}_{\pm}\hat{p}_{\pm}) \cdot p \Big(\sum_l e^{i\kappa \cdot (R - R_l)} \Big) e^{iw|z|}. \tag{D.10}$$

We now set $R = R_j + \Delta$, where R_j is some lattice site, and Δ is the displacement from the lattice site; using the lattice property that $e^{i\kappa\cdot(R_j - R_l)} = 1$, we get

$$E(R;z) = \frac{i\tilde{\omega}^2}{2\varepsilon_0}\int \frac{e^{i\kappa\cdot\Delta}d\kappa}{(2\pi)^2 w}(\hat{s}\hat{s} + \hat{p}_\pm\hat{p}_\pm)\cdot p\Big(\sum_l e^{i\kappa\cdot R_l}\Big)e^{iw|z|}. \tag{D.11}$$

We then use the standard lattice result

$$\frac{a^2}{(2\pi)^2}\sum_l e^{i\kappa\cdot R_l} = \sum_m \delta(\kappa - K_m),$$

in (B11) to get

$$E(R_j + \Delta; z) = \frac{i\tilde{\omega}^2}{2\varepsilon_0 a^2}\sum_m \frac{e^{iK_m\cdot\Delta}}{w}(\hat{s}\hat{s} + \hat{p}_\pm\hat{p}_\pm)\cdot p e^{iw|z|}, \tag{D.12}$$

where w, $\hat{s}$, and $\hat{p}_\pm$ are now functions of K_m given by

$$\begin{aligned}
\hat{s} &= \hat{K}_m \times \hat{z},\\
\hat{p}_\pm &= \frac{K_m\hat{z} \mp w(K_m)\hat{K}_m}{\tilde{\omega}n},\\
w &= \sqrt{\tilde{\omega}^2 n^2 - K_m^2}.
\end{aligned}$$

For $m = (0,0)$, $w \to \tilde{\omega}n$, and $K_{0,0} = 0$, and $\hat{K}_{0,0}$ is poorly defined in this limit. However, regardless of the choice of unit vector for $\hat{K}_{0,0}$, we have the condition

$$\hat{s}\hat{s} + \hat{p}_\pm\hat{p}_\pm \to \hat{x}\hat{x} + \hat{y}\hat{y},$$

which gives us the $m = (0,0)$ field component as

$$[E(R_j + \Delta; z)]_{\mathrm{m}=(0,0)} = \frac{i\tilde{\omega}}{2\varepsilon_0 a^2 n}(\hat{x}\hat{x} + \hat{y}\hat{y})\cdot p e^{i\tilde{\omega}n|z|}. \tag{D.13}$$

This is independent of displacement Δ, and has the form of a plane wave with no fast-decaying components. Hence this $m = (0,0)$ component is the radiative field contribution. For a small enough lattice constant a, the remaining terms in the sum

in Eq. (D.12) form the non-radiative contribution,

$$E_{\text{nrad}}(R_j+\Delta;z)=\sum_{\text{m}\neq(0,0)} e^{iK_m\cdot\Delta}\left[\frac{i\tilde{\omega}^2}{2\varepsilon_0 a^2 w}(\hat{s}\hat{s}+\hat{p}_{\pm}\hat{p}_{\pm})\right]\cdot p e^{iw|z|}. \tag{D.14}$$

The non-radiative field

Assuming that the lattice constant a is small enough that for $(m_x,m_y)\neq(0,0)$ we have w purely imaginary, we put

$$w=iq, \tag{D.15}$$

where $q=\sqrt{K_m^2-\tilde{\omega}^2n^2}$, which can be written in terms of the indices (m_x,m_y) as

$$q=\frac{2\pi}{a}\sqrt{(m_x^2+m_y^2)-\frac{\tilde{\omega}^2n^2a^2}{(2\pi)^2}}. \tag{D.16}$$

We now define

$$\frac{\tilde{\omega}na}{2\pi}=\eta, \tag{D.17}$$

and we can write

$$\frac{K_m}{\tilde{\omega}n}=\frac{2\pi}{\tilde{\omega}na}\sqrt{m_x^2+m_y^2}=\frac{D_m}{\eta}, \tag{D.18}$$

where $D_m=\sqrt{m_x^2+m_y^2}$. For the sub-wavelength lattice constants assumed here, where for $(m_x,m_y)\neq(0,0)$ we have q real, $\eta<1$, and we can write

$$\frac{w}{i\tilde{\omega}n}=\frac{q}{\tilde{\omega}n}=\frac{1}{\eta}\sqrt{(m_x^2+m_y^2)-\eta^2},$$

which simplifies to

$$\frac{q}{\tilde{\omega}n}=\frac{1}{\eta}\sqrt{D_m^2-\eta^2}=\frac{D_m\gamma_m}{\eta}, \tag{D.19}$$

where

$$\gamma_m=\sqrt{1-\frac{\eta^2}{D_m^2}},$$

and is always real and slightly less than unity for $\eta < 1$. We now simplify the prefactor of the unit dyadics in Eq. (D.14) as

$$\frac{i\tilde{\omega}^2}{2\varepsilon_0 a^2 w} = \frac{\tilde{\omega}}{2\varepsilon_0 a^2 n}\frac{\tilde{\omega}n}{q} = \frac{\pi}{\varepsilon_0 a^3 n^2}\frac{\eta^2}{D_m\gamma_m}. \tag{D.20}$$

The propagator $e^{iw|z|}$, which we define as $f_m(|z|)$ can also be simplified to

$$f_m(|z|) = e^{-q|z|} = e^{-\frac{\tilde{\omega}n}{\eta}D_m\gamma_m|z|} = e^{-2\pi D_m\gamma_m|\frac{z}{a}|}. \tag{D.21}$$

We also define

$$\Phi(\Delta) = K_m\cdot\Delta = 2\pi\left(m_x\frac{\Delta_x}{a} + m_y\frac{\Delta_y}{a}\right). \tag{D.22}$$

Substituting Eqs. (D.20)-(D.20) in Eq. (D.14), we get

$$E_{\text{nrad}}(R_j+\Delta;z) = \frac{\pi}{\varepsilon_0 a^3 n^2}\sum_{\text{m}\neq(0,0)} e^{i\Phi_m(\Delta)} f_m(|z|)\left[\frac{\eta^2}{D_m\gamma_m}(\hat{s}\hat{s} + \hat{p}_\pm\hat{p}_\pm)\right]\cdot p. \tag{D.23}$$

We now simplify the unit dyadics in Eq. (D.23) in terms of the cartesian vectors. So we have

$$\hat{K}_m = \frac{m_x\hat{x} + m_y\hat{y}}{D_m}$$
$$\hat{s} = \hat{K}_m\times\hat{z} = \frac{-m_x\hat{x} + m_y\hat{y}}{D_m}.$$

Hence we write

$$\hat{s}\hat{s} = \frac{m_y^2\hat{x}\hat{x} + m_x^2\hat{y}\hat{y} - m_x m_y(\hat{x}\hat{y} + \hat{y}\hat{x})}{D_m^2}, \tag{D.24}$$

and

$$\begin{aligned}\hat{p}_\pm\hat{p}_\pm &= \frac{K_m\hat{z}\mp w\hat{K}_m}{\tilde{\omega}n}\frac{K_m\hat{z}\mp w\hat{K}_m}{\tilde{\omega}n}\\ &= \frac{K_m^2}{\tilde{\omega}^2n^2}\hat{z}\hat{z} - \frac{q^2}{\tilde{\omega}^2n^2}\hat{K}_m\hat{K}_m \mp i\frac{K_m q}{\tilde{\omega}^2n^2}\left(\hat{z}\hat{K}_m + \hat{K}_m\hat{z}\right),\end{aligned} \tag{D.25}$$

where we have used Eq. (D.15) for simplification. We use Eqs. (D.18) and (D.19) to further simplify Eq. (D.25) above as

$$\hat{p}_\pm\hat{p}_\pm = \frac{D_m^2}{\eta^2}\hat{z}\hat{z} - \frac{D_m^2\gamma_m^2}{\eta^2}\hat{K}_m\hat{K}_m \mp i\frac{D_m^2\gamma_m}{\eta^2}\left(\hat{z}\hat{K}_m + \hat{K}_m\hat{z}\right). \tag{D.26}$$

We now simplify the second and the third unit dyadics on the right of Eq. (D.26). For the second unit dyadic, we have

$$\begin{aligned}\hat{K}_m\hat{K}_m &= \frac{m_x\hat{x}+m_y\hat{y}}{D_m}\frac{m_x\hat{x}+m_y\hat{y}}{D_m}\\ &= \frac{m_x^2\hat{x}\hat{x}+m_y^2\hat{y}\hat{y}+m_xm_y(\hat{x}\hat{y}+\hat{y}\hat{x})}{D_m^2}.\end{aligned} \tag{D.27}$$

The third unit dyadic in Eq. (D.26) can be written as

$$\begin{aligned}\hat{z}\hat{K}_m+\hat{K}_m\hat{z} &= \hat{z}\frac{m_x\hat{x}+m_y\hat{y}}{D_m}+\frac{m_x\hat{x}+m_y\hat{y}}{D_m}\hat{z}\\ &= \frac{m_x}{D_m}(\hat{z}\hat{x}+\hat{x}\hat{z})+\frac{m_y}{D_m}(\hat{z}\hat{y}+\hat{y}\hat{z}).\end{aligned} \tag{D.28}$$

Substituting Eqs. (D.27) and (D.28) in (D.26), we get

$$\begin{aligned}\hat{p}_\pm\hat{p}_\pm = &-\frac{m_x^2\gamma_m^2}{\eta^2}\hat{x}\hat{x}-\frac{m_y^2\gamma_m^2}{\eta^2}\hat{y}\hat{y}+\frac{D_m^2}{\eta^2}\hat{z}\hat{z}-\frac{m_xm_y\gamma_m^2}{\eta^2}(\hat{x}\hat{y}+\hat{y}\hat{x})\\ &\mp i\frac{m_yD_m\gamma_m}{\eta^2}(\hat{z}\hat{y}+\hat{y}\hat{z})\mp i\frac{m_xD_m\gamma_m}{\eta^2}(\hat{z}\hat{x}+\hat{x}\hat{z}).\end{aligned} \tag{D.29}$$

From Eqs. (D.24) and (D.29), we write

$$\begin{aligned}\eta^2(\hat{s}\hat{s}+\hat{p}_\pm\hat{p}_\pm) = &\,\hat{x}\hat{x}\Big(\frac{\eta^2m_y^2}{D_m^2}-m_x^2\gamma_m^2\Big)+\hat{y}\hat{y}\Big(\frac{\eta^2m_x^2}{D_m^2}-m_y^2\gamma_m^2\Big)+\hat{z}\hat{z}D_m^2+\\ &+(\hat{x}\hat{y}+\hat{y}\hat{x})\Big(-\frac{\eta^2m_xm_y}{D_m^2}-m_xm_y\gamma_m^2\Big)+(\hat{z}\hat{y}+\hat{y}\hat{z})(\mp im_yD_m\gamma_m)+\\ &+(\hat{z}\hat{x}+\hat{x}\hat{z})(\mp im_xD_m\gamma_m).\end{aligned} \tag{D.30}$$

The coefficients of the unit dyadics in Eq. (D.30) can be further simplified. So we have

$$\frac{\eta^2m_y^2}{D_m^2}-m_x^2\gamma_m^2=\frac{\eta^2m_y^2-m_x^2(D_m^2-\eta^2)}{D_m^2}=\eta^2\frac{m_x^2+m_y^2}{D_m^2}-m_x^2=\eta^2-m_x^2.$$

Similarly

$$\frac{\eta^2m_x^2}{D_m^2}-m_y^2\gamma_m^2=\eta^2-m_y^2,$$

and

$$-\frac{\eta^2 m_x m_y}{D_m^2} - m_x m_y \gamma_m^2 = m_x m_y \Big(\frac{-\eta^2 - \gamma_m^2 D_m^2}{D_m^2} \Big) = m_x m_y \Big(\frac{-\eta^2 - (D_m^2 - \eta^2)}{D_m^2} \Big) = -m_x m_y.$$

On making the above substitutions, Eq. (D.30) becomes

$$\begin{aligned} \eta^2 (\hat{s}\hat{s} + \hat{p}_\pm \hat{p}_\pm) = \hat{x}\hat{x}\Big(\eta^2 - m_x^2\Big) + \hat{y}\hat{y}\Big(\eta^2 - m_y^2\Big) + \hat{z}\hat{z} D_m^2 + (\hat{x}\hat{y} + \hat{y}\hat{x})(-m_x m_y) \\ + (\hat{z}\hat{y} + \hat{y}\hat{z})(\mp i m_y D_m \gamma_m) + (\hat{z}\hat{x} + \hat{x}\hat{z})(\mp i m_x D_m \gamma_m). \end{aligned} \tag{D.31}$$

Substituting Eq. (D.31) in (D.23), we can write

$$E_{\text{nrad}}(R_j + \Delta; z) = \frac{\pi}{\varepsilon_0 a^3 n^2} T(\Delta, z) \cdot p, \tag{D.32}$$

where $T(\Delta, z)$ is a dimensionless dyadic of the form

$$\begin{aligned} T(\Delta, z) = T_{xx}(\Delta, z)\hat{x}\hat{x} + T_{yy}(\Delta, z)\hat{y}\hat{y} + T_{zz}(\Delta, z)\hat{z}\hat{z} + T_{xy}(\Delta, z)(\hat{x}\hat{y} + \hat{y}\hat{x}) \\ + T_{yz}(\Delta, z)(\hat{z}\hat{y} + \hat{y}\hat{z}) + T_{zx}(\Delta, z)(\hat{x}\hat{z} + \hat{z}\hat{x}), \end{aligned}$$

with

$$\begin{aligned} T_{xx}(\Delta, z) &= \sum_{m \neq (0,0)} e^{i\Phi_m(\Delta)} f_m(|z|) \Big(\frac{\eta^2 - m_x^2}{D_m \gamma_m} \Big), \\ T_{yy}(\Delta, z) &= \sum_{m \neq (0,0)} e^{i\Phi_m(\Delta)} f_m(|z|) \Big(\frac{\eta^2 - m_y^2}{D_m \gamma_m} \Big), \\ T_{zz}(\Delta, z) &= \sum_{m \neq (0,0)} e^{i\Phi_m(\Delta)} f_m(|z|) \Big(\frac{D_m}{\gamma_m} \Big), \\ T_{xy}(\Delta, z) &= \sum_{m \neq (0,0)} e^{i\Phi_m(\Delta)} f_m(|z|) \Big(-\frac{m_x m_y}{D_m \gamma_m} \Big), \\ T_{yz}(\Delta, z) &= \sum_{m \neq (0,0)} e^{i\Phi_m(\Delta)} f_m(|z|) (\mp i m_y), \\ T_{zx}(\Delta, z) &= \sum_{m \neq (0,0)} e^{i\Phi_m(\Delta)} f_m(|z|) (\mp i m_x). \end{aligned} \tag{D.33}$$

The tensor components given in Eq. (D.33) can be further simplified by noting that

$$e^{i\Phi_m(\Delta)} = \cos(\Phi_m(\Delta)) + i\sin\cos(\Phi_m(\Delta)),$$

and we get

$$\begin{aligned}
T_{xx}(\Delta,z) &= \sum_{m\neq(0,0)} f_m(|z|)\Big(\frac{\eta^2-m_x^2}{D_m\gamma_m}\Big)\cos(\Phi_m(\Delta)),\\
T_{yy}(\Delta,z) &= \sum_{m\neq(0,0)} f_m(|z|)\Big(\frac{\eta^2-m_y^2}{D_m\gamma_m}\Big)\cos(\Phi_m(\Delta)),\\
T_{zz}(\Delta,z) &= \sum_{m\neq(0,0)} f_m(|z|)\Big(\frac{D_m}{\gamma_m}\Big)\cos(\Phi_m(\Delta)),\\
T_{xy}(\Delta,z) &= \sum_{m\neq(0,0)} f_m(|z|)\Big(-\frac{m_x m_y}{D_m\gamma_m}\Big)\cos(\Phi_m(\Delta)),\\
T_{yz}(\Delta,z) &= \mathrm{sign}(z)\sum_{m\neq(0,0)} f_m(|z|)m_y\sin(\Phi_m(\Delta)),\\
T_{zx}(\Delta,z) &= \mathrm{sign}(z)\sum_{m\neq(0,0)} f_m(|z|)m_x\sin(\Phi_m(\Delta)).
\end{aligned} \tag{D.34}$$

We note that all the tensor components given above are purely real, which is expected for $E_{\mathrm{nrad}}(R_j+\Delta;z)$ being a purely non-radiative field.

For all the dipoles aligned along $\hat{x}$, which is the case for the nanoantenna array excited by a normally incident plane wave polarized along the dipole moments oriented along the x-axis, only the $T_{xx}(\Delta,z)$ tensor component is non-zero. Hence, the x-polarized electric field from the sheet of dipoles given by the Eqs. (D.13) and (D.32) is as follows

$$E_x(R_j+\Delta;z) = \frac{i\tilde{\omega}}{2\varepsilon_0 n}\frac{p_x}{a^2}e^{i\tilde{\omega}|z|} + \frac{\pi}{\varepsilon_0 a n^2}T_{xx}(\Delta,z)\frac{p_x}{a^2}. \tag{D.35}$$

E. Supplementary Materials for Chapter 5

E.1 Basic Equations

E.1.1 Single Nanoantenna Array

We reintroduce the basic formalism introduced previously in Refs. [163, 194] describing the dipole moments of nanoantennas in a single array. We make the point dipole approximation and model the nanoantennas as electric dipoles of dipole moment p and electrostatic polarizability $\overleftrightarrow{\alpha}_0$, which are related by the following equation:

$$p = \varepsilon_0 n^2 \overleftrightarrow{\alpha}_0 \cdot E_{\text{tot}}. \tag{E.1.1.1}$$

with ε_0 being the vacuum pemittivity, and E_{tot} being the total electric field at the location of the nanoantenna given by

$$E_{\text{tot}} = E_{\text{inc}} + \frac{1}{4\pi\varepsilon_0}\frac{2}{3} in\tilde{\omega}^3 p + (\overleftrightarrow{\beta}_0 + \overleftrightarrow{\beta}) \cdot \frac{1}{\varepsilon_0 n^2} p. \tag{E.1.1.2}$$

Here, E_{inc} is the normally incident plane wave at the center of the nanoantenna, the dyadic $\overleftrightarrow{\beta}_0$ is purely real and denotes the dynamic depolarization term that describes the modification of the dipole moment p due to field retardation over the volume of the nanoantenna. The complex dyadic $\overleftrightarrow{\beta}$ is also called the dynamic interaction constant of the array and accounts for the modification of p due to field contributions from all the other nanoantennas in the array. After some rearranging

of the terms in Eq. (E.1.1.2), we write

$$\overleftrightarrow{\alpha}_{\text{eff}}^{-1} = \overleftrightarrow{\alpha}_{0}^{-1} - \frac{i}{6\pi}(n\tilde{\omega}^3)\,\overleftrightarrow{U} - (\overleftrightarrow{\beta}_0 + \overleftrightarrow{\beta}), \tag{E.1.1.3}$$

where

$$p = \varepsilon_0 n^2\, \overleftrightarrow{\alpha}_{\text{eff}} \cdot E_{\text{inc}}. \tag{E.1.1.4}$$

The expression for the electric field from this plane of dipoles at an arbitrary point $(x,y,z) = (ma+\Delta_x, na+\Delta_y, z)$ has been derived in Appendix B of Ref. [194], and is given below:

$$E(ma+\Delta_x, na+\Delta_y, z) = \frac{i\tilde{\omega}}{2\varepsilon_0 a^2 n}(\hat{x}\hat{x}+\hat{y}\hat{y})\cdot p e^{i\tilde{\omega}n|z|} + \frac{\pi}{\varepsilon_0 a^3 n^2}\mathrm{T}(\Delta_x,\Delta_y,z)p. \tag{E.1.1.5}$$

Here, (m,n) are the lattice indices in the xy-plane, and (Δ_x,Δ_y) denote the transverse displacements of the point (x,y,z) from these lattice points. The first term on the right of the above equation is the radiative or far-field contribution to the total field, and the second term on the right is the non-radiative or near-field contribution. The expressions for all the tensor components of the tensor $\mathrm{T}(\Delta_x,\Delta_y,z)$ are also given in Appendix B of Ref. [194]. The incident field E_{inc} is assumed to be linearly polarized along the length of the nanoantenna, which is aligned with the x-axis. Hence, we only list the relevant tensor component $\mathrm{T}_{\mathrm{xx}}(\Delta_x,\Delta_y,z)$ or $\mathrm{T}_{\mathrm{xx}}(\Delta,z)$ below:

$$\mathrm{T}_{\mathrm{xx}}(\Delta,z) = \sum_{m\neq(0,0)} f_m(|z|)\left(\frac{\eta^2 - m_x^2}{D_m\gamma_m}\right)\cos[\Phi_m(\Delta)], \tag{E.1.1.6}$$

where $m \equiv (m_x, m_y)$, and

$$\begin{aligned}
&\Phi_m(\Delta) = 2\pi\left(m_x\frac{\Delta_x}{a} + m_y\frac{\Delta_y}{a}\right),\\
&D_m \equiv \sqrt{m_x^2 + m_y^2},\\
&\eta \equiv \frac{\tilde{\omega}na}{2\pi},\\
&\gamma_m \equiv \sqrt{1-\frac{\eta^2}{D_m^2}},\\
&f_m(|z|) \equiv e^{-2\pi D_m\gamma_m|z/a|}.
\end{aligned}$$

E.1.2 Semi-Infinite Meta-Crystal

We now consider the system depicted in Fig. 5.1 with an infinite number of identical dipole planes located at $z_J = Jb$, with J varying from 1 to ∞. The incident field on the stack is assumed to have the form $E_{\text{inc}} = E_0 e^{i(\tilde{\omega} n z - \omega t)} \hat{x}$. Each dipole p_J in plane J is excited by the retarded incident field $E_0 e^{i(\tilde{\omega} n J b - \omega t)} \hat{x}$, the field from all the dipoles within plane J, and the radiative and near-field contributions from all the other dipole planes. Using Eqs. (E.1.1.2) and (E.1.1.5), we then write

$$p_J = \varepsilon_0 n^2 \overleftrightarrow{\alpha}_0 \cdot E_{\text{full}}(z_J), \tag{E.1.2.1}$$

where

$$E_{\text{full}}(z_J) = E_{\text{inc}}(z_J) + \frac{1}{4\pi\varepsilon_0}\frac{2}{3} i n \tilde{\omega}^3 p_J + \frac{\overleftrightarrow{\beta}_0 \cdot p_J}{\varepsilon_0 n^2} + \frac{\overleftrightarrow{\beta} \cdot p_J}{\varepsilon_0 n^2} + \\ + \frac{i\tilde{\omega}}{2\varepsilon_0 a^2 n}(\hat{x}\hat{x} + \hat{y}\hat{y}) \cdot \sum_{K=1}^{\infty}{}' e^{i\tilde{\omega} n |z_J - z_K|} p_K + \frac{\pi}{\varepsilon_0 a^3 n^2} \sum_{K=1}^{\infty}{}' \mathrm{T}(\Delta_{JK}, |z_J - z_K|) \cdot p_K. \tag{E.1.2.2}$$

Here, the primed sum denotes the sum of field contributions from all the layers except the J-th layer. For the x-polarized incident field, as stated previously, we only need to consider the p_x component of the dipole moment and the dyadic terms β_{xx}, $\beta_{0,\text{xx}}$, and T_{xx}. For now, we also consider the lattice points in each plane to be perfectly aligned, or $\Delta_{JK} = 0$ for all J and K. So we rewrite Eq. (E.1.2.2) below and drop the suffixes:

$$E_{\text{full}}(z_J) = E_0 e^{i\tilde{\omega} n z_J} + \frac{i n \tilde{\omega}^3}{6\pi\varepsilon_0} p_J + \frac{\beta_0 p_J}{\varepsilon_0 n^2} + \frac{\beta p_J}{\varepsilon_0 n^2} + \frac{i\tilde{\omega}}{2\varepsilon_0 a^2 n} \sum_{K=1}^{\infty}{}' e^{i\tilde{\omega} n |z_J - z_K|} p_K + \\ + \frac{\pi}{\varepsilon_0 a^3 n^2} \sum_{K=1}^{\infty}{}' \mathrm{T}(|z_J - z_K|) p_K. \tag{E.1.2.3}$$

The term $\mathrm{Im}[\beta]$, which includes the radiation reaction terms from all the other nanoantennas in a single array, has the following form [136]

$$\mathrm{Im}[\beta] = -\frac{1}{6\pi}(n\tilde{\omega})^3 + \frac{n\tilde{\omega}}{2a^2}. \tag{E.1.2.4}$$

Substituting Eq. (E.1.2.4) in (E.1.2.3) and simplifying, we get

$$E_{\text{full}}(z_J) = E_0 e^{i\tilde{\omega}nz_J} + \frac{\beta_0 p_J}{\varepsilon_0 n^2} + \frac{\text{Re}[\beta] p_J}{\varepsilon_0 n^2} + \frac{i\tilde{\omega}}{2\varepsilon_0 a^2 n} p_J + \\ + \frac{i\tilde{\omega}}{2\varepsilon_0 a^2 n} {\sum_{K=1}^{\infty}}' e^{i\tilde{\omega}n|z_J - z_K|} p_K + \frac{\pi}{\varepsilon_0 a^3 n^2} {\sum_{K=1}^{\infty}}' \text{T}(|z_J - z_K|) p_K. \tag{E.1.2.5}$$

We now combine the in-plane (third last) and inter-plane (second last) radiative coupling terms on the right to give a full sum over K. We can further simplify Eq. (E.1.2.5) by combining the in-plane and inter-plane non-radiative coupling by defining

$$\frac{\text{Re}[\beta] p_J}{\varepsilon_0 n^2} = \frac{\pi}{\varepsilon_0 a^3 n^2} \text{T}(0), \tag{E.1.2.6}$$

so as to write the last term on the right as an unrestricted sum over K as well. So we get

$$E_{\text{full}}(z_J) = E_0 e^{i\tilde{\omega}nz_J} + \frac{\beta_0 p_J}{\varepsilon_0 n^2} + \frac{i\tilde{\omega}}{2\varepsilon_0 a^2 n} \sum_{K=1}^{\infty} e^{i\tilde{\omega}n|z_J - z_K|} p_K + \\ + \frac{\pi}{\varepsilon_0 a^3 n^2} \sum_{K=1}^{\infty} \text{T}(|z_J - z_K|) p_K. \tag{E.1.2.7}$$

We now define

$$\alpha_{\text{atom}}^{-1} = \alpha_0^{-1} - \beta_0. \tag{E.1.2.8}$$

Here, α_{atom} is the electrostatic polarizability of the nanoantenna including the effect of field retardation over its volume, and similar to α_0, will be purely real in the absence of absorption in the nanoantenna. From Eqs. (E.1.2.1) and (E.1.2.8), we have

$$p_J = \varepsilon_0 n^2 \alpha_{\text{atom}} \left[E_{\text{full}}(z_J) - \frac{\beta_0 p_J}{\varepsilon_0 n^2} \right]. \tag{E.1.2.9}$$

Substituting Eqs. (E.1.2.7) and (E.1.2.9) in (E.1.2.1), we finally get

$$p_J = \varepsilon_0 n^2 \alpha_{\text{atom}} \left[E_0 e^{i\tilde{\omega}nz_J} + \frac{i\tilde{\omega}}{2\varepsilon_0 a^2 n} \sum_{K=1}^{\infty} e^{i\tilde{\omega}n|z_J - z_K|} p_K + \frac{\pi}{\varepsilon_0 a^3 n^2} \sum_{K=1}^{\infty} \text{T}(|z_J - z_K|) p_K \right]. \tag{E.1.2.10}$$

For notational convenience, we define

$$\phi = \tilde{\omega} n b. \tag{E.1.2.11}$$

We then have

$$p_J = \varepsilon_0 n^2 \alpha_{\text{atom}} E(J), \tag{E.1.2.12}$$

where

$$E(J) = E_0 e^{i\phi J} + \frac{i\phi}{2\varepsilon_0 a^2 b n^2} \sum_{K=1}^{\infty} e^{i\phi|J-K|} p_K + L(J), \tag{E.1.2.13}$$

with

$$L(J) = \frac{\pi}{\varepsilon_0 a^3 n^2} \sum_{K=1}^{\infty} \mathrm{T}(|z_J - z_K|) p_K. \tag{E.1.2.14}$$

E.2 The Effective Refractive Index

If $\rho(r,t)$ and $J(r,t)$ are the charge and current densities "in vacuum", then Maxwell's equations are

$$\frac{\partial B(r,t)}{\partial t} = -\nabla \times E(r,t), \tag{E.2.0.1a}$$

$$\frac{\partial E(r,t)}{\partial t} = \frac{1}{\mu_0 \varepsilon_0} \nabla \times B(r,t) - \frac{1}{\varepsilon_0} J(r,t), \tag{E.2.0.1b}$$

$$\nabla \cdot B(r,t) = 0, \tag{E.2.0.1c}$$

$$\nabla \cdot E(r,t) = \frac{\rho(r,t)}{\varepsilon_0}. \tag{E.2.0.1d}$$

And with the "full" polarization $\mathbb{P}(r,t)$, which consists of a background component $P_{\text{back}}(r,t)$ and the component of interest $P(r,t)$ such that

$$\mathbb{P}(r,t) = P_{\text{back}}(r,t) + P(r,t), \tag{E.2.0.2}$$

the Gauss's and Amperes' laws are modified to be

$$\rho(r,t) = -\nabla \cdot \mathbb{P}(r,t), \tag{E.2.0.3a}$$

$$J(r,t) = \frac{\partial \mathbb{P}(r,t)}{\partial t}. \tag{E.2.0.3b}$$

Now, we characterize the background polarization by a susceptibility χ_{back} such that

$$P_{\text{back}}(r,t) = \varepsilon_0 \chi_{\text{back}} E(r,t), \tag{E.2.0.4}$$

and introduce the background refractive index as

$$\chi_{\text{back}} = n^2 - 1. \tag{E.2.0.5}$$

So we have

$$P_{\text{back}}(r,t) = \varepsilon_0(n^2-1)E(r,t) + P(r,t). \tag{E.2.0.6}$$

So the Maxwell's equations stated above now become

$$\frac{\partial B(r,t)}{\partial t} = -\nabla \times E(r,t), \tag{E.2.0.7a}$$

$$\frac{\partial}{\partial t}(\varepsilon_0 n^2 E(r,t) + P(r,t)) = \nabla \times H(r,t), \tag{E.2.0.7b}$$

$$\nabla \cdot B(r,t) = 0, \tag{E.2.0.7c}$$

$$\nabla \cdot (\varepsilon_0 n^2 E(r,t) + P(r,t)) = 0, \tag{E.2.0.7d}$$

where $H(r,t), = B(r,t)/\mu_0$. Now we write

$$P(r,t)) = \varepsilon_0 n^2 \chi_\alpha E(r,t), \tag{E.2.0.8}$$

where χ_α is the susceptibility due to the dipole planes. We then have

$$\frac{\partial B(r,t)}{\partial t} = -\nabla \times E(r,t), \tag{E.2.0.9a}$$

$$\frac{\partial}{\partial t}(\varepsilon_0 n^2 (1+\chi_\alpha) E(r,t)) = \nabla \times H(r,t), \tag{E.2.0.9b}$$

$$\nabla \cdot B(r,t) = 0, \tag{E.2.0.9c}$$

$$\nabla \cdot (\varepsilon_0 n^2 (1+\chi_\alpha) E(r,t)) = 0. \tag{E.2.0.9d}$$

Now defining

$$\chi_\alpha = n_\alpha^2 - 1, \tag{E.2.0.10}$$

we get

$$\frac{\partial B(r,t)}{\partial t} = -\nabla \times E(r,t), \tag{E.2.0.11a}$$

$$\frac{\partial}{\partial t}(\varepsilon_0 n_{\text{eff},\alpha}^2 E(r,t)) = \nabla \times H(r,t), \tag{E.2.0.11b}$$

$$\nabla \cdot B(r,t) = 0, \tag{E.2.0.11c}$$

$$\nabla \cdot (\varepsilon_0 n_{\text{eff},\alpha}^2 E(r,t)) = 0. \tag{E.2.0.11d}$$

where

$$n_{\text{eff},\alpha} = n n_\alpha. \tag{E.2.0.12}$$

Comparing the equations in (E.2.0.11) with those in (E.2.0.9) for $P(r,t)) = 0$, we see that in the presence of polarization $P(r,t))$ the background index is modified to $n_{\text{eff},\alpha}$.

E.3 The Radiative Field at plane J in the Meta-crystal

In Eq. (5.2), the radiative field contributions at plane $z = Jb$ in the semi-infinite meta-crystal are given by the second term of the right, which is a summation over all the planes. We need to calculate this summation for the assumed solutions given by Eqs. (5.11) and (5.25) for the scenarios one and two, respectively. We work out this summation for the more general case given by scenario two, and the result for scenario one follows as a special case. To restate the problem, we need the expression for

$$i\phi \sum_{K=1}^{\infty} e^{i\phi|J-K|} p_K, \tag{E.3.0.1}$$

where

$$p_K = \sum_{\alpha=1}^{2} \mathscr{P} e^{i n_\alpha \phi K}. \tag{E.3.0.2}$$

So we have

$$i\phi \sum_{K=1}^{\infty} e^{i\phi|J-K|} p_K = i\phi \sum_{\alpha=1}^{2} \mathscr{P}_\alpha S_{J\alpha}, \tag{E.3.0.3}$$

where

$$S_{J\alpha} = \sum_{K=1}^{\infty} e^{i\phi|J-K|} e^{in_\alpha \phi K}. \tag{E.3.0.4}$$

For $J \geq 1$, we can break the summation as

$$\begin{aligned} S_{J\alpha} &= \sum_{K=1}^{J} e^{i\phi(J-K)} e^{in_\alpha \phi K} + \sum_{K=J+1}^{\infty} e^{i\phi(K-J)} e^{in_\alpha \phi K} \\ &= e^{i\phi J} \sum_{K=1}^{J} e^{i(n_\alpha - 1)\phi K} + e^{-i\phi J} \sum_{K=J+1}^{\infty} e^{i(n_\alpha+1)\phi K} \\ &= e^{i\phi J} \sum_{K=1}^{J} e^{i(n_\alpha - 1)\phi K} + e^{-i\phi J} \Big[\sum_{K=0}^{\infty} e^{i(n_\alpha+1)\phi K} - \sum_{K=0}^{J} e^{i(n_\alpha+1)\phi K} \Big]. \end{aligned} \tag{E.3.0.5}$$

Now using the geometric series expression

$$\sum_{m=M}^{N} r^m = \frac{r^M (1 - r^{N-M+1})}{1-r}, \tag{E.3.0.6}$$

we can write

$$\begin{aligned} S_{J\alpha} &= e^{i\phi J} \left(\frac{e^{i(n_\alpha-1)\phi} - e^{i(n_\alpha-1)\phi(J+1)}}{1 - e^{i(n_\alpha-1)\phi}} \right) + e^{-i\phi J} \left(\frac{1}{1 - e^{i(n_\alpha+1)\phi}} - \frac{1 - e^{i(n_\alpha+1)\phi(J+1)}}{1 - e^{i(n_\alpha+1)\phi}} \right) \\ &= \frac{e^{i\phi J} - e^{in_\alpha \phi J}}{e^{-i(n_\alpha-1)\phi} - 1} + \frac{e^{in_\alpha \phi J}}{e^{-i(n_\alpha+1)\phi} - 1} \\ &= e^{i\phi J} \left(\frac{1}{e^{-i(n_\alpha-1)\phi} - 1} \right) + e^{-in_\alpha \phi J} \left(\frac{1}{e^{-i(n_\alpha+1)\phi} - 1} - \frac{1}{e^{-i(n_\alpha-1)\phi} - 1} \right). \end{aligned} \tag{E.3.0.7}$$

Now simplifying the last term on the right, we have

$$\begin{aligned}
&\frac{1}{e^{-i(n_\alpha+1)\phi}-1}-\frac{1}{e^{-i(n_\alpha-1)\phi}-1}=\frac{1}{e^{-in_\alpha\phi}e^{-i\phi}-1}-\frac{1}{e^{-in_\alpha\phi}e^{i\phi}-1}\\
&=\frac{e^{-in_\alpha\phi}e^{i\phi}-e^{-in_\alpha\phi}e^{-i\phi}}{(e^{-in_\alpha\phi}e^{-i\phi}-1)(e^{-in_\alpha\phi}e^{i\phi}-1)}=\frac{e^{-in_\alpha\phi}(e^{i\phi}-e^{-i\phi})}{e^{-2in_\alpha\phi}-e^{-in_\alpha\phi}(e^{i\phi}+e^{-i\phi})+1}\\
&=\frac{2e^{-in_\alpha\phi}i\sin\phi}{e^{-2in_\alpha\phi}-2e^{-in_\alpha\phi}\cos\phi+1}=\frac{i\sin\phi}{\cos n_\alpha\phi-\cos\phi}\\
&=-\frac{i\sin\phi}{2(\sin^2\frac{n_\alpha\phi}{2}-\sin^2\frac{\phi}{2})},
\end{aligned} \tag{E.3.0.8}$$

where in the last step we have used the trigonometric identity

$$\cos\theta=1-2\sin^2\frac{\theta}{2}. \tag{E.3.0.9}$$

So, finally we have

$$S_{J\alpha}=e^{i\phi J}\left(\frac{1}{e^{-i(n_\alpha-1)\phi}-1}\right)-\frac{ie^{-in_\alpha\phi J}}{2}\frac{\sin\phi}{(\sin^2\frac{n_\alpha\phi}{2}-\sin^2\frac{\phi}{2})}. \tag{E.3.0.10}$$

So finally substituting Eq. (E.3.0.10) back in (E.3.0.3), we get

$$i\phi\sum_{K=1}^{\infty}e^{i\phi|J-K|}p_K=e^{i\phi J}\sum_{\alpha=1}^{2}\mathscr{P}_\alpha\left(\frac{i\phi}{e^{-i(n_\alpha-1)\phi}-1}\right)+\frac{1}{2}\sum_{\alpha=1}^{2}\mathscr{P}_\alpha e^{-in_\alpha\phi J}\left(\frac{\phi\sin\phi}{(\sin^2\frac{n_\alpha\phi}{2}-\sin^2\frac{\phi}{2})}\right). \tag{E.3.0.11}$$

E.4 Solving the Dispersion Equations

The characteristic equation for the single polariton solution in scenario one is the same for both the meta-crystal and the meta-film, which is as follows

$$\sin^2\frac{\Phi_0}{2}-\sin^2\frac{\phi}{2}=-\frac{\phi\sin\phi}{4\xi}, \tag{E.4.0.1}$$

where

$$\xi = -\left[\left(\frac{\alpha_{\text{atom}}}{a^2 b}\right)^{-1} - s_0\right], \tag{E.4.0.2}$$

$\Phi_0 = n_0\phi$ with n_0 being the effective index enhancement and nn_0 being the total effective index. We now use the well-known trigonometric identity to rewrite the characteristic equation as

$$\frac{1}{2}(1-\cos\Phi_0) - \frac{1}{2}(1-\cos\phi) = -\frac{\phi\sin\phi}{4\xi}, \tag{E.4.0.3}$$

or

$$\cos\Phi_0 = \cos\phi + \frac{\phi\sin\phi}{2\xi} \equiv Z_0. \tag{E.4.0.4}$$

The principal value of $\arccos Z_0$ is given by

$$\text{Arccos}Z_0 = \frac{1}{i}\text{Ln}\left(Z_0 + i|1-Z_0^2|^{1/2} e^{\frac{i}{2}\text{Arg}(1-Z_0^2)}\right) \tag{E.4.0.5}$$

for the complex-valued Z_0, where $Ln()$ stands for the natural logarithm. To satisfy the boundary condition at $z \to \infty$ for the fields, we must have the imaginary part of n_0 to be positive to ensure that the fields decay into the medium rather than being amplified. So we choose the solution to be

$$\Phi_0 = \text{sgn}[\text{Im}(\text{Arccos}Z_0)]\text{Arccos}Z_0, \tag{E.4.0.6}$$

and

$$n_0 = \frac{\Phi_0}{\phi} = \frac{1}{\phi}\text{sgn}[\text{Im}(\text{Arccos}Z_0)]\text{Arccos}Z_0. \tag{E.4.0.7}$$

The characteristic equation for scenario two is also the same for both the meta-crystal and the meta-film, and yields two solutions for refractive indices of two polaritons. Assuming

$$M \equiv \sin^2\frac{\Phi_\alpha}{2} = \frac{1}{2}(1-\cos\Phi_\alpha), \tag{E.4.0.8}$$

the characteristic equation is written as

$$\frac{M-\sin^2\frac{\phi}{2}}{\frac{1}{4}\phi\sin\phi} = \frac{\frac{\alpha_{\text{atom}}}{a^2 b}}{1-\frac{\alpha_{\text{atom}}}{a^2 b}(s_0+2s_1-4s_1 M)}. \tag{E.4.0.9}$$

Now we define

$$\xi = -\Big[\Big(\frac{\alpha_{\text{atom}}}{a^2 b}\Big)^{-1} - s_0 - 2s_1\Big]. \tag{E.4.0.10}$$

So the characteristic equation now becomes

$$\frac{M - \sin^2\frac{\phi}{2}}{\phi\sin\phi/4} = \frac{1}{4s_1 M - \xi}. \tag{E.4.0.11}$$

On rearranging, we get the following quadratic equation

$$4s_1 M^2 - M(\xi + 4s_1\sin^2\frac{\phi}{2}) + (\xi\sin^2\frac{\phi}{2} - \frac{1}{4}\phi\sin\phi) = 0, \tag{E.4.0.12}$$

whose solutions are the two indices given by

$$\begin{aligned} M &= \frac{(\xi + 4s_1\sin^2\frac{\phi}{2}) \pm \sqrt{(\xi + 4s_1\sin^2\frac{\phi}{2})^2 - 16s_1(\xi\sin^2\frac{\phi}{2} - \frac{1}{4}\phi\sin\phi)}}{8s_1} \\ &= \frac{(\xi + 4s_1\sin^2\frac{\phi}{2}) \pm \sqrt{(\xi - 4s_1\sin^2\frac{\phi}{2})^2 + 4s_1\phi\sin\phi}}{8s_1}. \end{aligned} \tag{E.4.0.13}$$

So from Eqs. (E.4.0.8) and (E.4.0.13) above, we have

$$\cos\Phi_\alpha = 1 - 2M \equiv Z_\alpha, \tag{E.4.0.14}$$

such that

$$Z_\alpha = \frac{(4s_1\cos^2\frac{\phi}{2} - \xi) \pm \sqrt{(\xi - 4s_1\sin^2\frac{\phi}{2})^2 + 4s_1\phi\sin\phi}}{4s_1}. \tag{E.4.0.15}$$

Following similar arguments as those regarding the solution for Φ_0 above, the two solutions for the indices are given by

$$\Phi_\alpha = \text{sgn}[\text{Im}(\text{Arccos}Z_\alpha)]\text{Arccos}Z_\alpha, \tag{E.4.0.16}$$

and

$$n_\alpha = \frac{\Phi_\alpha}{\phi} = \text{sgn}[\text{Im}(\text{Arccos}Z_\alpha)]\text{Arccos}Z_\alpha. \tag{E.4.0.17}$$

E.5 The Polariton Amplitudes and Reflectance from the Meta-crystal in Scenario Two

To get the amplitudes of the two polariton modes present in scenario two, we need to solve the following two coupled linear equations for $\mathscr{P}_1$ and $\mathscr{P}_2$

$$E_0 + \frac{1}{2\varepsilon_0 a^2 b n^2} \sum_{\alpha=1}^{2} \mathscr{P}_\alpha \left(\frac{i\phi}{e^{-i(n_\alpha - 1)\phi} - 1} \right) = 0, \tag{E.5.0.1a}$$

$$\sum_{\alpha=1}^{2} \mathscr{P}_\alpha = 0. \tag{E.5.0.1b}$$

From Eq. (E.5.0.1a), we have

$$2\varepsilon_0 a^2 b n^2 E_0 + i\phi(\mathscr{P}_1 F_1 + \mathscr{P}_2 F_2) = 0, \tag{E.5.0.2}$$

where

$$F_\alpha = \frac{1}{e^{-i(n_\alpha - 1)\phi} - 1}. \tag{E.5.0.3}$$

And from Eq. (E.5.0.1b) we have

$$\mathscr{P}_2 = -\mathscr{P}_1. \tag{E.5.0.4}$$

Solving Eqs. (E.5.0.3) and (E.5.0.4) together, we get

$$\mathscr{P}_1 = \frac{2i\varepsilon_0 a^2 n}{\tilde{\omega}(F_1 - F_2)} E_0, \tag{E.5.0.5a}$$

$$\mathscr{P}_2 = -\frac{2i\varepsilon_0 a^2 n}{\tilde{\omega}(F_1 - F_2)} E_0, \tag{E.5.0.5b}$$

and we have used the expression for $\phi (= \tilde{\omega} n b)$ defined earlier. Also,

$$\begin{aligned} F_1 - F_2 &= \frac{1}{e^{-i(n_1-1)\phi} - 1} - \frac{1}{e^{-i(n_2-1)\phi} - 1}, \\ &= \frac{e^{-i(n_2-1)\phi} - e^{-i(n_1-1)\phi}}{(e^{-i(n_1-1)\phi} - 1)(e^{-i(n_2-1)\phi} - 1)} = e^{i\phi} \frac{e^{-in_2\phi} - e^{-in_1\phi}}{(e^{-i(n_1-1)\phi} - 1)(e^{-i(n_2-1)\phi} - 1)} \end{aligned} \tag{E.5.0.6}$$

So we finally have

$$\mathscr{P}_1 = \frac{2i\varepsilon_0 a^2 n}{\tilde{\omega}} \left(\frac{(e^{-i(n_1-1)\phi}-1)(e^{-i(n_2-1)\phi}-1)}{e^{-i(n_2-1)\phi}-e^{-i(n_1-1)\phi}} \right) E_0, \tag{E.5.0.7a}$$

$$\mathscr{P}_2 = -\frac{2i\varepsilon_0 a^2 n}{\tilde{\omega}} \left(\frac{(e^{-i(n_1-1)\phi}-1)(e^{-i(n_2-1)\phi}-1)}{e^{-i(n_2-1)\phi}-e^{-i(n_1-1)\phi}} \right) E_0. \tag{E.5.0.7b}$$

The reflected field $E_R(z)$ is given by the sum of radiative fields from all the planes at the plane $z<0$. So we have

$$\begin{aligned} E_R(z) &= \frac{i\tilde{\omega}}{2\varepsilon_0 a^2 n} \sum_{K=1}^{\infty} e^{-i\tilde{\omega}n(z-z_K)} p_K \\ &= \frac{i\tilde{\omega}}{2\varepsilon_0 a^2 n} \sum_{\alpha=1}^{2} \sum_{K=1}^{\infty} e^{-i\tilde{\omega}n(z-bK)} \mathscr{P}_\alpha e^{in_\alpha \phi K} \equiv E_R e^{-i\tilde{\omega}nz}, \end{aligned} \tag{E.5.0.8}$$

where

$$\begin{aligned} E_R &= \frac{i\tilde{\omega}}{2\varepsilon_0 a^2 n} \sum_{\alpha=1}^{2} \mathscr{P}_\alpha \sum_{K=1}^{\infty} e^{i(n_\alpha+1)\phi K} \\ &= \frac{i\tilde{\omega}}{2\varepsilon_0 a^2 n} \sum_{\alpha=1}^{2} \mathscr{P}_\alpha \frac{1}{e^{-i(n_\alpha+1)\phi}-1} = \frac{i\tilde{\omega}}{2\varepsilon_0 a^2 n} (\mathscr{P}_1 H_1 + \mathscr{P}_2 H_2), \end{aligned} \tag{E.5.0.9}$$

where

$$H_\alpha = \frac{1}{e^{-i(n_\alpha+1)\phi}-1}. \tag{E.5.0.10}$$

Now, using Eqs. (E.5.0.7a) and (E.5.0.7b) in (E.5.0.9), we write

$$E_R = -\frac{H_1 - H_2}{F_1 - F_2} E_0. \tag{E.5.0.11}$$

Simplifying the numerator above, we have

$$\begin{aligned} H_1 - H_2 &= \frac{1}{e^{-i(n_1+1)\phi}-1} - \frac{1}{e^{-i(n_2+1)\phi}-1} \\ &= e^{-i\phi} \frac{e^{-in_2\phi} - e^{-in_1\phi}}{(e^{-i(n_1+1)\phi}-1)(e^{-i(n_2+1)\phi}-1)}. \end{aligned} \tag{E.5.0.12}$$

Substituting Eqs. (E.5.0.12) and (E.5.0.6) in (E.5.0.11), we finally get

$$E_R = -e^{-2i\phi}\frac{(e^{-i(n_1-1)\phi}-1)(e^{-i(n_2-1)\phi}-1)}{(e^{-i(n_1+1)\phi}-1)(e^{-i(n_2+1)\phi}-1)}. \tag{E.5.0.13}$$

E.6 The Radiative Field at Plane J in the Meta-film

The total radiative field contributions at plane $z = Jb$ in the meta-film is given by the term $iC\sum_{K=1}^{N} e^{i\phi|J-K|}p_K$ in Eqs. (5.40) and (5.58) for scenarios one and two, respectively. The assumed solutions for the dipole moments p_K are of the form

$$p_K = A'_0 e^{i\Phi_0(K-\frac{1}{2})} + B'_0 e^{-i\Phi_0(K-\frac{1}{2})}, \tag{E.6.0.1}$$

for scenario one, and

$$p_K = \sum_{\alpha=1}^{2} p_{K,\alpha} = \sum_{\alpha=1}^{2} (A'_\alpha e^{i\Phi_\alpha(K-\frac{1}{2})} + B'_\alpha e^{-i\Phi_\alpha(K-\frac{1}{2})}), \tag{E.6.0.2}$$

for scenario two. For both scenarios, we need to simplify the sum

$$S_J = \sum_{K=1}^{N} e^{i\phi|J-K|}p_{K,\alpha} = \sum_{K=1}^{N} e^{i\phi|J-K|}(Ae^{i\Phi_\alpha K} + Be^{-i\Phi_\alpha K}), \tag{E.6.0.3}$$

where $\alpha = \{0,1,2\}$, $p_K = p_{K,0}$ for scenario one, and we have assumed

$$A = A'_\alpha e^{-\frac{i}{2}\Phi_\alpha}, \tag{E.6.0.4a}$$

$$B = B'_\alpha e^{\frac{i}{2}\Phi_\alpha}. \tag{E.6.0.4b}$$

We can rewrite Eq. (E.6.0.3) as

$$S_J = T_J^{\text{lower}} + p_{J,\alpha} + T_J^{\text{upper}}, \tag{E.6.0.5}$$

where

$$T_J^{\text{lower}} = \sum_{K=1}^{J-1} e^{i\phi|J-K|} p_{K,\alpha}, \tag{E.6.0.6a}$$

$$T_J^{\text{upper}} = \sum_{K=J+1}^{N} e^{i\phi|J-K|} p_{K,\alpha}. \tag{E.6.0.6b}$$

The special cases for the summation are

$$T_1^{\text{lower}} = 0, \tag{E.6.0.7a}$$

$$T_N^{\text{upper}} = 0, \tag{E.6.0.7b}$$

$$S_1 = p_1. \tag{E.6.0.7c}$$

Now, expanding Eq. (E.6.0.6a), we have

$$T_J^{\text{lower}} = Ae^{i\phi J} \sum_{K=1}^{J-1} e^{i(\Phi_\alpha - \phi)K} + Be^{i\phi J} \sum_{K=1}^{J-1} e^{-i(\phi+\Phi_\alpha)K} \tag{E.6.0.8}$$

From the geometric series formula

$$\sum_{m=M}^{N} r^m = \frac{r^M(1-r^{N-M+1})}{1-r}, \tag{E.6.0.9}$$

we simplify Eq. (E.6.0.8) as

$$T_J^{\text{lower}} = Ae^{i\phi J}\left(\frac{e^{i(\Phi_\alpha-\phi)}(1-e^{i(\Phi_\alpha-\phi)(J-1)})}{1-e^{i(\Phi_\alpha-\phi)}}\right) + Be^{i\phi J}\left(\frac{e^{-i(\Phi_\alpha+\phi)}(1-e^{-i(\Phi_\alpha+\phi)(J-1)})}{1-e^{-i(\Phi_\alpha+\phi)}}\right). \tag{E.6.0.10}$$

Similarly, we expand and simplify Eq. (E.6.0.6b) as

$$T_J^{\text{upper}} = Ae^{-i\phi J} \sum_{K=J+1}^{N} e^{i(\Phi_\alpha+\phi)K} + Be^{-i\phi J} \sum_{K=J+1}^{N} e^{i(\phi-\Phi_\alpha)K}, \tag{E.6.0.11}$$

and then

$$T_J^{\text{upper}} = Ae^{-i\phi J}\left(\frac{e^{i(\Phi_\alpha+\phi)(J+1)}(1-e^{i(\Phi_\alpha+\phi)(N-J)})}{1-e^{i(\Phi_\alpha+\phi)}}\right)+Be^{-i\phi J}\left(\frac{e^{-i(\phi-\Phi_\alpha)(J+1)}(1-e^{-i(\phi-\Phi_\alpha)(N-J)})}{1-e^{-i(\phi-\Phi_\alpha)}}\right). \tag{E.6.0.12}$$

Substituting Eqs. (E.6.0.11) and (E.6.0.12) in (E.6.0.5), we get

$$\begin{aligned} S_J = {} & Ae^{i\phi J}\left(\frac{e^{i(\Phi_\alpha-\phi)}-e^{i(\Phi_\alpha-\phi)J}}{1-e^{i(\Phi_\alpha-\phi)}}\right)+Be^{i\phi J}\left(\frac{e^{-i(\Phi_\alpha+\phi)}-e^{-i(\Phi_\alpha+\phi)J}}{1-e^{-i(\Phi_\alpha+\phi)}}\right)+ \\ & +Ae^{-i\phi J}\left(\frac{e^{i(\Phi_\alpha+\phi)(J+1)}-e^{i(\Phi_\alpha+\phi)(N+1)}}{1-e^{i(\Phi_\alpha+\phi)}}\right)+Be^{-i\phi J}\left(\frac{e^{i(\Phi_\alpha-\phi)(J+1)}-e^{i(\phi-\Phi_\alpha)(N+1)}}{1-e^{i(\phi-\Phi_\alpha)}}\right)+ \\ & +Ae^{i\Phi_\alpha J}+Be^{-i\Phi_\alpha J}, \end{aligned} \tag{E.6.0.13}$$

or

$$\begin{aligned} S_J = {} & A\left(\frac{e^{i(\Phi_\alpha-\phi)}e^{i\phi J}-e^{i\Phi_\alpha J}}{1-e^{i(\Phi_\alpha-\phi)}}\right)+B\left(\frac{e^{-i(\Phi_\alpha+\phi)}e^{i\phi J}-e^{-i\Phi_\alpha J}}{1-e^{i(\Phi_\alpha+\phi)}}\right)+ \\ & +A\left(\frac{e^{i\Phi_\alpha(J+1)}e^{i\phi}-e^{-i\phi J}e^{i(\Phi_\alpha+\phi)(N+1)}}{1-e^{i(\Phi_\alpha+\phi)}}\right)+B\left(\frac{e^{-i\Phi_\alpha(J+1)}e^{i\phi}-e^{-i\phi J}e^{i(\phi-\Phi_\alpha)(N+1)}}{1-e^{i(\phi-\Phi_\alpha)}}\right)+ \\ & +Ae^{i\Phi_\alpha J}+Be^{-i\Phi_\alpha J}. \end{aligned} \tag{E.6.0.14}$$

Collecting the terms with the same J dependence together, we get after some manipulation

$$\begin{aligned} S_J = {} & e^{i\phi J}\left(A\frac{e^{-i(\phi-\Phi_\alpha)}}{1-e^{-i(\phi-\Phi_\alpha)}}+B\frac{e^{-i(\phi+\Phi_\alpha)}}{1-e^{-i(\phi+\Phi_\alpha)}}\right)+ \\ & +e^{-i\phi J}\left(A\frac{e^{i(\phi+\Phi_\alpha)N}}{1-e^{-i(\phi+\Phi_\alpha)}}+B\frac{e^{i(\phi-\Phi_\alpha)}}{1-e^{-i(\phi-\Phi_\alpha)}}\right)+ \\ & +e^{i\Phi_\alpha J}\left(-A\frac{1}{1-e^{-i(\phi-\Phi_\alpha)}}-A\frac{1}{1-e^{-i(\phi+\Phi_\alpha)}}+A\right)+ \\ & +e^{-i\Phi_\alpha J}\left(-B\frac{1}{1-e^{-i(\phi+\Phi_\alpha)}}-B\frac{1}{1-e^{-i(\phi-\Phi_\alpha)}}+B\right). \end{aligned} \tag{E.6.0.15}$$

We then substitute Eqs. (E.6.0.4a) and (E.6.0.4b) in (E.6.0.15) to switch to the notation used in the main text. Then the radiative field contribution $iC\sum_{K=1}^{N} e^{i\phi|J-K|}p_K$ can be written as

$$\begin{aligned} iC\sum_{K=1}^{N} e^{i\phi|J-K|}p_K = {} & e^{i\phi(J-\frac{1}{2})}\left(iA_0'C\frac{e^{-i\frac{1}{2}(\phi-\Phi_0)}}{1-e^{-i(\phi-\Phi_0)}}+iB_0'C\frac{e^{-i\frac{1}{2}(\phi+\Phi_0)}}{1-e^{-i(\phi+\Phi_0)}}\right)+ \\ & +e^{-i\phi J}\left(iA_0'Ce^{-\frac{1}{2}i\Phi_0}\frac{e^{i(\phi+\Phi_0)N}}{1-e^{-i(\phi+\Phi_0)}}+iB_0'C^{\frac{1}{2}i\Phi_0}\frac{e^{i(\phi-\Phi_0)}}{1-e^{-i(\phi-\Phi_0)}}\right)+ \\ & +e^{i\Phi_0(J-\frac{1}{2})}\left(-iA_0'C\frac{1}{1-e^{-i(\phi-\Phi_0)}}-iA_0'C\frac{1}{1-e^{-i(\phi+\Phi_0)}}+iA_0'C\right)+ \\ & +e^{-i\Phi_0(J-\frac{1}{2})}\left(-iB_0'C\frac{1}{1-e^{-i(\phi+\Phi_0)}}-iB_0'C\frac{1}{1-e^{-i(\phi-\Phi_0)}}+iB_0'C\right). \end{aligned} \tag{E.6.0.16}$$

for scenario one, and as

$$
\begin{aligned}
iC\sum_{K=1}^{N} e^{i\phi|J-K|}p_K = \sum_{\alpha=1}^{2}\Bigg[& e^{i\phi(J-\frac{1}{2})}\left(iA'_\alpha C\frac{e^{-i\frac{1}{2}(\phi-\Phi_\alpha)}}{1-e^{-i(\phi-\Phi_\alpha)}} + iB'_\alpha C\frac{e^{-i\frac{1}{2}(\phi+\Phi_\alpha)}}{1-e^{-i(\phi+\Phi_\alpha)}}\right) + \\
& + e^{-i\phi J}\left(iA'_\alpha C e^{-\frac{1}{2}i\Phi_\alpha}\frac{e^{i(\phi+\Phi_\alpha)N}}{1-e^{-i(\phi+\Phi_\alpha)}} + iB'_\alpha C^{\frac{1}{2}i\Phi_\alpha}\frac{e^{i(\phi-\Phi_\alpha)}}{1-e^{-i(\phi-\Phi_\alpha)}}\right) + \\
& + e^{i\Phi_\alpha(J-\frac{1}{2})}\left(-iA'_\alpha C\frac{1}{1-e^{-i(\phi-\Phi_\alpha)}} - iA'_\alpha C\frac{1}{1-e^{-i(\phi+\Phi_\alpha)}} + iA'_\alpha C\right) + \\
& + e^{-i\Phi_\alpha(J-\frac{1}{2})}\left(-iB'_\alpha C\frac{1}{1-e^{-i(\phi+\Phi_\alpha)}} - iB'_\alpha C\frac{1}{1-e^{-i(\phi-\Phi_\alpha)}} + iB'_\alpha C\right)\Bigg].
\end{aligned}
\tag{E.6.0.17}
$$

for scenario two.

With the radiative field contributions to the plane J known, we can now write the total electric field at the plane. For scenario one, we have defined the fields such that $p_J = \varepsilon_0 n^2 \alpha_{\text{atom}} E(J) = \varepsilon_0 n^2 \alpha_{s_0} E_J$, where $E(J)$ is defined by Eq. (5.47) and E_J by Eq. (5.45). So using Eq. (E.6.0.16) and (5.44), we get

$$
\begin{aligned}
E_J = & e^{i\phi(J-\frac{1}{2})}\left(iA'_0 C\frac{e^{-i\frac{1}{2}(\phi-\Phi_0)}}{1-e^{-i(\phi-\Phi_0)}} + iB'_0 C\frac{e^{-i\frac{1}{2}(\phi+\Phi_0)}}{1-e^{-i(\phi+\Phi_0)}} + E_I\right) + \\
& + e^{-i\phi J}\left(iA'_0 C e^{-\frac{1}{2}i\Phi_0}\frac{e^{i(\phi+\Phi_0)N}}{1-e^{-i(\phi+\Phi_0)}} + iB'_0 C^{\frac{1}{2}i\Phi_0}\frac{e^{i(\phi-\Phi_0)}}{1-e^{-i(\phi-\Phi_0)}}\right) + \\
& + e^{i\Phi_0(J-\frac{1}{2})}\left(-iA'_0 C\frac{1}{1-e^{-i(\phi-\Phi_0)}} - iA'_0 C\frac{1}{1-e^{-i(\phi+\Phi_0)}} + iA'_0 C\right) + \\
& + e^{-i\Phi_0(J-\frac{1}{2})}\left(-iB'_0 C\frac{1}{1-e^{-i(\phi+\Phi_0)}} - iB'_0 C\frac{1}{1-e^{-i(\phi-\Phi_0)}} + iB'_0 C\right).
\end{aligned}
\tag{E.6.0.18}
$$

For scenario two, we have from Eqs. (5.40), Eqs. (E.6.0.17) and (5.7)

$$
\begin{aligned}
E(J) &= e^{i\phi(J-\frac{1}{2})}\left[E_I + \sum_{\alpha=1}^{2}\left(iA'_\alpha C\frac{e^{-i\frac{1}{2}(\phi-\Phi_\alpha)}}{1-e^{-i(\phi-\Phi_\alpha)}} + iB'_\alpha C\frac{e^{-i\frac{1}{2}(\phi+\Phi_\alpha)}}{1-e^{-i(\phi+\Phi_\alpha)}}\right)\right] + \\
&+ e^{-i\phi J}\sum_{\alpha=1}^{2}\left(iA'_\alpha C e^{-\frac{1}{2}i\Phi_\alpha}\frac{e^{i(\phi+\Phi_\alpha)N}}{1-e^{-i(\phi+\Phi_\alpha)}} + iB'_\alpha C^{\frac{1}{2}i\Phi_\alpha}\frac{e^{i(\phi-\Phi_\alpha)N}}{1-e^{-i(\phi-\Phi_\alpha)}}\right) + \\
&+ \sum_{\alpha=1}^{2}\left[e^{i\Phi_\alpha(J-\frac{1}{2})}\left(-iA'_\alpha C\frac{1}{1-e^{-i(\phi-\Phi_\alpha)}} - iA'_\alpha C\frac{1}{1-e^{-i(\phi+\Phi_\alpha)}} + iA'_\alpha C\right) + \right. \\
&\left. + e^{-i\Phi_\alpha(J-\frac{1}{2})}\left(-iB'_\alpha C\frac{1}{1-e^{-i(\phi+\Phi_\alpha)}} - iB'_\alpha C\frac{1}{1-e^{-i(\phi-\Phi_\alpha)}} + iB'_\alpha C\right)\right] + L(J),
\end{aligned}
\tag{E.6.0.19}
$$

where $L(J)$ is given by Eq. (5.7). We now simplify $L(J)$ for $1 < J < N$, which we rewrite below

$$
L(J) = \frac{1}{\varepsilon_0 n^2 a^2 b}[s_0 p_J + s_1(p_{J+1} + p_{J-1})], \tag{E.6.0.20}
$$

Now we simplify the expression for $L(J)$ above for scenario two. Using Eq. (E.6.0.2) in (E.6.0.20) above, we have

$$
\begin{aligned}
L(J) &= \frac{1}{\varepsilon_0 n^2 a^2 b}\left[s_0\sum_{\alpha=1}^{2}(A'_\alpha e^{i\Phi_\alpha(J-\frac{1}{2})} + B'_\alpha e^{-i\Phi_\alpha(J-\frac{1}{2})}) + \right. \\
&\left. + s_1\sum_{\alpha=1}^{2}\{A'_\alpha e^{i\Phi_\alpha(J-\frac{1}{2})}(e^{i\Phi_\alpha} + e^{-i\Phi_\alpha}) + B'_\alpha e^{-i\Phi_\alpha(J-\frac{1}{2})}(e^{i\Phi_\alpha} + e^{-i\Phi_\alpha})\}\right] \\
&= \frac{1}{\varepsilon_0 n^2 a^2 b}\sum_{\alpha=1}^{2}[\{A'_\alpha e^{i\Phi_\alpha(J-\frac{1}{2})} + B'_\alpha e^{-i\Phi_\alpha(J-\frac{1}{2})}\}\{s_0 + s_1(e^{i\Phi_\alpha} + e^{-i\Phi_\alpha})\}]
\end{aligned}
\tag{E.6.0.21}
$$

Since there is only one nearest-neighbor plane for the planes at the two surfaces, or $J = 1$ and $J = N$, $L(J)$ for these two planes will be different from that derived in

Eq. (E.6.0.21). For $J = 1$, we have

$$\begin{aligned} L(1) &= \frac{1}{\varepsilon_0 n^2 a^2 b}[s_0 p_1 + s_1 p_2] \\ &= \frac{1}{\varepsilon_0 n^2 a^2 b}\sum_{\alpha=1}^{2}[s_0(A'_\alpha e^{i\frac{\Phi_\alpha}{2}} + B'_\alpha e^{-i\frac{\Phi_\alpha}{2}}) + s_1(A'_\alpha e^{i\frac{3\Phi_\alpha}{2}} + B'_\alpha e^{-i\frac{3\Phi_\alpha}{2}})] \\ &= \frac{1}{\varepsilon_0 n^2 a^2 b}\sum_{\alpha=1}^{2}[A'_\alpha e^{i\frac{\Phi_\alpha}{2}}(s_0 + s_1 e^{i\Phi_\alpha}) + B'_\alpha e^{-i\frac{\Phi_\alpha}{2}}(s_0 + s_1 e^{-i\Phi_\alpha})] \end{aligned} \tag{E.6.0.22}$$

and for $J = N$, we have

$$\begin{aligned} L(N) &= \frac{1}{\varepsilon_0 n^2 a^2 b}[s_0 p_N + s_1 p_{N-1}] \\ &= \frac{1}{\varepsilon_0 n^2 a^2 b}\sum_{\alpha=1}^{2}[s_0(A'_\alpha e^{i\Phi_\alpha(N-\frac{1}{2})} + B'_\alpha e^{-i\Phi_\alpha(N-\frac{1}{2})}) + s_1(A'_\alpha e^{i\Phi_\alpha(N-\frac{3}{2})} + B'_\alpha e^{-i\Phi_\alpha(N-\frac{3}{2})})] \\ &= \frac{1}{\varepsilon_0 n^2 a^2 b}\sum_{\alpha=1}^{2}[A'_\alpha e^{i\Phi_\alpha(N-\frac{1}{2})}(s_0 + s_1 e^{-i\Phi_\alpha}) + B'_\alpha e^{-i\Phi_\alpha(N-\frac{1}{2})}(s_0 + s_1 e^{i\Phi_\alpha})]. \end{aligned} \tag{E.6.0.23}$$

E.7 The Characteristic Equation for Polaritons in the Meta-film

The characteristic equation for the single (forward and backward propagating) polariton mode in meta-film is given by comparing the coefficients of the exponential term $e^{i\Phi_0(J-\frac{1}{2})}$ or $e^{-i\Phi_0(J-\frac{1}{2})}$ in the expressions for p_J. The equation is restated below

$$iC\varepsilon_0 n^2 \alpha_{s_0}\left(1 - \frac{1}{1-e^{-i(\phi+\Phi_0)}} - \frac{1}{1-e^{-i(\phi-\Phi_0)}}\right) = 1, \tag{E.7.0.1}$$

where

$$\alpha_{s_0} = \frac{\alpha_{\text{atom}}}{1 - \frac{\alpha_{\text{atom}}}{a^2 b} s_0}. \tag{E.7.0.2}$$

Rearranging Eq. (E.7.0.1), we write

$$1-\frac{1}{1-e^{-i(\phi+\Phi_0)}}-\frac{1}{1-e^{-i(\phi-\Phi_0)}}=\frac{1-\frac{\alpha_{\text{atom}}}{a^2b}s_0}{iC\varepsilon_0 n^2\alpha_{\text{atom}}}=\frac{1}{iC\varepsilon_0 n^2\alpha_{s_0}}. \tag{E.7.0.3}$$

Similarly for scenario two, we compare the coefficients of the exponential term $e^{i\Phi_\alpha(J-\frac{1}{2})}$ or $e^{-}i\Phi_\alpha(J-\frac{1}{2})$ in the expressions for p_J in the bulk planes $(1<J<N)$ to get the characteristic equations for the effective index of the polariton $\alpha=\{1,2\}$. So we have

$$iC\varepsilon_0 n^2\alpha_{\text{atom}}\left(1-\frac{1}{1-e^{-i(\phi+\Phi_\alpha)}}-\frac{1}{1-e^{-i(\phi-\Phi_\alpha)}}\right)+\frac{\alpha_{\text{atom}}}{a^2b}(s_0+2s_1\cos\Phi_\alpha)=1, \tag{E.7.0.4}$$

which after some rearranging can be written as

$$1-\frac{1}{1-e^{-i(\phi+\Phi_\alpha)}}-\frac{1}{1-e^{-i(\phi-\Phi_\alpha)}}=\frac{1}{iC\varepsilon_0 n^2\alpha_{\text{atom}}}\left(1-\frac{\alpha_{\text{atom}}}{a^2b}(s_0+2s_1\cos\Phi_\alpha)\right). \tag{E.7.0.5}$$

Recalling from the main text that we have defined

$$\chi_\alpha=\frac{\frac{\alpha_{\text{atom}}}{a^2b}}{1-\frac{\alpha_{\text{atom}}}{a^2b}(s_0+2s_1\cos\Phi_\alpha)}, \tag{E.7.0.6}$$

Eq. (E.7.0.5) can then be written as

$$1-\frac{1}{1-e^{-i(\phi+\Phi_\alpha)}}-\frac{1}{1-e^{-i(\phi-\Phi_\alpha)}}=\frac{1}{iC\varepsilon_0 n^2\alpha_{\text{atom}}}\frac{\alpha_{\text{atom}}}{a^2b\chi_\alpha}. \tag{E.7.0.7}$$

The left hand side of the characteristic equations for both scenarios (Eqs. (E.7.0.3) and (E.7.0.7)) are the same, which we now simplify as

$$\begin{aligned}
&1-\frac{1}{1-e^{-i(\phi+\Phi_\alpha)}}-\frac{1}{1-e^{-i(\phi-\Phi_\alpha)}}= \\
&=\frac{(1-e^{-i(\phi+\Phi_\alpha)})(1-e^{-i(\phi-\Phi_\alpha)})-(1-e^{-i(\phi-\Phi_\alpha)})-(1-e^{-i(\phi+\Phi_\alpha)})}{(1-e^{-i(\phi+\Phi_\alpha)})(1-e^{-i(\phi-\Phi_\alpha)})} \\
&=\frac{1+e^{-2i\phi}-e^{-i(\phi+\Phi_\alpha)}-e^{-i(\phi-\Phi_\alpha)}-1+e^{-i(\phi-\Phi_\alpha)}-1+e^{-i(\phi+\Phi_\alpha)}}{1+e^{-2i\phi}-e^{-i(\phi+\Phi_\alpha)}-e^{-i(\phi-\Phi_\alpha)}} \\
&=\frac{e^{-2i\phi}-1}{1+e^{-2i\phi}-e^{-i(\phi+\Phi_\alpha)}-e^{-i(\phi-\Phi_\alpha)}}=\frac{e^{-i\phi}-e^{i\phi}}{e^{i\phi}+e^{-i\phi}-e^{-i\Phi_\alpha}-e^{-i\Phi_\alpha}} \\
&=\frac{-2i\sin\phi}{2\cos\phi-2\cos\Phi_\alpha}=\frac{-i\sin\phi}{\cos\phi-\cos\Phi_\alpha},
\end{aligned} \tag{E.7.0.8}$$

and the final expression holds true for $\alpha=\{0,1,2\}$. Substituting the final expression for the left hand side of the characteristic equation in Eq. (E.7.0.3), and using $C=\frac{\phi}{2\varepsilon_0 a^2 b n^2}$ that we defined earlier, we get

$$\frac{\cos\phi-\cos\Phi_0}{\sin\phi}=C\varepsilon_0 n^2\alpha_{s_0}=\alpha_{s_0}\frac{\phi}{2a^2b} \tag{E.7.0.9}$$

or

$$\frac{2\sin^2\frac{\Phi_0}{2}-2\sin^2\frac{\phi}{2}}{\sin\phi}=\frac{\alpha_{s_0}}{a^2b}\frac{\phi}{2}, \tag{E.7.0.10}$$

and finally

$$\frac{\sin^2\frac{\Phi_0}{2}-\sin^2\frac{\phi}{2}}{\phi\sin\phi/4}=\frac{\alpha_{s_0}}{a^2b}. \tag{E.7.0.11}$$

Additionally, using an earlier form of the left hand side in Eq. (E.7.0.3), we have

$$\frac{e^{-2i\phi}-1}{(1-e^{-i(\phi+\Phi_\alpha)})(1-e^{-i(\phi-\Phi_\alpha)})}=\frac{1}{iC\varepsilon_0 n^2\alpha_{s_0}}, \tag{E.7.0.12}$$

or

$$iC\varepsilon_0 n^2\alpha_{s_0}=\frac{(1-e^{-i(\phi+\Phi_\alpha)})(1-e^{-i(\phi-\Phi_\alpha)})}{e^{-2i\phi}-1}. \tag{E.7.0.13}$$

Similarly, using Eqs. (E.7.0.5) and (E.7.0.8) we have for scenario two

$$\frac{2\sin^2\frac{\Phi_\alpha}{2}-2\sin^2\frac{\phi}{2}}{\sin\phi}=C\varepsilon_0 n^2\frac{\alpha_{\text{atom}}}{1-\frac{\alpha_{\text{atom}}}{a^2b}(s_0+2s_1\cos\Phi_\alpha)} \tag{E.7.0.14}$$

or

$$\frac{\sin^2\frac{\Phi_\alpha}{2}-\sin^2\frac{\phi}{2}}{\phi\sin\phi/4}=\frac{\frac{\alpha_{\text{atom}}}{a^2b}}{1-\frac{\alpha_{\text{atom}}}{a^2b}(s_0+2s_1\cos\Phi_\alpha)}. \tag{E.7.0.15}$$

Also, using an earlier form of the left hand side of the characteristic equation in (E.7.0.8) in (E.7.0.7), we have

$$\frac{e^{-2i\phi}-1}{(1-e^{-i(\phi+\Phi_\alpha)})(1-e^{-i(\phi-\Phi_\alpha)})}=\frac{1}{iC\varepsilon_0 n^2\alpha_{\text{atom}}}\frac{\alpha_{\text{atom}}}{a^2b\chi_\alpha}. \tag{E.7.0.16}$$

Or

$$iC\varepsilon_0 n^2\alpha_{\text{atom}}=\frac{\alpha_{\text{atom}}}{a^2b\chi_\alpha}\frac{(1-e^{-i(\phi+\Phi_\alpha)})(1-e^{-i(\phi-\Phi_\alpha)})}{e^{-2i\phi}-1}. \tag{E.7.0.17}$$

E.8 Transmitted Field through the Meta-film

E.8.1 Scenario One

We have defined the transmitted field E_T as the field at the plane $z=(N+\frac{1}{2})b$, which we restate below

$$E_T=E_I e^{i\phi N}+iC\sum_{J=1}^{N}e^{i\phi(N+\frac{1}{2}-J)}p_J, \tag{E.8.1.1}$$

with

$$p_J=A_0' e^{i\Phi_0(J-\frac{1}{2})}+B_0' e^{-i\Phi_0(J-\frac{1}{2})}. \tag{E.8.1.2}$$

So we have

$$E_T=E_I e^{i\phi N}+iA_0' Ce^{i\phi(N+\frac{1}{2})}e^{-i\Phi_0\frac{1}{2}}\sum_{J=1}^{N}e^{i(\Phi_0-\phi)J}++iB_0' Ce^{i\phi(N+\frac{1}{2})}e^{i\Phi_0\frac{1}{2}}\sum_{J=1}^{N}e^{-i(\Phi_0+\phi)J}, \tag{E.8.1.3}$$

or

$$E_T e^{-i\phi N} = E_I + iA_0' C e^{i\frac{1}{2}(\phi-\Phi_0)} \sum_{J=1}^{N} e^{-i(\phi-\Phi_0)J} + iB_0' C^{i\frac{1}{2}(\phi+\Phi_0)} \sum_{J=1}^{N} e^{-i(\phi+\Phi_0)J}. \tag{E.8.1.4}$$

Doing the sums we have

$$\begin{aligned} &E_T e^{-i\phi N} = \\ &= E_I + iA_0' C e^{i\frac{1}{2}(\phi-\Phi_0)} e^{-i(\phi-\Phi_0)} \frac{1-e^{-i(\phi-\Phi_0)N}}{1-e^{-i(\phi-\Phi_0)}} + iB_0' C e^{i\frac{1}{2}(\phi+\Phi_0)} e^{-i(\phi+\Phi_0)} \frac{1-e^{-i(\phi+\Phi_0)N}}{1-e^{-i(\phi+\Phi_0)}} \\ &= E_I + \frac{iA_0' C e^{-i\frac{1}{2}(\phi-\Phi_0)}}{1-e^{-i(\phi-\Phi_0)}}(1-e^{-i(\phi-\Phi_0)N}) + \frac{iB_0' C e^{-i\frac{1}{2}(\phi+\Phi_0)}}{1-e^{-i(\phi+\Phi_0)}}(1-e^{-i(\phi+\Phi_0)N}). \end{aligned} \tag{E.8.1.5}$$

Now we have from Eq. (5.43) of the main text

$$\frac{iA_0' C e^{-i\frac{1}{2}(\phi-\Phi_0)}}{1-e^{-i(\phi-\Phi_0)}} = -\frac{E_I}{1-r_{10,0}^2 e^{2iN\Phi_0}}, \tag{E.8.1.6}$$

and using the definition of the effective Fresnel reflection coefficient $r_{10,0}$ in Eqs. (5.53) and (5.52), we have

$$\frac{iB_0' C e^{-i\frac{1}{2}(\phi+\Phi_0)}}{1-e^{-i(\phi+\Phi_0)}} = r_{10,0} e^{2iN\Phi_0} \frac{iA_0' C e^{-i\frac{1}{2}(\phi+\Phi_0)}}{1-e^{-i(\phi+\Phi_0)}}. \tag{E.8.1.7}$$

Now substituting the expression for $iA_0' C$ from Eq. (E.8.1.6) in (E.8.1.7), we have

$$\begin{aligned} \frac{iB_0' C e^{-i\frac{1}{2}(\phi+\Phi_0)}}{1-e^{-i(\phi+\Phi_0)}} &= -r_{10,0} e^{2iN\Phi_0} \frac{e^{-i\Phi_0}(1-e^{-i(\phi-\Phi_0)})}{1-e^{-i(\phi+\Phi_0)}} \frac{E_I}{1-r_{10,0}^2 e^{2iN\Phi_0}} \\ &= \frac{r_{10,0}^2 e^{2iN\Phi_0} E_I}{1-r_{10,0}^2 e^{2iN\Phi_0}}. \end{aligned} \tag{E.8.1.8}$$

Substituting Eqs. (E.8.1.6) and (E.8.1.8) in (E.8.1.4), we now have

$$
\begin{aligned}
&E_T e^{-i\phi N} = \\
&= E_I - \frac{E_I}{1-r_{10,0}^2 e^{2iN\Phi_0}}(1-e^{-i(\phi-\Phi_0)N}) + \frac{r_{10,0}^2 e^{2iN\Phi_0} E_I}{1-r_{10,0}^2 e^{2iN\Phi_0}}(1-e^{-i(\phi+\Phi_0)N}) \\
&= E_I\left(1 - \frac{1}{1-r_{10,0}^2 e^{2iN\Phi_0}} + \frac{r_{10,0}^2 e^{2iN\Phi_0}}{1-r_{10,0}^2 e^{2iN\Phi_0}}\right) + \frac{E_I e^{-i(\phi-\Phi_0)N}}{1-r_{10,0}^2 e^{2iN\Phi_0}} - \frac{E_I r_{10,0}^2 e^{2iN\Phi_0} e^{-i(\phi+\Phi_0)N}}{1-r_{10,0}^2 e^{2iN\Phi_0}} \\
&= \frac{E_I e^{-i\phi N} e^{iN\Phi_0}}{1-r_{10,0}^2 e^{2iN\Phi_0}} - \frac{r_{10,0}^2 E_I e^{-i\phi N} e^{iN\Phi_0}}{1-r_{10,0}^2 e^{2iN\Phi_0}}.
\end{aligned}
\tag{E.8.1.9}
$$

Or

$$
E_T = \frac{E_I(1-r_{10,0}^2)e^{iN\Phi_0}}{1-r_{10,0}^2 e^{2iN\Phi_0}}. \tag{E.8.1.10}
$$

Now weuse the continuum electrodynamics relation

$$
1 - r_{10,0}^2 = t_{10,0}t_{01,0}, \tag{E.8.1.11}
$$

to get the final expression for E_T as

$$
E_T = \frac{t_{10,0}t_{01,0}e^{iN\Phi_0}}{1-r_{10,0}^2 e^{2iN\Phi_0}} E_I. \tag{E.8.1.12}
$$

We have previously defined $t_{01,0}$ as

$$
t_{01,0} = \frac{(1-e^{-2i\phi})e^{\frac{i}{2}(\phi-\Phi_0)}}{1-e^{-i(\phi+\Phi_0)}}, \tag{E.8.1.13}
$$

and $r_{10,0}$ as

$$
r_{10,0} = \frac{e^{-i(\phi-\Phi_0)}-1}{1-e^{-i(\phi+\Phi_0)}} e^{-i\Phi_0}. \tag{E.8.1.14}
$$

So we can now get the expression for $t_{10,0}$ by simplifying

$$
t_{10,0} = \frac{1-r_{10,0}^2}{t_{01,0}}. \tag{E.8.1.15}
$$

We first simplify the numerator as

$$\begin{aligned}1-r_{10,0}^2 &= \frac{(1-e^{-i(\phi+\Phi_0)})^2-(1-e^{-i(\phi-\Phi_0)})^2e^{-2i\Phi_0}}{(1-e^{-i(\phi+\Phi_0)})^2}\\ &= \frac{1-2e^{-i(\phi+\Phi_0)}+e^{-2i(\phi+\Phi_0)}-(1-2e^{-i(\phi-\Phi_0)}+e^{-2i(\phi-\Phi_0)})e^{-2i\Phi_0}}{(1-e^{-i(\phi+\Phi_0)})^2}\\ &= \frac{1+e^{-2i(\phi+\Phi_0)}-e^{-2i\phi}-e^{-2i\Phi_0}}{(1-e^{-i(\phi+\Phi_0)})^2} = \frac{(1-e^{-2i\phi})(1-e^{-2i\Phi_0})}{(1-e^{-i(\phi+\Phi_0)})^2},\end{aligned} \tag{E.8.1.16}$$

and then substitute in Eq. (E.8.1.15) to get

$$\begin{aligned}t_{10,0} &= \frac{(1-e^{-2i\phi})(1-e^{-2i\Phi_0})}{(1-e^{-i(\phi+\Phi_0)})^2}\frac{1-e^{-i(\phi+\Phi_0)}}{(1-e^{-2i\phi})e^{\frac{i}{2}(\phi-\Phi_0)}}\\ &= \frac{((1-e^{-2i\Phi_0})e^{\frac{i}{2}(\Phi_0-\phi)}}{(1-e^{-i(\phi+\Phi_0)})}.\end{aligned} \tag{E.8.1.17}$$

E.8.2 Scenario Two

We have defined the transmitted field in scenario two as the total field at the plane $z > Nb$, which is given by

$$E_T(z) = E_I e^{-i\frac{\phi}{2}}e^{i\tilde{\omega}nz} + iC\sum_{J=1}^{N} e^{i\tilde{\omega}n(z-bJ)}p_J, \tag{E.8.2.1}$$

where

$$p_J = \sum_{\alpha=1}^{2}(A'_\alpha e^{i\Phi_\alpha(J-\frac{1}{2})} + B'_\alpha e^{-i\Phi_\alpha(J-\frac{1}{2})}). \tag{E.8.2.2}$$

So we have

$$\begin{aligned}&E_T(z)e^{i\frac{\phi}{2}}e^{-i\tilde{\omega}nz} =\\ &= E_I + iCe^{i\frac{\phi}{2}}\sum_{\alpha=1}^{2}A'_\alpha\sum_{J=1}^{N}[e^{-i(\phi-\Phi_\alpha)J}e^{-i\frac{\Phi_\alpha}{2}} + r_{10,\alpha}e^{i2N\Phi_\alpha}e^{-i(\phi+\Phi_\alpha)J}e^{i\frac{\Phi_\alpha}{2}}],\end{aligned} \tag{E.8.2.3}$$

where we have used the definition of Fresnel reflection coefficient $r_{10,\alpha}$ from the main text

$$\frac{B'_\alpha}{A'_\alpha} = r_{10,\alpha} e^{i2N\Phi_\alpha} = \frac{e^{-i\phi} - e^{-i\Phi_\alpha}}{1 - e^{-i(\phi+\Phi_\alpha)}} e^{i2N\Phi_\alpha} \tag{E.8.2.4}$$

Doing the sums in Eq. (E.8.2.3), we have

$$\begin{aligned}
&E_T(z) e^{i\frac{\phi}{2}} e^{-i\tilde{\omega}nz} = \\
&= E_I + iCe^{i\frac{\phi}{2}} \sum_{\alpha=1}^{2} A'_\alpha e^{-i\frac{\Phi_\alpha}{2}} \left[e^{-i(\phi-\Phi_\alpha)} \left(\frac{1 - e^{-iN(\phi-\Phi_\alpha)}}{1 - e^{-i(\phi-\Phi_\alpha)}} \right) + \right. \\
&\left. + r_{10,\alpha} e^{i2N\Phi_\alpha} e^{i\frac{\Phi_\alpha}{2}} e^{-i(\phi+\Phi_\alpha)} \left(\frac{1 - e^{-iN(\phi+\Phi_\alpha)}}{1 - e^{-i(\phi+\Phi_\alpha)}} \right) \right] \\
&= E_I + iC \sum_{\alpha=1}^{2} A'_\alpha \left[\frac{e^{-\frac{i}{2}(\phi-\Phi_\alpha)}}{1 - e^{-i(\phi-\Phi_\alpha)}} (1 - e^{-iN(\phi-\Phi_\alpha)}) + r_{10,\alpha} e^{i2N\Phi_\alpha} \frac{e^{-\frac{i}{2}(\phi+\Phi_\alpha)}}{1 - e^{-i(\phi+\Phi_\alpha)}} (1 - e^{-iN(\phi+\Phi_\alpha)}) \right] \\
&= E_I + iC \sum_{\alpha=1}^{2} A'_\alpha \frac{e^{-\frac{i}{2}(\phi-\Phi_\alpha)}}{1 - e^{-i(\phi-\Phi_\alpha)}} \left[1 - e^{-iN(\phi-\Phi_\alpha)} + r_{10,\alpha} e^{i2N\Phi_\alpha} \frac{e^{-i\Phi_\alpha} - e^{-i\phi}}{1 - e^{-i(\phi+\Phi_\alpha)}} (1 - e^{-iN(\phi+\Phi_\alpha)}) \right] \\
&= E_I + iC \sum_{\alpha=1}^{2} A'_\alpha \frac{e^{-\frac{i}{2}(\phi-\Phi_\alpha)}}{1 - e^{-i(\phi-\Phi_\alpha)}} [1 - e^{-iN(\phi-\Phi_\alpha)} - r_{10,\alpha}^2 e^{i2N\Phi_\alpha} (1 - e^{-iN(\phi+\Phi_\alpha)})] \\
&= E_I + iC \sum_{\alpha=1}^{2} A'_\alpha \frac{e^{-\frac{i}{2}(\phi-\Phi_\alpha)}}{1 - e^{-i(\phi-\Phi_\alpha)}} (1 - r_{10,\alpha}^2 e^{i2N\Phi_\alpha}) - iC \sum_{\alpha=1}^{2} A'_\alpha \frac{e^{-\frac{i}{2}(\phi-\Phi_\alpha)}}{1 - e^{-i(\phi-\Phi_\alpha)}} (e^{-iN(\phi-\Phi_\alpha)} - \\
&- r_{10,\alpha}^2 e^{i2N\Phi_\alpha} e^{-iN(\phi+\Phi_\alpha)})
\end{aligned} \tag{E.8.2.5}$$

Recalling from main text that

$$E_I = -iC \sum_{\alpha=1}^{2} A'_\alpha \frac{e^{-\frac{i}{2}(\phi-\Phi_\alpha)}}{1 - e^{-i(\phi-\Phi_\alpha)}} (1 - r_{10,\alpha}^2 e^{i2N\Phi_\alpha}), \tag{E.8.2.6}$$

the first two terms on the right cancel in the final version of Eq. (E.8.2.5). So we now have

$$E_T(z)e^{i\frac{\phi}{2}}e^{-i\tilde{\omega}nz} = -iC\sum_{\alpha=1}^{2}A'_\alpha\frac{e^{-\frac{i}{2}(\phi-\Phi_\alpha)}}{1-e^{-i(\phi-\Phi_\alpha)}}(e^{-iN(\phi-\Phi_\alpha)}-r_{10,\alpha}^2e^{i2N\Phi_\alpha}e^{-iN(\phi+\Phi_\alpha)})$$
$$= -iC\sum_{\alpha=1}^{2}A'_\alpha\frac{e^{-i(\phi-\Phi_\alpha)(N+\frac{1}{2})}}{1-e^{-i(\phi-\Phi_\alpha)}}(1-r_{10,\alpha}^2e^{i2N\Phi_\alpha}) \tag{E.8.2.7}$$

or

$$E_T(z) = -iCe^{-i\frac{\phi}{2}}e^{i\tilde{\omega}nz}\sum_{\alpha=1}^{2}A'_\alpha\frac{e^{-\frac{i}{2}(\phi-\Phi_\alpha)}}{1-e^{-i(\phi-\Phi_\alpha)}}e^{-i(\phi-\Phi_\alpha)N}(1-r_{10,\alpha}^2). \tag{E.8.2.8}$$

E.9 Reflected Field from the Meta-film

E.9.1 Scenario One

The reflected field E_R is given by the total backward propagating field at the plane $z=-b/2$, or

$$E_R = iC\sum_{J=1}^{N}e^{i\phi(J-\frac{1}{2})}p_J, \tag{E.9.1.1}$$

where

$$p_J = A'_0e^{i\Phi_0(J-\frac{1}{2})}+B'_0e^{-i\Phi_0(J-\frac{1}{2})}. \tag{E.9.1.2}$$

So we have

$$E_R = iA'_0Ce^{-\frac{i}{2}(\phi+\Phi_0)}\sum_{J=1}^{N}e^{i(\phi+\Phi_0)J}+iB'_0Ce^{-\frac{i}{2}(\phi-\Phi_0)}\sum_{J=1}^{N}e^{i(\phi-\Phi_0)J}$$
$$= iA'_0Ce^{-\frac{i}{2}(\phi+\Phi_0)}e^{i(\phi+\Phi_0)}\frac{1-e^{i(\phi+\Phi_0)N}}{1-e^{i(\phi+\Phi_0)}}+iB'_0Ce^{-\frac{i}{2}(\phi-\Phi_0)}e^{i(\phi-\Phi_0)}\frac{1-e^{i(\phi-\Phi_0)N}}{1-e^{i(\phi-\Phi_0)}}$$
$$= \frac{iA'_0Ce^{-\frac{i}{2}(\phi+\Phi_0)}}{e^{-i(\phi+\Phi_0)}-1}(1-e^{i(\phi+\Phi_0)N})+\frac{iB'_0Ce^{-\frac{i}{2}(\phi-\Phi_0)}}{e^{-i(\phi-\Phi_0)}-1}(1-e^{i(\phi-\Phi_0)N})$$
$$= \frac{iA'_0Ce^{-\frac{i}{2}(\phi-\Phi_0)}}{1-e^{-i(\phi+\Phi_0)}}e^{-i\Phi_0}(e^{i(\phi+\Phi_0)N}-1)+\frac{iB'_0Ce^{-\frac{i}{2}(\phi+\Phi_0)}}{1-e^{-i(\phi-\Phi_0)}}e^{i\Phi_0}(e^{i(\phi-\Phi_0)N}-1). \tag{E.9.1.3}$$

Now we do some further processing

$$\begin{aligned}
E_R &= \frac{iA_0' C e^{-\frac{i}{2}(\phi-\Phi_0)}}{1-e^{-i(\phi-\Phi_0)}} \frac{1-e^{-i(\phi-\Phi_0)}}{1-e^{-i(\phi+\Phi_0)}} e^{-i\Phi_0}(e^{i(\phi+\Phi_0)N}-1) + \\
&+ \frac{iB_0' C e^{-\frac{i}{2}(\phi+\Phi_0)}}{1-e^{-i(\phi+\Phi_0)}} \frac{1-e^{-i(\phi+\Phi_0)}}{1-e^{-i(\phi-\Phi_0)}} e^{i\Phi_0}(e^{i(\phi-\Phi_0)N}-1) \\
&= \frac{iA_0' C e^{-\frac{i}{2}(\phi-\Phi_0)}}{1-e^{-i(\phi-\Phi_0)}} r_{10,0}(1-e^{i(\phi+\Phi_0)N}) + \frac{iB_0' C e^{-\frac{i}{2}(\phi+\Phi_0)}}{1-e^{-i(\phi+\Phi_0)}} \frac{1}{r_{10,0}}(e^{i(\phi-\Phi_0)N}-1).
\end{aligned} \tag{E.9.1.4}$$

Now using the following expression for E_I derived earlier in the main text

$$E_I = -\frac{iA_0' C e^{-\frac{i}{2}(\phi-\Phi_0)}}{1-e^{-i(\phi-\Phi_0)}}(1-r_{10,0}^2 e^{i2N\Phi_0}), \tag{E.9.1.5}$$

and Eq. (E.8.1.8) in the expression for E_R, we get

$$\begin{aligned}
E_R &= -\frac{E_I}{1-r_{10,0}^2 e^{i2N\Phi_0}} r_{10,0}(1-e^{i(\phi+\Phi_0)N}) + \frac{r_{10,0}^2 E_I e^{2iN\Phi_0}}{1-r_{10,0}^2 e^{i2N\Phi_0}} \frac{1}{r_{10,0}}(1-e^{i(\phi-\Phi_0)N}) \\
&= -\frac{r_{10,0} E_I}{1-r_{10,0}^2 e^{i2N\Phi_0}} + \frac{r_{10,0} E_I e^{i2N\Phi_0}}{1-r_{10,0}^2 e^{i2N\Phi_0}} + \frac{r_{10,0} E_I e^{iN(\phi+\Phi_0)}}{1-r_{10,0}^2 e^{i2N\Phi_0}} - \frac{r_{10,0} E_I e^{i2N\Phi_0} e^{iN(\phi-\Phi_0)}}{1-r_{10,0}^2 e^{i2N\Phi_0}} \\
&= \frac{-r_{10,0} + r_{10,0} e^{i2N\Phi_0}}{1-r_{10,0}^2 e^{i2N\Phi_0}} E_I.
\end{aligned} \tag{E.9.1.6}$$

Following the definition from continuum electrodynamics $r_{01,0} = -r_{10,0}$, we get

$$\begin{aligned} E_R &= \frac{r_{01,0} + r_{10,0}e^{i2N\Phi_0}}{1 - r_{10,0}^2 e^{i2N\Phi_0}} E_I \\ &= \frac{r_{01,0}(1 - r_{10,0}^2 e^{i2N\Phi_0}) + r_{01,0}r_{10,0}^2 e^{i2N\Phi_0} + r_{10,0}e^{i2N\Phi_0}}{1 - r_{10,0}^2 e^{i2N\Phi_0}} E_I \\ &= \left(r_{01,0} + \frac{r_{10,0}e^{i2N\Phi_0}(1 - r_{10,0}^2)}{1 - r_{10,0}^2 e^{i2N\Phi_0}} \right) E_I \\ &= \left(r_{01,0} + \frac{t_{01,0}r_{10,0}t_{10,0}e^{i2N\Phi_0}}{1 - r_{10,0}^2 e^{i2N\Phi_0}} \right) E_I, \end{aligned} \tag{E.9.1.7}$$

and we have used the relation from continuum electrodynamics $1 - r_{10,0}^2 = t_{01,0}t_{10,0}$.

E.9.2 Scenario Two

The reflected field $E_R(z)$ is given by the total backward propagating radiative field from the meta-film at the plane $z < 0$, or

$$E_R(z) = iC \sum_{J=1}^{N} e^{-i\tilde{\omega}n(z-bJ)} p_J, \tag{E.9.2.1}$$

where the expression for p_J has been derived earlier in the main text as

$$p_J = \varepsilon_0 n^2 \alpha_{\text{atom}} E_I \frac{\sum_{\alpha=1}^{2} a_\alpha [e^{i\Phi_\alpha(J-\frac{1}{2})} + r_{10,\alpha}e^{i2N\Phi_\alpha}e^{-i\Phi_\alpha(J-\frac{1}{2})}]}{\sum_{\alpha=1}^{2} \frac{1}{t_{01,\alpha}}(1 - r_{10,\alpha}^2 e^{i2N\Phi_\alpha})}. \tag{E.9.2.2}$$

So we have

$$E_R(z) = \frac{iC\varepsilon_0 n^2 \alpha_{\text{atom}} E_I e^{-i\tilde{\omega}nz}}{\sum_{\alpha=1}^{2} \frac{1}{t_{01,\alpha}}(1 - r_{10,\alpha}^2 e^{i2N\Phi_\alpha})} \sum_{J=1}^{N} \sum_{\alpha=1}^{2} a_\alpha e^{i\phi J} [e^{i\Phi_\alpha(J-\frac{1}{2})} + r_{10,\alpha}e^{i2N\Phi_\alpha}e^{-i\Phi_\alpha(J-\frac{1}{2})}]. \tag{E.9.2.3}$$

Now we first do the sums

$$\begin{aligned}
\mathscr{T}_\alpha &= \sum_{\alpha=1}^{2} a_\alpha \sum_{J=1}^{N} e^{i\phi J}\left[e^{i\Phi_\alpha(J-\frac{1}{2})} + r_{10,\alpha}e^{i2N\Phi_\alpha}e^{-i\Phi_\alpha(J-\frac{1}{2})}\right] = \\
&= \sum_{\alpha=1}^{2} a_\alpha \left[e^{-\frac{i}{2}\Phi_\alpha}\sum_{J=1}^{N} e^{i(\phi+\Phi_\alpha)J} + r_{10,\alpha}e^{i2N\Phi_\alpha}e^{\frac{i}{2}\Phi_\alpha}\sum_{J=1}^{N} e^{i(\phi-\Phi_\alpha)J}\right] \\
&= \sum_{\alpha=1}^{2} a_\alpha \left[e^{-\frac{i}{2}\Phi_\alpha}e^{i(\phi+\Phi_\alpha)}\left(\frac{1-e^{i(\phi+\Phi_\alpha)N}}{1-e^{i(\phi+\Phi_\alpha)}}\right) + r_{10,\alpha}e^{i2N\Phi_\alpha}e^{\frac{i}{2}\Phi_\alpha}e^{i(\phi-\Phi_\alpha)}\left(\frac{1-e^{i(\phi-\Phi_\alpha)N}}{1-e^{i(\phi-\Phi_\alpha)}}\right)\right] \\
&= \sum_{\alpha=1}^{2} a_\alpha \left[e^{-\frac{i}{2}\Phi_\alpha}\left(\frac{e^{i(\phi+\Phi_\alpha)N}-1}{1-e^{-i(\phi+\Phi_\alpha)}}\right) + r_{10,\alpha}e^{i2N\Phi_\alpha}e^{\frac{i}{2}\Phi_\alpha}\left(\frac{e^{i(\phi-\Phi_\alpha)N}-1}{1-e^{-i(\phi-\Phi_\alpha)}}\right)\right].
\end{aligned} \tag{E.9.2.4}$$

Now using the expression for $r_{10,\alpha}$ defined earlier, we have

$$\begin{aligned}
\mathscr{T}_\alpha &= \sum_{\alpha=1}^{2} a_\alpha \left[e^{-\frac{i}{2}\Phi_\alpha}\frac{e^{i(\phi+\Phi_\alpha)N}-1}{e^{-i\phi}-e^{-i\Phi_\alpha}}\frac{e^{-i\phi}-e^{-i\Phi_\alpha}}{1-e^{-i(\phi+\Phi_\alpha)}} + r_{10,\alpha}e^{i2N\Phi_\alpha}e^{\frac{i}{2}\Phi_\alpha}\frac{1-e^{-i(\phi+\Phi_\alpha)}}{1-e^{-i(\phi-\Phi_\alpha)}}\frac{e^{i(\phi-\Phi_\alpha)N}-1}{1-e^{-i(\phi+\Phi_\alpha)}}\right] \\
&= \sum_{\alpha=1}^{2} a_\alpha \left[e^{-\frac{i}{2}\Phi_\alpha}\frac{e^{i(\phi+\Phi_\alpha)N}-1}{e^{-i\phi}-e^{-i\Phi_\alpha}}r_{10,\alpha} + r_{10,\alpha}e^{i2N\Phi_\alpha}e^{-\frac{i}{2}\Phi_\alpha}\frac{1}{r_{10,\alpha}}\frac{1-e^{i(\phi-\Phi_\alpha)N}}{1-e^{-i(\phi+\Phi_\alpha)}}\right] \\
&= \sum_{\alpha=1}^{2} a_\alpha \left[e^{\frac{i}{2}\Phi_\alpha}\frac{1-e^{i(\phi+\Phi_\alpha)N}}{1-e^{-i(\phi-\Phi_\alpha)}}r_{10,\alpha} + e^{i2N\Phi_\alpha}e^{-\frac{i}{2}\Phi_\alpha}\frac{1-e^{i(\phi-\Phi_\alpha)N}}{1-e^{-i(\phi+\Phi_\alpha)}}\right] \\
&= \sum_{\alpha=1}^{2} \frac{a_\alpha e^{\frac{i}{2}\Phi_\alpha}}{1-e^{-i(\phi-\Phi_\alpha)}}\left[(1-e^{i(\phi+\Phi_\alpha)N})r_{10,\alpha} + e^{i2N\Phi_\alpha}e^{-i\Phi_\alpha}\frac{1-e^{-i(\phi-\Phi_\alpha)}}{1-e^{-i(\phi+\Phi_\alpha)}}(1-e^{i(\phi-\Phi_\alpha)N})\right] \\
&= \sum_{\alpha=1}^{2} \frac{a_\alpha e^{\frac{i}{2}\Phi_\alpha}}{1-e^{-i(\phi-\Phi_\alpha)}}\left[r_{10,\alpha} - e^{i(\phi+\Phi_\alpha)N}r_{10,\alpha} - r_{10,\alpha}e^{i2N\Phi_\alpha}(1-e^{i(\phi-\Phi_\alpha)N})\right] \\
&= -\sum_{\alpha=1}^{2} \frac{a_\alpha e^{\frac{i}{2}\Phi_\alpha}}{1-e^{-i(\phi-\Phi_\alpha)}}[r_{01,\alpha} + r_{10,\alpha}e^{i2N\Phi_\alpha}].
\end{aligned} \tag{E.9.2.5}$$

So finally we have

$$E_R(z) = \frac{-iC\varepsilon_0 n^2 \alpha_{\text{atom}} E_I e^{-i\tilde{\omega}nz}}{\sum_{\alpha=1}^{2} \frac{1}{t_{01,\alpha}}(1 - r_{10,\alpha}^2 e^{i2N\Phi_\alpha})} \sum_{\alpha=1}^{2} \frac{a_\alpha e^{\frac{i}{2}\Phi_\alpha}}{1 - e^{-i(\phi-\Phi_\alpha)}}[r_{01,\alpha} + r_{10,\alpha} e^{i2N\Phi_\alpha}], \tag{E.9.2.6}$$

and using $C = \frac{\phi}{2\varepsilon_0 n^2 a^2 b}$, we get

$$E_R(z) = -i\frac{\phi}{2}\frac{\alpha_{\text{atom}}}{a^2 b} E_I e^{-i\tilde{\omega}nz} \frac{\sum_{\alpha=1}^{2} \frac{a_\alpha e^{\frac{i}{2}\Phi_\alpha}}{1-e^{-i(\phi-\Phi_\alpha)}}[r_{01,\alpha} + r_{10,\alpha} e^{i2N\Phi_\alpha}]}{\sum_{\alpha=1}^{2} \frac{1}{t_{01,\alpha}}(1 - r_{10,\alpha}^2 e^{i2N\Phi_\alpha})}. \tag{E.9.2.7}$$

E.10 The Bragg Mode

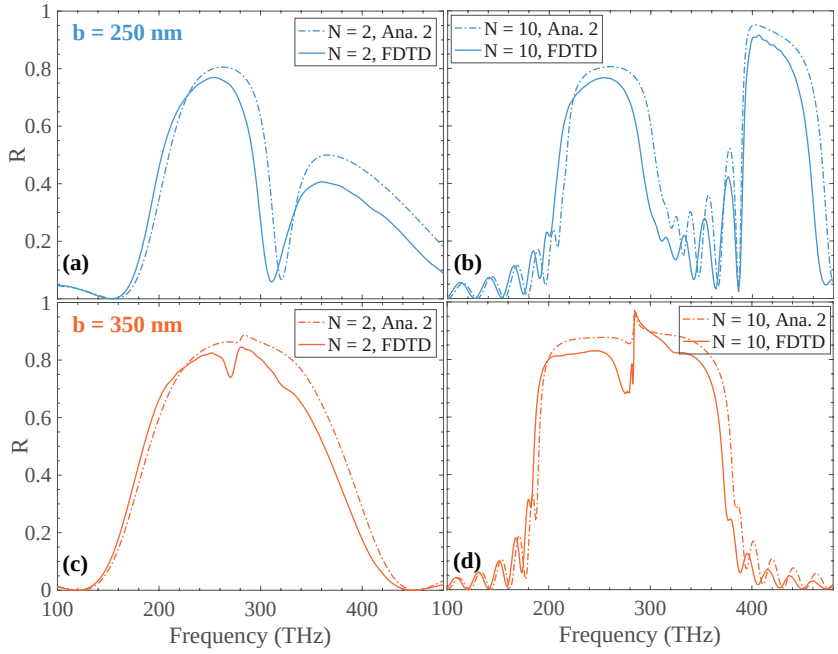

Figure E.1: Reflectance spectra of a meta-film of **two** (left) and **ten** (right) dipole planes with the lattice parameters taken to be $b = 250$ nm (top) and $b = 350$ nm (bottom), and $a = 250$ nm throughout.

Figure E.1 shows the reflectance spectra of meta-films with two (left panels)

and ten (right panels) dipole planes. The lattice parameters of the films are taken to be $b = 250$ nm (top panels) and $b = 350$ nm (bottom panels), and $a = 250$ nm throughout. The results from the analytical model in scenario two are shown as dot-dashed lines, and the results from the FDTD simulations are shown as solid lines. For the smaller plane separation (top), the reflectance peak around 250 THz is due to the resonance of the polaritons, while the peak at higher frequencies is due to the Bragg resonance. The Bragg peak unsurprisingly increases with the addition of more planes in the meta-film. At larger plane separations (bottom), the Bragg resonance redshifts until it overlaps with the polariton resonance, which broadens the stop band even further. We also note the appearance of another sharp peak at 300 THz that becomes more pronounced with a larger number of planes. This anomalous feature has been reported previously in Refs. [186, 189], and has been explained in Ref. [189] to occur due to the coherent enhancement of resonant scattering from the nanoparticles at the Bragg condition, which suppresses the absorption.

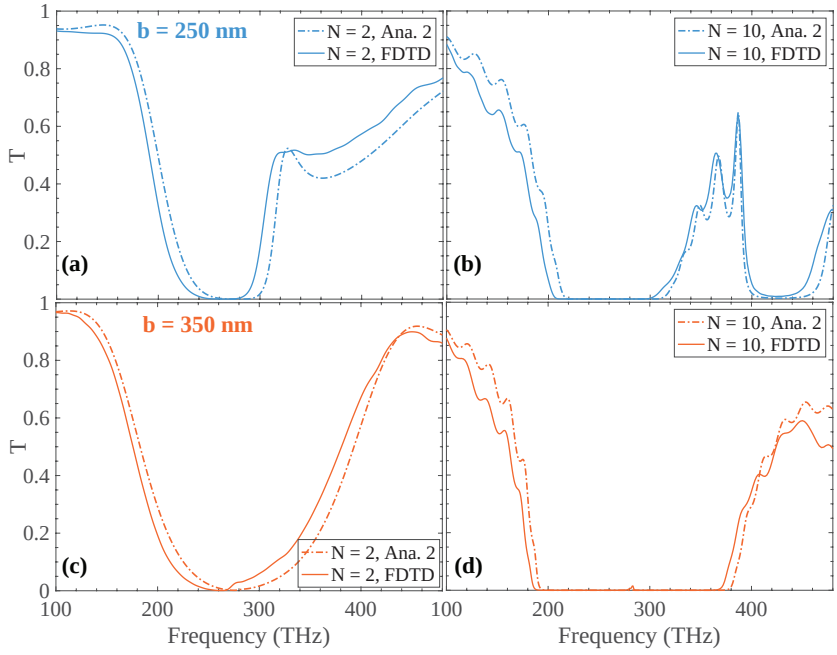

Figure E.2: Transmittance spectra of a meta-film of **two** (left) and **ten** (right) dipole planes with the lattice parameters taken to be $b = 250$ nm (top) and $b = 350$ nm (bottom), and $a = 250$ nm throughout.

Figure E.2 shows the transmittance spectra of the respective meta-films in

Fig. E.1. We note that in contrast to the polariton resonance, the Bragg resonance is an interference effect due to coherent scattering of light from all the planes in the meta-film. For $b = 250$ nm, where the Bragg resonance is in the wings of the polariton resonance, the reflectance and transmittance sum to near unity, and there is minimal absorption at the Bragg resonance. We also note that once again, the results from the analytical model in scenario two and the FDTD simulations agree reasonably well throughout. The effect of the quadrupole mode of the nanoantenna has little effect on the Bragg resonance at the higher frequencies the Bragg condition is fulfilled for the scattered light from the electric dipole modes of the nanoantennas, and the quadrupolar coupling is significantly more short-ranged than the dipolar mode.

F. Supplementary Materials for Chapter 6

F.1 Susceptibility of rubidium vapor

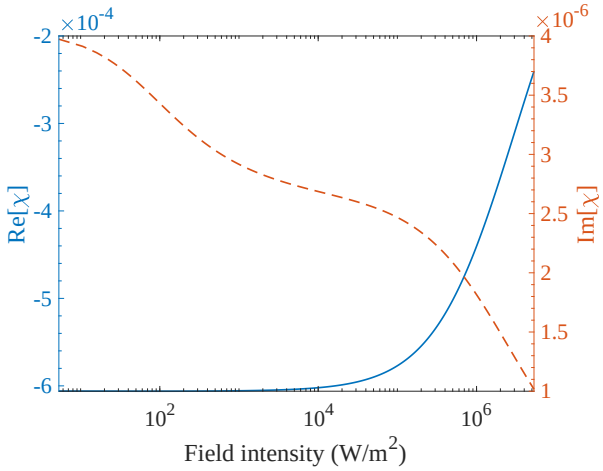

Figure F.1: Real (blue, left axis) and imaginary (red, right axis) parts of the total susceptibility of rubidium vapor versus the optical field intensity.

We use the method described in [261] to calculate the total susceptibility of rubidium vapor heated to 115 °C, and optically pumped at a detuning of 600 MHz above the ^{87}Rb D_2 $F = 1 \rightarrow F' = 2$ transition frequency. We first calculate the susceptibility contribution of each D_2 transition of rubidium to the total susceptibility using the equation (6.3.28) in ref. [4], and the parameters in ref. [262]. We include Doppler broadening of the spectrum of each resonant transition by convolving the respective spectrum with the Maxwell distribution of atom velocities [263]. We then sum these susceptibility contributions weighted by their oscillator strengths

[264]. Figure F.1 shows the real (blue, solid) and imaginary (red, dashed) parts of the total susceptibility χ of rubidium versus the optical pump intensity.

F.2 Power spectral density of the phase noise

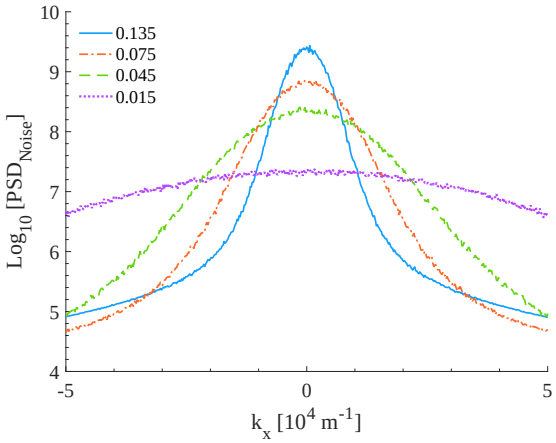

Figure F.2: The angular PSD of phase noise $e^{i\phi_{\text{rand}}(x,y)}$ of various spatial coherence lengths L_{coh}. The legend states the values of the corresponding L_{coh} normalized to the beam diameter D_0.

To calculate our phase masks $e^{i\phi_{\text{rand}}(x,y)}$, we first generate a matrix of uniformly distributed random numbers between 0 and 1. We then convolve the matrix with a Gaussian filter, whose response $G(k_x,k_y)$ in the angular frequency space (k_x,k_y) is given by Eq. (6.1) in the main text. We then multiply the entire matrix by π to rescale the phase variation to be between 0 and π rad. The spectral bandwidth of the phase noise can be estimated from its angular power spectral density (PSD), which we define as the squared magnitude of the 2D Fourier transform of $e^{i\phi_{\text{rand}}(x,y)}$. We take an ensemble average of the PSDs for 250 realizations of phase noise of a particular coherence length L_{coh}. In Fig. F.2, we show the PSD, of phase noise of normalized spatial coherence lengths L_{coh}/D_0 of 0.135 (blue, solid), 0.075 (red, dot-dashed), 0.045 (green, dashed) and 0.015 (purple, dotted), with D_0 being the Gaussian beam diameter. We note that the PSD, of noise becomes more broadband as L_{coh}/D_0 is reduced, while the total noise power remains constant.